



Scalar Fields as Dark Matter Candidates

Luis Enrique Padilla Albores

CINVESTAV, IPN
Physics department
Mexico city, Mexico
2020

Scalar Fields as Dark Matter Candidates

Luis Enrique Padilla Albores

A thesis submitted in fulfillment of the requirements
for the degree of **Doctoral in physics**

Supervisor:

Dr. Tonatiuh Matos Chassin

Co-supervisor:

Dr. José Alberto Vázquez González

CINVESTAV, IPN
Physics department
Mexico city, Mexico
2020

Publication List

a) Publications

- | | |
|----------------|--|
| Title | Consequences of the Core-Halo mass relation in the self-interacting SFDM model |
| Authors | Luis Padilla Albores , Tanja Rindler D., Alberto Vázquez, Paul R. Shapiro, Tonatiuh Matos
To be unuploaded to the arXiv. |
| Sec. in thesis | Chapter 7 |
| Title | Cosmological parameter inference with Bayesian statistics |
| Authors | Luis Padilla Albores , Alberto Vázquez, Luis O. Tellez, Luis A. Escamilla
Sent to Gravitation and Cosmology journal, arXiv:1903.11127 |
| Sec. in thesis | Appendix C |
| Title | Scalar Field Dark Matter spectator during inflation: the effect of self-interaction |
| Authors | Luis Padilla Albores , Alberto Vázquez, Gabriel Germán, Tonatiuh Matos
JCAP 05 (2019) 056, arXiv:1901.00947 |
| Sec. in thesis | Chapter 5 . |
| Title | Inflationary Cosmology: From Theory to Observations |
| Authors | Alberto Vázquez , Luis Padilla Albores , Tonatiuh Matos
Rev. Mexicana de Física E, 17, 1 Jan-Jun (2020), arXiv:1810.09934. |
| Sec. thesis | Chapter 1 |
| Title | On the possibility that ultra-light boson halos host and form super-massive black holes |
| Authors | Ana Ávilez Lopez, Tula Bernal Marin, Luis Padilla Albores , Tonatiuh Matos
Mon. Not. Roy. Astron. Soc. 477 (2018) no. 3, 3257-3272, arXiv:1704.07314 |
| Sec. thesis | Chapter 6 |

b) Conference proceedings

Title Cosmología Observacional y Estadística
Authors Alberto Vázquez, **Luis Padilla Albores**
 Conference proceeding of the Escuela de verano en física en la UNAM,
 ISSN: 2594-2697, p. 157-170
Sec. thesis Chapter **1**

c) In preparation

Title Formation and evolution of scalar field dark matter haloes
Authors **Luis Padilla Albores**, Paul R. Shapiro, Tanja Rindler D.,
 Taha Dawoodbhoy, Tonatiuh Matos
 In preparation.
Sec. thesis Chapter **9**

A mi familia

Agradecimientos

- De manera muy especial quiero agradecer a mis asesores, Dr. Tonatiuh Matos Chassin y Dr. José Alberto Vázquez González, por su paciencia y asesoría durante todo el tiempo que duró mi doctorado, así como cada uno de los consejos y apoyos que me otorgaron para hacer más simple de llevar mi trabajo doctoral. Así también quiero agradecer enormemente la amistad que me han brindado.
- Quiero agradecer también a mis sinodales, Dr. Omar Gustavo Miranda Romagnoli, Dra. Tula Bernal Marín, Dr. Josué De Santiago Sanabria y Dra. Abril Suárez Ramírez por sus útiles comentarios al revisar esta tesis.
- Al CONACyT, por la beca de doctorado que me otorgó.
- Al CINVESTAV por los apoyos económicos y las facilidades que me otorgó para hacer más amena mi estancia durante el doctorado.
- Quiero agradecer a mis profesores y amigos del CINVESTAV y de la UNAM por haberme compartido sus conocimientos y por los buenos momentos que pasamos durante todos estos años.
- Especialmente quiero agradecer a mis amigos que forman parte de mi grupo de trabajo, ya que consiero que con ellos, junto a mis asesores, Malu y a sus hijos (Karla y Carlitos), hemos formado un lazo especial más allá de lo académico, convirtiéndonos de cierta manera en una especie de familia.
- Quiero agradecer enormemente a Malu, quien me ha salvado en multiples ocasiones de quedar fuera de fechas para cumplir con varios requisitos para infinidad de cosas, como escuelas, procesos internos en CINVESTAV, viajes, etc. Le agradezco infinitamente toda su paciencia y por la amistad que me ha brindado.
- Agradezco mucho la amistad que me ha brindado Luis Adrián Escamilla en esta última etapa de mi doctorado. Ha sido muy importante para mí contar con su apoyo y sin lugar a duda ha sido el mejor roomie del mundo.
- Fuera del ambiente académico quiero agradecer de manera muy especial a Susana Plascencia (la Collie), por todo el cariño que me ha dado desde que la conozco. Aunque no siempre nos ha ido bien, siempre ha estado para mí cuando la necesito. Por eso y por más cosas, muchas gracias.

- Finalmente, pero no menos importante, agradezco infinitamente a mi familia, quienes han sido pieza clave durante toda mi vida y quienes han apoyado cada una de mis decisiones.

Resumen

Actualmente, la cosmología está pasando por una etapa de alta precisión; existen diversos experimentos a diferentes escalas que nos permiten entender cada vez más los diferentes constituyentes de nuestro Universo, así como el papel específico que cada uno de estos debe tomar en la descripción de nuestro Cosmos. En los últimos años, ha sido de particular importancia el constituyente responsable de formar la estructura a gran escala que podemos observar hoy en día. A este misterioso elemento se le suele denominar como “materia oscura”. Se han estudiado ampliamente diversos candidatos o extensiones a las teorías físicas que podrían actuar como este constituyente, resultando beneficiado de muchas maneras el modelo más simple — denominado el modelo estándar de la cosmología —, el cual asume que la materia oscura podría estar bien representada por una partícula no relativista y masiva, que interactúa débilmente con el resto de la materia. A pesar de los grandes aciertos que este modelo ha tenido, existen ciertas observaciones a escalas galácticas que sugieren, o por lo menos permiten, postular otros posibles escenarios. En este contexto, en esta tesis nos enfocamos en estudiar otro candidato que ha sido bastante popular en los últimos años; estudiamos la posibilidad de que la materia oscura en el Universo podría estar conformada de un campo escalar ultra-ligero que podría o no tener un término de auto-interacción. Este modelo ha mostrado ser bastante competitivo al poder ajustarse con muchas de las observaciones que se encuentran a nuestra disposición, así como poder resolver de manera natural muchas de las dificultades que el modelo estándar de la cosmología posee. Por tal motivo, es indispensable seguir estudiando y extendiendo la historia del modelo y así constreñir cada vez más los parámetros libres que este posee, con la finalidad de apoyar cada vez más su postulación como la materia oscura en el Universo, o en el caso opuesto, mostrar las inconsistencias que éste podría tener.

Siendo un poco más específicos en algunos de los problemas que enfrenta el modelo estándar de la cosmología, nos encontramos con las diversas observaciones de galaxias ya formadas a tiempos muy tempranos, mucho antes que lo predicho por la teoría. Más aún, en algunas de estas galaxias, se ha mostrado evidencia de que cuentan con agujeros negros súpermasivos en su núcleo galáctico. Estas últimas observaciones suponen un verdadero reto para el modelo tradicional.

En esta tesis revisamos diferentes estudios que se han hecho para el modelo de campo escalar, tanto en el caso de que éste cuente con un término de auto-interacción, así como en el caso libre. Extenderemos el estudio del modelo al considerar diferentes escenarios, como es la posibilidad de que este pudiera haber estado presente en el período inflacionario, o el estudio de campos escalares alrededor de agujeros negros súpermasivos para simular núcleos galácticos. Finalmente, para culminar con nuestro estudio, en esta tesis también propondremos un mecanismo de generación de agujeros negros súpermasivos por el colapso gravitacional de configuraciones de estos bosones de materia oscura.

Abstract

Currently, cosmology is going through a stage of high precision; there are several experiments at different scales that allow us to understand more and more the different constituents of our Universe, as well as the specific role that each of them take in the description of the cosmos. In recent years, the constituent responsible for the formation of the large-scale structure that we can observe today has been of particular importance. This mysterious element is often referred to as “Dark Matter”. There have been a great number of candidates and extensions to the standard physics theory that could act as said Dark Matter, where the simpler one — referred as the standard cosmological model —, assumes a Dark Matter represented by a non-relativistic and massive particle which interacts weakly with the rest of “normal” matter, has been favored by observational data. Despite the great successes that this model has, there are certain observations at galactic scales that suggest (or at least allow us) to postulate other possible scenarios. In this thesis, we focus on studying another candidate that has been quite popular in recent years; we study the possibility that the dark matter in the Universe could be made up of an ultra-light scalar field that could have a self-interaction term. This model has shown to be quite competitive in being able to fit many of the observations that are available to us, as well as solving in a natural manner many of the difficulties that the standard cosmological model has. For this reason, it is essential to continue studying and extending the history of this model and, thus, constrain more and more the free parameters that it has with the purpose of supporting its postulation as the true dark matter model for the Universe or, in the opposite case, to show the inconsistencies that it could have.

Being more specific in some of the problems faced by the standard cosmological model, we have several observations of galaxies already formed at very early times, much earlier than predicted by the theory. Moreover, in some of these galaxies, there is evidence that supports the existence of supermassive black holes in their galactic nuclei. The latter are a real challenge for the standard model.

In this thesis, we review different studies that have been done for the scalar field dark matter model, both in the case that it has a term of self-interaction, as well as in its free field limit. We will extend the story line of the model by considering different scenarios, such as the possibility that it could have been present during the inflationary era, or by studying scalar fields around supermassive black holes, simulating galactic nuclei. Finally, to conclude our study, in this thesis we also propose a mechanism for the generation of supermassive black holes by the gravitational collapse of configurations of these dark matter bosons.

Content

Resumen	xi
Abstract	xiii
1. Introduction	1
1.1. Some comments regarding this thesis	3
1.2. The standard cosmological model	4
1.2.1. The homogeneous Universe and the standard Big Bang theory	4
1.2.2. Content of the Universe	7
1.2.3. Thermal history of the Universe	8
1.2.3.1. Review of thermodynamic equilibrium	8
1.2.3.2. Energy and entropy density	9
1.2.3.3. History of the Universe	11
1.2.4. Distances and horizons	13
1.3. Cosmological inflation	14
1.3.1. Shortcomings of the SBB model	14
1.3.2. What is inflation?	17
1.3.3. Solution for the SBB problems	18
1.3.4. Single Field Inflation	19
1.3.5. Slow-roll approximation	21
1.3.6. Multi-field inflation	23
1.4. Cosmological Perturbations	24
1.4.1. Perturbing the background Universe	25
1.4.2. Fixing the gauge	26
1.4.3. The perturbed Einstein's and conservation equations	27
1.4.4. The adiabatic and isocurvature initial conditions	28
1.5. Power spectra	29
1.5.1. Primordial power spectrum	29
1.5.1.1. Linear perturbations during inflation: Single field model	29
1.5.1.2. Cosmological perturbations in multi-field inflation: The adiabatic and isocurvature perturbations	32
1.5.1.3. The spectator scenario	35
1.5.2. CMB power spectrum	36
1.5.2.1. General description	37

1.5.2.2. Angular power spectrum	37
1.5.3. Matter power spectrum	41
1.6. CMB observations and Planck constraints for inflation	42
2. Theoretical background for scalar fields in general relativity	46
2.1. First ideas for Scalar Fields	46
2.2. Scalar fields with gravity	48
2.2.1. The Lagrangian of the scalar field	48
2.2.2. The energy-momentum tensor for the scalar field	49
2.2.3. The generalized Klein-Gordon equation	49
2.3. Scalar field potentials	50
2.4. Gravitationally bound systems	53
2.4.1. Boson stars	53
2.4.2. Newtonian boson stars	56
3. The Dark Matter paradigm	60
3.1. Observational evidence for dark matter	60
3.1.1. Clusters of galaxies	60
3.1.2. Rotation curves in spiral galaxies	61
3.1.3. Gravitational lensing	62
3.2. The Λ CDM model	64
3.2.1. The CDM sector and structure formation	64
3.2.2. Problems with the CDM sector	67
3.2.2.1. The satellite plane problem	67
3.2.2.2. The cusp/core problem	67
3.2.2.3. The missing satellite problem	68
3.2.2.4. The too big to fail problem	69
4. The Scalar Field Dark Matter model	70
4.1. Overview of the SFDM model	70
4.2. Cosmological evolution for SFDM models	72
4.3. Linear growth in SFDM models	75
4.4. Galaxy formation in the SFDM scenario	78
4.4.1. The field vs the hydrodynamic approach in the SFDM model	79
4.4.2. Cosmological simulations, galaxies and the core-halo mass relation	81
4.5. Observational constrictions for the SFDM model	86
5. Constraining spectator scalar field dark matter from isocurvature constrictions	89
5.1. Constraints on inflationary parameters	90

5.2.	Constraining free and self-interacting ultra-light SFDM models	90
5.2.1.	Real ultra-light SFDM candidate	92
5.2.1.1.	Cosmological history	92
5.2.1.2.	Constraints from isocurvature perturbations	94
5.2.2.	Real self-interacting SFDM candidate with a repulsive self-interaction	95
5.2.2.1.	Cosmological history	95
5.2.2.2.	Constraints from isocurvature perturbations	100
6.	SFDM configurations around Super-massive Black Holes	106
6.1.	Black holes wigs as long-lasting dark matter solitons	108
6.2.	The model: Ultra-light scalar field configurations in a Schwarzschild space-time	109
6.2.1.	About the eigenvalue problem for the Schwarzschild-Klein-Gordon system	110
6.2.2.	The SFDM configuration far away from the black hole	113
6.3.	The driving effect of the black hole on the halo solution	114
6.4.	Dark Matter Mass and Density Profiles	115
6.5.	Constraint on the central DM density from the mass discrepancy-acceleration relation	118
6.5.1.	Theoretical upper bound for the central density of the SFDM configuration	120
6.6.	Kinematics of visible matter inside the gravitational potential of the SFDM halo	121
6.6.1.	Visible matter in the galaxies and the Jeans equation	123
6.6.2.	Determining the SSFDM characteristic length from the ‘ M sigma’ relation for the DMD case	124
6.6.3.	Determining the SSFDM characteristic length from the ‘ M sigma’ relation for a Sample of Luminous Galaxies	128
7.	Consequences of the core-halo mass relation in the self-interacting scalar field dark matter model	131
7.1.	Extending soliton properties	132
7.1.1.	The weak-field limit	132
7.1.1.1.	The Gaussian ansatz in the weak-field limit	134
7.1.1.2.	Understanding the $M_c - R_c$ relation from the hydrodynamic representation of the GPP system	137
7.1.2.	Fully relativistic treatment	140
7.2.	SFDM density profiles and the core-halo mass relation in the self-interacting scenario	141
7.3.	Contrasting two approximations	147

7.4. Understanding the NFW envelope structure from the hydrodynamic representation	147
7.5. Astrophysical consequences for the self-interacting SFDM model	149
7.5.1. Repulsive case ($\hat{\Lambda} > 0$)	149
7.5.2. Attractive case ($\hat{\Lambda} < 0$)	152
8. Conclusions	158
9. Future works	162
9.1. Scale-free gravitational collapse	162
9.1.1. Halo formation from scale-free linear perturbations	163
9.1.2. Halo formation from peaks of the Gaussian random noise primordial density fluctuations	163
9.2. Initial condition for the SFDM model	164
A. Compendium of General Relativity	169
B. Gauge invariant quantities	172
C. Bayesian statistics and parameter inference	173
C.1. Bayesian vs Frequentist statistics	173
C.1.1. Frequentist statistics	174
C.1.2. Bayesian statistics	175
C.2. A first look at Bayesian statistics	175
C.2.1. Bayes theorem, priors, posteriors and all that stuff	176
C.2.2. Updating the probability distribution	177
C.2.3. About the Likelihood	178
C.2.4. Letting aside the priors	179
C.2.5. Chi-square and goodness of fit	180
C.2.6. Contour plots and confidence regions	181
C.2.7. Marginalization	182
C.3. Numerical tools	182
C.3.1. MCMC techniques for parameter inference	182
C.3.2. Metropolis-Hastings algorithm	183
C.3.3. Convergence test	184
C.3.3.1. Some useful details	185
D. The attractor behaviour for the SFDM candidate	186
D.1. Justifying the slow-roll condition for the SFDM candidate	186
D.1.1. Attractor solution for the SFDM	187
E. Self-Gravity in the Newtonian Limit of the Klein-Gordon-Poisson System	188

F. Gaussian vs polynomial semi-analytic approximations	190
G. Appendix for future works	192
G.1. Effective index of the power spectrum	192
Bibliography	193

List of acronyms

Λ CDM	Λ Cold Dark Matter
ABM	Adam-Bashforth-Moulton
BBN	Big Bang Nucleosynthesis
BEC	Bose-Einstein condensate
BH	Black hole
CDM	Cold Dark Matter
CMB	Cosmic Microwave Background
DE	Dark Energy
DM	Dark Matter
DMD	Dark Matter dominated
dSph	Dwarf spheroidal galaxy
EHT	Event Horizon telescope
EKG	Einstien-Klein-Gordon
FLRW	Friedmann-Lemaitre-Robertson-Walker
GPP	Gross-Pitaevskii-Poisson
KG	Klein-Gordon
LGAL	Luminous-Galaxies
LSB	Low surface brightness
MDAR	Mass-discrepancy-acceleration-relation
MPS	Matter power spectrum
MW	Milky-Way
NFW	Navarro-Frenk-White
SBB	Standard Big Bang
SchP	Schrödinger-Poisson
SE	Schrödinger equation
SF	Scalar field
SFDM	Scalar field dark matter
SM	Stardad model
SMBH	Supermassive black hole
SSFDM	Schwarzschild scalar field dark matter
TF	Thomas-Fermi
UCD	Ultra-compact dwarf
UMA	Universal maxima acceleration
WIMP	Weakly-interacting massive particle

1. Introduction

The beginning of the standard cosmology as it is known today emerged after 1920, when the Shapley-Curtis debate was carried out ([Hetherington, 1970](#)). It was held between the astronomers Harlow Shapley and Heber Curtis, resulting in a revolution for astronomy at that time by reaching an important conclusion: “Our Universe had a larger scale than the Milky Way”. Several observations at that epoch established that the size and dynamics of the cosmos could be explained by Einstein’s General Theory of Relativity. In its childhood, cosmology was a speculative science based only on a few data sets, and it was characterized by a dispute between two cosmological models: the steady state model and the Standard Big Bang (SBB) theory. It was not until 1990 when the amount of data increased enough to discriminate and rule out compelling theories, being the SBB model awarded as the most accepted one.

The SBB cosmology continues to be the best model used to describe the central features of the observed Universe. The Big Bang model, with the addition of an inflationary era and dark matter (DM), assumed to be non-relativistic, and dark energy, assumed to be a cosmological constant – known as the Λ *Cold Dark Matter* (Λ CDM) model or *the Standard Cosmological model* –, has been successfully proved at cosmological levels. For instance, theoretical estimations of the abundance of primordial elements and numerical simulations of structure formation of galaxies and galaxy clusters are in good agreement with astronomical observations ([Kolb and Turner, 1994](#), [Springel et al., 2005](#), [Tegmark et al., 2001](#)). Also, the Λ CDM model predicts the temperature fluctuations observed in the Cosmic Microwave Background radiation (CMB) with a high degree of accuracy: inhomogeneities of about one part in one hundred thousand ([Ade et al., 2016a](#), [Komatsu et al., 2011](#)). These results, amongst many others, are the great success of the Λ CDM cosmology. Nevertheless, when we have a closer look at different scales observations seem to present certain inconsistencies or unexplained features in contrast with expected by the model. Some of these unsatisfactory aspects led to the emergence of different possible extentions of the theory or modifications to it that try to solve these inconsistencies. For example, two of these problems and that nowadays are considered as two of the greatest mysteries in cosmology and fundamental physics are:

1. The nature and origin of cosmic DM.
2. The mechanism for generating supermassive black holes (SMBHs) in the central region of most massive galaxies.

Regarding the first point, it is well established that the dark matter component must be non-interacting and have only gravitational effects on the ordinary matter. The standard model proposed to describe this new content of the Universe, named Λ CDM, suggests that DM is comprised of a nonrelativistic, collisionless gas – Cold Dark Matter (CDM) – and usually assumed to be a weakly-interacting massive particle (WIMP) which was originated as a thermal relic of the Big Bang (Peebles, 1982, White et al., 1987). Although this WIMP describes observations so well at cosmological levels, it is in apparent conflict with some observations on small-scales within galaxies (e.g. cuspy-halo density profiles, overproduction of satellite dwarfs within the Local Group, among some others, see section 3.2.2 and (Bullock and Boylan-Kolchin, 2017, Clowe et al., 2006, Klypin et al., 1999, Moore et al., 1999a, Penny et al., 2009)). In addition, all attempts to detect WIMPs directly in the laboratory or indirectly by astronomical signals from their decay or annihilation in distant objects (Gaskins, 2016) have so far failed, and a large range of the particle parameters originally predicted to be detectable have thereby been ruled out. For this reason, it seems necessary to explore alternative models to the standard Λ CDM which could help us to solve all these problems.

Now, turning to the second point, there is a host of observations that indicate the existence of SMBHs – with masses ranging between $(10^6 - 10^{10}) M_{\odot}$ – placed in the center of most massive galaxies (Cappellari, 2011, Lynden-Bell, 1969, McConnell et al., 2011), although some observations for SMBH in dwarf spheroidal galaxies (dSph) have been detected as well (see for example (Ahn et al., 2017)). In fact, recently there was a very impressive work where astronomers obtained for the first time an image of the accretion disk around the horizon of a SMBH using a world-wide network of radio observatories called the Event Horizon Telescope (EHT) (Akiyama et al., 2019). Although many researchers are trying to understand how these objects have formed, their origin is still mysterious, given their huge masses at the large redshifts ($z > 5.6$), where they have been observed (Bañados et al., 2014, Fan et al., 2003, Jiang et al., 2008, 2007, Matsuoka et al., 2018a, 2017, 2016, 2019, 2018b, Mortlock et al., 2011, Venemans et al., 2013, Willott et al., 2007, 2010, Wu et al., 2015). In order for stellar black holes (BHs) to become super-massive, they would need to accrete large amounts of baryonic material and DM over a long time, even if accretion happens at maximum Eddington rate. In addition to this puzzle of high- z SMBHs, there is also a problem in understanding why there seem to be no medium-sized black holes with masses $\sim (10^2 - 10^5)M_{\odot}$. Some standard scenarios of the formation of SMBHs consider the following: like stellar BHs which result from the collapse of massive stars, SMBHs could be produced by the collapse of massive clouds of gas during the early stages of formation of a galaxy (Silk and Rees, 1998). Another suggestion considers the formation of a cluster of stellar BHs, which eventually merge into a SMBH (Menou et al., 2001). However, so far under these standard scenarios, there is not a fully satisfactory explanation for the formation and evolution of such SMBHs at high redshifts, even taking into account effects from baryonic physics. Additionally, there exist some observations that appear to indicate that the masses

M_{SMBH} of the central SMBHs are correlated with various global properties of their host galaxies. The most important relationship concerns the mass of the SMBH and the bulge mass, and an even tighter correlation with the stellar velocity dispersion of the host galaxy bulge, first reported by (Merritt and Ferrarese, 2001) and (Gebhardt et al., 2000). As a result, it has been also suggested that the central SMBH mass is correlated with the total mass of its host galaxy (Bandara et al., 2009, Ferrarese, 2002). In this way, observations might thus indicate that the formation and growth of SMBHs over time could be related to the DM-dominated galactic halos¹, being a complication for the standard Λ CDM model.

1.1. Some comments regarding this thesis

This thesis is based in the different academic works that I have produced with more collaborators during my PhD. For example, this introductory chapter is strongly based in (Vázquez et al., 2018).

We also consider that the reader is familiar with Einstein's theory of general relativity, and then, throughout this thesis we will obviate many things about the formalism for gravity. However, if that is the case, we added an appendix A for that reader that requires an introduction of general relativity.

In this thesis, Greek letters α, β, \dots , will rank from 0 to 3 and denote space-time coordinates, while roman letters i, j, \dots rank from 1 to 3 and will be used only for space coordinates, unless otherwise specified.

The main subject of study in this thesis is the possibility that a scalar field could be used as a dark matter candidate. We will focus in a self-interacting potential of the form

$$V(\varphi) = \frac{\mu^2}{2}|\varphi|^2 + \frac{\nu}{4}|\varphi|^4, \quad (1-1)$$

where

$$\mu^2 = \frac{m^2 c^2}{\hbar^2}, \quad \nu = \frac{\lambda}{\hbar c}.$$

And then the scalar field will possess two free parameters: a mass term m (or μ) and a self-interacting term λ (or ν). Observe that in natural units ($\hbar, c = 1$) we will obtain that $\mu = m$ and $\lambda = \nu$. In this thesis, although we will work commonly in natural units, we decided to use m and λ always than we refer to the numerical values of both parameters. In fact, and taking advantage of the typical parameters that appears in the model, we will commonly refer to $m_{22} \equiv m/(10^{-22}\text{eV}/c^2)$ and $\lambda_{90} \equiv \lambda/10^{-90}$.

¹Indeed, there is another proposal to explain SMBHs from the DM side, namely so-called supermassive "dark stars", primordial stars of supermassive size which are powered by DM self-annihilation in models of WIMP and related dark matter, (Freese et al., 2010, Rindler-Daller et al., 2015). Once dark stars collapse, they could form seed black holes of about $10^5 M_{\odot}$.

In most of the thesis we will work in units where $\hbar = 1 = c$, except in section 4.4 and chapter 7, where we decided to work in units $\hbar \neq 1 \neq c$, in order to be consistent with common literature.

1.2. The standard cosmological model

1.2.1. The homogeneous Universe and the standard Big Bang theory

In its early years, the Big Bang model used to be known as the model of dynamical evolution. It was not until March 28th, 1948, that Fred Hoyle, one of its principal detractors, coined it with such a name during a BBC broadcast. One has to be aware that there exist many versions of this Big Bang model and that it tremendously evolved in the past century. In this section, we shall review the SBB model, which is the final description obtained after all these modifications took place. In the typical vocabulary of cosmologists the SBB already considers the inflationary mechanism for its description. However, in this section we shall not contemplate this era since in next section we will concentrate on it.

Before starting with the theoretical description, let us remember some assumptions about which the SBB model is built on (Coles and Lucchin, 2003):

1) The physical laws at the present time can be extrapolated further back in time and be considered as valid in the early Universe. In this context, gravity is described by the theory of General Relativity up to the Plank era.

2) The cosmological principle holds: “There do not exist preferred places in the Universe”. That is, the geometrical properties of the Universe over sufficiently large-scales are based on the homogeneity and isotropy, both of them encoded on the Friedmann-Lemaitre-Robertson-Walker (FLRW) metric

$$ds^2 = -dt^2 + a^2(t) \left[\frac{dr^2}{1 - kr^2} + r^2 (d\theta^2 + \sin^2\theta d\phi^2) \right], \quad (1-2)$$

where (t, r, θ, ϕ) describe the time-polar coordinates; the spatial curvature is given by the constant k , and the cosmic scale-factor $a(t)$ parameterises the relative expansion of the Universe, commonly normalized to today’s value $a(t_0) = 1$. Hereafter we use the criteria for the scale factor normalization and natural units $c = \hbar = 1$ unless otherwise specified, where the Planck mass m_{pl} is related to the gravitational constant G through $G \equiv m_{pl}^{-2}$.

3) On small scales, the anisotropic Universe is well described by a linear expansion of the metric around the FLRW background:

$$g_{\mu\nu}(\mathbf{r}, t) = g_{\mu\nu}^{FLRW}(\mathbf{r}, t) + \delta g_{\mu\nu}(\mathbf{r}, t). \quad (1-3)$$

To describe the general properties of the Universe, we assume its dynamics is governed by a source treated as a perfect fluid with pressure $p(t)$ and energy density $\rho(t)$. Both quantities are often related via an equation-of-state with the form of $p = p(\rho)$. Some of the well studied cases are

$$\begin{aligned} p &= \frac{\rho}{3} && \text{Radiation,} \\ p &= 0 && \text{Dust,} \\ p &= -\rho && \text{Cosmological constant } \Lambda. \end{aligned} \tag{1-4}$$

The metric (1-2) and these kind of constituents can be used to describe the observed expanding Universe along with the Einstein equations:

$$G_{\mu\nu} \equiv R_{\mu\nu} - \frac{1}{2}g_{\mu\nu}R = 8\pi GT_{\mu\nu} - g_{\mu\nu}\Lambda, \tag{1-5}$$

where $R_{\mu\nu}$ (R) is the Ricci tensor (scalar), $g_{\mu\nu}$ is the metric tensor, Λ is the cosmological constant, and $T_{\mu\nu}$ is the energy-momentum tensor, which satisfies

$$\nabla_{\nu}T^{\mu\nu} = 0, \tag{1-6}$$

i.e. the energy-momentum tensor is conserved. In the context of general relativity, a perfect fluid can be described by the energy-momentum tensor

$$T_{\mu\nu} = (\rho + p)u_{\mu}u_{\nu} + pg_{\mu\nu}, \tag{1-7}$$

where u_{μ} is the four-velocity of the fluid, satisfying

$$g^{\mu\nu}u_{\mu}u_{\nu} = -1. \tag{1-8}$$

In a FLRW Universe, the Einstein equations are reduced to the **Friedmann equation**

$$H^2 \equiv \left(\frac{\dot{a}}{a}\right)^2 = \frac{8\pi}{3m_{pl}^2}\rho - \frac{k}{a^2} + \frac{\Lambda}{3}, \tag{1-9}$$

the **acceleration equation**

$$\frac{\ddot{a}}{a} = -\frac{4\pi}{3m_{pl}^2}(\rho + 3p) + \frac{\Lambda}{3}, \tag{1-10}$$

and the energy conservation described by the **fluid equation**

$$\dot{\rho} + 3H(\rho + p) = 0, \tag{1-11}$$

where here and for the rest of this thesis overdots indicate time derivative, and H defines the *Hubble parameter*. Additionally ρ corresponds to the total energy density $\rho = \sum_i \rho_i$, where ρ_i is the density energy associated to each constituent in the Universe. Notice that we could get the acceleration equation by time-deriving (1-9) and using (1-11), therefore only two of

Table 1-1.: Evolution of the parameters of the Universe: $\rho(a)$, $a(t)$ and $H(t)$ when it is dominated by radiation, matter or a cosmological constant.

component	$\rho_i(a)$	$a(t)$	$H(t)$
radiation	$\propto a^{-4}$	$\propto t^{1/2}$	$1/(2t)$
matter	$\propto a^{-3}$	$\propto t^{2/3}$	$2/(3t)$
cosmological constant	$\propto a^0$	$\propto \exp(\sqrt{\frac{\Lambda}{3}}t)$	const

them are independent equations. Table 1-1 displays the solutions for the Friedmann and fluid equations for a flat geometry when it is considered that different components of the Universe dominate. It also shows the way the scale factor and the Hubble parameter evolve in each epoch.

From Eqn. (1-9), we can see that, for a particular Hubble parameter, there exists an energy density for which the Universe may be spatially flat ($k = 0$). This is known as the *critical density* ρ_c and is given by

$$\rho_c(t) = \frac{3m_{pl}^2 H^2}{8\pi}, \quad (1-12)$$

where ρ_c is a function of time due to the presence of H . In particular, its current value is denoted by $\rho_{c,0} = 1.87840 h^2 \times 10^{-26} \text{ kg m}^{-3}$, or in terms of more convenient units, taking into account large scales in the Universe, $\rho_{c,0} = 2.775 h^{-1} \times 10^{11} M_\odot / (h^{-1} \text{Mpc})^3$ (Ade et al., 2016c), with the solar mass denoted by $M_\odot = 1.988 \times 10^{33} \text{ g}$ and h parameterising the present value of the Hubble parameter

$$H_0 = 100h \text{ km s}^{-1} \text{Mpc}^{-1}. \quad (1-13)$$

The latest value of the Hubble parameter measured by the Planck experiment, and considering the standard cosmological model, is quoted to be (Aghanim et al., 2018):

$$H_0 = 67.4 \pm 0.5 \text{ kms}^{-1} \text{Mpc}^{-1}. \quad (1-14)$$

Unless otherwise stated, the subscript 0 refers to quantities evaluated at present time.

At the largest scales, an useful quantity to measure is the ratio of the energy density to the critical density defining the *density parameter* $\Omega_i \equiv \rho_i/\rho_c$. The Friedmann equation (1-9) can then be written in such a way to relate the total density parameter $\Omega = \sum_i \Omega_i$ and the curvature of the Universe as

$$\Omega - 1 = \frac{k}{a^2 H^2}. \quad (1-15)$$

Thus, the correspondence between the total density content Ω and the space-time curvature for different k values is:

- Open Universe : $0 < \Omega < 1 : k < 0 : \rho < \rho_c$.
- Flat Universe : $\Omega = 1 : k = 0 : \rho = \rho_c$.
- Closed Universe: $\Omega > 1 : k > 0 : \rho > \rho_c$.

Current cosmological observations, based on the standard cosmological model, suggest the present value of Ω is (McCoy, 2015)

$$\Omega_0 = 1.00 \pm 0.002, \quad (1-16)$$

that is, the present Universe is nearly flat.

1.2.2. Content of the Universe

Once the equations that define the dynamics of the Universe are known, it is necessary to specify the content of it. The Λ CDM model assumes such a content is provided by:

- **Dust:** It has no pressure. Dust is conformed by baryons (ordinary matter).
- **Dark Matter:** It is proposed to explain several astrophysical observations, like the dynamics of galaxies in the Coma cluster or the rotation curves of galaxies (see chapter 3 for a more accurate explanation). This type of matter only interacts gravitationally with the rest of the Universe and its energy density evolves in the same fashion than dust. The Λ CDM model assumes dark matter is conformed by WIMPs.
- **Radiation:** It considers photons ρ_γ and massless neutrinos ρ_ν , so the total radiation energy density in the Universe is given by

$$\rho_r = \rho_\gamma + \rho_\nu. \quad (1-17)$$

- **Dark Energy:** It is introduced to explain the current accelerated expansion of the Universe. In the Λ CDM model, dark energy is given by the cosmological constant Λ .

Table 1-1 gives the epoch at which each of the aforementioned components dominates during the evolution of the Universe. The most recent measurements from Planck (Aghanim et al., 2018) favor the value of $\Omega_b = 0.0444^{+0.0042}_{-0.0035}$, $\Omega_M \equiv \Omega_b + \Omega_{DM} = 0.266^{+0.025}_{-0.040}$, and $0.732^{+0.040}_{-0.025}$ for the density parameters at present time. In Figure 1-1 we can see the background evolution for the density parameters. Such plot can be obtained by solving the Friedmann equation 1-15, considering the time evolution described in table 1-1, and using the last measurements from Planck.

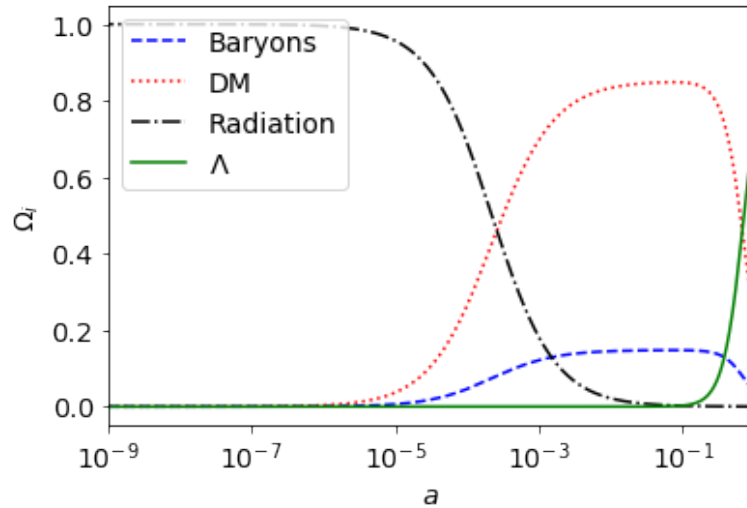


Figure 1-1.: Background evolution in terms of scale factor for the Λ CDM model.

1.2.3. Thermal history of the Universe

1.2.3.1. Review of thermodynamic equilibrium

In this section, we review the theory necessary to understand thermodynamic equilibrium. For such purpose, we follow (Rosa, 1999).

A system of particles in *kinetic equilibrium* has a phase space occupancy f , in units where the Boltzmann constant $k_b = 1$, given by

$$f(\vec{p}) = \frac{1}{e^{(E-\mu_Q)/T} \pm 1}, \quad (1-18)$$

where $E = \vec{p}^2 + \mu^2$ is the energy of the particles, \vec{p} its momentum, μ its mass, μ_Q the chemical potential, and the sign $+$ ($-$) corresponds to fermions (bosons). Commonly, the chemical potential contribution can be ignored for all particles, since all evidence indicates that this is a good approximation (Kolb and Turner, 1990). The above quantity allows to compute the associate number density n , energy density ρ , and pressure p for a dilute and weakly-interacting gas of particles with g internal degrees of freedom² as

$$n = g \int \frac{d^3\vec{p}}{(2\pi)^3} f(\vec{p}), \quad (1-19a)$$

$$\rho = g \int \frac{d^3\vec{p}}{(2\pi)^3} E(\vec{p}) f(\vec{p}), \quad (1-19b)$$

²The number of internal degrees of freedom g corresponds to the number of internal degrees of freedom of the particle. For example, an electron has two spin states $\pm 1/2$, and similarly a photon has two possible polarizations, so that $g_e = g_\gamma = 2$.

$$p = g \int \frac{d^3\vec{p}}{(2\pi)^3} \frac{|\vec{p}|^2}{3E(\vec{p})} f(\vec{p}). \quad (1-19c)$$

Two well known limits for the above quantities are

- **Relativistic species:** This limit is obtained when $T \gg \mu$, and then the Bose-Einstein and Fermi-Dirac distributions reduce to

$$f(\vec{p}) = \frac{1}{e^{|\vec{p}|/T} \pm 1}. \quad (1-20)$$

In such limit the different quantities defined in (1-19) can be solved, obtaining

$$n_{bose} = \frac{g}{\pi^2} \zeta(3) T^3, \quad \rho_{bose} = \frac{\pi^2}{30} g T^4, \quad p_{bose} = \frac{\rho_{bose}}{3}, \quad (1-21)$$

for bosons, and

$$n_{fermi} = \frac{3}{4} \frac{g}{\pi^2} \zeta(3) T^3, \quad \rho_{fermi} = \frac{7}{8} \frac{\pi^2}{30} g T^4, \quad p_{fermi} = \frac{\rho_{fermi}}{3}, \quad (1-22)$$

for fermions; where $\zeta(z)$ is the Riemann Zeta-function. Observe that in both cases, we have $p = \rho/3$, as expected.

- **Non-relativistic species:** This limit is obtained when $T \ll \mu$, and then the exponential factor dominates both the Bose-Einstein and the Fermi-Dirac distributions in (1-18), so that the bosonic or fermionic nature of the particles becomes indistinguishable. Furthermore, we have

$$E \simeq \mu \left(1 + \frac{|\vec{p}|^2}{\mu^2} \right)^{1/2} \simeq \mu + \frac{|\vec{p}|^2}{2\mu}. \quad (1-23)$$

In this limit, it is also possible to solve the different quantities defined in (1-19)

$$n = g \left(\frac{\mu T}{2\pi} \right)^{3/2} e^{-\mu/T}, \quad p = nT, \quad (1-24)$$

where it is not difficult to realize that the value obtained for p corresponds to a non-relativistic perfect gas. Additionally, since $T \ll \mu$, we have $p \ll \rho$ and the pressure may be ignored for a gas of non-relativistic particles, as we had anticipated.

1.2.3.2. Energy and entropy density

As we saw in a previous section, and is easy to see from Figure 1-1, the early Universe should be dominated by a radiation-like fluid. Let T denotes the temperature of the bath of photons in the early Universe. If there are other relativistic species during the early Universe, being the total energy of radiation given by

$$\rho_r = \frac{\pi^2}{30} g_*(T) T^4, \quad (1-25)$$

where $g_*(T)$ corresponds to the effective number of relativistic degrees of freedom presented in the Early Universe at the temperature T , including both bosons and fermions. This quantity should receive contributions from two types of species:

1. *Thermal bath*: relativistic species in thermal equilibrium with the photons $T_i = T \gg \mu_i$:

$$g_*^{th}(T) = \sum_{bosons} g_i + \frac{7}{8} \sum_{fermions} g_i. \quad (1-26)$$

2. *Decoupled species*: relativistic species that are not in thermal equilibrium with the photons, $T \neq T_i \gg \mu_i$:

$$g_*^D = \sum_{bosons} g_i \left(\frac{T_i}{T}\right)^4 + \frac{7}{8} \sum_{fermions} g_i \left(\frac{T_i}{T}\right)^4. \quad (1-27)$$

The full number of relativistic degrees of freedom for relativistic species is then given by $g_*(T) = g_*^{th}(T) + g_*^D(T)$.

On the other hand, the fundamental relation of thermodynamics for a system in equilibrium with negligible chemical potential is

$$dE = TdS - pdV. \quad (1-28)$$

In a cosmological volume V , we have $E = \rho V$. Since $V \propto a^3$, the energy conservation equation is

$$\frac{d\rho}{dt} = -3H(\rho + p) = -\frac{1}{V} \frac{dV}{dt}(\rho + p), \quad (1-29)$$

and then, by substituting the above expression into equation (1-28), we obtain

$$\frac{dS}{dt} = 0, \quad (1-30)$$

i.e., the total entropy in a comoving volume is a conserved quantity.

It is also useful to consider the entropy density $s \equiv S/V$, which from equation (1-28) follows the relation

$$d\rho - T = (Ts - \rho - p) \frac{dV}{V}. \quad (1-31)$$

For a system in equilibrium, we can write $\rho = \rho(T)$, $s = s(T)$, and $p = p(T)$, and then the above quantity depends only on the differential quantities dV and dT . Now, it is necessary that in the above expression the quantities that accompany each differential vanish, which implies from dV

$$s = \frac{1}{T}(\rho + p), \quad (1-32)$$

whereas the dT coefficient is zero by the $\dot{\rho}$ energy conservation. Particularly, for a relativistic species we have

$$s_i = \frac{4}{3} \frac{\rho_i}{T_i}. \quad (1-33)$$

The total entropy density of radiation in the early Universe is given by a sum over all relativistic species:

$$s = \frac{2\pi^2}{45} g_{*s}(T) T^3, \quad (1-34)$$

where $g_{*s}(T) = g_{*s}^{th} + g_{*s}^D$ is the effective number of relativistic degrees of freedom contributing to the entropy, $g_{*s}^{th} = g_*^{th}$ and

$$g_{*s}^D(T) = \sum g_i \left(\frac{T_i}{T} \right)^3 + \frac{7}{8} \sum_{fermions} g_i \left(\frac{T_i}{T} \right)^3. \quad (1-35)$$

Finally, entropy conservation implies that $S = a^3 s = Constant$. This implies:

$$g_{*s} T^3 a^3 = Constant \quad \Rightarrow \quad T \propto g_{*s}^{-1/3} a^{-1}. \quad (1-36)$$

As long as g_{*s} remains constant, then the T of the thermal bath decreases as the inverse of the scale factor, $T \propto a^{-1}$, and $s \propto T^3 \propto a^{-3}$.

1.2.3.3. History of the Universe

In the very early Universe, all of its content were in an homogeneous gas in thermal equilibrium. As it expanded and cooled, different species decoupled from the gas, giving rise to different epochs each of them with very particular properties. In this section we review a summary of these epochs by following ([Liddle and Lyth, 2000](#)):

- **Very early Universe:** This period is considered when the cosmic time was $10^{-42} \text{ s} < t < 10^{-14} \text{ s}$, and the energy density of the Universe was above 10 TeV. This energy scales have not been reached by particle accelerators and it is not well understood the way physical interactions were carried out. Then, all processes that could occur during this period of time (like the Big Bang, inflation, etc) are considered only as speculative.
- **Early Universe:** It happened at a cosmic time $t \sim 10^{-5} - 1 \text{ s}$. At this epoch, the energy density of the Universe was around 200 MeV, and then, there was a phase transition for the quark-gluon: free quarks and gluons where confined in baryons and mesons. At this epoch the Universe was a hot plasma where all species (electrons, photons, neutrinos, baryons, etc) were in thermal equilibrium. As the Universe expanded, its temperature and energy decreased, and the interaction rate for a given species was reduced, cooled and decoupled from the plasma. Once decoupled, that species continued its evolution as a thermal relic. When the energy of the Universe was around $\sim 0.5 \text{ MeV}$, the only species that remain coupled in the plasma were photons, electrons, protons and neutrons.
- **Nucleosynthesis:** It happened when $t_{nuc} \sim 3 - 5 \text{ min}$ and the energy of the Universe was $\sim 0.05 \text{ MeV}$. At this epoch, nuclear reactions started to be efficient, and free neutrons and protons started to form light elements like helium, lithium and deuterium.

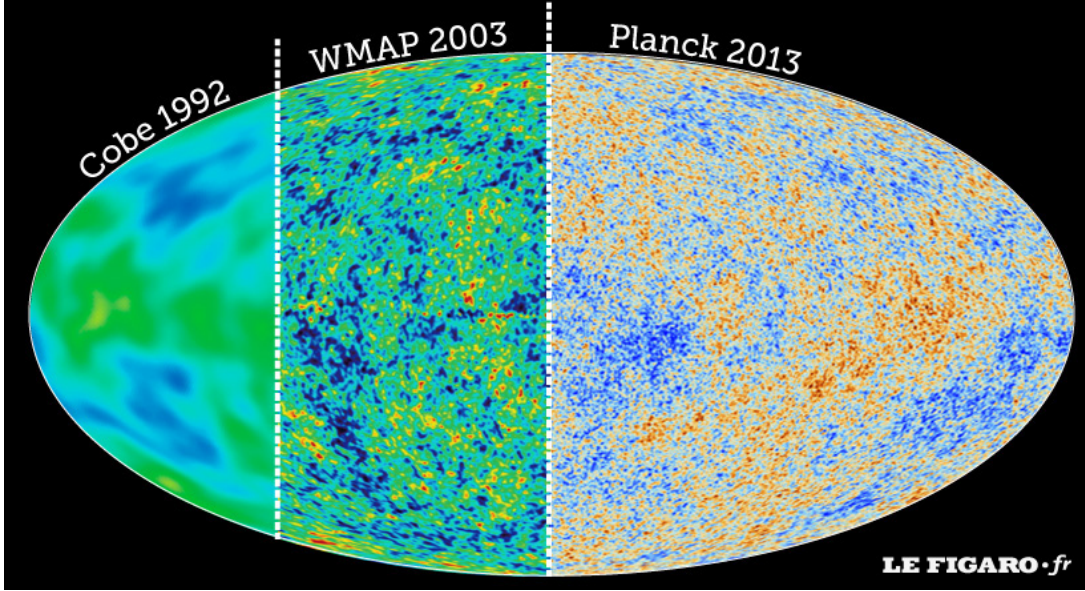


Figure 1-2.: Temperature fluctuations observed in the CMB using COBE-WMAP-Planck data (Ade et al., 2016a, Aghanim et al., 2016, Gold et al., 2011)

- **Matter-radiation equality:** This epoch occurs at $t_{eq} \sim 6 \times 10^4$ years, when the mean density in the Universe was ~ 1 eV. At this time, the energy density for matter and radiation were equal; before matter-radiation equality the Universe was dominated by radiation, while after this moment it was dominated by matter. CMB observations prefer this epoch to occur at redshift $z \simeq 3100$.
- **Recombination:** It happened at $t \sim 380,000$ years. Before this epoch, photons and electrons were coupled via Compton dispersion, while electrons and protons via Coulomb dispersion. When the energy of the Universe decreased to ~ 0.3 eV, photons were decoupled from ordinary matter. Then, free electrons recombined with protons and neutrons, producing in this way atoms. From this time on, photons streamed freely and travelled basically uninterrupted until they reached us, giving rise to the region known as the *Observable Universe*. This spherical surface, at which decoupling process occurred, is called *surface of last scattering*. The primordial photons are responsible for the CMB radiation observed today, then looking at its fluctuations is analogous of taking a picture of the Universe at that time ($t_{dec} \approx 380,000$ yrs old). In Figure 1-2, we present the CMB data measured by different experiments. It presents small anisotropies compared to the background temperature $\Delta T/T \sim 10^{-5}$.
- **Structure formation:** It happened at $t \sim 0.1 - 13.7$ Giga-years, when matter dominated the energy density in the Universe. During this period – at redshift $z \sim 1089$ – small perturbations in the DM distribution grew because of the gravitational force, giving rise to the gravitational wells necessary to attract the baryonic matter that

constitute the galaxies we can observe today.

- **Accelerated expansion:** Observations of type Ia supernovae have strongly supported that the Universe is currently in an stage of accelerated expansion. These observations, together with the ones from CMB, suggest that there exists a dominant exotic energy component in the cosmos whose functionality is to produce this acceleration.

1.2.4. Distances and horizons

The particle horizon is the distance that light could have traveled since the origin of the Universe; distances larger than the horizon are said to be causally disconnected. Massless particles travel along null geodesics ($ds^2 = 0$). Assuming the trajectory to be radial, and a FLRW spacetime (1-2) in a flat geometry, the speed of light at a given time t is simple given by $dr = dt/a(t)$. Thus, the total comoving distance travelled since the Big Bang corresponds to

$$\eta \equiv \int_0^t \frac{dt}{a(t)} = \int_0^a \frac{da}{a^2 H(a)} = \int_z^\infty \frac{dz}{H(z)} \quad (1-37)$$

where $1 + z \equiv 1/a$ is defined as the *redshift*³⁴. No information could be propagated further than η since the beginning of time (Dodelson, 2003), hence η is called the *comoving horizon*. The above quantity can be used as a temporal coordinate, called as *conformal time*, where the FLRW metric is rewritten as

$$ds^2 = a^2(\eta) \left[d\eta^2 - \frac{dr^2}{1 - kr^2} + r^2(d\theta^2 + \sin^2\theta d\phi^2) \right]. \quad (1-38)$$

In a similar way, we can define the *comoving distance* or *event horizon*

$$d_c = \int_{t_i}^{t_0} \frac{dt}{a(t)}, \quad (1-39)$$

defined as the distance that a light ray emitted at time t_i has traveled at the instant t_0 . Notice that this quantity corresponds to the radius of the region that, at time t_0 , is causally connected with the point r_0 , at which the light ray was emitted, at time t_i . For simplicity in the above expressions we considered $r_0 = 0$.

On the other hand, the *Hubble radius* or *Hubble distance* is defined by

$$d_H(t) = H^{-1}(t). \quad (1-40)$$

³Redshift is used to refer to the time at which the scale factor was a fraction $1/(1+z)$ of its present value.

It is also used to refer to the distance that light has travelled since that time.

⁴The equation $dr = 1/a(t)$ tell us that subsequent emissions of light from the source that are separated certain period of time δt can be related by $\delta t_1/a(t_1) = \delta t_2/a(t_2)$. If this subsequent emissions are the wave crests of light, δt has a frequency associate $\nu = 2/\delta t$ and then $1 + z \equiv \nu_0/\nu = a(t)$. As a increases, the frequency ν decreases, which is a redshift by definition.

This expression, usually referred simply as *horizon*, corresponds to the typical length-scale over which physical processes in the Universe operate coherently. It is also the length-scale at which general-relativity effects become important; on scales smaller than the horizon (whithin the horizon), Newtonian gravity is usually enough to describe the properties of the Universe.

Finally, the *comoving Hubble distance* is defined as

$$\chi_H = \frac{1}{aH}. \quad (1-41)$$

1.3. Cosmological inflation

Even though the SBB model possesses a strong observational support, there are still several inconsistencies or unexplained features to deal with. The inflationary model offers the most elegant way so far proposed to solve these problems, and therefore to understand why the Universe is so remarkably in agreement with the standard cosmology. It does not replace the Big Bang model, but rather, it is considered as an ‘auxiliary patch’ which occurred at the earliest stages without disturbing any of its successes. It was proposed by Guth (1981), followed by Linde (Linde, 1982). In this section we review the most relevant concepts necessary to understand this process.

1.3.1. Shortcomings of the SBB model

This section presents some of the shortcomings the SBB faced. We have to stress out that in this section we only consider the problems which are presented in the SBB model and not in the ones presented in the complete Λ CDM model since we shall concentrate on them later in this thesis.

Flatness problem

Notice that $\Omega = 1$ is a special case of equation (1-15). If the Universe was perfectly flat at the earliest epochs, then it remained so for all time. Nevertheless, a flat geometry is an unstable critical situation; that is, even a tiny deviation from it would cause that Ω evolved quite differently, and very quickly the Universe would have become more curved. This can be seen as a consequence due to aH is a decreasing function of time during a radiation or matter domination epoch, as it can be observed in Table 1-1, then

$$\begin{aligned} |\Omega - 1| &\propto t && \text{during radiation domination,} \\ |\Omega - 1| &\propto t^{2/3} && \text{during dust domination.} \end{aligned}$$

Since the present age of the Universe is estimated to be $t_0 \simeq 13.787$ Gyrs (Aghanim et al., 2018), from the above equation, we can deduce the required value of $|\Omega - 1| = |\Omega_0 - 1|t/t_0$

at different times to obtain the correct spatial-geometry at the present time $|\Omega_0 - 1|$. For instance, let us consider some particular epochs in a nearly flat Universe:

- At Decoupling time ($t \simeq 10^{13}$ sec), we need that $|\Omega - 1| \leq 10^{-3}$.
- At Nucleosynthesis time ($t \simeq 1$ sec), we need that $|\Omega - 1| \leq 10^{-16}$.
- At the Planck epoch ($t \simeq 10^{-43}$ sec), we need that $|\Omega - 1| \leq 10^{-64}$.

Because there is no reason to prefer a Universe with critical density, hence $|\Omega - 1|$ should not necessarily be exactly zero. Consequently, at early times $|\Omega - 1|$ has to be fine-tuned extremely close to zero to reach its actual observed value.

Horizon problem

The horizon problem is one of the most important problems in the SBB model, as it refers to the communication between different regions of the Universe. Bearing in mind the existence of the Big Bang, the age of the Universe is a finite quantity and hence even light should have only traveled a finite distance by all this time.

As we already mentioned, Figure 1-2 shows light seen in all directions of the sky. These photons randomly distributed have nearly the same temperature $T_0 = 2.725$ K plus small fluctuations (about one part in one hundred thousand) (Ade et al., 2016c, Groom and Scott, 2017), being at the same temperature a property of thermal equilibrium. Observations are therefore easily explained if different regions of the sky had been able to interact and moved towards thermal equilibrium. In other words, the isotropy observed in the CMB might imply that the radiation was homogeneous and isotropic within regions located on the last scattering surface. Oddly, the comoving horizon right before photons decoupled was significantly smaller than the corresponding horizon observed today. This means that photons coming from regions of the sky separated by more than the horizon scale at last scattering, typically about 2° , and would not had been able to interact and established thermal equilibrium before decoupling. A simple calculation displays that at decoupling the comoving horizon was $90 h^{-1}$ Mpc, and would be stretched up to $2998 h^{-1}$ Mpc at present time. Then, the volume ratio provides that the microwave background should have consisted of about $\sim 10^5$ causally disconnected regions (McCoy, 2015). Therefore, the Big Bang model, by itself, does not offer an explanation on why temperatures seen in opposite directions of the sky are so accurately the same; the homogeneity must had been part of the initial conditions? On the other hand, the microwave background is not perfectly isotropic, but instead exhibits small fluctuations as detected initially by the Cosmic Background Explorer satellite (COBE) (Smoot et al., 1992), and then, with improved measurements, by the Wilkinson Microwave Anisotropy Probe (WMAP) (Hinshaw et al., 2009, Larson et al., 2011), and nowadays with the Planck satellite (Collaboration et al., 2006). These tiny irregularities are thought to be the ‘seeds’ that grew up until becoming the observed structure in the Universe.

Monopole problem

Following the line to find out the simplest theory to describe the Universe, several models in particle physics were suggested in order to unify three of the four forces present in the Standard Model of Particle Physics (SM): strong force, described by the group $SU(3)$, weak and electro-magnetic force, with an associated group $SU(2) \otimes U(1)$. These classes of theories are called *Grand Unified Theories (GUT)* (Georgi and Glashow, 1974). An important point to mention in favour of GUT is that they are the only ones that predict the equality electron-proton charge magnitude. Also, there are good reasons to believe the origin of *baryon asymmetry* might have been generated on the GUTs (Kolb and Turner, 1983).

Basically, these kind of theories assert that in the early stages of the Universe ($t \sim 10^{-43}$ sec), at highly extreme temperatures ($T_{GUT} \sim 10^{32}$ K), existed a unified or *symmetric phase* described by a group G . As the Universe temperature dropped off, it went through different phase transitions until reach the symmetries associated to the standard model of particle physics, generating hence the matter particles such as electrons, protons, and neutrons. When a phase transition happens, its symmetry is broken, and thus the symmetry group changes by itself, for instance:

- GUT transition:

$$G \rightarrow SU(3) \otimes SU(2) \otimes U(1).$$

- Electroweak transition:

$$SU(3) \otimes SU(2) \otimes U(1) \rightarrow SU(3) \otimes U(1).$$

The phase transitions have plenty of implications. One of the most important is the *topological defects* production, which depends on the type of symmetry breaking and the spatial dimension (Vilenkin and Shellard, 2000), some of them are:

- Monopoles (zero dimensional).
- Strings (one dimensional).
- Domain Walls (two dimensional).
- Textures (three dimensional).

Monopoles are therefore expected to emerge as a consequence of unification models. Besides that, from particle physics models, there are not theoretical constraints on the mass a monopole should carry out. However, from LHC constrictions and grand unification theories, the mass of the monopole could be $4 \times 10^3 - 10^{16}$ GeV (Mermud, 2013). Hence, based on their non-relativistic character, a crude calculation predicts an extremely high abundance at present time (Ambrosio et al., 2002, Coles and Lucchin, 2003):

$$\Omega_M \simeq 10^{16}.$$

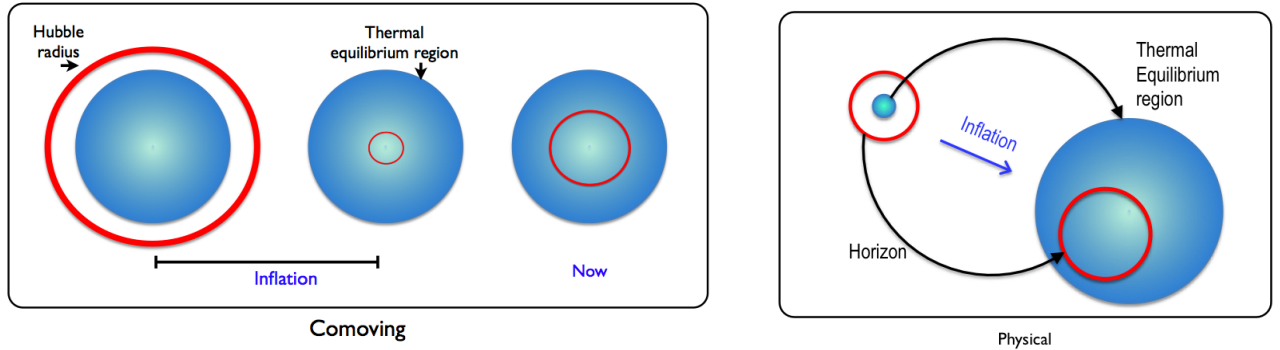


Figure 1-3.: Left: Schematic behaviour of the comoving Hubble radius during the inflationary period. Right: Physical evolution of the observable universe during the inflationary period (Figure taken from (Vázquez et al., 2018)).

According to this prediction, the Universe would be dominated by magnetic monopoles in contrast with current observations; no one has found anyone yet!

1.3.2. What is inflation?

Inflation is defined as the epoch in the early Universe in which the scale factor is exponentially expanded in just a fraction of a second:

$$\text{INFLATION} \iff \ddot{a} > 0 \quad (1-42)$$

$$\iff \frac{d}{dt} \left(\frac{1}{aH} \right) < 0. \quad (1-43)$$

The factor $1/(aH)$ corresponds to the comoving Hubble length (1-41), which is interpreted as the observable Universe becoming smaller during inflation. This process allows our observable region to lay down within a region that was inside the Hubble radius at the beginning of inflation. In (Liddle, 1999) words: “is something similar to zooming in on a small region of the initial Universe”, see Figure 1-3.

From the acceleration equation (1-10), the condition for inflation, in terms of the material required to drive the expansion, is

$$\ddot{a} > 0 \iff (\rho + 3p) < 0. \quad (1-44)$$

Because in standard physics it is always postulated ρ as a positive quantity, and hence in order to satisfy the acceleration condition it is necessary for the overall pressure to have

$$\text{INFLATION} \iff p < -\rho/3. \quad (1-45)$$

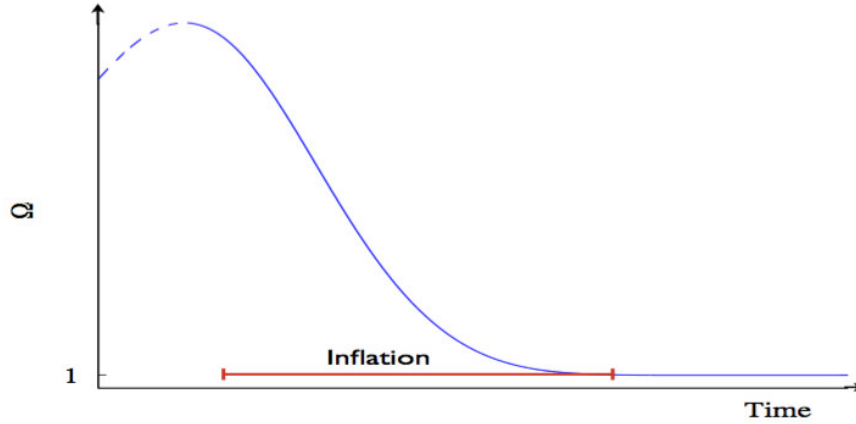


Figure 1-4.: Evolution of the density parameter Ω during the inflationary period. Ω is driven towards unity, rather than away from it (Figure taken from (Vázquez et al., 2018)).

Nonetheless, neither a radiation nor a matter component satisfies such condition. Let us postpone for a bit the problem of finding a candidate which may satisfy this inflationary condition and just concentrate in seeing how this stage can help us to solve the problems mentioned in section 1.3.1.

1.3.3. Solution for the SBB problems

Flatness problem

A typical solution is a Universe with a cosmological constant Λ , which can be interpreted as a perfect fluid with equation-of-state $p = -\rho$. Having this condition, we observe from Table 1-1 that the Universe is exponentially expanded and the Hubble parameter H constant, then, the condition (1-43) is naturally fulfilled. This epoch is called *de Sitter stage*. However, postulating a cosmological constant as a candidate to drive inflation might create more problems than solutions by itself, i.e., reheating process (Carroll, 2001).

Let us look at what happens when a general solution is considered. If somehow there was an accelerated expansion, $1/(aH)$ tends to be smaller on time and hence, by the expression (1-15), Ω is driven towards the unity rather than away from it. Then, we may ask ourselves by how much should $1/(aH)$ decrease. If the inflationary period started at time $t = t_i$ and ended up approximately at the beginning of the radiation dominated era ($t = t_f$), then

$$|\Omega - 1|_{t=t_f} \sim 10^{-60},$$

and

$$\frac{|\Omega - 1|_{t=t_f}}{|\Omega - 1|_{t=t_i}} = \left(\frac{a_i}{a_f}\right)^2 \equiv e^{-2N}. \quad (1-46)$$

So, the required condition to reproduce the value of Ω_0 measured today is that inflation lasted for at least $N \equiv \ln a \gtrsim 60$, then Ω must be extraordinarily close to one that we still observe such quantity today. In this sense, inflation magnifies the curvature radius of the Universe, so locally the Universe seems to be flat with great precision (see Figure 1-4).

Horizon problem

As we have already seen, during inflation, the universe expanded drastically, and there was a reduction in the comoving Hubble length. This allowed a tiny region located inside the Hubble radius to evolve and constitute our present observable Universe. Fluctuations were hence stretched outside of the horizon during inflation and re-entered the horizon in the late Universe, see Figure 1-3. Scales that were outside the horizon at CMB-decoupling were, in fact, inside the horizon before inflation. The region of space corresponding to the observable universe, therefore, was in thermal equilibrium before inflation, and the uniformity of the CMB is essentially explained.

Monopole problem

The monopole problem was initially the motivation to develop the inflationary cosmology (Guth, 1997). During the inflationary epoch, the Universe led to a dramatic expansion over which the density of the unwanted particles were diluted away. Generating enough expansion, the dilution made sure the particles stayed completely out of the observable Universe, making pretty difficult to localise even a single monopole.

1.3.4. Single Field Inflation

Throughout the literature, there exists a broad diversity of models that have been suggested to carry out the inflationary process (Liddle and Lyth, 2000, Lyth and Riotto, 1999, Olive, 1990). In this section, we review the model of scalar fields (SFs) as the responsible for this process. We only describe the necessary concepts to understand this mechanism. However, in the next chapter, we shall concentrate a little more in the theory for SFs in general relativity. Then, if there are some details in this description that could appear to the reader difficult to understand, we encourage to review this section together with the next chapter in parallel. In this section, we also explain how to relate theoretical predictions to observable quantities. Here, we limit ourselves to models based on general gravity, i.e., derived from the Einstein-Hilbert action, and single-field models described by a homogeneous slow-rolling scalar field ϕ . Nevertheless, in section 1.5.1.2 we provide a very brief introduction to several scalar fields and the concept of spectator SFs during inflation.

Inflation relies on the existence of an early epoch in the Universe dominated by a very different form of energy; remember the requirement of the unusual property of a negative pressure. Such condition can be satisfied by a single real SF. The SF which drives the

Universe to an inflationary epoch is often termed as the *inflaton field*.

Consider a SF minimally coupled to gravity with an arbitrary potential $V(\phi)$. The energy-momentum tensor corresponding to this field is given by

$$T_{\mu\nu}^{(\phi)} = \partial_\mu\phi\partial_\nu\phi - g_{\mu\nu}\mathcal{L}_\phi. \quad (1-47)$$

where

$$\mathcal{L}_\phi = \frac{1}{2}\partial_\mu\phi\partial^\mu\phi - V(\phi), \quad (1-48)$$

In the same way as the perfect fluid treatment, the energy density ρ_ϕ and pressure density p_ϕ in the FLRW metric (1-2) are found to be

$$T_{00}^{(\phi)} = \rho_\phi = \frac{1}{2}\dot{\phi}^2 + V(\phi) + \frac{(\nabla\phi)^2}{2a^2}, \quad (1-49)$$

$$T_{ii}^{(\phi)} = p_\phi = \frac{1}{2}\dot{\phi}^2 - V(\phi) - \frac{(\nabla\phi)^2}{6a^2}. \quad (1-50)$$

Considering a homogeneous field, its corresponding equation-of-state is

$$w_\phi = \frac{p_\phi}{\rho_\phi} = \frac{\frac{1}{2}\dot{\phi}^2 - V(\phi)}{\frac{1}{2}\dot{\phi}^2 + V(\phi)}. \quad (1-51)$$

Usually it is splited the inflaton field as

$$\phi(\mathbf{x}, t) = \phi_0(t) + \delta\phi(\mathbf{x}, t), \quad (1-52)$$

where ϕ_0 is considered a classical field, that is, the mean value of the inflaton on the homogeneous and isotropic state, whereas $\delta\phi(\mathbf{x}, t)$ describes the quantum fluctuations around ϕ_0 .

The evolution equation for the background field ϕ_0 is given by

$$\ddot{\phi}_0 + 3H\dot{\phi}_0 = -V'(\phi_0), \quad (1-53)$$

and moreover, the Friedmann equation (1-9) with negligible curvature becomes

$$H^2 = \frac{8\pi}{3m_{pl}^2} \left[\frac{1}{2}\dot{\phi}_0^2 + V(\phi_0) \right], \quad (1-54)$$

where we have used primes as derivatives with respect to the scalar field ϕ_0 .

From the structure of the effective energy density and pressure, the acceleration equation (1-10) becomes,

$$\frac{\ddot{a}}{a} = -\frac{8\pi}{3m_{pl}^2} \left(\dot{\phi}_0^2 - V(\phi_0) \right). \quad (1-55)$$

Therefore, the inflationary condition to be satisfied is $\dot{\phi}_0^2 < V(\phi_0)$, which is easily fulfilled with a suitably flat potential. Now on in this section, we shall omit the subscript '0' by convenience.

1.3.5. Slow-roll approximation

As we have noted, a period of accelerated expansion can be generated by the cosmological constant (Λ) and hence solve the aforementioned problems. After a brief period of time, inflation must end up, and its energy being converted into conventional matter/radiation; this process is called *reheating*. In a Universe dominated by a cosmological constant, the reheating process is seen as Λ decaying into conventional particles, however claiming that Λ is able to decay is still a naive way to face the problem. On the other hand, scalar fields have the property to behave like a *dynamical cosmological constant*. Based on this approach, it is useful to suggest a scalar field model starting with a nearly flat potential, i.e., initially satisfies the *first slow-roll* condition $\dot{\phi}^2 \ll V(\phi)$. This condition may not necessarily be fulfilled for a long time, but to avoid this problem, a *second slow-roll* condition is defined as $|\ddot{\phi}| \ll |V_{,\phi}|$, or equivalently $|\ddot{\phi}| \ll 3H|\dot{\phi}|$. In this case, the scalar field is slowly rolling down its potential and, by obvious reasons, such approximation is called *slow-roll* (Liddle and Lyth, 1992, Liddle and Turner, 1994). The equations of motion (1-53) and (1-54), for slow-roll inflation, then become

$$3H\dot{\phi} \simeq -V'(\phi), \quad (1-56)$$

$$H^2 \simeq \frac{8\pi}{3m_{pl}^2}V(\phi). \quad (1-57)$$

It is easily verifiable that the slow-roll approximation requires the slope and curvature of the potential to be small: $V', V'' \ll V$.

The inflationary process happens when the kinetic part of the inflaton field is subdominant over the potential field $V(\phi)$. When both quantities become comparable, the inflationary period ends up giving rise finally to the reheating process, see Fig. 1-5.

It is now useful to introduce the potential *slow-roll parameters* ϵ_v and η_v in the following way (Liddle and Lyth, 1992, Riotto, 2003):

$$\epsilon_v(\phi) \equiv \frac{m_{pl}^2}{16\pi} \left(\frac{V'(\phi)}{V(\phi)} \right)^2, \quad (1-58)$$

$$\eta_v(\phi) \equiv \frac{m_{pl}^2}{8\pi} \frac{V''(\phi)}{V(\phi)}. \quad (1-59)$$

Equations (1-56) and (1-57) are in agreement with the slow-roll approximation when the following conditions hold:

$$\epsilon_v(\phi) \ll 1, \quad |\eta_v(\phi)| \ll 1.$$

These conditions are sufficient, but not necessary, because the validity of the slow-roll approximations was a requirement in its derivation. The physical meaning of $\epsilon_v(\phi)$ can be explicitly seen by expressing equation (1-42) in terms of ϕ , then, the inflationary condition is equivalent to

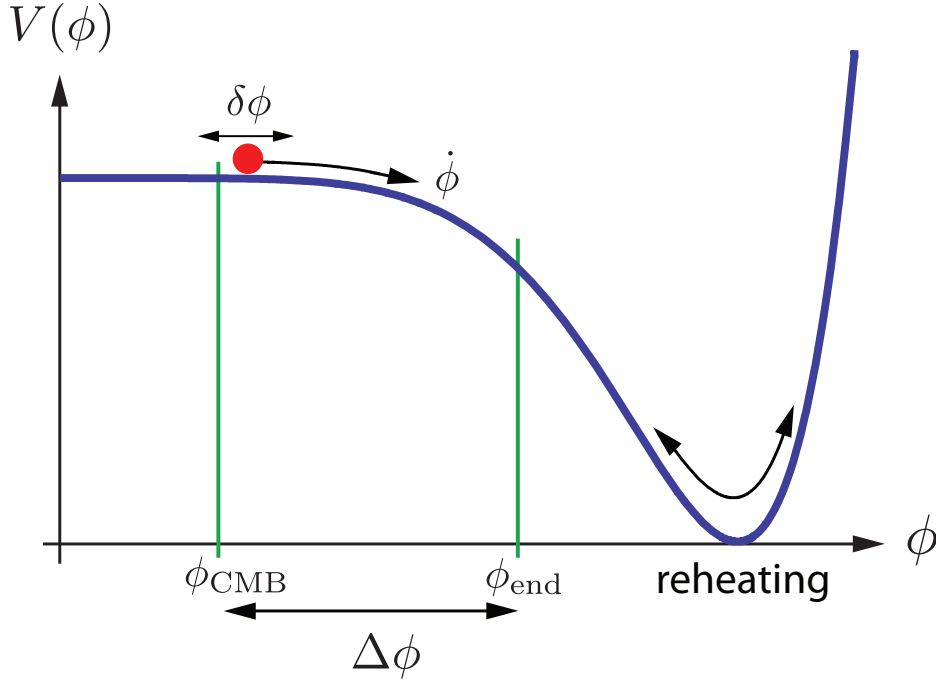


Figure 1-5.: Schematic inflationary process (Baumann, 2009).

$$\frac{\ddot{a}}{a} > 0 \implies \epsilon_v(\phi) < 1. \quad (1-60)$$

Hence, inflation concludes when the value $\epsilon_v(\phi_{end}) = 1$ is approached.

Within these approximations, it is straightforward to find out the scale factor a between the beginning and the end of inflation. Because the size of the expansion is an enormous quantity, it is useful to compute it in terms of the e -fold number N , defined by

$$N \equiv \ln \frac{a(t_{end})}{a(t)} = \int_t^{t_e} H dt \simeq \frac{8\pi}{m_{pl}^2} \int_{\phi_e}^{\phi} \frac{V}{V'} d\phi. \quad (1-61)$$

To give an estimate of the number of e -folds, let us suppose that the evolution of the Universe can be split up into different epochs and concentrate on a particular scale k (at this point we only consider a generic scale, however, in a next section, we shall explain that such scales can be associated to perturbations in a Fourier space) which was inside the horizon at the beginning of inflation and that, at certain time, during the inflationary epoch, left the horizon. If we consider particularly the moment when the size of such scale was equal to the horizon, i.e. $k = aH$, then we can assume the following cosmological history:

- Inflationary era: horizon crossing ($k = aH$) \rightarrow end of inflation a_{end} .
- Radiation era: reheating a_{reh} \rightarrow matter-radiation equality a_{eq} .
- Matter era: a_{eq} \rightarrow present a_0 .

Assuming the transition between one era to another is instantaneous, then $N(k) = \ln(a_k/a_0)$ can be easily computed with:

$$\frac{k}{a_0 H_0} = \frac{a_k H_k}{a_0 H_0} = \frac{a_k}{a_{end}} \frac{a_{end}}{a_{reh}} \frac{a_{reh}}{a_{eq}} \frac{a_{eq}}{a_0} \frac{H_k}{H_0},$$

where $a_h(H_k)$ refers to the scale factor (Hubble parameter) measured at the moment when k equals the horizon. Then, one has (Liddle and Lyth, 2000)

$$N(k) = 62 - \ln \frac{k}{a_0 H_0} - \ln \frac{10^{16} GeV}{V_k^{1/4}} + \ln \frac{V_k^{1/4}}{V_{end}} - \frac{1}{3} \ln \frac{V_{end}^{1/4}}{\rho_{reh}^{1/4}}.$$

The last three terms are small quantities related with energy scales during the inflationary process and usually can be ignored. The precise value for the second quantity depends on the model as well as the Planck normalisation; however, it does not present any significant change to the total amount of e -folds. Thus, the value of total e -foldings is ranged from 50-70 (Lyth and Riotto, 1999). Nevertheless, this value could change if a modification of the full history of the Universe is considered. For instance, thermal inflation can alter N up to a minimum value of $N = 25$ (Lyth and Stewart, 1995, 1996).

As we noted, the parameters to describe inflation can be presented as a function of the scalar field potential. That is, specifying an inflationary model with a single scalar field is just selecting an inflationary potential $V(\phi)$. At this point, it is necessary to mention that these potentials are not chosen arbitrarily, but in fact, there is a whole line of research motivated by fundamental physics.

1.3.6. Multi-field inflation

Assuming a single scalar field is responsible for inflation might be only an approximation, since the presence of multiple fields could also drive this process. In this section, we show how the cosmological equations are modified when two scalar fields are responsible for driving the inflationary process (Byrnes and Wands, 2006). The generalization to more than two fields can be easily obtained and is described by (Gong, 2017).

Consider a two-field inflationary model with canonical kinetic terms, and dynamics described by an arbitrary interaction potential $V(\phi, \varphi)$. As usual, it is assumed the classical fields are real, homogeneous and evolve in a FLRW background. Thus, the background equation of motion for each scalar field and the Hubble parameter are

$$\ddot{\phi}_i + 3H\dot{\phi}_i + \frac{dV_i}{d|\phi_i|^2} \phi_i = 0, \quad (i = \phi, \varphi), \quad (1-62a)$$

$$H^2 = \frac{8\pi}{3m_{pl}^2} \left[V + \frac{1}{2} (\dot{\phi}^2 + \dot{\varphi}^2) \right], \quad (1-62b)$$

where $V_i \equiv \partial V / \partial \phi_i$. During inflation it is adopted the slow-roll approximation for each field. This occurs as long as the condition $\epsilon_i, |\eta_{ij}| \ll 1$ is fulfilled; ϵ_i and η_{ij} are now a new set of slow-roll parameters defined by

$$\epsilon_i = \frac{m_{pl}^2}{16\pi} \left(\frac{V_i}{V} \right)^2, \quad \eta_{ij} = \frac{m_{pl}^2}{8\pi} \left(\frac{V_{ij}}{V} \right). \quad (1-63)$$

The set of equations (1-62) are re-written in the slow-roll approximation as

$$\dot{\phi}_i \simeq -\frac{V_i}{3H} \left(1 + \frac{1}{3} \delta_i^H \right), \quad H^2 \simeq \frac{8\pi}{3m_{pl}^2} V \left(1 + \frac{1}{3} \epsilon^H \right), \quad (1-64)$$

with δ_i^H and ϵ^H the new slow-roll parameters:

$$\delta_i^H = -\frac{\ddot{\phi}_i}{H\dot{\phi}_i}, \quad \epsilon^H = \epsilon_\phi + \epsilon_\varphi. \quad (1-65)$$

1.4. Cosmological Perturbations

The homogeneous and isotropic model provides an accurate description for the Universe at large scales. However, in this description, there is no chance for structures to be formed. At small scales, there exist several cosmological objects (as galaxies, clusters, etc) which are overdensities of matter. Those objects emerged as a consequence of gravitational instabilities suffered by small fluctuations of the matter content, i.e., inhomogeneities in the matter field. As we will see later, such initial perturbations can be also related to the fluctuations found in the CMB measurements. As we already mentioned, the CMB presents small anisotropies $\delta T/T = 10^{-5}$, which suggest to use the theory of linear perturbations for the description of the perturbed Universe. This idea is straightforward: perturb the metric and energy-momentum tensor in Einstein's equations about the background and, to first order, drop small quantities. Then solve the coupled system of equations

$$\delta G_{\mu\nu} = 8\pi G \delta T_{\mu\nu}. \quad (1-66)$$

for a particular scale perturbation k^5 .

As we already commented in 1.2.4, the study of cosmological perturbations can be divided in two scenarios depending on the wavelength of the perturbation λ compared with the Hubble horizon: when the scale perturbations are well within the Hubble horizon $\lambda \ll H^{-1}$, and when the wavelength is larger than the Hubble horizon $\lambda \gg H^{-1}$. Here, we present the basic description for the cosmological perturbations theory. For our purpose we review different references, which we recommend for the reader to review if he/she is interested in a more detailed description of this formalism. These are: (Bardeen, 1980, Dodelson, 2003, Hu and Dodelson, 2002, Kodama and Sasaki, 1984, Liddle and Lyth, 2000, Mukhanov, 2005, Mukhanov et al., 1992).

⁵We don't have to confuse between the scale perturbation and the curvature parameter. In this section, always that appears letter k will represent the first of these two possibilities.

1.4.1. Perturbing the background Universe

The first step that is necessary in the general relativistic description for small perturbations is to perturb the metric and energy-momentum tensor in the following way

$$g_{\mu\nu} \rightarrow \bar{g}_{\mu\nu} + a^2 h_{\mu\nu}, \quad T_{\mu\nu} \rightarrow \bar{T}_{\mu\nu} + \delta T_{\mu\nu}, \quad (1-67)$$

where the bar refers to background quantities. Up to linear order in the perfect fluid description, the energy-momentum perturbations can be expressed as

$$T_0^0 = -\bar{\rho}(1 + \delta), \quad (1-68a)$$

$$T_0^i = (\bar{\rho} + \bar{p})\delta u^i \equiv q^i, \quad (1-68b)$$

$$T_i^0 = -(\bar{\rho} + \bar{p})(\delta u_i + B_i), \quad (1-68c)$$

$$T_j^i = \bar{p} [(1 + \pi_L)\delta_j^i + \Pi_j^i], \quad (1-68d)$$

where δu_μ is the perturbation of the four-velocity u_μ , $\delta \equiv \delta\rho/\bar{\rho}$ is the total *density contrast*, $\delta\rho$ is the perturbation in the energy density, q_i is defined as the 3-momentum density, Π is the anisotropic-stress tensor with traceless part $\pi_j^i = \bar{p}\Pi_j^i$, $\Pi_0^0 = \Pi_i^0 = \Pi_0^i = 0$, and $\bar{p}\pi_L \equiv \delta p$, being δp the total perturbation in pressure.

Due to the background homogeneity and isotropy in the Universe, we can decompose the perturbation of the metric $h_{\mu\nu}$ as

$$h_{\mu\nu}dx^\mu dx^\nu = -2A d\eta^2 - 2B_i dx^i d\eta + 2H_{ij} dx^i dx^j \quad (1-69)$$

where $A(\eta, \mathbf{x})$ is a scalar perturbation, B_i is a vector perturbation, and H_{ij} is a symmetric trace-free tensor perturbation. Particularly these quantities can be also decomposed as

$$B_i = \partial_i B + B_i^{(V)}, \quad (1-70a)$$

$$H_{ij} = H_L \delta_{ij} + \partial_{(i} \partial_{j)} H_T + \partial_{(i} \partial_{j)} H^{(V)} + H_{ij}^{(T)} \quad (1-70b)$$

where

$$\begin{aligned} \partial_{(i} \partial_{j)} H_T &\equiv \partial_i \partial_j H_T - \frac{1}{3} \delta_{ij} \nabla^2 H_T, \\ \partial_{(i} \partial_{j)} H^{(V)} &= \partial_i \partial_j H + \frac{1}{3} \delta_{ij} \nabla^2 H^{(V)}, \end{aligned} \quad (1-71)$$

B , H_L and H_T are new scalar perturbations, $B_i^{(V)}$ and $H_j^{(V)}$ are vector perturbations and $H_{ij}^{(T)}$ is a new tensor perturbation. Additionally these quantities have the properties that H_T is trace-free, $H_i^{(V)}$ is transverse, and $H_{ij}^{(T)}$ is symmetric, trace-free and transverse. Then, the most general scalar perturbation of the metric has therefore ten separate degrees-of-freedom: 1 from A , 3 from B_i and 6 from H_{ij} . This represents a problem given that in the Einstein field equations there are 6 independent equations and then the system is not closed. However, we shall see that this problem can be avoided always that we fix completely the gauge in our theory.

1.4.2. Fixing the gauge

The theory of General Relativity is invariant under general coordinate transformations. This implies that a generic field $Q = \bar{Q} + \epsilon Q^{(1)}$ obeys a gauge transformation law

$$Q^{(1)} \rightarrow Q^{(1)} + \mathcal{L}_X \bar{Q}, \quad (1-72)$$

where \mathcal{L}_X is the Lie derivative in direction of the vector field X . Observe that we have a limitation from the above description given that we have seen that the general perturbed metric $g_{\mu\nu}$ can be described in terms of a homogeneous and isotropic background spacetime $\bar{g}_{\mu\nu}$, which we set to be the FLRW metric, and a small metric perturbation $h_{\mu\nu}$. Then, by demanding the theory to be invariant under general coordinate transformations, the quantity $h_{\mu\nu}$ should have a particular transformation rule. This process is the well known *gauge transformation*. From the above relation we have

$$h_{\mu\nu} \rightarrow h_{\mu\nu} + \mathcal{L}_\chi \bar{g}_{\mu\nu}, \quad \text{with} \quad \chi^\alpha = (T, L^i), \quad (1-73)$$

where $T(\eta)$ is a scalar function and the vector $L_i(\eta)$ is decomposed into its scalar and vector part. It happens that at linear order the scalar, vector and tensor perturbations evolve independently from each other, which allow us to analyse them separately. In particular vector perturbations evolve as $1/a^2$ and then they are not relevant at cosmological levels. On the other hand, in this thesis it will be important to study both scalar and tensor perturbations since they are related to longitudinal density fluctuations and the production of gravitational waves, respectively. However, in this section we will concentrate mostly in the scalar sector and just quote tensor results at the end.

From (Durrer, 2001) the final gauge transformations for the scalar metric variables are:

$$A \rightarrow A - \frac{a'}{a} T - T', \quad (1-74a)$$

$$B \rightarrow B + L' + kT, \quad (1-74b)$$

$$H_L \rightarrow H_L - \frac{a'}{a} T - \frac{k}{3} L, \quad (1-74c)$$

$$H_T \rightarrow H_T + kL, \quad (1-74d)$$

while for energy-momentum perturbations:

$$\delta \rightarrow \delta + 3(1 + \omega) \frac{a'}{a} T, \quad (1-75a)$$

$$\delta u \rightarrow \delta u + L' \quad (1-75b)$$

$$\pi_L \rightarrow \pi_L - \frac{\bar{p}'}{p} T = \pi_L + 3(1 + \omega) \frac{c_s^2}{\omega} \frac{a'}{a} T, \quad (1-75c)$$

where superscript $'$ means derivative with respect to conformal time (1-37) and $c_s^2 \equiv \bar{p}'/\bar{\rho}'$ is defined as the *sound speed*.

In general, there is an infinite number of choices for the function $T(\eta)$ and $L(\eta)$, however it is common to fix them in such a way that two of the variable perturbations vanish. A popular choice is the *longitudinal* or *Newtonian gauge*. It is given when $kL = -H_T$ and $kT = -L' - B$, so that $H_T = B = 0$. With these conditions the scalar part of the metric perturbation is rewritten as (Mukhanov and Chibisov, 1981)

$$h_{\mu\nu}^{(S)} = -2\Psi d\eta^2 + 2\Phi\delta_{ij}dx^i dx^j, \quad (1-76)$$

where Φ and Ψ are gauge invariant and are known as *Bardeen potentials* (Bardeen, 1980). Usually Φ plays the role of the gravitational potential, however they are defined in a general form as

$$\Psi \equiv A - \frac{a'}{a}k^{-1}\sigma - k^{-1}\sigma', \quad (1-77a)$$

$$\Phi \equiv H_L + \frac{1}{3}H_T - \frac{a'}{a}h^{-1}\sigma, \quad (1-77b)$$

where $\sigma \equiv k^{-1}H_T' - B$ vanishes in the longitudinal gauge.

Although by choosing a particular gauge allow us to simplify the set of differential equations and help us to close the complete system, it is important to mention that by doing such simplification we also introduce “gauge artifacts”, i.e. degrees of freedom which are not physical.

1.4.3. The perturbed Einstein's and conservation equations

After understanding how to perturb the geometry and the energy contents in the background equations for the Universe, and then how we can close the system of equations by considering a gauge transformation, it is time to understand how the Einstein's and conservation equations are rewritten. For simplicity we shall derive the equation in the longitudinal Newtonian gauge and quote the gauge-invariant quantities in Appedix B. However, along this thesis we will also work in the well-known synchronous gauge of metric perturbations given by

$$ds^2 = -dt^2 + a^2(\delta_{ij} + h_{ij})dx^i dx^j, \quad (1-78)$$

where h_{ij} is the spatial perturbation in the metric.

The first-order Einstein's equations for the scalar perturbations are given by (Mukhanov, 2005)

$$k^2\Phi + 3\frac{a'}{a}\left(\Phi' - \frac{a'}{a}\Psi\right) = 4\pi Ga^2\bar{\rho}\delta, \quad (1-79a)$$

$$k\left(\frac{a'}{a}\Psi - \Phi'\right) = 4\pi Ga^2\delta u(\bar{\rho} + \bar{p}), \quad (1-79b)$$

$$-k^2(\Phi + \Psi) = 8\pi G a^2 \bar{\rho} \Pi, \quad (1-79c)$$

while the perturbed energy-momentum conservation equations are:

$$-\delta' = (1 + \omega)[k\delta u + 3\Phi'] + 3\frac{a'}{a}\omega\Gamma + 3\frac{a'}{a}(c_s^2 - \omega), \quad (1-80a)$$

$$\delta u' = \frac{a'}{a}(3c_s^2 - 1)\delta u + k\Psi + \frac{kc_s^2}{1 + \omega}\delta + \frac{k\omega}{1 + \omega}\left[\Gamma - \frac{2}{3}\Pi\right], \quad (1-80b)$$

where $\Gamma \equiv \pi_L - c_s^2\delta/\omega$ is the entropy production rate. Notice that in the case of perfect fluids, where $\Pi_\nu^\mu = 0$, we have $\Psi = \Phi$. We can also observe that perturbations vanish for a cosmological constant since $\delta'_\Lambda = 0$.

Since it will be of special interest for this thesis, we shall show how the above equations are reduced at scales deep inside the horizon ($k \ll aH$). At such scales we have that

$$\frac{k^2}{a^2}|F| \gg H^2|F|, \quad \text{and} \quad |\dot{F}| \lesssim |FH|. \quad (1-81)$$

And then we finally obtain

$$k^2\Phi = 4\pi G a^2 \bar{\rho} \delta, \quad (1-82a)$$

which is the classical Poisson equation, and

$$\delta'' + \frac{a'}{a}\delta' = -k^2\Phi. \quad (1-82b)$$

1.4.4. The adiabatic and isocurvature initial conditions

First of all, let us consider the following quantity:

$$S_{\alpha\beta} \equiv \frac{\delta_\alpha}{1 + \omega_\alpha} - \frac{\delta_\beta}{1 + \omega_\beta}, \quad (1-83)$$

where δ_α (ω_α) is the density contrast (equation-of-state) for a particular matter specie $\alpha = b, dm, \gamma, \nu$. $S_{\alpha\beta}$ measures the relative fluctuation between different components.

Adiabatic initial conditions are obtained when matter and radiation perturbations are initially in thermodynamic equilibrium, and then $S_{\alpha\beta} = 0$ for all components. This implies that their velocity field agree

$$\delta u^{(\gamma)} = \delta u^{(\nu)} = \delta u^{(b)} = \delta u^{(dm)}, \quad (1-84)$$

and the density contrast satisfy the relation

$$\frac{1}{3}\delta_b = \frac{1}{3}\delta_{dm} = \frac{1}{4}\delta_\gamma = \frac{1}{4}\delta_\nu = \left(\frac{1}{4}\delta\right), \quad (1-85)$$

The price to be paid in this scenario is that the curvature perturbation changes.

Isocurvature initial conditions refer to those metric perturbations that initially disappear, i.e. $\Psi = 0$, and that satisfy $S_{\alpha\beta} \neq 0$. This implies that the ratio between different species should change. Typically, these entropy perturbations are written in terms of one of the components, for example photons, and then

$$S_\alpha = \frac{\delta_\alpha}{1 + \omega_\alpha} - \frac{1}{4}\delta_\gamma. \quad (1-86)$$

The most general initial perturbations of the energy-density are described by a linear combination between adiabatic and isocurvature perturbations.

1.5. Power spectra

The density contrast δ , introduced in the previous section, can be considered statistically as a random field with zero mean, $\langle \delta(\mathbf{x}) \rangle = 0$. The measure of the clustering degree in the spatial direction \mathbf{r} is determined by the *correlation function* ξ , which is defined as the product of the density contrast at two separate points \mathbf{x} and $\mathbf{x} + \mathbf{r}$:

$$\xi(r) \equiv \langle \delta(\mathbf{x})\delta(\mathbf{x} + \mathbf{r}) \rangle. \quad (1-87)$$

where in the above expression we have considered that the correlation function can only depend on $r = |\mathbf{r}|$ thanks to the statistical homogeneity and isotropy of the random field. On the other hand, the amplitude of fluctuations of different lengths are described by the *power spectrum* $\mathcal{P}(k)$, which is simply the inverse Fourier transform of the correlation function ξ :

$$\langle \hat{\delta}(\mathbf{k})\hat{\delta}(\mathbf{k}') \rangle = \frac{2\pi^2}{k^3} \mathcal{P}(k) \delta_D(\mathbf{k} - \mathbf{k}'), \quad (1-88)$$

where $\hat{\delta}$ is the Fourier transform of the density contrast δ . The Dirac's delta distribution δ_D guarantees that modes relative to different wave-numbers are uncorrelated in order to preserve homogeneity.

1.5.1. Primordial power spectrum

1.5.1.1. Linear perturbations during inflation: Single field model

Inflationary models have the merit that they do not only explain the homogeneity of the Universe on large-scales, but also provide a theory for explaining the observed level of anisotropy. During the inflationary period, quantum fluctuations of the field were driven to scales much larger than the Hubble horizon. Then, in this process, the fluctuations were frozen and turned into metric perturbations. As we mentioned in section 1.4.2, metric perturbations created during inflation can be described by two terms. The scalar, or curvature, perturbations are coupled with matter in the Universe and form the initial “seeds” of structure

observed in galaxies today. Although the tensor perturbations do not couple to matter, they are associated to the generation of primordial gravitational waves. As we shall see, scalar and tensor perturbations are seen as important components to the CMB anisotropy (Hu and Dodelson, 2002).

As already mentioned, if inflation provides an exponential expansion, then the horizon remains practically constant while all other scales grow up. In this way, we can focus on the evolution of the quantum perturbations of the inflaton in a small region compared to the horizon. In this region, it is possible to assume the space as locally flat and ignore the metric perturbations. Thus, working in the Fourier space, the classical equation of motion for the perturbation part of $\phi(\mathbf{x}, t)$ in (1-52) is

$$(\delta\phi_k)'' + 3H(\delta\phi_k)' + \left(\frac{k}{a}\right)^2 \delta\phi_k = 0, \quad (1-89)$$

where it is assumed $\delta\phi$ is linear and neglect higher orders. This basically means that perturbations generated by vacuum fluctuations have uncorrelated Fourier modes, the signature of *Gaussian perturbations*.

The above equation can be rewritten as a harmonic oscillator equation with a variable frequency. If we now move to the quantum world and make the corresponding associations of operators to classical variables, the quantum dynamics will be determined by (Lyth and Liddle, 2009)

$$\hat{\chi}_k(\eta) = \frac{\chi_k(\eta) \hat{a}(k) + \chi_k^*(\eta) \hat{a}^\dagger(-k)}{(2\pi)^3} \quad \text{with} \quad \chi_k(\eta) = -\frac{e^{-ik\eta} k\eta - i}{\sqrt{2k} k\eta}, \quad (1-90)$$

where \hat{a} and \hat{a}^\dagger are the typical particle creation and annihilation operators, η is the proper time defined in (1-37), and $\chi \equiv a\delta\phi$. An important quantity above is the wave number k which is related to the size of the perturbation as $\lambda \propto 1/k$.

The inflationary process dilutes all possible particles existing before this period. Taking this into account, the ground state of the system is given by the vacuum. We notice that well after horizon exit, $\eta \rightarrow 0$, $\chi_k(\eta)$ approaches the value

$$\chi_k(\eta) = -\frac{i}{\sqrt{2k} k\eta}, \quad (1-91)$$

so that equation (1-90) is rewritten as

$$\hat{\chi}_k(\eta) = \chi_k(\eta) \frac{\hat{a}(k) - \hat{a}^\dagger(-k)}{(2\pi)^3}. \quad (1-92)$$

The temporal dependence of $\hat{\chi}_k$ is now trivial and implies that once $\chi_k(\eta)$ is measured after horizon exit, it will continue having a definite value, becoming a classical perturbation. That this quantum fluctuations become classical is of special interest, since, in this way, it can be taken as the initial inhomogeneities that will later give rise to the structure formation.

However these initial conditions will be slightly modified due to the amount of inflation remaining, once the k -scale has left the horizon.

Defining the spectrum of perturbations as

$$\langle \chi_k \chi_{k'}^* \rangle = \frac{2\pi^2}{k^3} \mathcal{P}_\chi(k) \delta_D(\vec{k} - \vec{k}') = \frac{2\pi^2}{k^3} a^2 \mathcal{P}_\phi(k) \delta_D(\vec{k} - \vec{k}'),$$

where the quantities \mathcal{P}_ϕ (\mathcal{P}_χ) are the spectra generated by field ϕ (χ). Evaluating the left hand side of the equation by a few Hubble times after the horizon exit, $\eta = (1/aH)|_{k=aH}$, with the Hubble constant value evaluated at the time the scale k has left the horizon ($k = aH$) yields to the spectrum

$$\mathcal{P}_\phi(k) = \left(\frac{H}{2\pi} \right)_{k=aH}^2. \quad (1-93)$$

In this scenario it is introduced the *primordial curvature perturbation* $\mathcal{R}_k(t)$, which has the property to be constant within few Hubble times after the horizon exit. This value is called the *primordial value*, and is related to the scalar field perturbation $\delta\phi$ by

$$\mathcal{R}_k = - \left[\frac{H}{\dot{\phi}} \delta\phi_k \right]_{k=aH}. \quad (1-94)$$

From the two above equations, the primordial curvature power spectrum $\mathcal{P}_{\mathcal{R}}(k)$, computed in terms of the scalar field spectrum $\mathcal{P}_\phi(k)$, is given by

$$\begin{aligned} \mathcal{P}_{\mathcal{R}}(k) &= \left[\left(\frac{H}{\dot{\phi}} \right)^2 \mathcal{P}_\phi(k) \right]_{k=aH} \\ &= \left[\left(\frac{H}{\dot{\phi}} \right) \left(\frac{H}{2\pi} \right) \right]_{k=aH}^2. \end{aligned} \quad (1-95)$$

On the other hand, the creation of primordial gravitational waves corresponds to the tensor part of the metric perturbation $h_{\mu\nu}$ in (1-3) or (1-67). In Fourier space, tensor perturbations h_{ij} can be expressed as the superposition of two polarisation modes

$$h_{ij} = h_+ e_{ij}^+ + h_\times e_{ij}^\times, \quad (1-96)$$

where $+$, \times represent the longitudinal and transverse modes. From Einstein equations, it is found that each amplitude h_+ and h_\times behaves as a free scalar field in the sense that

$$\chi_{+, \times} \equiv \frac{m_{pl}}{\sqrt{8}} h_{+, \times}. \quad (1-97)$$

Therefore, taking the results of the scalar perturbations, each $h_{+, \times}$ has a spectrum \mathcal{P}_T given by

$$\mathcal{P}_T(k) = \frac{8}{m_{pl}^2} \left(\frac{H}{2\pi} \right)_{k=aH}^2. \quad (1-98)$$

The canonical normalisation of the field $\chi_{+,x}$ was chosen such that the *tensor-to-scalar ratio* of the spectra is

$$r \equiv \frac{\mathcal{P}_T}{\mathcal{P}_\mathcal{R}} = 16\epsilon_v. \quad (1-99)$$

During the horizon exit, H and $\dot{\phi}$ have tiny variations during few Hubble times. In this case, the scalar and tensor spectra are nearly scale invariant, and therefore well approximated to a power law

$$\mathcal{P}_\mathcal{R}(k) = \mathcal{P}_\mathcal{R}(k_0) \left(\frac{k}{k_0}\right)^{n_s-1}, \quad \mathcal{P}_T(k) = \mathcal{P}_T(k_0) \left(\frac{k}{k_0}\right)^{n_T}. \quad (1-100)$$

where the spectral indices are defined as

$$n_s - 1 \equiv \frac{d \ln \mathcal{P}_\mathcal{R}(k)}{d \ln k}, \quad n_T \equiv \frac{d \ln \mathcal{P}_T(k)}{d \ln k}. \quad (1-101)$$

A scale-invariant spectrum, called Harrison-Zel'dovich, has constant variance on all length scales and it is characterised by $n_s = 1$; small deviations from scale-invariance are also considered as a typical signature of the inflationary models. Then, the spectral indices n_s and n_T can be expressed in terms of the slow-roll parameters ϵ_v and η_v , to lowest order, as:

$$\begin{aligned} n_s - 1 &\simeq -6 \epsilon_v(\phi) + 2 \eta_v(\phi), \\ n_T &\simeq -2 \epsilon_v(\phi). \end{aligned} \quad (1-102)$$

These parameters are not completely independent each other, but the tensor spectral index is proportional to the tensor-to-scalar ratio $r = -8n_T$. This expression is the *first consistency relation* for slow-roll inflation. Hence, any inflationary model, to the lowest order in slow-roll, can be described in terms of three independent parameters: the amplitude of density perturbations $A_r \sim \mathcal{P}_\mathcal{R}(k_0)^{1/2}$ ($\approx 5 \times 10^{-5}$ initially measured by COBE satellite), the scalar spectral index n_s , and the tensor-to-scalar ratio r . If we require a more accurate description, we should consider higher-order effects, and then include parameters for describing the running of scalar ($n_{srun} \equiv dn_s/d \ln k$) and tensor ($n_{Trun} \equiv dn_T/d \ln k$) index and higher order corrections.

An important point to emphasise is that A_r , r and n_s are parameters that nowadays are tested from several observations. This allows us to compare theoretical predictions with observational data, for instance, those provided by the Cosmic Microwave Background radiation. In other words, future measurements of these parameters may probe or at least constrain the inflationary models and therefore the shape of the inflaton's potential $V(\phi)$.

1.5.1.2. Cosmological perturbations in multi-field inflation: The adiabatic and isocurvature perturbations

The equation of motion for the perturbed fields is described by

$$\ddot{\delta\phi}_i + 3H\dot{\delta\phi}_i + \sum_j \left[V_{ij} - \frac{8\pi}{a^3 m_{pl}^2} \frac{d}{dt} \left(\frac{a^3}{H} \dot{\phi}_i \dot{\phi}_j \right) \right] \delta\phi_j = 0. \quad (1-103)$$

On the largest scales ($k \ll aH$) it is better to work on a rotating basis of the fields, defined by the relation:

$$\begin{pmatrix} \delta\sigma \\ \delta s \end{pmatrix} = \mathcal{S}^\dagger \begin{pmatrix} \delta\phi \\ \delta\varphi \end{pmatrix}, \quad (1-104a)$$

where

$$\mathcal{S} = \begin{pmatrix} \cos\theta & -\sin\theta \\ \sin\theta & \cos\theta \end{pmatrix}, \quad \tan\theta = \frac{\dot{\phi}}{\dot{\varphi}} \simeq \pm \sqrt{\frac{\epsilon_\varphi}{\epsilon_\phi}}. \quad (1-104b)$$

The field σ is parallel to the trajectory on the field space, and it is usually called *adiabatic field*, whereas the field s is perpendicular, and named the *entropy field*. If the background trajectory is curved, then $\delta\sigma$ and δs are correlated at Hubble exit, and therefore, at this point, the *power spectrum* and *cross-correlation* are described by the expressions:

$$\mathcal{P}_\sigma(k)|_{k=aH} \simeq \left(\frac{H}{2\pi} \right)_{k=aH}^2 (1 + (-2 + 6C)\epsilon - 2C\eta_{\sigma\sigma}), \quad (1-105a)$$

$$\mathcal{C}_{\sigma s}(k)|_{k=aH} \simeq -2C\eta_{\sigma s} \left(\frac{H^*}{2\pi} \right)_{k=aH}^2, \quad (1-105b)$$

$$\mathcal{P}_s(k)|_{k=aH} \simeq \left(\frac{H}{2\pi} \right)_{k=aH}^2 (1 + (-2 + 2C)\epsilon - 2C\eta_{ss}), \quad (1-105c)$$

where $C \simeq 0.7296$, $\epsilon \equiv \epsilon_\sigma + \epsilon_s$, and η_{ij} ($i, j = \sigma, s$) are slow-roll parameters defined in a similar way than equation (1-63), but now in terms of the new fields σ and s .

Final power spectrum and spectral index

The curvature and isocurvature perturbations are usually defined as

$$\mathcal{R} \equiv \frac{H}{\dot{\sigma}} \delta\sigma, \quad \mathcal{S} \equiv \frac{H}{\dot{s}} \delta s. \quad (1-106)$$

In the slow-roll limit, on large scales, the evolution of curvature and isocurvature perturbations can be written using the formalism of transfer matrix:

$$\begin{pmatrix} \mathcal{R} \\ \mathcal{S} \end{pmatrix} = \begin{pmatrix} 1 & T_{RS} \\ 0 & T_{SS} \end{pmatrix} \begin{pmatrix} \mathcal{R} \\ \mathcal{S} \end{pmatrix}_{k=aH}, \quad (1-107)$$

where

$$T_{SS}(t^*, t) = \exp \left(\int_{t^*}^t \beta H dt' \right), \quad T_{RS}(t^*, t) = \exp \left(\int_{t^*}^t \alpha T_{SS} H dt' \right), \quad (1-108)$$

being t^* the time measured at horizon crossing and at linear order in slow-roll parameters

$$\alpha \simeq -2\eta_{\sigma s}, \quad \beta \simeq -2\epsilon + \eta_{\sigma\sigma} - \eta_{ss}. \quad (1-109)$$

On the other hand, the primordial curvature perturbation during a radiation-dominated era (some time after inflation ended) is given, on large scales, by

$$\mathcal{R} = \Phi + \frac{H\delta\rho}{\rho}, \quad (1-110)$$

where Φ is the gravitational potential (see section 1.4), while the conventional definition of the isocurvature perturbation for an i -specie is given by (1-86). Then, at the beginning of the radiation-domination era, we get the final power spectra

$$\mathcal{P}_{\mathcal{R}} \simeq \mathcal{P}|_{k=aH}(1 + \cot^2 \Delta), \quad (1-111a)$$

$$\mathcal{P}_S = T_{SS}^2 \mathcal{P}|_{k=aH}, \quad (1-111b)$$

$$\mathcal{C}_{\mathcal{R}S} = T_{\mathcal{R}S} T_{SS} \mathcal{P}|_{k=aH}, \quad (1-111c)$$

where at linear order in slow-roll parameters $\mathcal{P}|_{k=aH}$ is

$$\mathcal{P}|_{k=aH} = \frac{1}{2\epsilon} \left(\frac{2H}{m_{pl}} \right)_{k=aH}^2, \quad (1-112)$$

with Δ the observable correlation angle defined at lower order as

$$\cos \Delta = \frac{T_{RS}}{\sqrt{1 + T_{RS}^2}}. \quad (1-113)$$

The final spectral index for each contribution, defined as $n_x - 1 = d \ln \mathcal{P}_x / d \ln k$, at linear order in slow-roll parameters, are

$$\begin{aligned} n_s - 1 &\simeq -(6 - 4 \cos^2 \Delta) \epsilon + 2 \sin^2 \Delta \eta_{\sigma\sigma}, \\ &\quad + 4 \sin \Delta \cos \Delta \eta_{\sigma s} + 2 \cos^2 \Delta \eta_{ss}, \end{aligned} \quad (1-114a)$$

$$n_S - 1 \simeq -2\epsilon + 2\eta_{ss}, \quad (1-114b)$$

$$n_{\mathcal{C}} - 1 \simeq -2\epsilon + 2 \tan \Delta \eta_{\sigma s} + 2\eta_{ss}. \quad (1-114c)$$

Notice that we have left the subindex s in order to be consistent with the scalar spectral index defined in the single inflationary scenario.

Sometimes, it is also common to parameterised the primordial adiabatic and entropy perturbations on super-horizon scales as power laws

$$P_R = A_r^2 \left(\frac{k}{k_0} \right)^{n_{ad1}-1} + A_s^2 \left(\frac{k}{k_0} \right)^{n_{ad2}-1}, \quad (1-115a)$$

$$C_{RS} = A_s B \left(\frac{k}{k_0} \right)^{n_{cor}-1}, \quad (1-115b)$$

$$P_s = B^2 \left(\frac{k}{k_0} \right)^{n_{iso}-1}, \quad (1-115c)$$

where at linear order $n_{ad1} = -6\epsilon + 2\eta_{\sigma\sigma}$, $n_{ad2} = 2n_C - n_S$, $n_{cor} = n_C$, $n_{iso} = n_S$. The amplitude values A_r^2 , A_s^2 and B can be written in terms of the correlation angle as

$$A_r^2 = [P_R \sin^2 \Delta]_{k_0}, \quad A_s^2 = [P_R \cos^2 \Delta]_{k_0}, \quad (1-116a)$$

$$B^2 = [T_{SS}^2 P_R]_{k_0}. \quad (1-116b)$$

A_r^2 and A_s^2 are the contributions of the adiabatic and entropy fields to the amplitude of the primordial adiabatic spectrum.

Primordial gravitational waves

Given the fact that scalar and tensor perturbations are decoupled at linear order, gravitational waves at horizon crossing are the same than in the single-field case. Also, their amplitude should remain frozen on large scales after Hubble exit. Therefore, the tensor power spectrum and the spectral index are finally

$$\mathcal{P}_T = \mathcal{P}_T|_{k=aH} \simeq 8 \left(\frac{H}{2\pi m_{pl}} \right)_{k=aH}^2 (1 + 2(-1 + C)\epsilon), \quad (1-117)$$

$$n_T \simeq -2\epsilon \left[1 + \left(\frac{4}{3} + 4C \right) \epsilon + \left(\frac{2}{3} + 2C \right) \eta_{\sigma\sigma} \right], \quad (1-118)$$

The tensor-to-scalar ratio at Hubble exit is the same than in the single field case. However, at super-horizon scales, the curvature perturbations continue evolving as (1-111a). In this way, the value of r some time after the end of inflation is

$$r \simeq 16\epsilon \sin^2 \Delta \left[1 - \left(\frac{4}{3} + 4C \right) \epsilon + \left(\frac{2}{3} + 2C \right) \eta_{\sigma\sigma} \right]. \quad (1-119)$$

Observe from (1-99) that the single scalar field case works as an upper constraint on r .

1.5.1.3. The spectator scenario

The simplest extension to the single field model – referred as the *inflaton scenario* – is to consider that only one SF was dynamically important during inflation and the extra SF observer contributed to the primordial spectrum just by generating isocurvature fluctuations. Even though the idea of adding an extra spectator that does not contributed for the inflationary

process could be considered as not necessary, there are several well motivated theoretical aspects where more than one SF could exist during this era.

The inflaton scenario is obtained when considering that the trajectory in field space evolved in the inflaton direction ϕ , whereas the direction perpendicular to the trajectory corresponded to an spectator field φ . Notice that it is necessary to have $\eta_{\sigma s} = \eta_{\varphi\phi} = 0$ and that the spectator field evolves much slower than the inflaton. Then, we can see that the last conditions demand that the potential should be written as $V(\phi, \varphi) = V(\phi) + V(\varphi)$ and $\epsilon_\varphi \ll \epsilon_\phi$.

During the inflationary scenario, the entropy and adiabatic perturbations are uncorrelated, which leads to $T_{\mathcal{R}S} = 0$ (and $\mathcal{C}_{RS} = 0$) as can be seen from (1-108), imposing initial conditions at horizon crossing. In this way, we have that $\cos \Delta = 0$. On the other hand, as it is expected from (1-115a) and (1-116), in the inflationary scenario the primordial power spectrum for the adiabatic perturbations is produced purely by the inflaton, while quantum fluctuations of the spectator give entry to the generation of uncorrelated isocurvature perturbations. In this way, the primordial power spectrum of adiabatic, isocurvature and tensor perturbations are

$$\mathcal{P}_{\mathcal{R}} = P_R|_{k=aH}, \quad \mathcal{P}_S = T_{SS}^2 \mathcal{P}_{\mathcal{R}}|_{k=aH}, \quad \text{and} \quad P_T = \frac{8}{M_{pl}^2} \left(\frac{H}{2\pi} \right)_{k=aH}^2. \quad (1-120)$$

From (1-114) and (1-118) the tilts at linear order are

$$n_R \simeq -6\epsilon + 2\eta_{\phi\phi}, \quad n_s \simeq -2\epsilon + 2\eta_{\varphi\varphi}, \quad \text{and} \quad n_T \simeq -2\epsilon. \quad (1-121)$$

Finally the tensor-to-scalar ratio in this scenario is the same than in the single-inflaton scenario (1-99), which implies that the spectator field does not contribute to r .

1.5.2. CMB power spectrum

Although we will not work directly with CMB in this thesis, we consider instructive and complementary to review a little this kind of measurements. In addition, we believe that this review will help us to understand different concepts that will appear later. In this section, we review the main properties of the CMB. It is important to mention that until now we have only considered the background evolution in the Λ CDM, while for the CMB it is necessary to take into account the perturbed Universe, i.e., the evolution for the small perturbations of the Λ CDM constituents over the background. In particular, in order to understand the CMB, we need to concentrate on the perturbations associated to photons and the different processes that could affect to it. For simplicity, we shall consider only adiabatic initial conditions. To provide an accurate description of these processes it is necessary to consider dynamics that occurs at microscopic levels. In particular, this description is necessary to describe some stages (such as recombination) where the Universe is expected to be out of equilibrium.

1.5.2.1. General description

As we already commented in the previous section, depending on the scale of energy, different interactions between photons and ordinary matter can take place. At high energy, such interactions can be, for example: creation of particle-antiparticle pairs by photons in presence of heavy neutral particles, annihilation of particle-antiparticle pairs that generate photons, production of a photon due to the interaction between two charged particles, Compton scattering or production of photons due to radiative (double) Compton scattering. While the average energy of the Universe decreases, all these interactions become less and less frequent until they reach the point where the least energetic of them, the Compton scattering, stop to occur (at an energy scale of around 0.3 eV), and then the Universe left to be invisible to us. It is at this moment when the CMB is created and is usually referred to as the *time of last scattering* or, as we already mentioned, the surface of last scattering.

When the energy of the Universe was above 0.5 keV all previous mentioned processes, except for Compton scattering, continue being very efficient, and then, such interactions ensure thermal equilibrium. In this regime, the photon can be well described by a blackbody spectrum, and any perturbation that may distort it is expected to be quickly smoothed by the interactions. At energy scales below 0.5 keV, it is not expected that the above description continue being true, and then, if some perturbations are introduced, they may not be efficiently smoothed and should leave an observable signature in the spectrum. An accurate measurement of the CMB spectrum can be seen in Figure (1-6) as was obtained by the FIRAS instrument onboard the COBE satellite (Mather et al., 1990). As can be seen, CMB looks to be a pure blackbody spectrum, obtaining deviations of order 10^{-5} that were measured by COBE (Smoot et al., 1992). The origin and the distribution of these fluctuations are of great interest give that they may give accurate information about our Universe at high energy scales. For example, the inflationary process provides an elegant mechanism to explain the presence of these fluctuations (see chapter 1.3). For such reason, since COBE results, there have been several CMB experiments which try to measure these fluctuations with increasing precision.

1.5.2.2. Angular power spectrum

When we refer to CMB, we usually think in the temperature two-point correlation function defined as

$$C(\vec{n}_1, \vec{n}_2) \equiv \langle \Delta(\vec{n}_1) \Delta(\vec{n}_2) \rangle, \quad (1-122)$$

which is the difference in temperature for photons received by two antennas pointing in two different directions of the sky. Here \vec{n}_1, \vec{n}_2 are the direction of the two antennas, $\Delta(\vec{n}_i) \equiv \Delta T(\vec{n}_i)/\bar{T}$, \bar{T} is the mean temperature measured by the CMB and $\Delta T(\vec{n}_i)$ is the difference of temperature measured with respect to \bar{T} , and $\langle \cdot \rangle$ means average over all possible statistical realization of the Universe. Thanks to the Universe being isotropic, the above quantity should only depend on the angle θ between \vec{n}_1 and \vec{n}_2 , i.e. $\vec{n}_1 \cdot \vec{n}_2 = \cos \theta$.

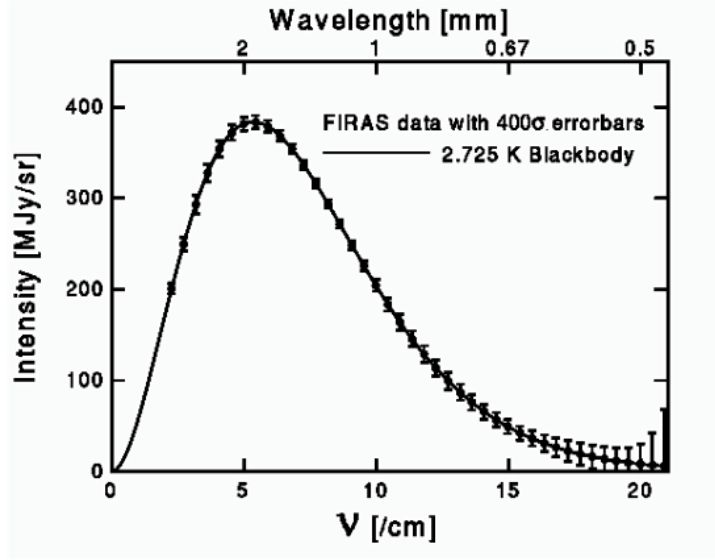


Figure 1-6.: CMB blackbody spectrum (Figure taken from (Mather et al., 1990))

For such reason a convenient basis to rewrite $\Delta(\vec{n}_i)$ are the spherical harmonics $Y_l^m(\vec{n}_i)$ in the form

$$\Delta(\vec{n}_i) = \sum_{l=1}^{\infty} \sum_{m=-l}^l a_{lm}^T Y_l^m(\vec{n}_i), \quad (1-123)$$

where $i = 1, 2$. On the other hand $C(\vec{n}_1, \vec{n}_2)$ can be rewritten also in terms of spherical harmonic functions as

$$C(\vec{n}_1, \vec{n}_2) = \sum_{l=0}^{\infty} C_l \sum_{m=-l}^{m=l} Y_l^{m*}(\vec{n}_1) Y_l^m(\vec{n}_2) = \sum_l \frac{2l+1}{4\pi} C_l P_l(\cos \theta). \quad (1-124)$$

Using (1-123) and (1-124) in (1-122) we finally obtain

$$C_l = \langle a_{lm}^T a_{lm}^{*T} \rangle. \quad (1-125)$$

Coefficients C_l are referred to as *angular power spectrum* and l is referred to as *multipole*. Given the fact that for each value l there are $2l + 1$ values of m , the azimuthal angle is divided into $2l$ parts and then the multipole l is associated to an angle $\theta = 180^\circ/l$.

Now, we consider initial conditions in terms of the conformal Newtonian gauge $\Phi_{ini} = \mathcal{R}$. Thanks to the evolution equation being Δ independent of the direction \vec{k} , we can write

$$\Delta_l(\eta_0, \vec{k}, \vec{n}) = \Phi_{ini} \Delta_l(\eta_0, k, \vec{n}). \quad (1-126)$$

Therefore the C_l 's are found to be

$$C_l^{XY} = \frac{4\pi}{(2l+1)^2} \int \frac{d^3k}{(2\pi)^3} \mathcal{P}_{\mathcal{R}}(k) \Delta_l^X(k) \Delta_l^Y(k), \quad (1-127)$$

where X and Y represents the temperature T and polarization (E or B); quantity $\mathcal{P}_{\mathcal{R}}$ is the initial scalar power spectrum (1-100). The moments obtained from the line of sight integration method (Seljak and Zaldarriaga, 1996), in terms of the spherical Bessel functions j_l are given by

$$\Delta_l^T = (2l + 1) \int d\eta j_l(k[\eta - \eta_0]) S_T(k, \eta), \quad (1-128)$$

$$\Delta_l^E = (2l + 1) \sqrt{\frac{(l-2)!}{(l+2)!}} \int d\eta S_E(k, \eta) j_j(k[\eta - \eta_0]), \quad (1-129)$$

where S_E and S_T are sourced terms. On the other hand, for the tensor contribution we have

$$C_{XY,l}^{tens} = \frac{4\pi}{(2l+1)^2} \int \frac{d^3k}{(2\pi)^3} \mathcal{P}_T \Delta_{X,l}^{tens}(k) \Delta_{Y,l}^{tens}(k), \quad (1-130)$$

where \mathcal{P}_T is the primordial tensor power spectrum (1-100), and the moments:

$$\Delta_{T,l}^{tens} = \sqrt{\frac{(l+2)!}{(l-2)!}} \int d\eta S_T^{tens}(k, \eta) \frac{j_l(k[\eta - \eta_0])}{k^2[\eta - \eta_0]^2}, \quad (1-131)$$

$$\Delta_{E,B;l}^{tens} = \int d\eta S_{E,B}^{tens}(k, \eta) j_l(k[\eta - \eta_0]), \quad (1-132)$$

with S_T^{tens} , S_E^{tens} and S_B^{tens} sources terms.

In Figure 1-7 it is shown the CMB spectra for all the different modes: temperature, E -mode, B -mode and $T-E$ cross-correlation. The left-hand side displays the modes associated to the scalar perturbations whereas the right-hand side shows the ones associated to the tensor perturbations.

Let us examine in more detail the temperature power spectrum C_l^T . It is determined by (1-128) where S_T is provided by (Seljak and Zaldarriaga, 1996):

$$\begin{aligned} S_T = & - \frac{g}{\kappa'} [\Psi' - \Phi'] + g' \left[\frac{V_b}{k} + \frac{3}{k^2} \mathcal{C}' \right] + g'' \frac{3}{2k^2} \mathcal{C} \\ & + g \left[\frac{1}{4} D_g^\gamma + \frac{V_b'}{k} - (\Phi - \Psi) + \frac{\mathcal{C}}{2} + \frac{3}{2k^2} \mathcal{C}'' \right], \end{aligned} \quad (1-133)$$

where $g \equiv \kappa' \exp[\kappa(\eta) - \kappa(\eta_0)]$. The density contrast D_g^γ is the main contribution, driving the spectrum towards the oscillatory behaviour. It can be seen as an intrinsic temperature variation over the background last-scattering surface $\delta T/T \propto D_g^\gamma/4$. The Doppler shift, V_b -term, describes the blueshift caused by last scattering electrons moving towards the observer. The term involving time derivatives of the potentials, $(\Phi' - \Psi')$, is known as the *integrated Sachs-Wolfe* effect. It describes the change of the CMB photon energy due to the evolution of the potentials along the line of sight. The terms involving \mathcal{C} and its derivatives describe polarisation effects and are far less important than the D_g^γ term. Finally, the $(\Phi - \Psi)$

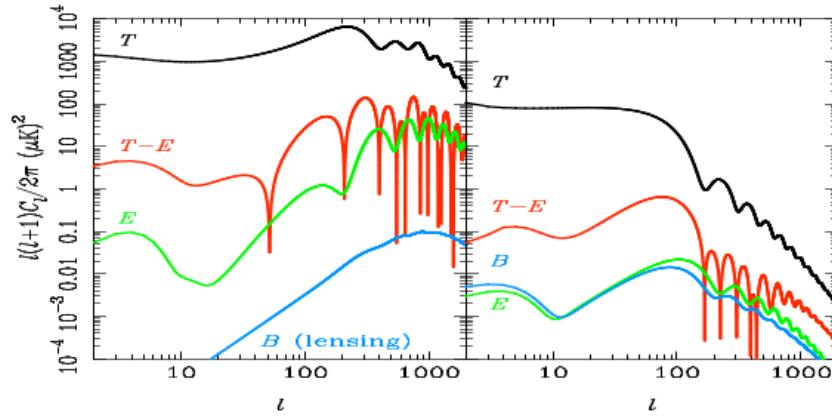


Figure 1-7.: CMB spectra for all the contributions: temperature, E -modes, B -modes and $T - E$ cross-correlation. (left panel) shows the scalar perturbations, (right panel) shows the tensor perturbations (Figure taken from (Challinor and Peiris, 2009)).

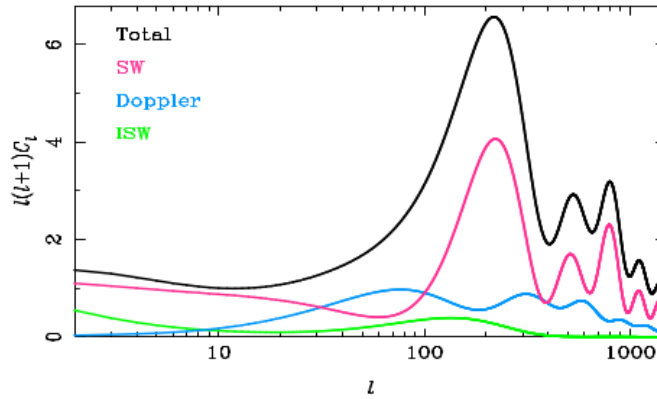


Figure 1-8.: Total CMB temperature spectrum and its different contributions (Figure taken from (Challinor and Peiris, 2009)).

term arises from the gravitational redshift when climbing out of the potential well at last scattering. The combination $D_g^2/4 - (\Phi - \Psi)$ is known as the *ordinary Sachs-Wolfe* effect. This gives the main contribution on scales that at decoupling well outside the horizon.

Nowadays, thanks to CMB observation experiments (see next section) we have an extremely accurate measurement for the angular power spectrum. In Figure 1-9 we show the CMB temperature-power spectrum data measured by Planck (Aghanim et al., 2018) together with the best fit for the Λ CDM model.

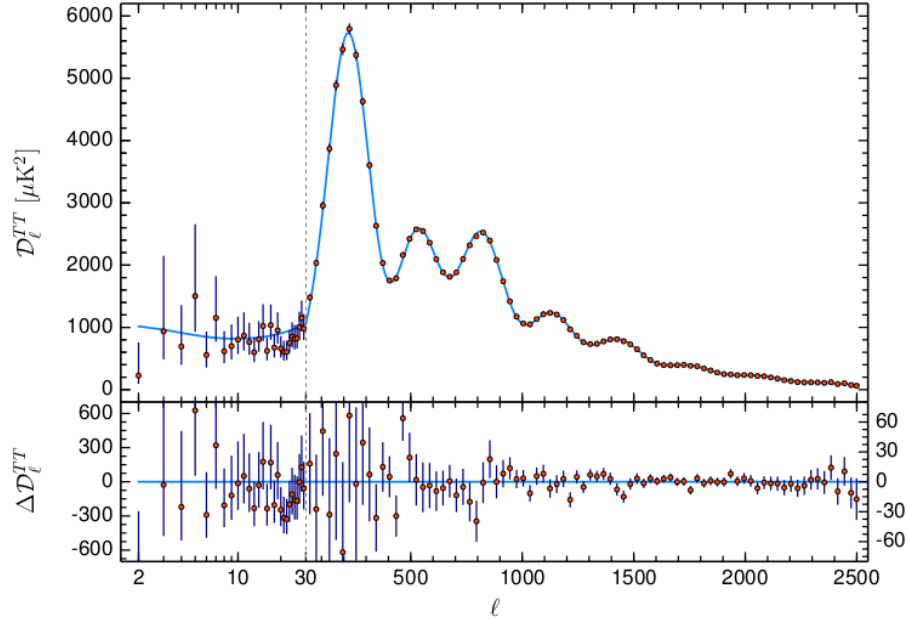


Figure 1-9.: Planck 2018 temperature power spectrum. In the figure it is also showed the best fit for the Λ CDM model. Here $D_l^{TT} \equiv l(l+1)C_l/(2\pi)$ (Figure taken from (Aghanim et al., 2018)).

1.5.3. Matter power spectrum

The *matter power spectrum* (MPS) \mathcal{P}_m encodes the distribution of galaxies over the observed Universe. It is defined by

$$\langle \delta_m(\vec{k}) \delta_m(\vec{k}') \rangle = \frac{2\pi^2}{k^3} \mathcal{P}_m(k) \delta_D(\vec{k} - \vec{k}'), \quad (1-134)$$

where the matter overdensity δ_m is related to the potential $\Phi(a, \vec{k})$ via the poisson equation (1-82a) as

$$\delta_m(a, \vec{k}) = \frac{2}{3} \left(\frac{k}{aH} \right) \Phi(a, \vec{k}). \quad (1-135)$$

On the other hand, the gravitational potential Φ can be written in terms of the primordial value Φ_{ini} , set up during inflation, as

$$\Phi(a, \vec{k}) = T(k)g(a)\Phi_{ini}, \quad (1-136)$$

where $T(k)$ is a transfer function which describes the evolution of perturbations through the epoch of horizon crossing and radiation/matter equality, while the growth factor $g(a)$ describes the wavelength-independent growth at late times.

The above quantity can be also associated to the comoving curvature perturbation $\mathcal{R}^{(m)}$, which can be written in terms of the potentials, in comoving coordinates, as

$$\mathcal{R}^{(m)} = \frac{5 + 3\omega}{3 + 3\omega} \Phi, \quad (1-137)$$

and then the matter overdensity can be associated to the curvature perturbation via

$$\delta_m(a, k) = \frac{2}{5} \left(\frac{k}{aH} \right) \mathcal{R}^{(m)}. \quad (1-138)$$

With this last expression, the matter power spectrum can be rewritten as

$$\mathcal{P}_m(a, k) = \frac{4}{25} \left(\frac{k}{aH} \right)^4 T^2(k) \mathcal{P}_{\mathcal{R}}(k). \quad (1-139)$$

An alternative defining for the matter power spectrum is given by $P_m \equiv 2\pi^2 \mathcal{P}_m / k^3$. On the other hand, it has been shown that the transfer function of a matter component follows asymptotic behaviour

$$T(k) = \begin{cases} 1 & \text{if } k_{eq}/k \gg 1 \\ (k_{eq}/k)^2 & \text{if } k_{eq}/k \ll 1, \end{cases} \quad (1-140)$$

where k_{eq} is the mode that enters the horizon at matter-radiation equality⁶. Then, the matter power spectrum in its asymptotic form follows:

$$P_m(k) = \begin{cases} \propto k & \text{large scales} \\ k^{-3} & \text{small scales.} \end{cases} \quad (1-141)$$

In Figure 1-10 we show the MPS at present time in the Λ CDM model. Observe that the figure presents the behavior described in the above relation.

1.6. CMB observations and Planck constraints for inflation

In this section, we show how the inflationary models can affect the CMB power spectrum. We already studied in the above section, the CMB power spectra depend on the primordial power spectra via equations (1-127) and (1-130). In the single field scenario, the most common observables considered during inflation are the amplitude of adiabatic perturbations A_r , the tensor-to-scalar ratio r , and the spectral index n_s . During several years, many projects, at different scales, have been carried out in order to look for observational data to constrain cosmological models. That is, different models may imprint different behaviours over the CMB spectra, see Figure 1-11. Amongst many projects, they are: Cosmic Background Explorer (COBE), Wilkinson Microwave Anisotropy Probe (WMAP), Cosmic Background Imager observations (CBI), Ballon Observations of Millimetric Extra-galactic Radiation and Geophysics (BOOMERang), the Luminous Red Galaxy (LRG) subset DR7 of the Sloan Digital Sky Survey (SDSS), Baryon Acoustic Oscillations (BAO), Supernovae (SNe) data, Hubble Space Telescope (HST) and recently the South Pole Telescope (SPT), the Atacama Cosmology Telescope (ACT) and the Planck Satellite. These different data measurements

⁶The precise form of the transfer function at all scales should be found by solving the general relativistic Boltzmann equation.

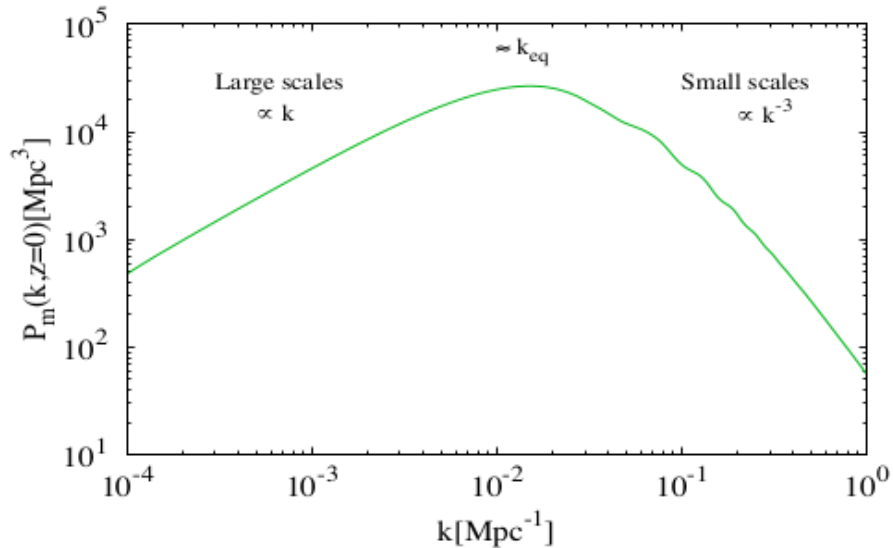


Figure 1-10.: Matter power spectrum $P_m(k)$ at $z = 0$ (Figure taken from (Vázquez, 2013)).

have been extensively used together with Bayesian statistics to constraint the different parameters for inflationary models. The way it is commonly done such process is by confronting the model parameters with the data with the help of Bayes theorem (see appendix C for a review). Then, after obtaining a range for the more probable parameters, it is usually reported confidence regions where parameters are more likely to match the observations. In this section, we review some of the constraints obtained from inflationary parameter after considering historical and current data. We stress that the results are given for the parameters n_s and r , and therefore our interest is mainly focused on the case with no running, $dn_s/d\ln k = 0$. We encourage to the reader that is not familiarized with Bayesian parameter inference to review appendix C in order to understand completely this section.

The results obtained from WMAP3 observations constrained the inflationary parameters to be $0.94 < n_s < 1.04$ and $r < 0.60$ (95% CL). Those models that present $n_s < 0.9$ were therefore ruled out at high confidence level. The same was applied for models with $n_s > 1.05$. However, WMAP data by itself cannot lead to strong constraints because the existence of parameter degeneracies, like the well known geometrical degeneracy involving Ω_m , Ω_Λ and Ω_k . However, when it was combined with different types of datasets, together they increased the constraining power and removed degeneracies. Once the SDSS data was included, the limit of the gravitational wave amplitude and the spectral index constraints were reduced, that is, for WMAP3+SDSS the constraints on n_s and r were $0.93 < n_s < 1.01$ and $r < 0.31$. On the other hand, WMAP5 data alone constrained the tensor to scalar ratio to be $r < 0.43$ (95% CL) while $0.964 < n_s < 1.008$. When BAO and SN data were added, the limits improved significantly to $r < 0.22$ (95% CL) and $0.953 < n_s < 0.983$ (Komatsu et al., 2009). Following the same history line for datasets, by consider WMAP seven year

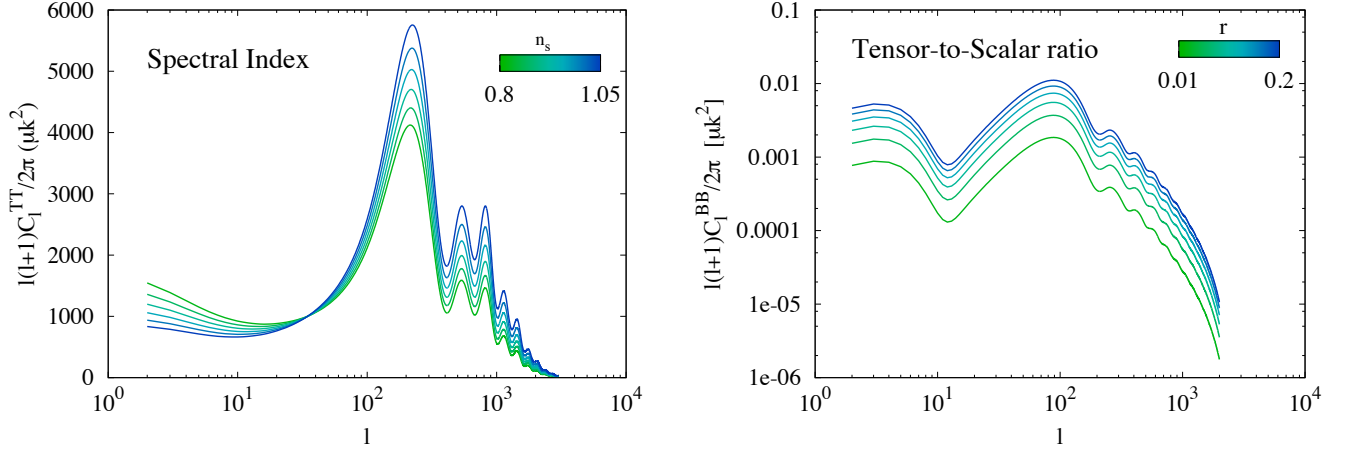


Figure 1-11.: Variations of the CMB scalar spectrum for different values of the spectral index n_s (left), and variations of the CMB tensor spectrum with respect to the tensor-to-scalar ratio r (right) (Taked from (Vázquez et al., 2018)).

data, the spectral index was constrained to be in the range $n_s = 0.982^{+0.020}_{-0.019}$, whereas the tensor-to-scalar ratio should fulfill the maximum value $r < 0.37$ (95% CL). When WMAP-7 was combined with different datasets, the constraints were tightened as it is shown by (Larson et al., 2011). Finally, the most recent satellite that provides new constrictions for the inflationary parameters is Planck satellite. It has yielded results 3 times: in 2013, 2015, and 2018. At this point we shall only present the final results it obtains, i.e., the ones from 2018, which are, for now, the most recent constrictions for inflationary parameters. For such purpose we decided to show, in Figure 1-12, 2D marginalised probability constraints on n_s and r , as it was reported in (Aghanim et al., 2018). Gray regions correspond to the constrictions when considering the contribution of the temperature power spectrum (TT), the temperature-polarization cross spectrum (TE), the polarisation power spectrum (EE), lensing and the low- l temperature-only likelihood (lowE). In the red region it was also included the BICEP2/Keck array BK15 data, whereas in the blue region it was included also BAO observations. Given that we showed the figure as it was reported in the Planck results, there are different inflationary models that were tested by such constrictions.

Finally, it is time to talk about the constrictions that comes when there are more than one SF during the inflationary era. As we already mentioned, in that circumstance it is possible to obtain isocurvature perturbations generated by those extra SFs in the early Universe. Of special interest in this thesis are the isocurvature perturbations generated for the DM for uncorrelate models. Parameterizing the isocurvature power spectrum for DM in terms of the curvature power spectrum $P_R(k)$ (see equation (1-120)), we have

$$P_{DM}(k) = \frac{\beta_{iso}(k)}{1 - \beta_{iso}(k)} P_R(k), \quad (1-142)$$

where $P_{DM} = \delta\rho_{DM^*}/\rho_{DM}$, $\delta\rho_{DM^*}$ are the isocurvature perturbations for the DM gener-

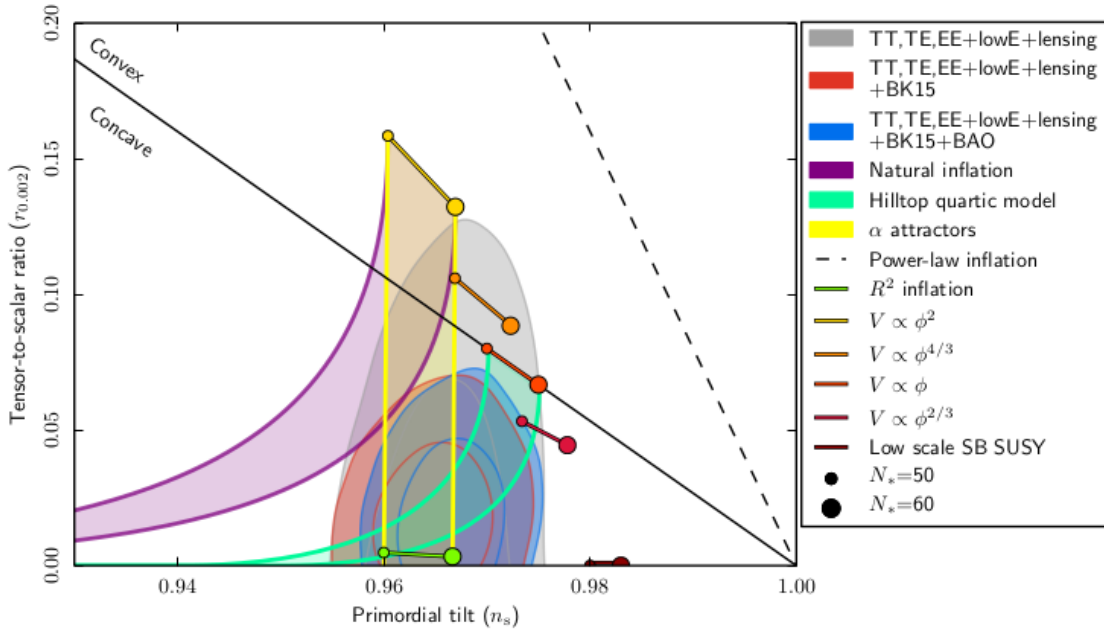


Figure 1-12.: 2D marginalised probability constraints on n_s and r for the most recent results of (Ade et al., 2016b). 2D constraints are plotted with 1σ and 2σ confidence contours.

ated by extra scalar fields during inflation, ρ_{DM} is the initial condition of DM and $\beta(k) \equiv P_{DM}/(P_R + P_{DM})$. We could follow also in this case the story line for the constraints that have been done for these isocurvature perturbations. However, we do not want to divert the reader too much by repeating the same procedure, so here we will only show the most recent constraints there are for this kind of perturbations. The uncorrelated scale-invariant DM isocurvature is constrained by Planck data (Akrami et al., 2018) at pivot scale k_0 as

$$\beta_{iso}(k_0) < 0.038 \quad \text{at 95\% CL.} \quad (1-143)$$

2. Theoretical background for scalar fields in general relativity

2.1. First ideas for Scalar Fields

A very intuitive way to understand the concept of a SF is by thinking of the temperature field in a room. The field is a scalar field in the sense that it is enough to associate a scalar value to every point in the room to completely describe it, unlike, for example, a vector field which requires a magnitude and a direction to be fully specified. It is expected that SFs vary continuously across the space in such a way that it should be possible to plot their variation in any chosen direction. In Figure 2-1 we show, for example, the temperature that should be measured in a room to exemplify the idea.

Although this simple description is very convenient to introduce the concept of SFs thanks to the simplicity associating it with a well-known situation, it is necessary to mention that temperature is not a *fundamental* SF, given that it is a macroscopic property of the space at each point, determined by other factors such as the proximity of heat sources. In the usual vocabulary of a physicist, a field (scalar or otherwise) is usually understood as something more abstract – a fundamental field of nature, which takes a determined value at each point in a given space, and may couple with other fields –. In fact, in quantum field theory, particles are localized fluctuations in these fundamental fields, and particle collisions create new particles because they transfer energy to, and thus produce fluctuations on, other coupled fields.

In general, SFs are ubiquitous in modern physics, either as a fundamental form of matter, such as the recently discovered Higgs boson, or as an effective description of some aspect of nature. In the simplest scenario, their evolution is described by the Klein-Gordon (KG) equation ([Gordon, 1926](#), [Klein, 1926, 1927](#))

$$(\square + \mu^2)\varphi = 0, \tag{2-1}$$

which can be considered as a relativistic generalization of the Schrödinger equation (SE) being μ the mass of the SF particle in natural units, φ a complex/real scalar field, and $\square \equiv d^2/dt^2 - \nabla^2$ the four-D’Alambert operator in a flat geometry and a metric signature $(+, -, -, -)$. It represented one of the first attempts to unify the ideas of quantum mechanics and the Einstein’s theory of special relativity. Its derivation can be easily obtained from the

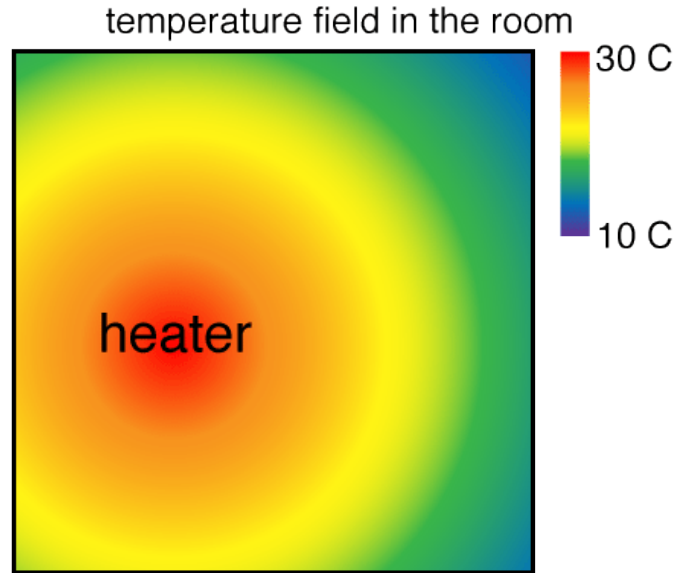


Figure 2-1.: Example for a Scalar Field: temperature in a room (Figure taken from (N., 2019)).

relativistic equation for the energy of a free particle:

$$E^2 = p^2 + \mu^2. \quad (2-2)$$

Then, by performing a canonical quantization and associating the corresponding Hermitian operators in the Schrödinger picture ($\hat{x} \rightarrow \hat{x}$, $\hat{p} \rightarrow -i\nabla$ and $E \rightarrow i\partial/\partial t$), it is easy to see that we arrive to (2-1). The KG equation can be generalized to describe a field in some potential $V(\varphi)$ as

$$\square\varphi + \frac{dV}{d\varphi^*} = 0. \quad (2-3)$$

It was called with such a name in honor of Oscar Klein and Walter Gordon, who in 1926 tried to describe relativistic electrons with this formalism. Although they were not right in their model given that modeling electron's spin required the Dirac equation, the KG equation correctly describes a spinless particle, as the Higgs boson.

The importance of studying SFs is due to the fact that they usually appear in most of the extensions for the Standard Model for particle physics (super-symmetric theories, GUTs, strings, etc). And, if that was not enough, those extensions have not only theoretical motivation, but also cosmological and astrophysical. Particularly, SFs in cosmology have been very useful as forms of DM, dark energy (DE), and inflationary candidates. Also, within the astrophysical context, they have been considered in models describing compact objects made of bosons with an appealing phenomenology (see (Dalfovo et al., 1999, Dodelson, 2003, Zee, 2010)). For this reason, we have enough motivation to continue extending the studies already done for SFs, being the main purpose in this thesis their application to DM.

2.2. Scalar fields with gravity

The coupling between the KG equation and gravity through Einstein equations, leading to the so called Einstein-Klein-Gordon (EKG) system, was first considered in the context of boson stars, which were initially introduced as a proposal of a “gravitational atom”, that corresponds to a macroscopic quantum state of a SF with an astronomical-sized wave-length. More recent studies consider that those objects are not actual “gravitational atoms” but rather Bose-Einstein condensates (BECs), made of excitations of a SF laying in the ground state (Kaup, 1968, Ruffini and Bonazzola, 1969). It was motivated by the axion field, a pseudo-Nambu-Goldstone boson of the Peccei-Quinn phase transition, which was proposed to solve the strong CP problem in QCD. Since then, the system continues being widely studied by the scientific community given that, as we already mentioned, there are several astrophysical objects where a SF could play an important role.

In this section, we review in a simple way the main equations used to describe a SF in the context of general relativity, close following Suárez and Chavanis (2015).

2.2.1. The Lagrangian of the scalar field

The general form of the action that considers a SF coupled to gravity can be expressed as

$$S = S_v + S_\varphi + S_{ext}, \quad (2-4)$$

where S_v is the vacuum contribution which can be decomposed in a gravitational term S_G and a cosmological contribution S_Λ , $S_v = S_G + S_\Lambda$, S_φ is the action that possesses all the information about the SF, and S_{ext} is an action associated to extra matter components in the system. In this thesis, we shall consider only SFs minimally coupled to gravity, and no coupled with other matter components. This kind of SFs can be described by the action:

$$S_\varphi = \int d^4x \sqrt{-g} \mathcal{L}_\varphi, \quad (2-5)$$

where $g = \det(g_{\mu\nu})$ and the Lagrangian is

$$\mathcal{L}_\varphi = \frac{1}{2} g^{\mu\nu} \partial_\mu \varphi^* \partial_\nu \varphi - V(\varphi). \quad (2-6)$$

Here, as mentioned before, $V(\varphi)$ is the SF potential, and ∂_α is a partial derivative with respect to α . Observe that in the particular case where the SF potential is of the form $V(|\varphi|^2)$, the Lagrangian is invariant under a global $U(1)$ transformation

$$\varphi \rightarrow \varphi e^{i\hat{\theta}}. \quad (2-7)$$

This symmetry implies that there is a Noether current density J_α defined as

$$J_\alpha = \frac{i}{2} \sqrt{-g} [\varphi^* \partial_\alpha \varphi - \varphi \partial_\alpha \varphi^*], \quad (2-8)$$

satisfying the conservation law $\nabla_\alpha J^\alpha = 0$ ¹, where in the above expression ∇_α is the covariant derivative.

2.2.2. The energy-momentum tensor for the scalar field

The energy-momentum tensor for the SF can be obtained by considering the variation of the SF's action with respect to the metric tensor, i.e.,

$$\delta S_\varphi = \frac{1}{2} \int d^4x \sqrt{-g} T_{\mu\nu}^{(\varphi)} \delta g^{\mu\nu}, \quad (2-9)$$

where

$$T_{\mu\nu}^{(\varphi)} \equiv 2 \frac{\partial \mathcal{L}_\varphi}{\partial g^{\mu\nu}} - g_{\mu\nu} \mathcal{L}_\varphi, \quad (2-10)$$

or equivalently

$$T_{\mu\nu}^{(\varphi)} = \frac{1}{2} (\partial_\mu \varphi^* \partial_\nu \varphi + \partial_\nu \varphi^* \partial_\mu \varphi) - g_{\mu\nu} \left[\frac{1}{2} g^{\rho\sigma} \partial_\rho \varphi^* \partial_\sigma \varphi - V(\varphi) \right]. \quad (2-11)$$

If we make the analogy with a perfect fluid, we could define a 4-velocity u^μ , and then, from the above equation,

$$\rho_\varphi = \frac{1}{2} \partial^\mu \varphi \partial_\mu \varphi + V(\varphi), \quad (2-12a)$$

$$p_\varphi = \frac{1}{2} \partial^\mu \varphi \partial_\mu \varphi - V(\varphi), \quad (2-12b)$$

$$u^\mu = \frac{\partial^\mu \varphi}{\sqrt{\partial^\mu \varphi \partial_\mu \varphi}}. \quad (2-12c)$$

In the general relativistic context, equation (2-11) must be used as a source term in the Einstein equations (1-5) :

$$G_{\mu\nu} \equiv R_{\mu\nu} - \frac{1}{2} g_{\mu\nu} R = 4\pi G T_{\mu\nu} - g_{\mu\nu} \Lambda, \quad (2-13)$$

where $T_{\mu\nu}$ contains, in general, all the energy constituents associated to the system, i.e., $T_{\mu\nu} = T_{\mu\nu}^{(\varphi)} + \text{extra sources}$.

2.2.3. The generalized Klein-Gordon equation

The generalized KG equation can be obtained in two different ways. First, by considering the conservation of the energy-momentum tensor (2-11) associated to the SF, $\nabla_\nu T^{\mu\nu} = 0$, or by considering the variation of the action S_φ with respect to the SF. In both cases we obtain

$$\square_c \varphi + \frac{dV}{d\varphi^*} = 0, \quad (2-14)$$

¹In the case the SF is charged, which for our purpose in this thesis it will be enough to consider it this way, this conservation law is related with the conservation of the total number of boson particles.

where \square_c is the four-D'Alembert operator in a curved spacetime geometry. Particularly, when we apply it to a scalar quantity

$$\square_c = \nabla_\mu (g^{\mu\nu} \partial_\nu) = \frac{1}{\sqrt{-g}} \partial_\mu (\sqrt{-g} g^{\mu\nu} \partial_\nu). \quad (2-15)$$

From now on we shall neglect subscript c in \square_c in order to simplify the notation of this thesis. Observe that this operator is reduced to the one used in (2-3) in a flat geometry. Additionally, notice that if the SF potential is of the form $V(|\varphi|^2)$, the KG equation can be rewritten as

$$\square\varphi + 2 \frac{dV}{d|\varphi|^2} \varphi = 0. \quad (2-16)$$

Then, the complete set of equations necessary to describe the SF is the Einstein-Klein-Gordon system (2-13) and (2-14) or equivalently (2-16).

2.3. Scalar field potentials

Until now, we have studied in a general way the main equations used to describe a SF minimally coupled to gravity. For this, we used the SF potential $V(\varphi)$ without mentioning so much about the nature of this quantity. The term $V(\varphi)$ results, in general, in a non-linear self-interaction of the field. That is, for a general SF potential, two plane waves in the field should not only superpose, but also interact in a non trivial way. The form of $V(\varphi)$ can be considered as a property of the field. For example, in the simple case where $V(\varphi) = \frac{1}{2}\mu^2\varphi^2$, being φ a real field, the potential represents a mass term for the SF. On the other hand, in more complicated scenarios, the potential could represent more complicated interactions, as it could be the case of couplings with some other quantities (as a temperature source or couples with some other particles, for example).

The shape of the potential for a field must be obtained from some higher energy theory in the case where the field is only an effective description. In the case of the inflaton and DM candidates – which we shall call as scalar field dark matter (SFDM) model –, that shape is essential in determining its behaviour and properties. To exemplify what we mean let us consider the KG equation (2-16) in a FLRW background (1-2)

$$\ddot{\varphi} + 3H\dot{\varphi} + 2 \frac{dV}{d|\varphi|^2} \varphi = 0, \quad (2-17)$$

where, for simplicity, we maintain the $|\varphi|^2$ dependence for the SF potential. In a similar way, the energy density and pressure for the SF is given, from equation (2-12a) and (2-12b), by

$$\bar{\rho}_\varphi = \frac{1}{2}|\dot{\varphi}|^2 + V(|\varphi|^2), \quad \text{and} \quad \bar{p}_\varphi = \frac{1}{2}|\dot{\varphi}|^2 - V(|\varphi|^2). \quad (2-18)$$

If we decompose the SF as

$$\varphi = |\varphi|e^{i\theta}, \quad (2-19)$$

the KG equation can be rewritten as

$$|\ddot{\varphi}| + 3H|\dot{\varphi}| + \left(2\frac{dV}{d|\varphi|^2} - \Omega^2\right)|\varphi| = 0, \quad (2-20)$$

where

$$\Omega \equiv \dot{\theta} = -\frac{Q}{|\varphi|^2 a^3}, \quad (2-21)$$

is defined as the pulsation of the SF, and Q its conserved charge (Arbey et al., 2002a, Gu and Hwang, 2001, Li et al., 2014, Suárez and Chavanis, 2015, 2017)². As it is explained in (Li et al., 2014, Suárez and Chavanis, 2017), the SF dynamics can be separated in a slow ($H \gg \Omega$) and a fast ($H \ll \Omega$) oscillating regime. In the slow regime, at sufficiently early times, the energy density and pressure (2-18) are both dominated by the first kinetic term, and then the equation of state for such regime is given by

$$\bar{p}_\varphi \simeq \bar{\rho}_\varphi \simeq \frac{1}{2}|\dot{\varphi}|^2, \quad (2-22)$$

which represents a stiff-like fluid. During that period, the energy density for the SF evolves as

$$\bar{\rho}_\varphi \propto \frac{1}{a^6}. \quad (2-23)$$

However, if the SF is real, the acceleration term ($|\varphi|$)'' will decrease by Hubble dragging until it can be ignored in (2-20), and the slow-roll condition is fulfilled. In such circumstance, the SF transits from the stiff-like fluid to a cosmological constant-like behavior. Such transition has been shown to be an attractor for the real SF in the slow oscillating regime (Belinsky et al., 1985, Piran and Williams, 1985). By considering the above description and if we consider that the energy density of the Universe is dominated by the one associated to the SF, we should obtain that the SF should drive an inflationary era during its attractor behavior (see chapter 1.3). On the other hand, in the fast oscillating regime, the SF oscillates several occasions in a Hubble time, and then, an effective equation of state can be obtained by averaging over a time interval that is much longer than the field oscillation period Ω^{-1} , but much shorter than the Hubble time H^{-1} . In that circumstance, the equation of state for the SF is given by

$$\bar{p}_\varphi \simeq \frac{(dV(\langle|\varphi|^2\rangle)/d\langle|\varphi|^2\rangle\langle|\varphi|^2\rangle) - V(\langle|\varphi|^2\rangle)}{(dV(\langle|\varphi|^2\rangle)/d\langle|\varphi|^2\rangle\langle|\varphi|^2\rangle) + V(\langle|\varphi|^2\rangle)}\bar{\rho}_\varphi. \quad (2-24)$$

For the SF as a DM candidate, what is expected is that it possesses a parabolic minimum at some critical value φ_c , around which it is possible to define a non-vanishing mass scale μ through the general relation $\mu^2 \equiv \partial^2 V/\partial|\varphi|^2$. If that happens, and after the SFDM

²To obtain (2-20) it was necessary to decompose the KG equation into its real and imaginary parts. Then, after solving the imaginary equation and substituting into the real one we finally arrive at equation (2-20).

candidate evolves and perform small oscillations around such minimum, i.e. it starts to evolve effectively through the potential

$$V(|\varphi|^2) = \frac{1}{2}\mu^2|\varphi|^2, \quad (2-25)$$

where for simplicity we took $\varphi_c = 0$ since the dynamical equations for the SF do not change, we can see that from equation (2-24) we obtain

$$\bar{p}_\varphi \simeq 0, \quad (2-26)$$

which is the equation of state used to describe a dust-like fluid (see equation (1-4)), and what is expected for a DM candidate (see next chapter). However, one can not discard, in general, the presence of higher terms $|\varphi|^4, |\varphi|^6, \dots$, which, at some scales or critical value, could be important. For example, in the context of extensions of the Standard Model of particle physics, there are several more complicated potentials that have been proposed for a SF that, at their minima, behave effectively as the above potential. Some examples are the axion-like trigonometric potentials (Cedeño et al., 2017, Zhang et al., 2018)

$$V(\varphi) = \mu^2 f^2 [1 - \cos(\varphi/f)], \quad (2-27)$$

where f is a decay constant, or its hyperbolic counterpart (Sahni and Wang, 2000, Tonatiuh et al., 2000)

$$V(\varphi) = \mu^2 f^2 [\cosh(\varphi/f) - 1]. \quad (2-28)$$

Notice that in both cases, the potential is reduced to (2-25) when $\varphi/f \ll 1$.

From potentials (2-27) and (2-28) it is suggested the minimum extension to (2-25) as

$$V(\varphi) = \frac{1}{2}\mu^2|\varphi|^2 + \frac{1}{4}\nu|\varphi|^4, \quad (2-29)$$

being ν a constant. The above quantity represents a short-range self-interacting potential, where $\nu > 0$ ($\nu < 0$) is for repulsive (attractive) self-interaction. This extension results to be very interesting given that, after adding this new degree of freedom, there is extra physics emerging associated to the model. For instance, by using the above potential and (2-24), we obtain

$$\bar{p}_\varphi \simeq \frac{1}{3} \left[\frac{1}{1 + \frac{4\mu^2}{3\nu\langle|\varphi|^2\rangle}} \right] \bar{\rho}_\varphi. \quad (2-30)$$

Then, the equation of state of the SF turns out to be more complicated, so that the behavior obtained in the case without self-interaction is not always fulfilled. Particularly, when $2\mu^2/(3|\nu|\langle|\varphi|^2\rangle) \gg 1$ we recover the dust-like behavior.

As we can see, the selection of the SF potential is not trivial and, in general, it should be motivated by different arguments, as it is the case of justify them by extensions of standard physics or from the nature of the problem we are dealing with. In a general scenario, what should be expected for such a SF potential is that it should be well supported in all contexts, i.e., from a theoretical point of view, observationally by its effects in nature and, in the best case, the particle subject to this potential being detected by some experiment.

2.4. Gravitationally bound systems

The formation of gravitationally bound objects comprised by SF configurations has been extensively studied in the literature (see eg. [Jetzer, 1992](#), [Lee and Pang, 1992](#), [Liddle and Madsen, 1992](#), [Mielke, 2016](#), [Schunck and Mielke, 2003](#), [Seidel and Suen, 1990](#), [Straumann, 1992](#), for some reviews). Depending on whether the field is complex or real, they are called boson stars or oscillatons. The characteristic behavior for them is very similar in average, although oscillatons are distinguished by being oscillatory solutions (as their name's suggest), whereas boson stars correspond to stationary distributions. In this section, we shall review the main properties of boson stars following the above references, since for this thesis it will be very important to understand them.

2.4.1. Boson stars

The simplest form to study a SF in nature is by considering it as the only source appearing in the Einstein's equations (2-13). Within this context, the concept of boson stars has been well studied. For stars, we usually think of an object that entails a configuration which remains localized. However, it is well known that no-regular, static and non-topological localized SF solutions are stable in a three (spatial) dimensional flat space (see Derrick's Theorem ([Derrick, 1964](#))). This constraint is avoided by adopting a harmonic decomposition for the SF of the form

$$\varphi(\mathbf{x}, t) = \varphi_0(\mathbf{x})e^{i\gamma t}, \quad (2-31)$$

where φ_0 is a real scalar, and γ is a real constant denoting the angular frequency of the oscillations of the SF. Although the SF evolves in time harmonically, the spacetime remains constant. Given the quantum nature of the KG equation, these configurations can be understood, in the simplest case of having a free field, as a result of the balance between the attraction due to gravity, and the repulsion due to the Heisenberg uncertainty principle of quantum mechanics.

The typical way to construct boson stars is just by considering spherical symmetry and requiring the space-time to be static. In a 3 + 1 decomposition³, and Swarzschild-like coordinates, the general metric that is used to describe the above description is given by

$$ds^2 = -\alpha(x)^2 + a(x)^2 + x^2(d\theta^2 + \sin^2\theta\phi^2), \quad (2-32)$$

³A 3 + 1 decomposition uses the total number of particles in the configuration, is equal to zero. This binding energy is particularly important in the analysis of stability for this kind of objects. In all cases, distributions corresponding to central densities $\varphi_c < \varphi_{c,\Lambda}^{(b)}$, possesses an $E_b < 0$, while in the opposite direction $\varphi_c > \varphi_{c,\Lambda}^{(b)}$, we have $E_b > 0$. A positive bi

a succession of spacetime geometries to describe how an initial configuration evolves towards the future, where the evolution of a given slice is given by the Einstein equations. For an introduction for this formalism we encourage the reader to look at ([Alcubierre, 2008](#), [Baumgarte and Shapiro, 2010](#), [Bona et al., 2009](#)).

where α and a^4 are real metric functions, and r is usually called Areal radius. For this reason the above coordinates are usually called polar-areal coordinates. After using the above metric with the ansatz (2-31) in the EKG system (2-13) and (2-14) or equivalently (2-16), we obtain that boson stars are described by the set of differential equations:

$$\frac{\partial_x a}{a} = \frac{1 - a^2}{2x} + 2\pi x \left[\gamma^2 \varphi_0^2 \frac{a^2}{\alpha^2} + \Psi_0^2 + a^2 \varphi_0^2 \left(\mu^2 + \frac{1}{2} \nu \varphi_0^2 \right) \right], \quad (2-33a)$$

$$\frac{\partial_x \alpha}{\alpha} = \frac{a^2 - 1}{x} + \frac{\partial_x a}{a} - 4\pi x a^2 \varphi_0^2 \left(\mu^2 + \frac{1}{2} \nu \varphi_0^2 \right), \quad (2-33b)$$

$$\partial_x \varphi_0 = \Psi_0, \quad (2-33c)$$

$$\partial_x \Psi_0 = -\Psi_0 \left(\frac{2}{x} + \frac{\partial_x \alpha}{\alpha} - \frac{\partial_x a}{a} \right) - \gamma \varphi_0^2 \frac{a^2}{\alpha^2} + a^2 (\mu^2 + \nu \varphi_0^2) \varphi_0, \quad (2-33d)$$

where for simplicity we have used in the above expressions the quartic potential (2-29), which is the potential we mainly focused on in this thesis.

The above system of differential equations has been solved numerically in the case of a repulsive self-interaction, and in its free-field limit,⁵ by imposing regularity at the origin $\varphi_0(0) = \varphi_c$, $\Psi(0) = 0$ and $a(0) = 1$, and asymptotic isolated flat space $\varphi_0(x \rightarrow \infty) = 0$ and $\alpha(x \rightarrow \infty) = a(x \rightarrow \infty)^{-1}$ (see for example (Escorihuela-Tomàs et al., 2017)). With such conditions, we make sure that the final configuration resulting from the above solution is regular at all space. Depending on the central value of the SF φ_c , there should exist an infinite number of solutions which satisfy all the asymptotic conditions, each of them differentiating from each other by the number of nodes that they possess before decaying asymptotically, and the numerical value for their parameter γ . It happens that the solution without nodes – considered as the ground state of the EKG system – possesses the smallest numerical value for γ , and the value of this parameter increases while the number of nodes of each solution – referred as excited boson stars – increases.

Let us first talk about the ground state solution, which from now on we will refer to as the “soliton” solution⁶. In Figure 2-2 we show a plot for the mass of each soliton, defined as⁷

$$M_{BS}(x_{max}) = \frac{x}{2} \left(1 - \frac{1}{a^2(x_{max})} \right), \quad (2-34)$$

⁴We should not be confused with the scale factor a . In this section we decided to reuse this letter to refer to this new function so that we can be consistent with the usual notation of most authors working on this subject.

⁵The attractive scenario has not been completely studied in the general relativistic regime. However, there are some works where this case was studied in the weak-field limit. We shall review such results in the next section.

⁶We decided to use this name in order to be consistent with the literature about scalar fields as the dark matter.

⁷This way of calculating the mass of the boson star is by using the definition of the Misner-Sharp mass function.

where x_{max} is the radius at the boundary of the numerical grid well after the soliton profile has decayed, vs the central values of the SF for different self-interactions

$$\Lambda \equiv \frac{\nu}{4\pi G\mu^2}. \quad (2-35)$$

First at all, we can notice that as long as the value of the self-interaction Λ increases, the final boson star generated allows more massive configurations. This is an expected behavior given that a repulsive self-interaction indicates that there exist a repulsive force (aditional to the one generated by the uncertainty principle) that opposes matter to agglomerate at the center. On the other hand, observe that in the plot there are two important points for each curve: a pink square (at $\varphi_c = \varphi_{c,\Lambda}^{(max)}$, where we decided to left explicitly the Λ dependence of such point) which corresponds to the maximum mass allowed by a boson star for a given Λ , and that divided a stable (for $\varphi_c \in (0, \varphi_{c,\Lambda}^{(max)})$) from an unstable ($\varphi_c > \varphi_{c,\Lambda}^{(max)}$) branch, and a cyan triangle (at $\varphi_c = \varphi_{c,\Lambda}^{(b)}$), which points to the value at which the binding energy of the boson star, defined as

$$E_b = M_{BS} - N\mu, \quad (2-36)$$

where

$$N = \int g^{0\alpha} J_\alpha d^3\mathbf{x} \quad (2-37)$$

is the total number of particles in the configuration, is equal to zero. This binding energy is particularly important in the analysis of stability for this kind of objects. In all cases, distributions corresponding to central densities $\varphi_c < \varphi_{c,\Lambda}^{(b)}$, possess an $E_b < 0$, while in the opposite direction $\varphi_c > \varphi_{c,\Lambda}^{(b)}$, we have $E_b > 0$. A positive binding energy implies that the configuration possesses an excess of energy, enough to dissipate the soliton profile, while in the opposite case, the configuration is confined and stable under perturbations if it is in the stable branch, or unstable to collapse and form a BH if it is in the unstable branch.

Finally, regarding the soliton profile, we need to talk about the maximum mass allowed for a SF configuration (the pink square). The first study that found a parameter dependence for such quantity in the free field limit was obtained in (Ruffini and Bonazzola, 1969). In their studies, they found that the parameter dependence for such quantity is given by

$$M_{crit} \sim \frac{m_{pl}^2}{\mu}. \quad (2-38)$$

Later, by means of numerical simulations assuming spherical symmetry, (Seidel and Suen, 1991, 1994) figured out a more precise relation for the critical mass of collapse of a system of free bosonic particles, given by

$$M_{crit} \simeq 0.633 \frac{m_{pl}^2}{\mu}. \quad (2-39)$$

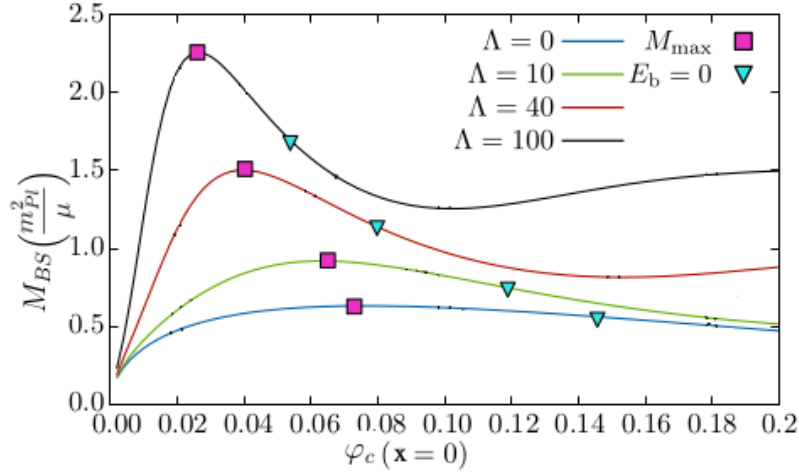


Figure 2-2.: Boson star mass as a function of the central value of the SF φ_c for different values of Λ . For each value of Λ the pink square represents the maximum possible mass for a boson star, separating the stable and unstable branches, while the inverted cyan triangles indicate the point at which the binding energy is equal to zero (Figure taken from (Escorihuela-Tomàs et al., 2017)).

On the other hand, in the case of a self-interacting SF with a repulsive self-interaction, the critical mass of collapse reads (Colpi et al., 1986)

$$M_{crit} \simeq 0.22\sqrt{\Lambda} \frac{m_{pl}}{\mu}. \quad (2-40)$$

Notice that the self-interaction allows much larger masses than in its free field counterpart as long as $\nu/\mu^2 \gg 1$.

In the case of SFDM configurations including excited states of a scalar field with a given mass (Bernal et al., 2010, Hawley and Choptuik, 2003, Seidel and Suen, 1990, Ureña-López, 2009, Ureña-López and Bernal, 2010), it was found that the resulting configurations can have larger masses. However, they have been found to be unstable and migrate by *gravitational cooling* to the ground state solution.

2.4.2. Newtonian boson stars

In the weak-field limit, we can consider that the spacetime metric tensor can be approximated as $g_{\mu\nu} = \delta_{\mu\nu} + \delta g_{\mu\nu}$, where $\delta_{\mu\nu}$ is the Minkowski spacetime. Under such condition, the metric functions a and α can be re-expressed as

$$\alpha^2 \simeq 1 + 2\Phi \simeq a^2. \quad (2-41)$$

Then, by assuming a decomposition of the SF given by

$$\varphi(\mathbf{x}, t) = \frac{1}{\sqrt{\mu}} \psi(\mathbf{x}, t) e^{i\mu t}, \quad (2-42)$$

the EKG system is rewritten as

$$\nabla^2\Phi = 4\pi G\mu|\psi|^2, \quad (2-43a)$$

$$i\dot{\psi} = -\frac{1}{2\mu}\nabla^2\psi + \mu\Phi\psi + \frac{\nu}{\mu^2}|\psi|^2\psi. \quad (2-43b)$$

These equations are the so-called Gross-Pitaevskii-Poisson (GPP) system. The first equation is the Poisson equation, used to describe Newtonian systems. This is the reason that boson stars constructed in this limit are usually called Newtonian boson stars. The second equation is the Gross-Pitaevskii equation, which is reduced to the Schrödinger equation in the free-field limit. Then, when the self-interacting parameter is equal to zero, the above system is called the Schrödinger-Poisson (SchP) system.

Two important quantities that are necessary to describe SF configurations, and that are well defined in the Newtonian limit, are the total mass M_t and total energy E_t associated to the system:

$$M_t = \mu \int_V |\psi|^2 d^3\mathbf{x}, \quad (2-44a)$$

$$E_t = \int_V \left[\frac{1}{2\mu} |\nabla\psi|^2 + \frac{\mu}{2} \Phi |\psi|^2 + \frac{\nu}{2\mu^2} |\psi|^4 \right] d^3\mathbf{x}. \quad (2-44b)$$

Notice that the total energy can be written in a very instructive way:

$$E_t = K_t + W_t + U_{SI,t}, \quad (2-45)$$

where

$$K_t = \int_V \frac{1}{2\mu} |\nabla\psi|^2 d^3\mathbf{x}, \quad (2-46a)$$

is the total kinetic energy,

$$W_t = \int_V \frac{\mu}{2} \Phi |\psi|^2 d^3\mathbf{x}, \quad (2-46b)$$

is the total gravitational potential energy and

$$U_{SI,t} = \int_V \frac{\nu}{2\mu} |\psi|^4 d^3\mathbf{x}, \quad (2-46c)$$

is the total energy associated to the self-interaction. This last way of writing each energy contribution is very convenient, because they also appear in the scalar Virial theorem of an isolated mass distribution:

$$2K_t + W_t + 3U_{SI,t} = 0. \quad (2-47)$$

By considering the following transformation

$$\hat{\psi} = \sqrt{\frac{4\pi G}{\mu}} \psi, \quad \hat{\Phi} = \Phi, \quad \hat{\mathbf{x}} = \mu\mathbf{x}, \quad \hat{t} = \mu t, \quad (2-48)$$

the GPP equations are rewritten in such a way that all the constants disappear:

$$\hat{\nabla}^2 \hat{\Phi} = |\hat{\psi}|^2, \quad (2-49a)$$

$$i\partial_{\hat{t}} \hat{\psi} = -\frac{1}{2} \hat{\nabla}^2 \hat{\psi} + \hat{\Phi} \hat{\psi} + \Lambda |\hat{\psi}|^2 \hat{\psi}, \quad (2-49b)$$

where in the above expression we used explicitly $\partial_{\hat{t}}$ instead of an over-dot, since we are deriving with respect to \hat{t} instead of t . The above expression results to be very interesting given that it implies that the properties of the system are the same, independently of the mass parameter of the boson particle, being important only the parameter Λ , present when there is a self-interaction. Additionally, there is a rescaling property for this GPP system given by

$$\{\tilde{t}, \tilde{\mathbf{x}}, \Lambda, \tilde{\psi}, \tilde{\Phi}\} \Rightarrow \{\gamma^2 \hat{t}, \gamma \hat{\mathbf{x}}, \gamma^2 \hat{\Lambda}, \gamma^{-2} \hat{\psi}, \gamma^{-2} \hat{\Phi}\}, \quad (2-50)$$

which are traduced in a rescaling property for the energy quantities as

$$\{\tilde{M}_t, \tilde{K}_t, \tilde{W}_t, \tilde{U}_{SI,t}\} \Rightarrow \{\gamma^{-1} \hat{M}_t, \gamma^{-3} \hat{K}_t, \gamma^{-3} \hat{W}_t, \gamma^{-3} \hat{U}_{SI,t}\}. \quad (2-51)$$

Newtonian boson stars are constructed similarly to their general relativistic counterpart, this is, it is necessary to consider an harmonic ansatz for the SF of the form

$$\hat{\psi}(\hat{\mathbf{x}}, \hat{t}) = \hat{\phi}(\hat{x}) e^{-i\hat{\mu}_Q \hat{t}}, \quad \hat{\mu}_Q, \hat{\phi} \in \mathcal{R}, \quad (2-52)$$

where \hat{x} is the dimensionless spherical radial coordinate, and $\hat{\mu}_Q$, in analogy to the standard physics of boson particles in a flat geometry, is the dimensionless GPP chemical potential which should be fixed by the conservation of particle number. Then, it is necessary to impose correct boundary conditions: regularity at the origin $\hat{\phi}(0) = \hat{\phi}_c$ and $\partial_{\hat{x}} \hat{\phi}(0) = 0$, and asymptotic isolated flat space $\hat{\phi}(\hat{x} \rightarrow \infty) = 0 = \hat{\Phi}(\hat{x} \rightarrow \infty)$. The final kind of configurations obtained adopt the same properties of the boson stars in the general relativistic treatment: there is a ground state without nodes – the soliton – that possesses the smallest value of the μ_Q parameter, and excited Newtonian boson stars. Additionally, all of these boson stars fulfill the virial condition (2-47). In Figure 2-3, we show, in the left plot, different soliton configurations for the same initial value $\hat{\phi}_c = 1$, while in the right one, we show the total number of particles given by

$$N = \int |\psi|^2 d^3 \mathbf{x} = \int \psi^2 d^3 \mathbf{x}, \quad (2-53)$$

vs the radius x_{95} that contains the 95% of the mass of the configuration. Observe that the bigger the Λ , the less compact the configuration is and then it is less dense. As we discussed before, this property is expected by the nature of the force that is provided by the self-interacting term: a repulsive self-interaction forbids the matter to agglomerate at the center of the configuration, and then the distribution should be more diluted.

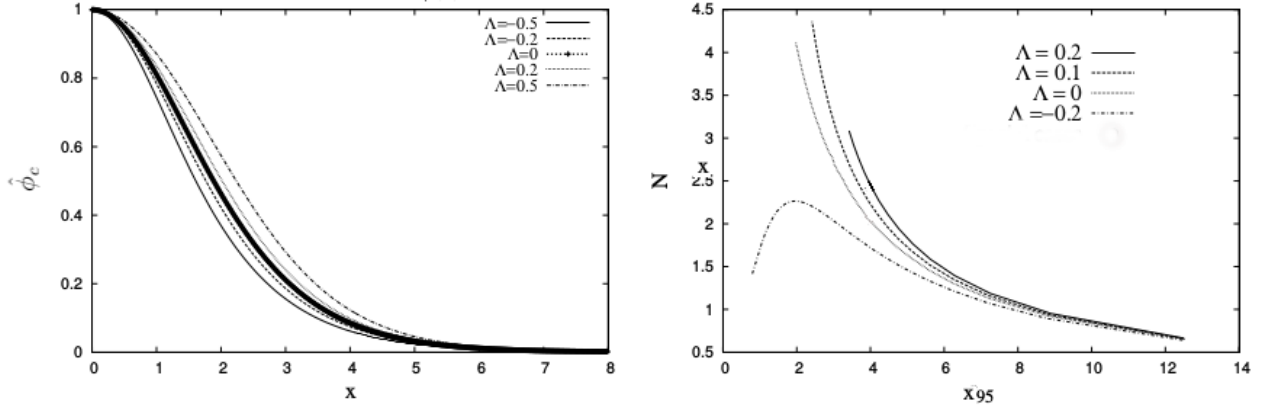


Figure 2-3.: (Left) Profiles $\hat{\phi}$ of equilibrium configurations for different values of Λ s. (Right) Mass-Radius relation for different values of Λ (Figure taken from (Guzman and Urena-Lopez, 2006)).

Observe that from (2-50), it is possible to construct different solutions for the soliton once one of them is known. In fact, as it is explained in Guzman and Urena-Lopez (2006), in the free case, it is possible to construct all the ground state solutions for any central scalar field value just by using the rescaling property given in (2-50). On the other hand, in the self-interacting case, it occurs something similar: once a ground state solution is known for a given value of $\hat{\Lambda}$, it is possible to construct all the ground state solutions for different central values of the SF and the same value of $\hat{\Lambda}$, just by using the rescaling properties provided in (2-50). However, if we were interested in finding a new soliton solution with a different $\hat{\Lambda}$, it should be necessary to solve the differential equations (2-49) for such $\hat{\Lambda}$ one more time.

Remark: Notice that thanks to the rescaling property of the GPP system, in the Newtonian approximation it does not appear a maximum mass allowed for the configuration. However, this result is not expected to happen given that, at some point, it should be necessary to take into account the relativistic corrections. On the other hand, in the numerical treatment when $\hat{\Lambda} < 0$ it appears a maximum mass allowed for a Newtonian soliton given by (Eby et al., 2016)

$$M_{c,max} \simeq 10.03 \frac{m_{pl}}{\sqrt{|\nu|}}, \quad (2-54)$$

where we have decided to use ν instead of $\hat{\Lambda}$ for simplicity in the writing of the above expression. However, the $\hat{\Lambda}$ dependence for the above critical mass can be easily obtained from (2-48).

3. The Dark Matter paradigm

In section 1.2.2 we have mentioned that one of the components necessary to describe the Universe consists in a DM candidate. We did not notice the existence of DM up to the first half of XX century. However, after obtaining more precise astrophysical and cosmological data, it appeared necessary the incorporation of such ingredient into the cosmological model to explain satisfactorily the different gravitational effects that could not be explained with the typical amount of baryonic matter of the studied systems. Such “missing matter” problem has appeared at different scales (like galaxies, group of galaxies, clusters, super clusters, etc), which has led to put under question the need to incorporate a dark component to the theory to solve all these discrepancies.

In this chapter, we present the different observational evidences that have suggested the incorporation of DM to the total matter-energy content of the Universe. Additionally, we briefly review the Λ CDM model. We will mention the different achievements and issues that such description possesses after different observational data is considered, focusing particularly in the problems coming from small scales, which allows the possibility of considering new cosmological models which could help explaining in a more satisfactory way the nature of DM. This last step is particularly interesting for us, given that, in the next section, we shall consider an alternative model to Λ CDM model.

3.1. Observational evidence for dark matter

3.1.1. Clusters of galaxies

In 1933, the Swiss-American astronomer Fritz Zwicky was one of the first researchers who suggested the necessity of extra matter when studying the dynamics of the COMA cluster. By using the Virial theorem

$$2\langle T \rangle = q\langle U \rangle, \tag{3-1}$$

where in the above result it was considered a radial dependence of the potential of the form $U(r) \propto r^q$, being q a constant, T (U) is the kinetic (potential) energy, and $\langle \cdot \rangle$ meaning average over time, Zwicky (1933) On the other hand, Boylan-Kolchin et al. (2011) pointed out that there still a problem with the most massive subhalos, the so-called *too big to fail* problem, This aspect of satellites arises because the most

calculated the mass of the COMA cluster as follows: Starting from the kinetic and gravitational energy associated to the cluster

$$T = \frac{1}{2}Mv^2, \quad U = -\frac{GM^2}{r}, \quad (3-2)$$

where G is the Newton constant, M is the mass of the cluster, v is the velocity and $r = ax$ is the physical radius measured from the center of the cluster. Here and for the rest of this thesis we decided not to use $\langle \cdot \rangle$ in order to simplify the notation. However, in all cases it shall be easy to understand when we refer to mean quantities or not. In the above relation has been assumed point particle interactions between the elements of the cluster, and an uniformly distributed matter content. Then, by using (3-2) in (3-1), and identifying $q = -1$, the mass of the cluster can be estimated as

$$M = \frac{v^2}{G/r}. \quad (3-3)$$

Considering the mass measured by its luminosity distribution ($M \sim 10^{11}M_{\odot}$), he obtained that the velocity of the cluster's constituents should be around 400 times smaller than what was being measured. With this result, Zwicky concluded that in order to be consistent with his observations, it should be necessary that an invisible matter content, which he called dark matter, should exist and affect considerably the dynamics of the COMA cluster.

3.1.2. Rotation curves in spiral galaxies

Vera Rubin was one of the pioneers in measuring rotation curves in spiral galaxies with high precision (Rubin et al., 1985, Rubin and Ford Jr, 1970). Since then, such measurements have been one of the main observations that have justified the existence of an extra contributor to the visible matter in galaxies.

Spiral galaxies are stable gravitationally bound systems in which visible matter is composed of stars and interstellar gas. Most of the observable matter is on a relatively thin disk, where stars and gas rotate around the galactic center in almost circular orbits. If the circular speed of a star at radius r is v in a galaxy with mass $M(r)$ within r , the stability condition implies that the centrifugal acceleration v^2/r must be equal to the gravitational force $GM(r)/r^2$, which results in a Keplerian law for the radial dependence of v :

$$v = \sqrt{\frac{GM(r)}{r}}. \quad (3-4)$$

Interestingly, the findings of Vera Rubin were completely different to the above consequence. She found that orbital velocities remain constant as distance increases. In Figure (3-1), we show such behavior for NGC 6503 galaxy, where each contributor to the velocity is shown. Observe that with only the contribution of the baryonic matter (gas and disk), it is not

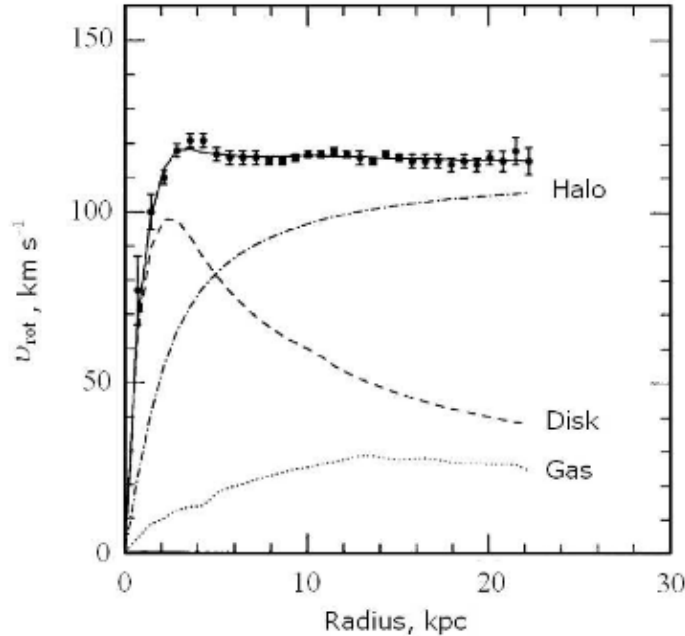


Figure 3-1.: Rotational velocity for NGC 6503. The contribution of several constituents to the galaxy is shown (Figure from (Pécontal et al., 2009)).

enough to reproduce the observational data. For such reason, it seems necessary the incorporation of a non-visible matter lying far from the center of galaxies, or in Vera Rubin words

“It appears that much of the matter in spiral galaxies emits no light. Moreover, it is not concentrated near the center of the galaxies.”

This implies that a DM halo is necessary to be incorporated to the content of matter to correctly reproduce the observational data.

In the same direction, (Ostriker, 85) found with numerical simulation that galactic disks from spiral galaxies are unstable when there is only a baryonic component. Then, the incorporation of a DM halo is necessary to explain not only rotation curves, but also the stability of this kind of galaxies.

3.1.3. Gravitational lensing

Another interesting idea used to measure the amount of matter in a given galaxy, is through the deviation of light in the vicinity of such gravitational source. This effect is the so-called *gravitational lensing*, and is one of the predictions of Einstein’s General theory of Relativity. It can be understood as the distortion of a source of light when it passes near a massive

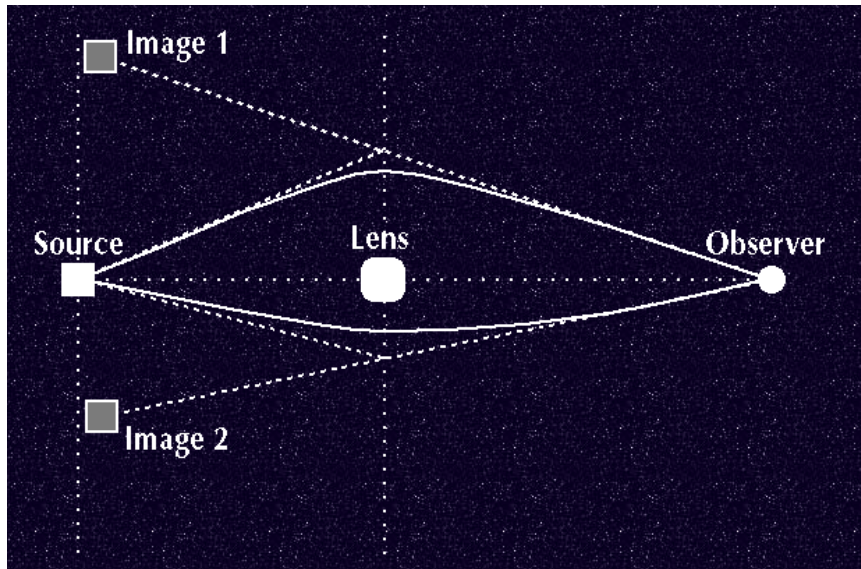


Figure 3-2.: Representation of gravitational lensing (figure taken from (Int., 2019)).

object before reaching an observer. A representation of this effect is shown in Figure 3-2. Such effect is analogue to the case when light passes through an optical lense; that is the reason for its name.

Although Einstein made some calculations in 1912 about this phenomenon (Sauer, 2008), it was Orest Khvolson and Frantisek Link (Bičák and Ledvinka, 2014) who first discussed the effect in print. Posteriorly, Fritz Swicky postulated in 1937 that the effects could allow galaxy clusters to act as gravitational lenses. However, it was not until 1979 that this effect was confirmed by observation of the so-called Twin QSO SBS 0957+561.

Given that gravitational lensing occurs by the effect of a gravitational potential of a massive object, it is possible to reconstruct the mass distribution which causes such effect. This can be seen very easy in the so-called Bullet cluster, which consisted in two colliding clusters of galaxies. In this event, it was possible to obtain an image of the baryonic component of the system (determined by optical images in the case of stars, and by X-rays in the case of the plasma), and the mass distribution of the gravitational potentials reconstructed by lensing. The final result obtained can be appreciated in Figure 3-3, where in red is shown the measurements obtained for the baryonic matter, while the main gravitational sources are represented in blue. For such image, authors in (Clowe et al., 2006) concluded that

“The observed displacement between the bulk of the baryons and the gravitational potential proves the presence of dark matter for the most general assumptions regarding the behavior of gravity.”

Since then, gravitational lensing studies of the Bullet cluster are considered as the most important observation that supports the existence of a DM component in the Universe. In

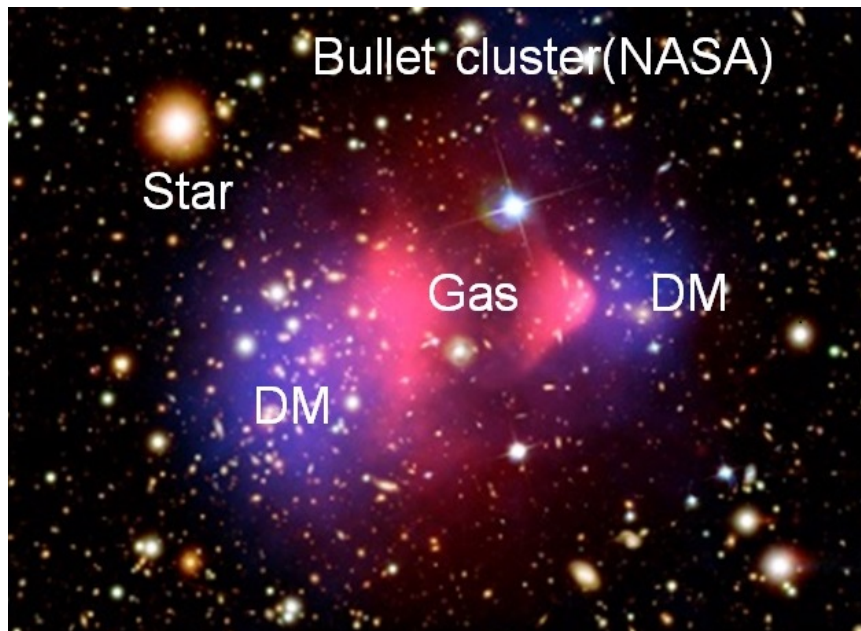


Figure 3-3.: Observation of the Bullet cluster. In red is shown the measurements of the baryonic component while the gravitational sources are represented in blue (figure taken from (Nanoqed, 2019)).

addition, there have been more observations for the collision of other clusters, supporting this conclusion.

3.2. The Λ CDM model

In the above section, we saw that there exist a host of observational evidence that supports the introduction of a new mechanism for generating an extra gravitational contribution at different scales in the Universe. For such reason, it has been proposed to introduce a new substance in the Universe that should only interact gravitationally, or a modification of the theory of gravity. Both of such possibilities have been extensively studied in the literature, where, at the moment, the Λ CDM model has been the preferred to describe our Cosmos.

In the introduction of this thesis 1, we have extensively talked about the Λ CDM model. We have also comment that it possesses several problems when it is tested with different observational data. In this section, we shall review in more detail its description, paying special attention on results coming from the structure formation process for this model, and the problems that it possesses in its final results.

3.2.1. The CDM sector and structure formation

Of special interest in the Λ CDM model is the result obtained in the structure formation process (see (Bertschinger, 1998, Del Popolo, 2007, Primack, 2017) for a review). As we already

mentioned, at very large scales, linear perturbation calculations from Λ CDM allow accurate predictions for the Universe. However, at scales where structure forms, the fluctuations have grown enormously, and became highly non-linear. At such scales, it is necessary to make use of numerical simulations that allow us to solve the system of nonlinear differential equations that arises for this description. Particularly, CDM dynamics is described in comoving coordinates by

$$\begin{aligned} \dot{\vec{x}} &= \frac{1}{a}\vec{v}, & \nabla^2\Phi &= -4\pi Ga[\rho(\vec{x}, t) - \bar{\rho}(t)], \\ \rho\dot{\vec{v}} + \frac{1}{a^2}\rho(\vec{v} \cdot \nabla)\vec{v} &= -\rho\nabla\Phi, & \dot{\rho} + \frac{1}{a^2}\nabla \cdot (\rho\vec{v}) &= 0, \end{aligned} \quad (3-5)$$

where \vec{v} is the *peculiar velocity*, Φ is the gravitational potential, ρ is the mass density, and $\bar{\rho}$ is the spatial mean density. The structure formation process considers regions that started out with a density a little higher than the mean density of the Universe. Then, such regions possessed a highly gravitational attraction than the homogeneous background, in such case they expanded until reaching a maximum expansion radius, known as the *turn-around radius*, and then collapsed to its geometrical center until relax and form a virialized structure.

From 2005 to 2010, the bench-mark simulations were Milenium I (Springel et al., 2005) and Milenium II (Boylan-Kolchin et al., 2009), which were the basis for a large number of scientific letters. However, the improvement of cosmological parameters, computer power, and simulation codes have permitted increasingly more accurate simulations, for instance (Klypin et al., 2016, 2011, Kuhlen et al., 2012, Prada et al., 2012, Riebe et al., 2013, Skillman et al., 2014). For example, in Figure 3-4, we show the schematic results obtained for several simulations at large (cluster of galaxies) and small (single galaxies) scales, and considering or not the contribution of the baryonic component. As it is evident, high-resolutions simulations permit detailed predictions of the distribution and properties of galaxies and clusters, unfortunately, our understanding for structure at large scales remains far to be satisfactory. The description for the evolution of structure from inhomogeneities, i.e., primordial density perturbations, is complicated since there exist several physical processes like the gas dynamics, radiative cooling, photo-ionization or recombination. Additionally, for whichever theoretical prediction, we have to compare it with the Universe structures, being particularly difficult the regions where there could exist several discipative effects.

The universal shape found of these virialized dark matter density profiles can be well described by the so called Navarro-Frenk-White (NFW)

$$\rho(r) = 4\frac{\rho_s}{(r/r_s)[1 + r/r_s]^2}, \quad (3-6)$$

where $r = ax$ is the radial coordinate in physical units, r_s is known as the *scale radius*, and ρ_s is the value of the density at radius $r = r_s$. It is necessary to mention that the above profile was obtained by numerical simulations that used CDM without considering a baryonic contribution.

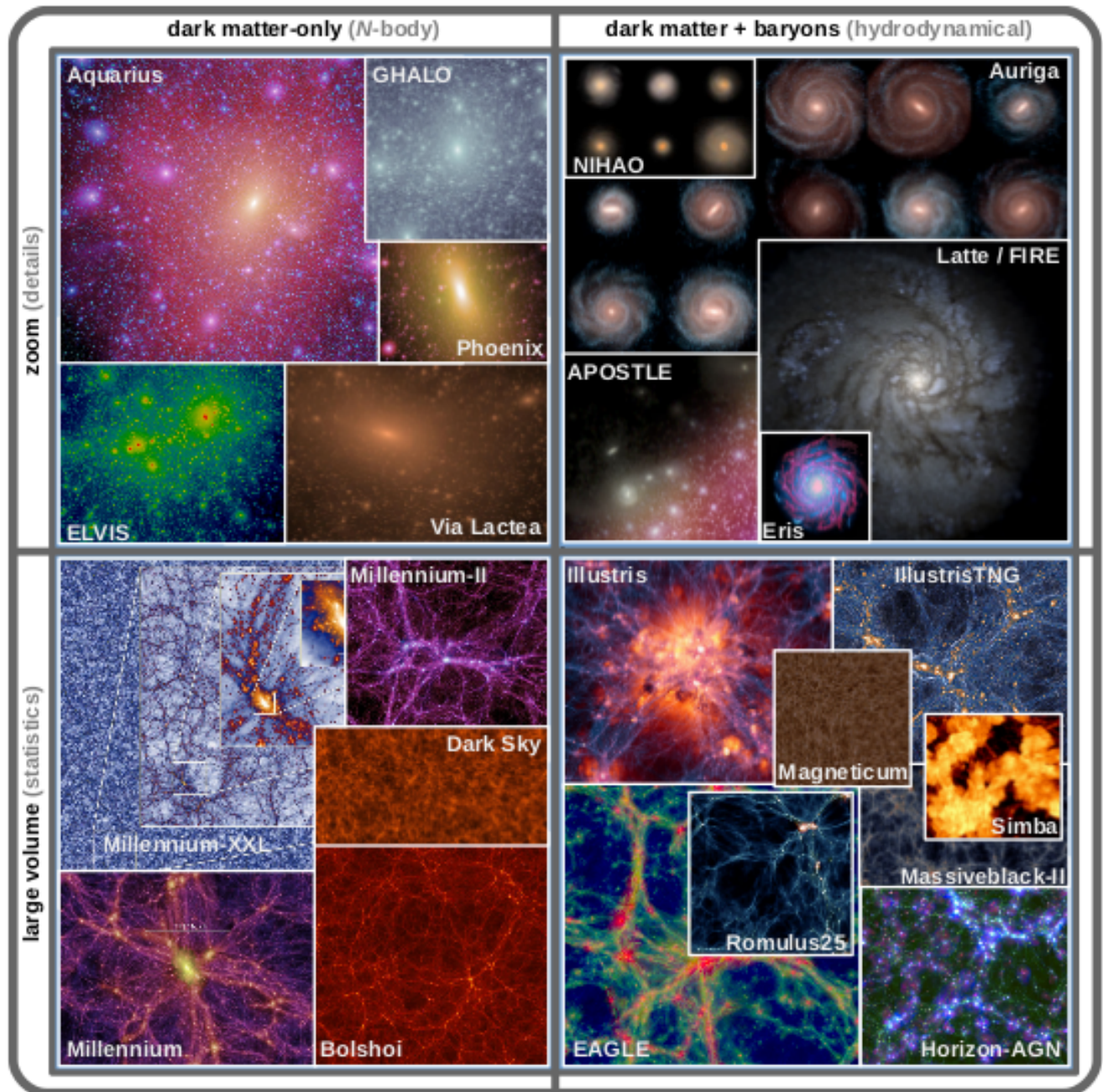


Figure 3-4.: Schematic results for structure formation in the Λ CDM model (Vogelsberger et al., 2020). It is presented the results obtained when baryons are considered and when they are not.

3.2.2. Problems with the CDM sector

3.2.2.1. The satellite plane problem

Since the 1990s, there has been a large range of observations suggesting that the Milky Way (MW) satellites are distributed on a planar structure, the so-called “Magellanic Plane” (Kunkel and Demers, 1976, Lynden-Bell, 1976), the disc of satellites (Kroupa et al., 2005, Metz et al., 2008), the MW “vast popular structure”, and the “great plane of Andromeda” (Ibata et al., 2013, Pawlowski et al., 2014, 2015, Pawlowski and Kroupa, 2013). Recent studies by Kroupa et al. (2005), Metz et al. (2006), Pawlowski and Kroupa (2013) described the structure as a thin disc, having a height of 20 kpc, and 9 of the 11 classical dwarfs of the MW (Metz et al., 2008) co-orbiting within the structure. In a similar way, in Conn et al. (2013), Ibata et al. (2013), Koch and Grebel (2006), McConnachie and Irwin (2006), Metz et al. (2006), it was shown a similar distribution around M31. In the local group (LG), there have found similar alignments in isolated dwarf galaxies (Bellazzini et al., 2013, Pawlowski and Kroupa, 2013, Pawlowski et al., 2013, Pawlowski and McGaugh, 2014), as well as in more distant galaxies (Duc et al., 2014, Galianni et al., 2010, Karachentsev et al., 2014, Paudel et al., 2013). According to several authors, all the above results should represent an enormous challenge for the Λ CDM model. This is because, in cosmological simulations of DM sub-haloes, they are found to be isotropically distributed, and then, in disagreement with the planar-like distributions. There have been several proposals to solve this disagreement, however, at present time, there are not yet a fully satisfactory explanation to understand these inconsistencies, and then the issue is still open. Additionally, it is highly improbable that it would be connected to baryonic physics.

3.2.2.2. The cusp/core problem

Observe that close to the center, the NFW profile shows a density distribution described by a power law $\rho \sim r^\alpha$ with $\alpha \simeq -1$. Such behaviour is what is usually called as a “cusp”, opposite to “cored” distributions, which are described by flat slopes with $\alpha \simeq 0$. Some other Λ CDM simulations have shown different results for the value of α : going from even steeper profile predictions with $\alpha \simeq -1.5$ (Fukushige and Makino, 2001, Moore et al., 1998) to a minimum value $\alpha \simeq 0.8$ (Stadel et al., 2009), namely the Einasto profile (which seems to give the best fit to simulations (Springel et al., 2008b)). Unfortunately for the model, in general, the Λ CDM should always possess a cusp-like inner density profile.

The cusp/core problem refers to the behaviour the DM density profile should have at the innermost regions of galaxies. It lies in the fact that even the smallest values for α , obtained by N-body simulations, are larger than the value obtained by several astronomical observations. For example, Flores and Primack (Flores and Primack, 1994), and also Moore (Moore, 1994), ruled out cuspy density profiles from rotation curves of DDO galaxies, and showed them to be well approximated by cored (or pseudo-)isothermal density profiles. Ho-

wever, this discrepancy has been fervently debated for two decades since several studies have obtained different results, occasionally favoring cuspy central density profiles, while in other occasions the cored distributions are preferable (see [Diemand et al. \(2007\)](#) for a review). Particularly, the most confusing results are the ones in which different conclusions have even been obtained using similar techniques for the same object. For example, the dark matter profile inner slope of NGC2976 is obtained to be $-0.17 < \alpha < -0.01$, according to [Simon et al. \(2003\)](#), while in [Gnedin \(2000\)](#) the authors obtained $\alpha = -0.90 \pm 0.15$. In a similar way, the fact that there seem to be some dwarf galaxies on which cuspy-like profiles at their centers appear to match better with the observational data, complicates enormously the correct description of this topic, and then, in general, the determination of the inner slope of galaxies is not an easy task.

In the above discussion, we concentrated in several DM profiles that have been obtained in the literature. Such profiles were obtained in DM-only simulations, i.e., without taking into account the baryonic component, in such case they should be coherent and compare the results with galaxies where baryons are not dominant. The suitable candidates that satisfy this condition are dSphs and low surface brightness (LSB) galaxies. Then, since most of the observations for such galaxies preferred a cored density profile, this represents an enormous problem for the Λ CDM model. Adding baryons may reduce the problem, but as we see below, this is not the only issue that seems to require baryons to agree with observations.

3.2.2.3. The missing satellite problem

This problem relies in the discrepancy between the number of satellite galaxies found in simulations around large galaxies, and the ones that have been observed. In the hierarchical galaxy formation scenario, a large number of haloes are consumed by more massive ones; however, there are still many dark matter substructures that are not disrupted, and that remain orbiting a massive halo. The scale invariant CDM primordial fluctuations at small scales leads to a large number of these subhaloes.

It was noticed by [Klypin et al. \(1999\)](#), [Moore et al. \(1999b\)](#) that N-body simulations presented many more subhaloes than observed satellite galaxies. For example, the Milky Way counts 9 bright dSphs, Saggitarius, the LMC and the SMC. In contrast, N-body simulations predict that such kind of galaxies should possess around 500 satellites with larger circular velocities than Draco and Ursa-Minor (i.e. bound masses $> 10^8 M_{\odot}$ and tidally limited sizes $> \text{kpc}$ ([Boylan-Kolchin et al., 2011](#), [Boylan-Kolchin et al., 2012](#))). Such conclusion was confirmed by several cosmological simulations (Aquarius, Via Lactea, and GALO simulations ([Diemand et al., 2007](#), [Springel et al., 2008b](#), [Stadel et al., 2009](#))), where in all cases they obtained that Milky Way-like galaxies should be surrounded with at least one order of magnitude more small subhaloes (dwarf galaxies) than observed.

Some solutions of this problem lie in considering the distinction between visible satellites and the entire population: if only a subset of the population is visible, the observed

vs predicted satellites discrepancy can be reduced. This solution relies on the efficiency of star formation, which requires baryons to be included, and forcing the use of hydrodynamic simulations. Some possible mechanisms to suppress the rate of star formation in these galaxies could be ionizing radiation photoevaporation (Alvarez et al., 2009, Gnedin, 2000, Simon et al., 2003) or due to heating by cosmic rays. Photoionization is expected to suppress star formation in haloes with masses under $\sim 10^9 M_{\odot}$. In more massive halos, where gas is retained and star formation can continue, there could be additional suppression due to supernova feedback (Benson et al., 2002, Governato et al., 2007). It is also important to consider the number of dim satellites that remain undetected due to incompleteness in the observations (Rashkov et al., 2012, Simon and Geha, 2007, Walsh et al., 2008).

3.2.2.4. The too big to fail problem

On the other hand, Boylan-Kolchin et al. (2011) pointed out that there still a problem with the most massive subhalos, the so-called *too big to fail* problem. This aspect of satellites arises because the most massive subhaloes in high-resolution simulations for Milky Way-like galaxies, with only dark matter (Diemand et al., 2008, Springel et al., 2008a), are too dense to host the satellites observed in the Milky Way. Simulations always contain a population of subhalos that are more massive than any of the spheroidal dwarfs observed in the Milky Way. In other words, while the abundance of low luminosity satellites can be consistent with CDM predictions, the too big to fail problem is still unsatisfactory because simulations predict too many massive satellites.

4. The Scalar Field Dark Matter model

4.1. Overview of the SFDM model

Among several candidates that have been proposed to be the DM in the Universe, a very promising one is the possibility that an ultra-light SF could fulfill with such objective¹. This proposal is a consequence of the fact that, for a correct potential, the SF can behave as a dust-like fluid, as we explained in 2.3. The main idea of this scenario was originated about two decades ago (Arbey et al., 2001, 2002a, 2003, Hu et al., 2000, Matos and Arturo Ureña-López, 2001, Matos et al., 2000, Matos and Urena-Lopez, 2000, Sahni and Wang, 2000), however, some hints can be traced further back in (Ji and Sin, 1994, Sin, 1994). Since then the idea has been rediscovery by various authors with different names, for example: SFDM (Matos et al., 2000), fuzzy DM (Hu et al., 2000), wave DM (Schive et al., 2014a), Bose-Einstein condensate DM (Boehmer and Harko, 2007), or ultra-light axion DM (Marsh and Ferreira, 2010) (see also (Membrado et al., 1989)). However, its first systematic study was started in (Guzmán and Matos, 2000, Guzmán and Matos, 2000).

Before continuing, it is necessary to mention the following: In common literature of SFDM models there have been people trying constraint the free parameters of the model. Putting the values for c and \hbar in our equations, the complete potential in the self-interacting case is given by

$$V(|\varphi|^2) = \frac{m^2 c^2}{2\hbar^2} |\varphi|^2 + \frac{\lambda}{4\hbar c} |\varphi|^4, \quad (4-1)$$

and then, from (2-29)

$$\mu = \frac{mc}{\hbar}, \quad \text{and} \quad \nu = \frac{\lambda}{\hbar c}. \quad (4-2)$$

Observe that the units of the SFDM physical quantities are $[\varphi] = (\text{energy}/\text{length})^{1/2}$, $[\mu] = 1/\text{length}$ and $[\nu] = (\text{energy} * \text{length})^{-1}$. If we choose to use natural units, the mass and the self-interacting parameter becomes $\mu = m$ and $\nu = \lambda$, and the units of the field quantities will be $[\varphi] = [\mu] = \text{energy}$, whereas ν becomes a dimensionless quantity. Although we will continue using natural units in this chapter, except in the structure formation section, we will refer in all the thesis to m and λ when we consider the numerical value for the parameters of the SFDM. In fact and because most of the values of such free parameters are very small, we

¹This ultra-light particles (with masses as small as $m \sim 10^{-33} \text{eV}/c^2$) have been predicted by a variety of unification theories, e.g., string theories and other multidimensional theories (Arkani-Hamed et al., 1999, Arvanitaki et al., 2010, Kallosh et al., 2002, Sikivie, 2012).

will refer to the parameters $m_{22} \equiv m/(10^{-22}\text{eV}/c^2)$ (or in natural units $m_{22} \equiv m/(10^{-22}\text{eV})$, and $\lambda_{90} \equiv \lambda/10^{-90}$. It is important for the reader to remember this statement, given that in future chapters we shall use the four quantities: μ , ν , m_{22} and λ_{90} .

Historically, the SFDM potential that has been more frequently used in literature is just the massive free scenario (2-25), with φ as a real field. In such case, this simplest model – considered as the fuzzy limit of the SFDM – has only one free parameter μ , or equivalently m_{22} , typically in the range $m_{22} \sim 100 - 1$. With this value for the mass, it was demonstrated that its cosmological regime matches to the Λ CDM model (Chavanis, 2012, Magaña et al., 2012, Matos and Arturo Ureña-López, 2001, Schive et al., 2014a, Suárez et al., 2014a)², it is consistent with the acoustic peaks of the cosmic microwave background radiation (Rodríguez-Montoya et al., 2010), and presents a cut-off in the power spectrum which suppresses the small-scale structure formation for halo masses $M < 10^8 M_\odot$ (Bozek et al., 2015, Hu et al., 2000, Marsh and Silk, 2013, Matos and Arturo Ureña-López, 2001) (for a review of this SFDM see (Hui et al., 2017, Magana and Matos, 2012, Marsh, 2016, Suárez et al., 2014b)). In addition, different numerical simulations (Levkov et al., 2018, Mocz et al., 2017a, Schive et al., 2014a,b, Schwabe et al., 2016, Veltmaat and Niemeyer, 2016) have shown that the SFDM forms core density profiles in the inner region of the galactic haloes (solving naturally the cuspy-halo problem) with a size compared to its de Broglie wave length

$$x_{dB} \propto \frac{1}{mv}, \quad (4-3)$$

where v is the velocity associated to the SFDM particle. These cores, referred as “solitons” in the literature (Chavanis, 2011, Chen et al., 2017, Levkov et al., 2018, Marsh and Pop, 2015), are assumed to be surrounded by a NFW envelope³ generated by the quantum interference provided by the SFDM and following the relation

$$M_c \propto M_h^{1/3}, \quad (4-4)$$

where M_c (M_h) is the total core (halo) mass. This correlation between the central region of the halo and its exterior offers a unique opportunity to understand and extend the numerical simulations by considering novel physical effects that could also be important for the halo that would form at the end. In fact, in a future chapter of this thesis we will focus on the addition of self-interaction to the above result.

Although the free SFDM is considered a serious alternative candidate to standard Λ CDM, it is necessary to recognize that the simplest model possesses some difficulties when its mass parameter is fitted with astrophysical and cosmological observations. For example,

²However as it is shown in (Li et al., 2014) when the SFDM is complex there exists an early stiff-like epoch for the SFDM which represents a difference between the SFDM and the Λ CDM model at cosmological levels.

³This NFW envelope has been obtained only under radial average. However, the real structure of the SFDM results in a more complicated relation.

constraining the model with galactic rotation velocity and velocity dispersion data (Arbey et al., 2001, Calabrese and Spergel, 2016, Lesgourgues et al., 2002), the value of the mass for SFDM which results, $m_{22} \lesssim 0.1$, is in tension with the constraints from the cut-off necessary to avoid small-scale structure formation, $m_{22} \sim 1$ (Bozek et al., 2015, Hu et al., 2000, Marsh and Silk, 2013, Matos and Arturo Ureña-López, 2001). However, this discrepancy can be understood by noticing that the analysis in (Arbey et al., 2001, Calabrese and Spergel, 2016, Lesgourgues et al., 2002) assumed that the soliton comprises the entire DM halo, and then from (4-3) the resulting value of m_{22} is underestimated. On the other hand, when the mass parameter for SFDM is tested with the matter power spectrum inferred from Ly- α forest analyses (Armengaud et al., 2017, Bozek et al., 2015, Iršič et al., 2017, Kobayashi et al., 2017, Zhang et al., 2017), a bound of $m_{22} \gtrsim 10$ is obtained, which is also in tension with the two constraints mentioned above. However, the Ly- α analysis is subject to uncertainties in our understanding of the intergalactic medium at high redshifts. Overall, we should caution that a shallow comparison between different methods can be vulnerable to criticism.

Nevertheless, motivated by these discrepancies, some previous literature considered extensions to the most basic SFDM models by adding a new parameter λ related to the self-interaction between particles⁴, where a positive (negative) self-interaction follows from a repulsive (attractive) interaction. The most studied of these extensions has been the repulsive scenario (Arbey et al., 2002b, Fernández-Hernández et al., 2018, Harko, 2011, Li et al., 2014, 2017, Rindler-Daller and Shapiro, 2012, Robles and Matos, 2012), being most of the academic works studied in the strong self-interacting regime where it is reached the so-called Thomas-Fermi (TF) approximation (see later in this chapter). On the other hand, for an attractive self-interaction, it has been motivated from a particle physics point of view, considering that such ultra-light particles can be understood as axion-like particles – a pseudo Nambu-Goldstone boson generated by a spontaneously broken global $U(1)$ symmetry –. The addition of this self-interacting parameter results to be very promising since it adds extra physics to the SFDM that could help to discriminate between SFDM models. For this reason, it is natural to ask what the consequences of such a self-interacting SFDM candidate should entail when contemplating a more general region of parameters for the self-interaction, also with regard to studies already done for the free case.

4.2. Cosmological evolution for SFDM models

In section 2.3 we have commented a little about the cosmological behavior for the SFDM by following its equation of state. However, in the general formalism, the correct way to follow its cosmological dynamics should be by solving the Friedmann equation (1-9) together with the Klein-Gordon equation in a FLRW background (2-17) and the fluid conservation equation

⁴This extension would also result if we include the next-leading terms in a Taylor expansion of a more general potential.

(1-11) for each of the other constituents existing in the Universe. In general, after the SFDM arrives at its fast oscillating regime, the KG equation starts to be so complicated when trying to solve it numerically and then, for such reason, there have been several proposals which try to simplify this task. For example, in (Suárez and Chavanis, 2017) the background SFDM model was solved semi-analytically and considering that it is self-interacting. On the other hand, in (Urena-Lopez and Gonzalez-Morales, 2016) the background dynamics was also studied by considering a polar decomposition for the SFDM variables of the form

$$\Omega_\varphi^{1/2} \sin(\theta/2) \equiv \frac{\sqrt{8\pi}\dot{\varphi}}{\sqrt{6}m_{pl}H}, \quad \Omega_\varphi^{1/2} \cos(\theta/2) \equiv -\frac{\sqrt{8\pi}\mu\varphi}{\sqrt{6}m_{pl}H}, \quad y_1 \equiv 2\frac{\mu}{H}, \quad (4-5)$$

in such a way it was possible to avoid most of the oscillating behavior. With such new variables the system of differential equations necessary to describe the SFDM model are rewritten as

$$\theta' = -3 \sin \theta + y_1, \quad (4-6a)$$

$$y_1' = \frac{3}{2}(1 + \omega_{tot})y_1, \quad (4-6b)$$

$$\Omega_\varphi' = 3(\omega_{tot} - \omega_\varphi)\Omega_\varphi, \quad (4-6c)$$

where

$$\omega_{tot} \equiv \frac{p_{tot}}{\rho_{tot}} = \sum_i \Omega_i \omega_i + \Omega_\varphi \omega_\varphi, \quad (4-6d)$$

is the total equation of the state in the Universe and

$$\omega_\varphi \equiv -\cos \theta \quad (4-6e)$$

is the equation of state for the SFDM. For such study it was considered a real SFDM with a cosmological constant-like initial condition at early times, i.e. considering the inflationary attractor solution (see section 2.3). To solve the system of differential equations a free version of the numerical code Class was modified in order to replace the CDM sector. The result can be seen in Figure 4-1. A similar study was done in (Magaña et al., 2012) where they used the Adams-Bashforth-Moulton (ABM) method to solve the system of differential equations that could manage the oscillatory behavior for the SFDM model. In their work, they obtained a similar result to that obtained by (Urena-Lopez and Gonzalez-Morales, 2016). On the other hand, in (Li et al., 2014) the background SFDM model was studied by considering it as a complex field with a repulsive self-interaction. Then, at early times it should behaved as a stiff-like fluid (see Figure 4-2). The motivation for such new exploration in the SFDM parameters was because they were trying to fulfill the constrictions coming from the effective number of extra-relativistic degrees of freedom during Big Bang Nucleosynthesis (see section 4.5). In such case, they demonstrated that the complex self-interacting model is preferable than its free field counterpart. The case when the SFDM possesses an attractive self-interaction has not been studied in the same way the other models given that a negative

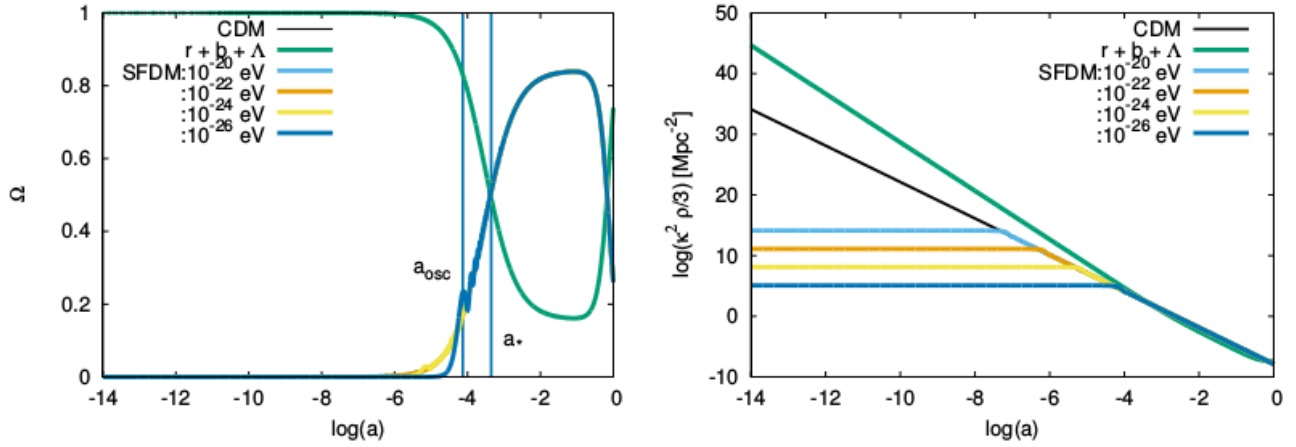


Figure 4-1.: Background evolution for the SFDM model in the free limit. The label CDM in the plot refers to the standard DM component, whereas r , b and Λ stand for radiation, baryons and cosmological constant. In the figures (left) we show the cosmological evolution of the density parameter Ω and (right) the evolution of the energy density ρ of the different matter components (Figure taken from [Urena-Lopez and Gonzalez-Morales \(2016\)](#)).

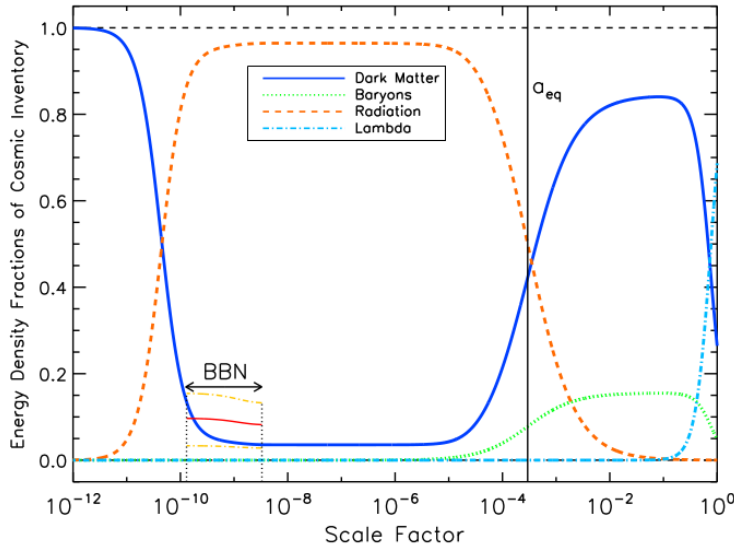


Figure 4-2.: Background evolution for a complex self-interacting SFDM model with a repulsive self-interaction. Observe that thanks to the complex nature of the field there exist an early epoch where the SFDM dominates the mean density of the Universe (Figure taken from ([Li et al., 2014](#))).

self-interaction possesses more observational difficulties, as it is the case of the generation of topological defects, and then the self-interacting parameter must be extremely small to avoid such constrictions ([Visinelli, 2017](#)). This implies that the attractive self-interacting parameter should not be important at cosmological scales.

As we saw in the above discussion and in section 2.3, we could have different dynamics

for the SFDM model depending on the value of its free parameters. However if the SFDM is consider to be the total DM in the Universe, a constrictio that should be fulfilled for all SFDM candidates is that at the radiation-matter equality it should behave as a dust-like fluid. Such constrictions implies that the SFDM parameters should fulfill (Li et al., 2014)

$$|\lambda_{90}| \leq 1.04m_{22}^4. \quad (4-7)$$

4.3. Linear grown in SFDM models

After knowing the background dynamics of the SFDM model, it is time to talk about the evolution of its linear perturbations. Of course, at such scales, one of the main necessities for whichever DM candidate is to verify that the perturbations for such candidate grow and allow the formation of structure in the Universe. The most studied model is the one that considers a real SF in the free-field limit, being the only one that has been tested with the help of Boltzmann codes⁵, although some semianalytical studies have been done in the complex self-interacting case in (Suárez and Chavanis, 2015). In this section we will review the basic results obtained in both scenarios close following (Urena-Lopez and Gonzalez-Morales, 2016) for the free case and (Suárez and Chavanis, 2015) for the self-interacting scenario. Then, if the reader is interested in reviewing this topic a little more formal, we encourage him/her to look at those references.

It is convenient to represent the perturbed KG equation in the synchronous gauge (1-78). In such case and by considering a decomposition for the SFDM as $\varphi(t, k) = \bar{\varphi}(t) + \delta\varphi(t, k)$ in Fourier space, the equation of motion for the perturbed field $\delta\varphi$ for wavenumber k reads

$$\delta\ddot{\varphi} + 3H\delta\dot{\varphi} + \left(\frac{k^2}{a^2} - \mu^2\right)\delta\varphi = -\frac{1}{2}\bar{\varphi}\dot{\bar{h}}, \quad (4-8)$$

where $\bar{h} = h_i^i$ is the trace of the spatial perturbations in the metric. In the same way they worked with the background equations, it is convenient to work in a set of new variables

$$\delta_\varphi \equiv \delta\rho_\varphi/\rho_\varphi = -e^\alpha \sin(\theta/2 - \vartheta/2), \quad \delta_1 = -e^\alpha \cos(\theta/2 - \vartheta/2), \quad (4-9)$$

in such a way it is possible to avoid the rapid oscillating behavior for the perturbations of the SFDM. Under the above new set of dynamical variables the differential equations that describes the SFDM are

$$\delta'_\varphi = \left[-3\sin\theta - \frac{k^2}{k_J^2}(1 - \cos\theta)\right]\delta_1 + \frac{k^2}{k_J^2}\sin\theta\delta_\varphi - \frac{1}{2}\bar{h}'(1 - \cos\theta), \quad (4-10a)$$

$$\delta'_1 = \left[-3\cos\theta - \frac{k^2}{k_J^2}\sin\theta\right]\delta_1 + \frac{k^2}{k_J^2}(1 + \cos\theta)\delta_\varphi - \frac{1}{2}\bar{h}'\sin\theta, \quad (4-10b)$$

⁵There are some works with more complicated potentials that have been also tested with Boltzmann codes. For example in (Cedeño et al., 2017) it was studied a SFDM candidate with an axion-like potential of the form $v(\varphi) = \mu^2 f^2 [1 + \cos(\varphi/f)]$.

where $k_J^2 \equiv 2a^2 H \mu$ is the squared Jeans wavenumber that naturally arises because of the wave nature of the SF.

Particularly, in the fast oscillating regime the above equations are reduced to

$$\delta'_\varphi = -\frac{k^2}{k_J^2} \delta_1 - \frac{1}{2} \bar{h}', \quad \delta'_1 = \frac{k^2}{k_J^2} \delta_\varphi. \quad (4-11)$$

Observe then, that for length scales $k \ll k_J$ the same expression as that for CDM, $\delta'_\varphi = -(1/2)\bar{h}'$, is recovered, with the usual growing mode $\delta_\varphi \propto a$, whereas δ_1 remains approximately constant. On the opposite regime $k \gg k_J$ the above equations resemble that of a harmonic oscillator, and then the density contrast oscillates. Given the fact that k_J is a quantity that evolves on time, the evolution for a given scale k should transit from one behavior to another, i.e. a typical SFDM perturbation should oscillate at early times until the scale $k \sim k_J$ and then grows as in the CDM case. This is a particular behavior for the SFDM that differs from CDM for scales below the Jeans scale.

The above system of differential equations was also implemented in the Class code in order to solve it together with the perturbations of the other constituents in the Universe (as radiation and baryons). The idea, of course, was to use the SFDM as DM instead of CDM. In Figure 4-3 we show the CMB (upper) calculated for different masses $m_{22} = 10^{-4} - 100$ as (Urena-Lopez and Gonzalez-Morales, 2016) obtained in their work together with the calculation for the best fit of the Λ CDM model. In the same figure (bottom) we also show the relative deviation for each CMB with respect to the Λ CDM. Observe that as long as the value of the mass of the SFDM increases, the difference with the Λ CDM decreases, being practically not noticeable for masses greater than (Hlozek et al., 2015)

$$m_{22} > 10^{-2}. \quad (4-12)$$

On the other hand, in Figure 4-4 we presented the MPS calculated by the same authors. Observe that differently to the Λ CDM model, in the SFDM there exists a cut off for large k (provoked by the Jeans scale). This implies that structure at small scales should not be formed. This result is very important given that with such property it is possible to solve naturally the missing satellite problem (see section 3.2.2.3). The preferred value needed for such porpoise is

$$m_{22} \sim 1. \quad (4-13)$$

On the other hand, in (Suárez and Chavanis, 2015) the evolution of the perturbations during a matter dominated Universe for a complex SFDM candidate in the nonrelativistic regime was studied. For such purpose, a Universe with only a SF as its constituent was considered and then it does not represent a realistic scenario. However, some of their results can be important to differentiate between SFDM models so we will review them. They worked in the Newtonian gauge (1-76) where the dynamical equations for the perturbations of the SFDM in the nonrelativistic limit and for scales well inside the cosmological horizon

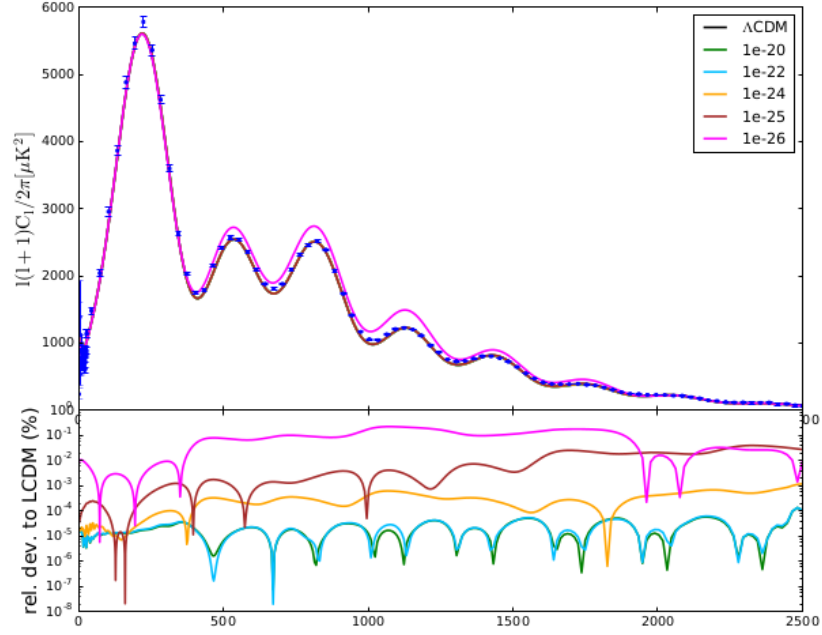


Figure 4-3.: CMB power spectrum for different masses of the SFDM model calculated from Class (Figure taken from (Urena-Lopez and Gonzalez-Morales, 2016)).

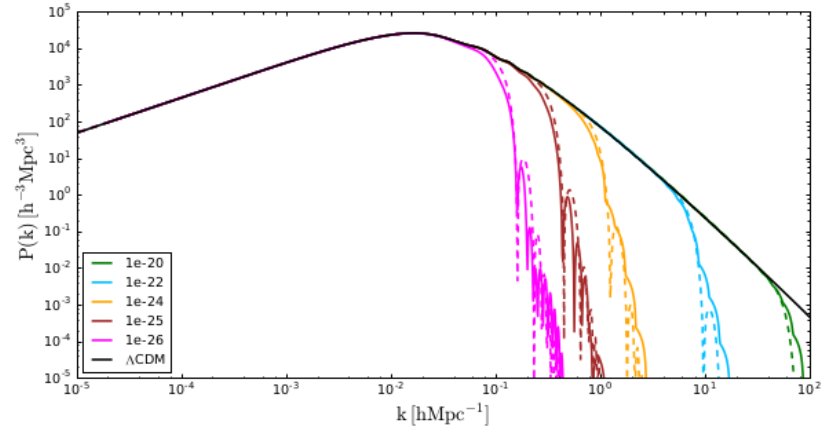


Figure 4-4.: MPS for different masses in the SFDM model. We also show the CDM result in a black curve (Figure taken from (Urena-Lopez and Gonzalez-Morales, 2016)).

are described by

$$\delta_\varphi'' + \frac{3}{2a}\delta_\varphi' + \frac{3}{2a^2}\left(\frac{k^4}{a\kappa_J^4} + \frac{k^2}{\kappa_{SI}^2 a^2} - 1\right)\delta_\varphi = 0, \quad (4-14)$$

where they defined κ_J (κ_{SI}) as the reduced quantum (self-interacting) Jeans wavenumbers as

$$\kappa_J \equiv \left(\frac{16\pi|\bar{\varphi}|^2 a^3 \mu^2}{m_{pl}^2}\right)^{1/4}, \quad \kappa_{SI} \equiv \left(\frac{4\pi\mu^4}{m_{pl}^2 \nu}\right) \quad (4-15)$$

As expected the CDM model is recovered by taking the limit $\kappa_J, \kappa_{SI} \rightarrow \infty$.

After solving the above equations from different limits (depending on what term inside the parenthesis in equation (4-14) dominates) they obtained different behaviours depending on the value of the SFDM self-interaction. We can see their results in Figure 4-5. In the upper left figure what they showed is a comparison between the free field limit (dashed curve), the repulsive self-interacting scenario when the self-interaction strongly dominates – known as the TF limit, see later – (oscillatory solid curve) and the CDM (solid curve). Observe that in all cases, SFDM perturbations oscillate at early times and then it starts to grow in the same way than CDM. In particular, in the repulsive scenario, the SFDM evolution for its perturbations can be understood as follows (right-upper figure): an early behavior where the self-interaction dominates ($k^2/(\kappa_{SI}^2 a^2) \gg k^4/(\kappa_J^4 a) \gg 1$), then transiting to a limit where the self-interaction is not important anymore and the field behaves effectively as a free field ($k^2/(\kappa_{SI}^2 a^2) \ll k^4/(\kappa_J^4 a) \gg 1$) and finally the SFDM transiting to a CDM-like behavior ($k^2/(\kappa_{SI}^2 a^2) \ll k^4/(\kappa_J^4 a) \ll 1$). On the other hand, in the attractive scenario they showed that the perturbations for the SFDM grow faster than in the free and repulsive scenarios thanks to the attraction provided by the self-interaction. In the figure (down figure) they showed the evolution of the perturbations for different values of the self-interaction obtaining that as long as the absolute value of it increases, the SFDM perturbations grow faster.

Remark: It is important to mention that in such studies they obtained that in all cases the SFDM perturbations grow faster than its CDM counterpart, being the attractive case where the perturbations grow even faster. In their work they mentioned that in this last case it is necessary for the absolute value of the SFDM self-interaction not to be so large in order to avoid the formation of structure in extremely early times. However, this rapid growth of the perturbations is also a very important result for the model given that there are some observations that indicate the existence of galaxies at very early times (see for example (Lehnert et al., 2010)).

4.4. Galaxy formation in the SFDM scenario

Once the background and linear perturbations in the SFDM model have been understood, it is time to consider the structure formation process. In the literature, there have been some dedicated numerical simulations which have studied this mechanism. Most of them rely in standard N-body simulations with modified initial conditions that reflect the properties of SFDM at the level of linear density perturbations in the matter power spectrum, as obtained from the amended Boltzmann codes (see Figure 4-4). However, there are other works that solve directly the EKG system in the weak-field limit, i.e., the GPP system (Mocz et al., 2017a, Schive et al., 2014a,b), which should be the most reliable ones, and also that take advantage of a hydrodynamic formulation that exists for the SFDM model (Levkov et al., 2018, Schwabe et al., 2016, Veltmaat and Niemeyer, 2016). In this section, we shall review the most important results obtained for such works in order to understand the kind of structures

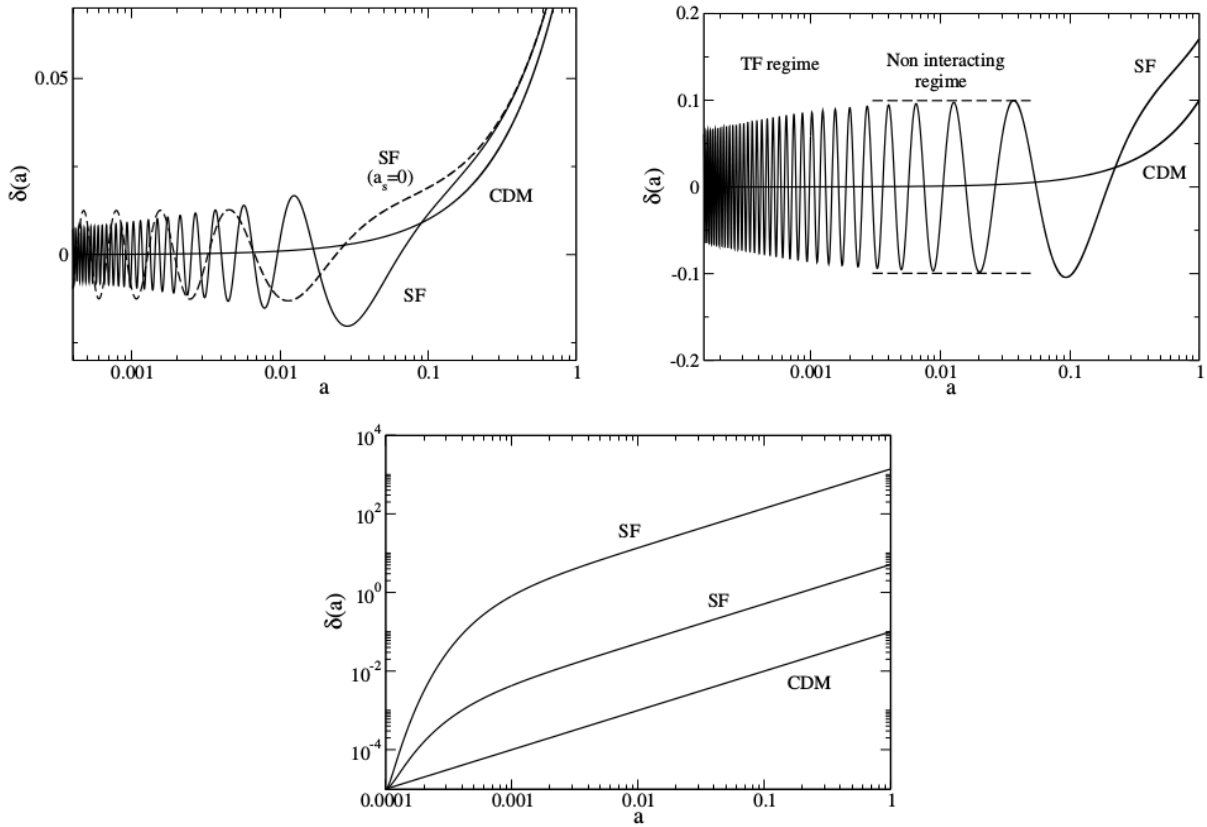


Figure 4-5.: Evolution of the perturbations for the self-interacting SFDM model. (upper left) shows the evolution of the free case (dashed curve), the repulsive case (oscillatory solid curve) and the CDM evolution (solid curve). (upper right) shows the evolution of the repulsive scenario distinguishing the moment when the self-interacting dominates the evolution of the SFDM (TF-regime) and the moment when the mass term dominates over the self-interaction. It is also shown the CDM evolution for the perturbations. (bottom) shows the evolution of the self-interacting scenario in the case of an attractive self-interaction. The curves go from the CDM limit (bottom line) to increase the value of the self-interaction (upper) (Taken from (Suárez and Chavanis, 2015)).

that are generated in the SFDM model. For simplicity, and in order to be consistent with most of the academic papers that works with galaxies formed in the SFDM model, we decided to reintroduce \hbar and c (see equation (4-2)) in the differential equations that arises in the formalism described in this chapter.

4.4.1. The field vs the hydrodynamic approach in the SFDM model

In order to study the clustering of SFDM particles, it is necessary to consider some approximations. The structure formation process take place in regions well within the horizon and where overdensities are not small anymore ($\delta_\varphi \geq \mathcal{O}(10^5)$), and then, linear perturbation theory can not be applied. Additionally, typical virial velocities in a galaxy are non-relativistic

($v_{vir} \ll c$). Considering the above argument, it happens that the Newtonian limit for the EKG system applies, and then the dynamics that describes the structure formation process in the SFDM model is given by

$$i\hbar\dot{\psi} = -\frac{\hbar^2}{2ma^2}\nabla^2\psi + m\Phi\psi + g|\psi|^2\psi, \quad (4-16a)$$

$$\nabla^2\Phi = \frac{4\pi G}{a}[\rho - \bar{\rho}(t)], \quad (4-16b)$$

where $g \equiv \lambda\hbar^3/(2m^2c)$, $\bar{\rho}$ is the mean density in the simulation, and

$$\varphi(\mathbf{x}, t) = \frac{\hbar}{\sqrt{ma^3}}e^{-imc^2t/\hbar}\psi(\mathbf{x}, t), \quad (4-17a)$$

if φ is a complex field or

$$\varphi(\mathbf{x}, t) = \frac{\hbar}{\sqrt{2ma^3}}\left(e^{-imc^2t/\hbar}\psi(\mathbf{x}, t) + e^{imc^2t/\hbar}\psi^*(\mathbf{x}, t)\right), \quad (4-17b)$$

if φ is a real field.

In general, ρ ($\bar{\rho}$) possesses the contribution of all the components in the Universe. However, in simulations already done in the SFDM model, it is usually limited to the contribution of the SFDM content⁶, in such case $\rho = \rho_\psi = m|\psi|^2$.

There is also a fluid equivalence of the GPP system that has been extensively used in the literature. It can be obtained by considering the well known Madelung transformation

$$\psi(\mathbf{x}, t) = |\psi(\mathbf{x}, t)|e^{iS(\mathbf{x}, t)} = \sqrt{\frac{\rho(\mathbf{x}, t)}{m}}e^{iS(\mathbf{x}, t)}, \quad (4-18)$$

and defining a velocity field as the phase gradient

$$\vec{v} = \frac{\hbar}{m}\nabla S. \quad (4-19)$$

With such new variables, the GPP system is rewritten as

$$\rho\dot{\vec{v}} + \frac{1}{a^2}\rho(\vec{v} \cdot \nabla)\vec{v} = -\rho\nabla Q - \rho\nabla\Phi - \nabla P_{SI}, \quad (4-20a)$$

$$\dot{\rho} + \frac{1}{a^2}\nabla \cdot (\rho\vec{v}) = 0, \quad (4-20b)$$

where

$$Q \equiv -\frac{\hbar^2}{2m^2a^2}\frac{\nabla^2\sqrt{\rho}}{\sqrt{\rho}} \quad \text{and} \quad P_{SI} \equiv \frac{g}{2m^2}\rho^2. \quad (4-21)$$

⁶In the structure formation process it is Dark Matter which plays the most important role on it and that is the reason why in the simplest case it is usually considered only the DM contribution for simulation of structure formation. However a most realistic scenario should be one where baryonic physics is also taken into account, being no already completely done for the SFDM model, although some first works have been studied by some authors (see for example (Veltmaat et al., 2019))

Observe that the velocity is irrotational outside of vortex lines, i.e. it obeys $\nabla \times \vec{v} = 0$.

The system (4-20) corresponds to an Euler-like equation and a conservation equation of fluid dynamics with a new term ∇Q , which is usually called the *quantum force* while Q is the *quantum potential*. In a similar analogy P_{SI} is a pressure term that is provoked by the self-interaction between particles. Of course such names are given because of the analogy to the classical Euler equation.

Remark: Observe that the above system is equivalent to the dynamical equations necessary to describe the structure formation in the Λ CDM model (see equations (3-5)) plus the contributions for the quantum potential and the pressure due to self-interaction. Then, the structure formation process for the SFDM model should be similar to the Λ CDM model as long as the scales for the structures are much larger than the scales where the Q and the P_{SI} terms are important. In the case when the self-interacting term can be ignored, such scales corresponds to the de-Broglie wave-length associated to the SFDM particle, whereas in the case the quantum pressure can be ignored, such scales should corresponds to the radius obtained in the TF regime (see next subsection).

4.4.2. Cosmological simulations, galaxies and the core-halo mass relation

The first realistic simulations from cosmological initial conditions in the SFDM model were provided by (Schive et al., 2014a). In their work, they solved the GPP system (4-16) in the free limit ($g = 0$), i.e., they solved the SchP system, and by considering the SFDM as the only constituent of the Universe. One of their main results was that the final kind of galaxies formed for this model can be well described by an inner soliton profile, which at some radius transits to a NFW-like envelope (3-6) that is generated as a result of incoherent fluctuations of the SFDM (see Figure 4-6 and 4-7). In their work, Schive et al. gave a numerical fit to the soliton density profile, and given by

$$\rho_c(r) \simeq \rho_{c0} [1 + 0.091(r/r_c)^2]^{-8}, \quad (4-22)$$

where r is the physical radial coordinate $r = ax$, r_c is the radius at which the density drops to one-half its peak value, and their central density value in their simulations is given by

$$\rho_{c0} \simeq 3.1 \times 10^{15} \left(\frac{2.5}{m_{22}} \right)^2 \left(\frac{\text{kpc}}{r_c} \right)^2 \frac{M_\odot}{\text{Mpc}^3}. \quad (4-23)$$

These solitons can be easily understood by considering the following simplification: At redshift $z = 0$, we can set $a = 1$, which results in $x = r$ in equation (4-16). We can also consider that $\rho \gg \bar{\rho}$ ⁷. Then, we can consider that the central soliton formed in the inner region of

⁷As in the numerical simulations performed by Schive et. al. we are considering that the only constituent in the Universe are the SFDM particles. Then ρ ($\bar{\rho}$) must be taken as the total (background) SFDM density profile.

SFDM haloes can be tough as stationary solutions, in such case they should be represented by an harmonic time dependence. But, by adopting such simplifications, we should have that these configurations are represented by the same differential equations than the Newtonian boson stars described in section 2.4.2, and with similar boundary conditions. In this way, soliton profiles in the free SFDM model are represented by boson stars in the Newtonian regime. In a similar way, in the hydrodynamic representation, these solutions arise by demanding spherical symmetry, and from the conditions $a = 1$, $\rho(r, t) = \rho(r)$ and $\vec{v} = 0$. After considering these simplifications, the conservation equation (4-20b) is identically satisfied, whereas the Euler equation (4-20a) results in $\nabla\Phi = -\nabla Q$ (an equilibrium between the quantum and the gravitational forces⁸). Using the Poisson equation, one finally arrives at the expression

$$\nabla^2 \left(\frac{\nabla^2 \sqrt{\rho}}{\sqrt{\rho}} \right) = 8\pi G\rho. \quad (4-24)$$

Additionally, an important relation than the central soliton profile fulfills is the $M_c - R_c$ relation

$$R_c = 9.9 \frac{\hbar^2}{GM_c m^2}, \quad (4-25)$$

where M_c (R_c) is the total core (radius) of the soliton profile, i.e., $R_c = R_{99}$. From here and for the rest of this thesis subindex c will be used for total soliton quantities, until otherwise is specified.

On the other hand, in (Schive et al., 2014b), they obtained a core-halo(envelope) mass relation valid in the free field limit

$$M_{c,7} \simeq 1.4 \times 10^2 M_{h,12}^{1/3} m_{22}^{-1} M_\odot, \quad (4-26)$$

where $M_{c,7} \equiv M_c / (10^7 M_\odot)$ ⁹, and $M_{h,12} \equiv M_h / (10^{12} M_\odot)$. From here and for the rest of this thesis subindex h should refer to total halo quantities, unless otherwise specified. Observe that the above relation implies a maximum halo mass at which the soliton should be enough for modeling the total halo of a galaxy, given by equating $M_c = M_h$. Usually these kind of galaxies are assumed to model the well-known dSph galaxies.

The NFW-envelope structure has been confirmed by various groups that considered simpler scenarios, as it is the case of merging many solitons nearly simultaneously (Levkov et al., 2018, Mocz et al., 2017a, Schwabe et al., 2016, Veltmaat and Niemeyer, 2016), and by considering the field description as well as the hydrodynamic representation (see previous section). In all cases, they obtained the same kind of configurations (the inner soliton and the NFW-like exterior), although each of such simulations have reported a different

⁸For this result we have neglected the self-interacting parameter given that until now we have only reviewed the simulations already done in the free case by (Schive et al., 2014a,b).

⁹Observe that in (4-4) we referred to M_c as the total core mass which, as introduced by Schive et al., corresponds to a smaller mass given that it is the mass enclosed within radius r_c . However, and because for the rest of this thesis we shall only consider total soliton quantities, we decided to redefine this index.

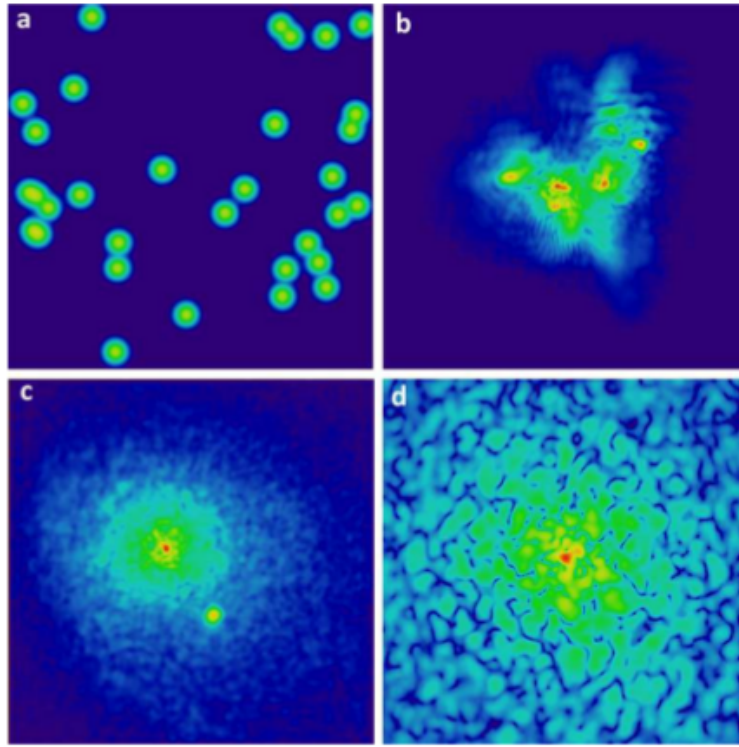


Figure 4-6.: Collision of soliton profiles at different stages. Panel a shows the initial condition in the simulation while b and c shows intermediate distribution. Finally panel d shows a zoom-in of the final configuration in the simulation (Taken from (Schive et al., 2014b)).

match between both structures (see Figure 4-7) which results in a different core-halo mass relation. However, in (Bar et al., 2018), it was studied the physical meaning of each of the different results obtained by numerical simulations, agreeing that the result from Schive et al. represents a better physical consequence for galaxies in the SFDM model. In a more recent work (Bar et al., 2019), it was suggested that the above relation can be understood if the following relation

$$\frac{K_c}{M_c} \simeq \frac{K_h}{M_h}, \quad (4-27)$$

is fulfilled by the model, where K_i is the kinetic energy defined in (2-46a). As discussed in (Bar et al., 2019), the above rough equality ignores the effect of the gravitational potential of the halo envelope onto the central soliton. On the other hand, in the free case (the case studied by (Schive et al., 2014a,b)), the above equation is equivalent to $|E_c|/M_c \simeq |E_h|/M_h$ (see equation (2-47)), which was the first relation proposed by the same authors in (Bar et al., 2018). However, when they tried to extend the model by including a baryonic component in (Bar et al., 2019), they demonstrated and agreed that (4-27) represents a more realistic consequence of the core-halo relation.

There have been another porpoise to explain the core-halo mass relation, inspired by physical arguments. Some other authors (Chavanis, 2019, Mocz et al., 2017b) consider that

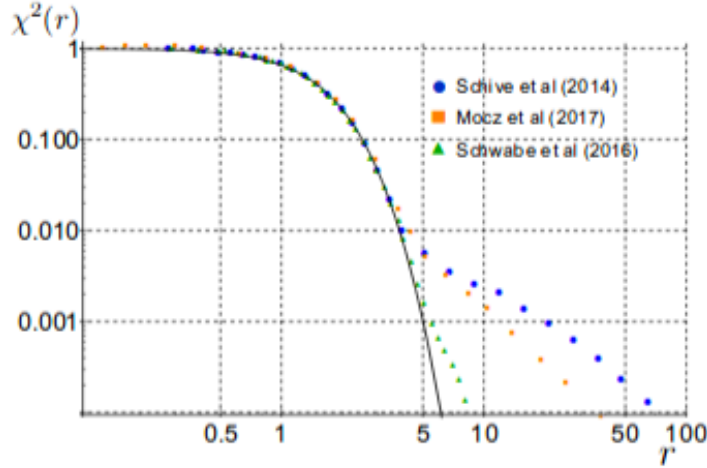


Figure 4-7.: Density profile of the SFDM model in the free limit reported by different authors (Taken from (Bar et al., 2018)).

the $M_c - M_h$ relation can be understood if the circular velocity for the core and halo are of the same order, i.e., if it is fulfilled the relation

$$v_c^2 \sim v_h^2, \quad \text{or} \quad M_c \sim \frac{R_c}{R_h} M_h. \quad (4-28)$$

Whether or not a soliton forms in the first place under realistic conditions cannot, however, be addressed by the previous simulations. Some earlier works that consider even simpler scenarios – for example by considering a simple top-hat model at time of turn-around – have been carried-out (see for example (Guzman and Urena-López, 2004)) and showed that soliton profiles can be formed in considerably short time. In (Levkov et al., 2018), they showed that by providing a non-vanishing initial velocity to the SFDM particles, solitons are able to form in small galaxies, and the cusp-core problem can be solved in this scenario always that the mass parameter fulfills the constriction:

$$m_{22} \lesssim 20. \quad (4-29)$$

It is important to mention that the correct physical meaning of SFDM halo structures continue being not well understood by researchers. For example, although central soliton profiles are well understood that they are supported by the repulsive nature of the uncertainty principle of quantum mechanics via the quantum potential term (4-21), the NWF exterior is not clear under which mechanism it could be supported. In this context, in (Matos and Ureña-López, 2007), it was proposed that the gravitational co-existence of different energy eigenstates of the SFDM wavefunction, i.e., different (Newtonian) boson stars, could be the responsible for this kind of configurations. In fact, in (Bernal et al., 2010, Urena-Lopez and Bernal, 2010) it was shown that two-state solutions (the ground state and the first excited state) are virialized and stable under perturbations for both the non-relativistic and

relativistic regimes. These two state solutions have been also proposed in (Matos et al., 2019) to solve the galactic satellite plane problem studied in section 3.2.2.1. Following this idea, (Lin et al., 2018) constructed self-consistently haloes that follows relation (4-26) with these multi-state solutions, where they obtained that a fermionic King model (Chavanis et al., 2014) reproduce better SFDM haloes. In an even simpler description (Robles and Matos, 2013) (see also (Ureña-López et al., 2002)) it was proposed to model SFDM haloes in the free field limit by considering a flat geometry, and then, by dealing only with the KG equation. In such description, it was possible to obtain an analytic solution for the SFDM given by

$$\rho(r) = \sum_j \rho_j(r) \quad \text{with} \quad \rho_j(r) = \rho_0^j \frac{\sin^2(r/r_s^j)}{(r/r_s^j)^2}, \quad (4-30)$$

where ρ_0^j is the central density, $r_s^j \equiv 1/k_s^j$, being the dispersion relation k_s^j defined as $k_s^j \equiv \omega_j^2 - \mu^2 = \pi_j R$, R the radius of the SFDM halo, and ω_j a free constant parameter that is related to the harmonic frequency of oscillation for the SFDM. They showed that the value of each ω_j can be understood by meaning of finite temperature corrections. Then, the above solutions are multi-state configurations in the sense that each ρ_j oscillates inside the galactic halo. We shall understand a little more this parameter ω_j in chapter 6. Although the above multi-state configuration is not a real solution for the complete EKG system, or the SchP system, and it also does not possess a finite energy in all space, since it does not decays faster than $\sim r^{-2}$, it has been shown that this approximation gives good estimations for the mass parameter in the SFDM and then, for its simplicity, these configurations results to be a good alternative to model the free SFDM at galactic scales.

My small contributions to the SFDM density profile (4-30):

- Observe that equation (4-30) was obtained by neglecting the self-gravitation of the SFDM particles. That condition should be applicable always that the halo is diluted enough, and then, from (4-22), (4-23) and (4-26), and by considering the $M_c - R_c$ relation (4-25), which follows easily from the reescaling property (2-50), it should apply for the smallest galaxies, i.e. for dSph galaxies. Now, since typically dSphs are mostly modeled by only the soliton profile, then $R \simeq R_{99}$, where, as we saw in section 2.4, R_{99} is the radius that contains the 99% percent of the total soliton mass. In this way, it should apply that $\rho_{j=0}$ represents the soliton in this approximation, whereas $\rho_{j \neq 0}$ are for excited configurations, i.e. excited boson stars. On the other hand, one of the first studies that used the profile (4-30) to constrain the free SFDM model with dSphs was provided by (Martinez-Medina et al., 2015). In their work, they obtained that in all their fits, each dSph should be mostly modeled by $\rho_{j=0}$. Then, we could consider that for this case, both descriptions (4-26) and (4-30) are equivalent. On the other hand, if we attempt to model big galaxies with (4-30), we can observe that $R \neq R_{99}$, which implies that both models are not equivalent anymore. In this way, both SFDM models

for galaxies are different. Either way, in this thesis we use both SFDM models for our purposes.

- Observe that (4-30) represents a basis that, in principle, could map any positive function sufficiently well behaved. This would imply that, at the point where this model is found, it still maintains too much freedom to confront it with galactic dynamics. In this way, we consider that this model, although quite well founded, still lacks an extra step in trying to make it a bit more restrictive. For example, by considering a similar study than the one done in (Lin et al., 2018).

Finally, it is time to talk about the kind of structures that should be formed in the self-interacting case. Unfortunately, in this scenario, there have not been carried-out numerical simulations of structure formation. In the case of having an attractive self-interaction, this has been justified by the fact that this self-interacting parameter must be very small in order to avoid several problems that the model would have observationally, such as the generation of topological defects (see for example (Visinelli, 2017)), whereas in the repulsive scenario, such simulations have not been carried out since there is not a large group that study this model, although several works have been done in the so-called TF regime. They have worked with TF solitons that are found similarly than in the free case (see for example (Rindler-Daller and Shapiro, 2012)), i.e., by demanding in (4-20) that $a = 1$, $x = r$, $\rho(r, t) = \rho(r)$ and $\vec{v} = 0$, but now introducing the self-interacting parameter. In this way, the conservation equation (4-20b) is identically satisfied, whereas from the Euler equation (4-20a) follows $\nabla\Phi = -\nabla Q - \nabla P_{SI}$. In the case when the quantum term can be ignored – the so-called TF regime – we obtain $\nabla\Phi = -\nabla P_{SI}$ (there is a balance between the gravitational attraction and the repulsion provoked by the self-interaction). This last relation can be seen as a Lane-Emden equation of motion, which solution gives

$$\rho_c^{TF}(r) = \rho_0^{TF} \sin\left(\sqrt{\frac{2\pi G}{K_p}} r\right) / \left(\sqrt{\frac{2\pi G}{K_p}} r\right). \quad (4-31)$$

A spherical TF soliton results in a (n=1)-polytrope with radius

$$R^{(TF)} = \pi\sqrt{\frac{K_p}{2\pi G}} = \pi\sqrt{\frac{g}{(4\pi G m^2)}}. \quad (4-32)$$

Observe that this radius is constant for any galaxy mass. This scenario avoids small-scale structure by matching the size of typical dSphs with $R^{(TF)}$. In fact, commonly this TF soliton profile is used to model only dSphs, and then, it remains to be understood how the model should allow the introduction of larger galaxies.

4.5. Observational constrictions for the SFDM model

In this section, we complement this chapter by reviewing different constrictions that have been carried out for the SFDM parameters. It is very likely that we are not contemplating

all the constraints that exist for the model, since the literature for the SFDM is very large, so we could easily missed some results. However, we trust that the constraints presented here represent a good set of values that would largely summarize all those works that we may not be mentioning in this section. Additionally, we do not introduce ourselves in trying to explain how each of the constrictions were obtained, since this would make the reading of this thesis very tedious. For this reason, we only comment on the results that were obtained in each work, and we leave the reader to, if required, review the different references that we mention on each constriction to better understand each of the processes to restrict the parameters of the model.

The free case.- Considering the hydrodynamical representation of the SFDM model, in (Paredes and Michinel, 2016) it was suggested the SFDM's quantum pressure as the origin of the offset between dark matter and ordinary matter in Abel 3827. For this purpose, they required a mass $m_{22} \simeq 2 \times 10^{-2}$. When the model is tested with the dynamics of dSphs – Fornax and Sculpture–, in reference (González-Morales et al., 2017) was obtained a mass constriction of $m_{22} < 0.4$ at 97.5%. The constriction obtained when the survival of the cold clump in Ursa and the distribution of globular clusters in Fornax is considered requires a mass $m_{22} \sim 0.3 - 1$ (Lora et al., 2012). Explaining the half-light mass in the ultra-faint dwarfs fits the mass term to be $m_{22} \sim 3.7 - 5.6$ (Calabrese and Spiegel, 2016). The model has also been constrained by observations of the reionization process. In (Sarkar et al., 2016a), using N-body simulations and demanding an ionized fraction of HI of 50% by $z = 8$, was obtained the result of $m_{22} > .26$. Finally, using the Lyman- α forest flux power spectrum demands that the mass parameter fulfills $m_{22} \gtrsim 20 - 30$ (Armengaud et al., 2017, Iršič et al., 2017).

The repulsive scenario.- In the repulsive scenario, it is usually constrained the ratio of the parameters $m_{22}/\lambda_{90}^{1/4}$, or the parameter $g/(c^4 m^2)$. Observe that both quantities constrain the free parameters in the same way, given that $g/m^2 \propto (m_{22}/\lambda^{1/4})^{-4}$ (see line just after equation (4-16)). In this section, we shall show the parameter constrictions in the way they were reported by authors, considering that moving from one notation to another is easy, since the relationship between both quantities is only multiplying by constants.

First, we comment in the works that constrain the ratio $m_{22}/\lambda_{90}^{1/4}$. In (Diez-Tejedor et al., 2014), it was studied the possibility that a SFDM candidate could be self-interacting. In their work they constrain the ratio $m_{22}/\lambda_{90}^{1/4}$ to be $m_{22}/\lambda_{90}^{1/4} \sim 3.1623$ by analyzing the line-of-sight velocity dispersion for the eight dSphs satellites of the MW. This study was complementary to the ones done in (Arbey et al., 2003, Böhmer and Harko, 2007, Harko, 2011, Robles and Matos, 2012) where the SFDM model was studied by using rotational curves of the most Dark Matter dominated galaxies from different surveys, and where they obtained the constriction $m_{22}/\lambda_{90}^{1/4} \sim 8.222 - 9.171$. On the other hand, in (Arbey et al., 2002b) the model was studied in a cosmological context by demanding that the SFDM

candidate behaves as a dust-like component before the time of matter-radiation equality. In such work they obtain the result $m_{22}/\lambda_{90}^{1/4} > 2.5298$. Finally, it was also possible to test the self-interacting scenario by considering the number of extra relativistic species at Big Bang Nucleosynthesis (BBN). When such observations are confronted with the SFDM it is obtained that it must be fulfilled that $m_{22}/\lambda_{90}^{1/4} \gtrsim 12.649$ (see (Arbey et al., 2003)).

Now, we comment in the constrictions that considers the ratio $g/(m^2c^4)$. In (Li et al., 2014), it was studied the SFDM as a complex field. In such work, they obtained the constriction $g/(m^2c^4) \leq 4 \times 10^{-17} \text{eV}^{-1} \text{cm}^3$ by considering again that the SFDM should behave as a dust-like fluid at the time of radiation-matter equality. On the other hand, by considering again the complex SFDM and studying the model more accurately for the consequences that appears in its early stiff-like era, it was also tested it by considering BBN constrictions and considering measurements for the primordial gravitational waves. In (Li et al., 2017) it was obtained the constriction $2.3 \times 10^{-18} \text{eV}^{-1} \text{cm}^3 \leq \frac{g}{m^2c^4} \leq 4.1 \times 10^{-17} \text{eV}^{-1} \text{cm}^3$.

The attractive scenario.- Usually, the self-interacting parameter in the attractive scenario is ignored, given that it should be extremely small. However, there have been some works that consider its contribution. For example, if the SFDM is an ultra-light axion-like particle ($m_{22} \simeq 1$), it was shown that it should be generated during inflation (Visinelli, 2017), in such case its self-interacting parameter should fulfill $\lambda_{90} \sim -10^{-4}$. On the other hand, from the string axiverse theory, the self-interacting parameter has been also constrained to be (Cicoli et al., 2012) $\lambda_{90} \sim -10^4$. Finally, by matching the more compact soliton profile with Willman I, in (Chavanis, 2016) obtained the values $m_{22} = 193$ and $\lambda_{90} = -2.04 \times 10^4$.

5. Constraining spectator scalar field dark matter from isocurvature constrictions

As we already seen in the last chapter, the SFDM model appears to be a promising candidate to account for the DM in the Universe. Despite several works about this model, it continues being unclear the mechanism that generated this ultra-light SFDM particle and the time it should have been produced. Some works in this direction consider the SFDM as an axion-like particle, which in our context can be understood as a SFDM with an attractive self-interaction. In such studies, the axion is understood as a particle that could be created before or after the inflationary era by the misalignment mechanism ([Visinelli, 2017](#)). If it is created after inflation, then the ultra-light SFDM particle could not account for the total amount of the DM because of the production of topological defects, whereas if it is produced during (or before) the inflationary era, then it is plausible that the SFDM accounts for the total DM in the Universe. In that work, they obtained after considering isocurvature constrictions for the SFDM that for an ultra-light SFDM particle $m_{22} \sim 1$, its self-interacting parameter should follows the constriction $\lambda_{90} \sim -10^{-4}$ (see section 4.5), whereas the mass parameter for the SFDM should follow the same constrictions that are obtained in the free case.

Although now a days there exist a host of observations that support adiabatic initial conditions in the Universe, and then a single field model for inflation, it is necessary to mention that this mechanism is not completely well understood. This is because the physics that occurs at such energies has not been reached by accelerators yet and then it continue being a mystery for the scientific community the different processes or the different constituents that should be presented during that epoch. In this way and by considering that the repulsive scenario for the SFDM candidate is also a good alternative for DM in the Universe, it is natural to question the consequences obtained if it was generated during the inflationary era. In this chapter, we study such possibility strongly following our published work ([Padilla et al., 2019](#)). For simplicity, we do not contemplate a mechanism of creation for this particle and we only consider the possibility that it was presented during the inflationary period with a free or repulsive self-interacting potential. We investigate this scenario as a complement to the work done by ([Visinelli, 2017](#)) for the attractive case.

5.1. Constraints on inflationary parameters

In section 1.6 we comment a little about the different constraints that exist for the inflationary parameters. However, since it will be important for this chapter to remember them, let us summarize the main results in this section. In the standard approximation the inflationary observables are given by the tensor-to-scalar ratio r , the spectral index for adiabatic perturbations n_s , and the amplitude for adiabatic perturbations A_r^2 . The constraints of these parameters are quoted at the pivot scale $k_0 = 0.05 Mpc^{-1}$ by (Akrami et al., 2018)

$$A_r^2(k_0) = (2.215_{-0.079}^{+0.032}) \times 10^{-9}, \quad \text{at 68\% CL}, \quad (5-1a)$$

$$r_{k_0} < 0.064 \quad \text{at 95\% CL}, \quad (5-1b)$$

$$n_s(k_0) = 0.968 \pm 0.006. \quad (5-1c)$$

Using these measurements, we are able to compute the value of the Hubble expansion rate during inflation as (Lyth, 1984, Lyth and Stewart, 1992)

$$r = 1.6 \times 10^{-5} \left(\frac{H}{10^{12} \text{GeV}} \right)_{k_0=aH}^2. \quad (5-2)$$

As we have noted before, if more than one SF is present during inflation we will obtain isocurvature perturbations generated by extra scalar fields perpendicular to the trajectory of the field-space. Of special interest is the isocurvature power spectrum for dark matter. From (1-142) and (1-143) we obtain the constriction

$$\beta_{iso}(k_0) < 0.038 \quad \text{at 95\% CL.} \quad \text{where} \quad P_{DM}(k) = \frac{\beta_{iso}(k)}{1 - \beta_{iso}(k)} P_{\mathcal{R}}(k), \quad (5-3)$$

where $P_{DM} \equiv \delta\rho_{DM^*}/\rho_{DM}$, $\delta\rho_{DM^*}$ are the isocurvature perturbations for the DM generated by extra scalar fields during inflation, ρ_{DM} are the DM initial conditions and $P_{\mathcal{R}}$ is the primordial power spectrum for adiabatic perturbations. Notice that isocurvature perturbations can be used to compute the inflationary scale, just by combining equations (5-1) to (5-3).

5.2. Constraining free and self-interacting ultra-light SFDM models

In this section, we study the possibility that our SFDM candidate coexisted with the inflaton during the inflationary epoch. For this, we require that the SFDM candidate be a stable spectator field with negligible classical dynamics and energy density¹. Such scenario is

¹We need that the SFDM candidate dominates the energy of the Universe just after matter-radiation equality and not before.

reached by taking the inflaton scenario (see section 1.5.1.3), i.e., within the field space, the evolution of the system is on the inflaton direction ϕ , whereas the direction perpendicular to the trajectory corresponds to the SFDM φ . Notice that this requirement implies that our dark matter candidate evolves much slower than the inflaton and its density is smaller than the associated to the inflaton.

As we mentioned before, to constrain the free parameters of our model the isocurvature perturbations have to be taken into account. For this reason, we review the cosmological history that a free and a repulsive self-interacting scalar fields should have gone through the evolution of the Universe, to then match the present value of the field with that during the inflationary era and, therefore, use the isocurvature constrictions. We consider a semi-analytic description for such dynamics, instead of the full treatment we reviewed in section 4.2, given that we want to have control of the free parameters in the model. We shall also make use of different cosmological and astrophysical constraints for each SFDM model in order to compare our results.

The dynamics of the SFDM candidate during the inflationary era can be well represented by the KG equation in a FLRW spacetime. In principle, such candidate could be complex or real and then, the most general equation that must represent its dynamics should be given by equation (2-20)

$$|\ddot{\varphi}| + 3H|\dot{\varphi}| + M_{eff}^2|\varphi| - \frac{Q^2}{|\varphi|^3 a^6} = 0, \quad (5-4)$$

where, as we mentioned before, $|\varphi|$ is the absolute value of the SFDM, Q arises completely from the complex nature of the SF and it can be interpreted as a charge of the SFDM related to the conservation of the total number of particles, and $M_{eff}^2 \equiv 2(dV/d|\varphi|^2)$ is seen as an effective mass term of the SFDM. Particularly, as explained in (Li et al., 2014), this mass term matches with the pulsation of the SFDM defined in (2-21) in the fast oscillating regime. Notice that if we assume $Q/(|\varphi|^3 a^6) \ll 1$, by assuming the SFDM candidate fulfills the slow-roll condition (1-63) during inflation, then the field $|\varphi|$ will remain frozen with value $|\varphi|_i$ until $H \sim M_{eff}$. Here and for the rest of this chapter subindex i means values right after inflation ends, unless otherwise specified. Then, when $H \sim M_{eff}$ the field will start evolving depending on the effective mass term. It is not difficult to see that, in order to get the slow-roll behavior of the SFDM, it is necessary that $Q \simeq 0$, as explained in (Suárez and Chavanis, 2017)². On the other hand, for the inflaton ϕ , it is usually considered as a real field.

In this chapter we consider only situations where the general potential can be decomposed as $V(\phi, \varphi) = \hat{V}(\phi) + V_{SFDM}(|\varphi|^2)$.

²In fact, as we already commented in a previous chapter in this thesis, the inflationary behavior is an attractor solution of the KG equation for a real field in the limit when $M_{eff}^2 \ll H^2$ (Belinsky et al., 1985, Piran and Williams, 1985). In this limit the typical dynamics of a real SF is a stiff-like epoch, followed by an inflationary-like era.

5.2.1. Real ultra-light SFDM candidate

5.2.1.1. Cosmological history

The possibility that an ultra-light SFDM candidate could coexist with the inflaton has been studied in (Kobayashi et al., 2017) by considering a potential of the form

$$V(\phi, |\varphi|^2) = \hat{V}(\phi) + \frac{1}{2}\mu^2\varphi^2, \quad (5-5)$$

and by fixing $Q = 0$ for the SFDM in equation (5-4). Such study was performed by assuming the SFDM is an axion-like particle. However, their results can be extrapolated for almost any free SFDM candidate. Then, in this section, we shall follow closely their main results in order to understand how it is possible to constrain the free-field model with isocurvature perturbations.

For the above particular potential, we observe that $M_{eff}^2 = \mu^2$. Equivalently to the complex scenario 2.3, in the fast oscillating regime $H \gg \mu$, the term with μ^2 in equation (5-4) can be neglected. Bearing in mind the field is slowly rolling during the inflationary era, we can neglect second derivatives in (5-4), and thus the field φ remains frozen with its initial value given by the Hubble dragging during the early universe (Harigaya et al., 2013). On the other hand, when the $\mu \sim H$ condition is approached, the SFDM starts evolving and oscillates as a free field. During this fast oscillating phase, we already saw that the free field behaves effectively as a dust component and then the dependence of φ with respect to the scale factor a is $\varphi \sim 1/a^{3/2}$, whereas its energy density behaves as $\rho_\varphi \sim 1/a^3$. So the energy density of the SFDM can be written as

$$\rho_\varphi = \begin{cases} \frac{1}{2}\mu^2\varphi_i^2 & \text{when } H \gg \mu, \\ \frac{1}{2}\mu^2\varphi_i^2 \left(\frac{a_{osc}}{a}\right)^3 & \text{when } H \ll \mu. \end{cases} \quad (5-6)$$

with a smooth transition between both behaviours when $H \simeq \mu$.

For typical masses of a SFDM candidate, $m_{22} \sim 1$, the field started its fast oscillating regime during the radiation-dominated Universe. During this period, it is easy to see from table 1-1 that the Hubble parameter evolves in terms of the scale factor as $H \propto a^{-2}$, and the KG equation (5-4) can be solved exactly in terms of a , giving

$$\varphi = \varphi_i \Gamma\left(\frac{5}{4}\right) \left(\frac{4H}{\mu}\right)^{1/4} J_{1/4}\left(\frac{\mu}{2H}\right), \quad (5-7)$$

where in the above expression it is fulfilled that $\varphi \rightarrow \varphi_i$ when $\mu/H \rightarrow 0$, i.e., it is demanded the slow-roll condition at early times. On the other hand, when $\mu/H \rightarrow \infty$, we have

$$\lim_{\frac{\mu}{H} \rightarrow \infty} \rho_\varphi = \frac{4}{\pi} \left[\Gamma\left(\frac{5}{4}\right) \right]^2 \mu^{1/2} \varphi_i^2 H^{3/2}. \quad (5-8)$$

Observe that (5-7) is not valid for all redshifts in the fast oscillating regime given that, for its derivation, we demanded a Universe that is dominated by a radiation-like fluid. Then, and because we already know that the history of the Universe should start, after inflation, with a radiation dominated era and transit at certain redshift z_{eq} to an era dominated by a dust-like fluid, we can assume that (5-7) should be valid for redshifts $z_i > z > z_{eq}$. On the other hand, if we consider an ultra-light SFDM candidate with a mass $m_{22} \sim 1$, we obtain that $\mu/H_{eq} \sim 10^{10}$ and then we could consider that the above expression is valid for certain values of the redshift parameter. If we concentrate in the time at which the above expression is valid and we compare with (5-6), we obtain

$$\frac{1}{2}\mu^2\varphi_i^2\left(\frac{a_{osc}}{a}\right)^3 = \frac{1}{2}\mu^2\varphi_i^2\left(\frac{H}{H_{osc}}\right)^{3/2}, \quad (5-9)$$

where the Hubble parameter H_{osc} at the time the SFDM starts its fast oscillating regime was obtained to be

$$\frac{\mu^2}{H_{osc}^2} = \left(\frac{8}{\pi}\right)^{4/3} \left[\Gamma\left(\frac{5}{4}\right)\right]^{8/3} \simeq 2.68 \quad (5-10)$$

On the other hand, in section 1.2.3.2 we saw that, for a radiation-dominated Universe, we can relate the temperature of the Universe at a given epoch with the energy density of radiation as (see equation (1-25) and (1-9))

$$\rho_r = \frac{3m_{pl}^2 H^2}{8\pi} = \frac{\pi^2}{30} g_*(T) T^4. \quad (5-11)$$

Particularly, at the time the SFDM starts its fast oscillating regime we have

$$T_{osc} \simeq 0.5 \text{ keV} \left(\frac{g_{*osc}}{3.36}\right)^{-1/4} m_{22}^{1/2}. \quad (5-12)$$

Using that the entropy of the Universe is conserved since the time the SFDM started its fast oscillating regime to present, the SFDM density today can be expressed in terms of the entropy density s as

$$\rho_{\varphi_0} = \frac{1}{2}\mu^2\varphi_i^2 \frac{s_0}{s_{osc}}, \quad (5-13)$$

where the subscript "0" denotes quantities in the present Universe. However, from equation (1-34) we can express s_{osc} as

$$s_{osc} = \frac{2\pi^2}{45} g_{s*osc} T_{osc}^3 = \frac{2\pi^2}{45} g_{s*osc} \left(\frac{90 m_{pl}^2 H_{osc}^2}{\pi^2 8\pi g_{*osc}}\right)^{3/4}. \quad (5-14)$$

Then, by combining equation (5-10), (5-13) and (5-14), and by considering that the total of the DM is produced by the SFDM, it is finally obtained the initial condition for the SFDM as

$$\varphi_i^2 \simeq \frac{10^{34} \text{ GeV}^2}{0.6} \left(\frac{g_{*osc}}{3.36}\right)^{-3/4} \left(\frac{g_{s*osc}}{3.91}\right) m_{22}^{-1/2}. \quad (5-15)$$

As we explained in section 1.2.3.2, g_{*osc} and g_{s*osc} are the effective degrees of freedom associated to the total particles and to the entropy at the moment when the SFDM starts its fast oscillating regime. In particular, for an ultra-light SFDM that started its oscillations during the radiation-dominated Universe, we have³ $g_{*osc} = 3.36$ and $g_{s*osc} = 3.91$. Notice also that the above expression is not only fulfilled by an ultra-light SFDM, but in fact it is correct for whichever SFDM that started its fast oscillating regime during the radiation-dominated Universe, always that the correct value for g_{*osc} and g_{s*osc} is provided for such candidate.

5.2.1.2. Constraints from isocurvature perturbations

For this case we demand the energy density contribution of the SFDM being small during inflation (DM dominates right after radiation-matter equality) and hence it is necessary from the total Friedmann equation (1-9) and the dynamics during the inflationary era in the inflaton scenario, which is equivalent to the dynamics of a single-field inflation (1-56), that

$$\frac{\mu^2}{2} < \frac{\hat{V}(\phi)}{\varphi_i^2} \sim \frac{H_{inf}^2 m_{pl}^2}{\varphi_i^2}, \quad (5-16)$$

where we have introduced the parameter H_{inf} , which is the constant value of the Hubble parameter during inflation and we have considered that during this period our field remains frozen at value φ_i . Notice that for an ultra-light SFDM candidate ($m_{22} \sim 1$) the above expression is fulfilled for most of the initial conditions given by φ_i . On the other hand, we can constrain isocurvature perturbations generated by a SFDM using equation (5-3). The analysis was performed in (Kobayashi et al., 2017) by noticing that we can re-express the primordial spectrum as $\delta\rho_{\varphi^*}/\rho_\varphi = 2\delta\varphi/\varphi_i$ (since from equation (5-6) we have $\rho_\varphi \propto \varphi^2$), which implies that $P_{SFDM} = 4P_\varphi/\varphi_i^2$, where P_φ is given by equation (1-105c) (which can be expressed in terms of the tensor to scalar ratio r using (5-2)) and φ_i by equation (5-15), and then equating it with P_{DM} in equation (5-3). When such procedure is done, they finally obtain from the inequality in (5-3) the result

$$m_{22} < \left(\frac{2 \times 10^{-4}}{r} \right)^2. \quad (5-17)$$

Then, the isocurvature restrictions allow us to constrain the mass parameter of the SFDM in terms of the tensor-to-scalar ratio measurements. The above relation for the mass parameter must be in agreement with cosmological and astrophysical observations. For such purpose we considered the different constrictions reviewed in the last chapter, especially in section 4.5. We need to stress out that we cannot use all the constrictions in the literature since some

³Although g_* and g_{*s} are functions that depends on the temperature of the Universe, it remains constant for temperatures below $T = 511$ keV with the value (Husdal, 2016) $g_* = 3.36$ and $g_{*s} = 3.91$. On the other hand, observe from (5-12) that for an ultra-light SFDM candidate with a mass $m_{22} \sim 1$, the temperature at which it starts its fast oscillating regime is $T_{osc} \sim O(1)$ keV.

of them consider different cosmological evolutions for the SFDM. For example in (Li et al., 2014) it was studied the CMB and the BBN by understanding the SFDM was generated right after inflation with a stiff-like equation of state ($p_\varphi \simeq \rho_\varphi$). Then, these kind of restrictions are not applicable to our model.

Fig. 5-1 displays the different constraints on a $m_{22} - r$ plane. In order to simplify the lecture of the figure we have only plotted the upper (lower) value for the constrictions that fit the mass of the SFDM with an upper (lower) limit. We have also added arrows that points out the region that remains valid for such constrictions. Firstly, the gray region is fulfilled by isocurvature observations (5-17). The dot-dashed black line corresponds to the equality values in equation (5-17). Then, the figure must be interpreted as follows: suppose we have measured a value for r . Notice that such value will intersect with the dot-dashed black line for a given mass $m_{22}^{(max)}$. Then, the masses allowed by the model must be those lower than $m_{22}^{(max)}$.

The region that fulfills observations obtained by CMB is specified in green, while the value provided by Abel 3827 is given by the dot-dashed red line. The region for dwarf spheroidal galaxies is indicated in blue, Ursa with Fornax in light blue, ultra-faint dwarfs in teal, reionization in purple and Lyman- α in orange. We notice that isocurvature perturbations cannot constrain observations of the dynamics of dSphs galaxies given that both provide an upper limit for the mass of the SFDM. However, the detectability of gravitational waves and the different constrictions by cosmological and astrophysical observations can be used to test the free model. For example, if we ignore by the moment the dynamics of dSphs galaxies and we would like to fulfill at least observations provided by CMB, we should not detect gravitational waves until $r \simeq 1.3 \times 10^{-3}$ (fuchsia straight-line), while if we are interested on the rest of observations we should not detect gravitational waves until $r \lesssim 2.33 \times 10^{-5}$ (gold straight-line).

We also plotted the actual upper limit for r in a navy blue dashed-line. By the moment this value is not very restrictive for the model since it represents an upper value for r . Nevertheless the information it provides is that masses smaller than $m_{22}^{(upper)}$ – the blue dashed-line and black dot-dashed-line intersection – are allowed by the data. However, masses bigger than $m_{22}^{(upper)}$ cannot be discarded since the only possible way to do it is if r would be detected.

5.2.2. Real self-interacting SFDM candidate with a repulsive self-interaction

5.2.2.1. Cosmological history

Once we understood the way the real free-field model can be tested with isocurvature constrictions, it is time to consider the self-interacting scenario. In this section a self-interacting SFDM with a positive interaction is considered. This scenario is described by the general

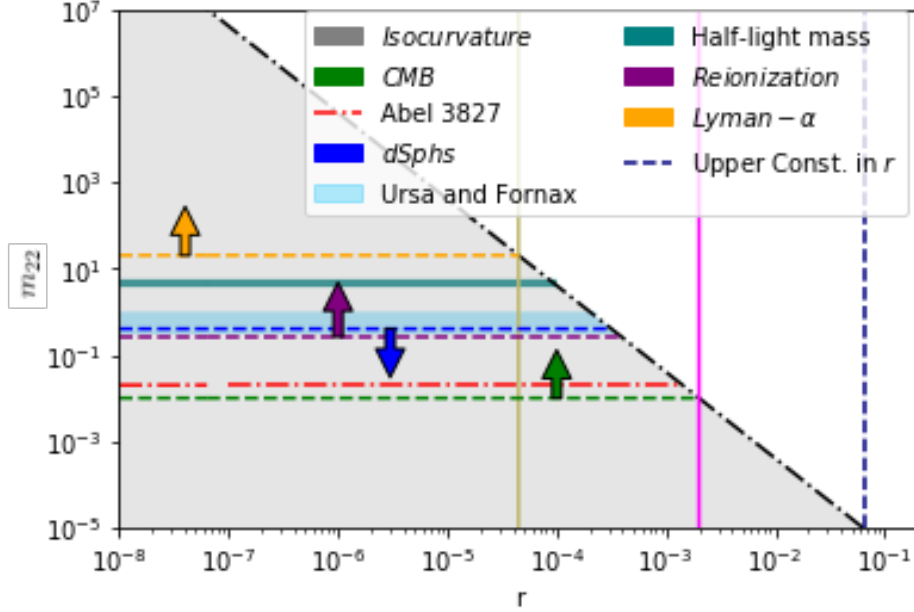


Figure 5-1.: Isocurvature constraints for the SFDM candidate (Figure taken from (Padilla et al., 2019)).

potential

$$V(\phi, |\varphi|^2) = \hat{V}(\phi) + \frac{1}{2}\mu^2\varphi^2 + \frac{1}{4}\nu\varphi^4, \quad (5-18)$$

and fixing again $Q = 0$ for the SFDM in equation (5-4). In what follows we omit the hat in the potential $\hat{V}(\phi)$ in order to make simpler the lecture of the article. Then, always that appears V must be understood that we are referring to \hat{V} .

Notice that for this case $M_{eff}^2 = \mu^2 + \nu\varphi^2$. As we have previously discussed the effective mass of the field after inflation remains constant at $M_{eff}^2 = \mu^2 + \nu\varphi_i^2$ until $M_{eff} \sim H$. Then, depending of each contribution to M_{eff}^2 , we can have two different dynamics:

Weakly self-interacting regime.- This limit is obtained when the constant term μ^2 dominates, that is when

$$\mu^2 \gg \nu\varphi_i^2. \quad (5-19)$$

In this regime it is possible to ignore the self-interacting term in equation (5-4) when the fast oscillating phase of the SFDM begins. However, by ignoring this term, the field behaves as a free field and, from (5-6), the field value always decreases. Therefore, the self-interacting term never dominates and all the cosmological history remains the same as in the pure free SFDM scenario. In fact, thanks to the decreasing behavior of this scenario, we can consider that this regime is fulfilled always that $\mu^2 \geq \nu\varphi_i^2$, or, equivalently, when $\nu \leq \mu^2/\varphi_i^2$. If the SFDM oscillations start at the same time than in the free case (which is a good approximation since the effective mass of the SFDM is $M_{eff}^2 = \mu^2 + \nu\varphi_i^2 \leq 2\mu^2$), we observe from (5-15)

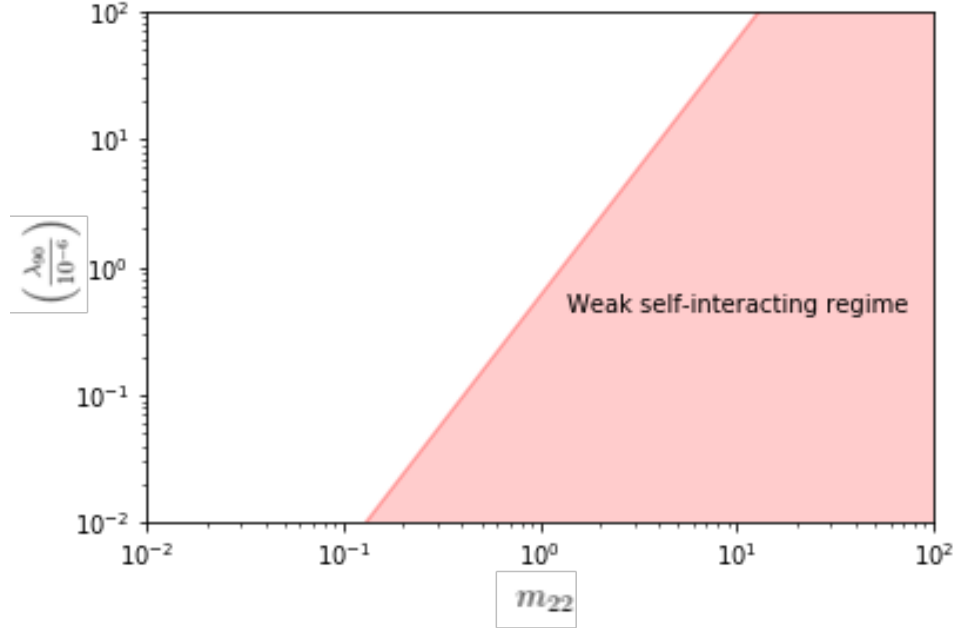


Figure 5-2.: Weakly self-interacting regime (Figure taken from (Padilla et al., 2019)).

that it should be satisfied that

$$\left(\frac{\lambda_{90}}{10^{-6}}\right) \leq 0.6m_{22}^{5/2}. \quad (5-20)$$

In Fig. 5-2 we plot the weak self-interacting limit obtained by our approximation. However this overestimates the maximum value of λ_{90} since the dust-like behavior is obtained when the λ_{90} term is completely negligible.

Strong self-interacting regime.- This scenario is obtained when

$$\mu^2 \ll \nu\varphi_i^2. \quad (5-21)$$

Here, the SFDM follows the dynamical equation (see equation (D-5) of appendix D)

$$\frac{1}{\varphi^2} - \frac{1}{\varphi_{it}^2} = 2\nu \int_{\phi}^{\phi_{it}} \frac{d\phi}{V_{,\phi}}, \quad (5-22)$$

where subindex it means quantities at the beginning of the inflationary period. Notice that if the inflationary process does not last for long enough time – meaning that φ_{it}^{-2} is much smaller than the right hand side value of the above expression –, the SFDM remains frozen with value φ_{it} , while if it lasts long enough time, the SFDM reaches an attractor solution.

Attractor behavior of the SF during inflation.- In the strong self-interacting regime,

and after enough time, the SFDM follows the attractor solution (D-6)⁴

$$\varphi_{att} = \left(2\nu \int_{\phi}^{\phi_{it}} V_{,\phi}^{-1} d\phi \right)^{-1/2}, \quad (5-23)$$

where ϕ_{it} is the value of the inflaton at the beginning of inflation. As we can see from the above expression, whether or not the SFDM reaches the attractor solutions depends entirely on the inflationary process and the value of the self-interacting term of the SFDM. In the above expression we can identify two possible branches:

- $\varphi_{att} < \mu/\sqrt{\nu}$

The SFDM follows the attractor solution until $\varphi \simeq \mu/\sqrt{\nu}$. Then the field reaches $\varphi_i = \mu/\sqrt{\nu}$ for the rest of inflation. Notice that this value corresponds to the upper limit that the weakly self-interacting regime allows. Then the field starts evolving when $H \sim M_{eff} \simeq \mu$, behaving as a free SFDM. In this way, the constrictions given in the non-interacting case apply and the initial conditions are also fixed by φ_i . Using both relations the λ_{90} value is approximated

$$\left(\frac{\lambda_{90}}{10^{-6}} \right) \simeq 0.6 \left(\frac{g_{*osc}}{3.36} \right)^{3/4} \left(\frac{g_{s*osc}}{3.91} \right)^{-1} m_{22}^{5/2}. \quad (5-24)$$

- $\varphi_{att} > \mu/\sqrt{\nu}$

In this scenario the dynamics of the inflaton, given by (5-23), implies that the initial condition of the field after the inflationary period is

$$\varphi_{att}^i = \left(2\nu \int_{\phi_{end}}^{\phi_{it}} V_{,\phi}^{-1} d\phi \right)^{-1/2}, \quad (5-25)$$

where ϕ_{end} is the value of the inflaton at the end of inflation. We need to stress out that this is the value of the field until its oscillation period starts (i.e. when $M_{eff} \sim H$).

In this scenario and for $\varphi_{att} > \mu/\sqrt{\nu}$ (regardless of whether the scalar field reached the attractor behavior or not), we observe that at the time the SFDM starts its fast oscillating regime, its effective mass is linear in the field. In that regime, the scalar field evolves as $\varphi \sim 1/a$ and its energy density as $\rho_{\varphi} \sim 1/a^4$, behaving as radiation. Then, when $\mu^2 \sim \nu\varphi_t^2$,

⁴In (Harigaya et al., 2013) was obtained the attractor behavior for a curvaton-like scalar field in a chaotic-like inflationary scenario. However their results can be used as well in this context were the attractor behavior can be easily obtained for whichever inflationary potential.

the effective scalar field mass is now constant, obtaining the dust-like behavior already analyzed. Therefore, the history of the scalar field density is

$$\rho_\varphi = \begin{cases} \frac{1}{4}\nu\varphi_i^4 & \text{when } H^2 \gg \nu\varphi_i^2 \\ \frac{1}{4}\nu\varphi_i^4 \left(\frac{a_{osc}}{a}\right)^4 & \text{when } H_t^2 \leq \nu\varphi^2 \leq H^2 \\ \frac{1}{2}\mu^2\varphi_t^2 \left(\frac{a_t}{a}\right)^3 & \text{when } H^2 \leq \mu^2 \text{ and } \nu\varphi^2 < \mu^2 \end{cases} \quad (5-26)$$

Here sub-index t means quantities measured at transition between radiation-like to dust-like behavior of the SFDM and

$$\varphi_i^2 = \left[\frac{2\mu^2}{\nu}\varphi_t^2 \right]^{1/2} \left(\frac{a_t}{a_{osc}} \right)^2. \quad (5-27)$$

Notice that, for simplicity, we have taken an instantaneous transition between radiation-like to dust-like behaviors.

Since the self-interacting KG equation cannot be solved exactly, we work with approximated solutions. By using a pure approximated description of the system, (Suárez and Chavanis, 2017) obtained the relation (see its equation 80 and 86 and also (Li et al., 2014))⁵

$$\left(\frac{a_t}{a_{osc}} \right)^2 = \frac{3}{7^{1/3} f^2\left(\frac{a_s}{r_S}\right)}, \quad (5-28a)$$

where

$$f(\sigma) = \frac{1}{s^{1/3}(1+4s)^{1/6}}, \quad (5-28b)$$

with

$$s = \frac{4\sigma - 1 + \sqrt{(4\sigma - 1)^2 + 12\sigma}}{6}. \quad (5-28c)$$

where $a_s/r_S = \nu/\mu^2$. Rearranging the expression in a more convenient way we have

$$\sigma \simeq 5.93 \times 10^2 m_{22}^{-2} \left(\frac{\lambda_{90}}{10^{-6}} \right). \quad (5-29)$$

Notice that when $a_t/a_{osc} \simeq 1$, i.e. $3/(7^{1/3} f^2(\sigma)) \sim 1$, there is no radiation-like epoch. This scenario should match with the non-interacting scenario that we present previously. Inserting equation (5-28a) into (5-27) yields to

$$\varphi_i^2 = \frac{3}{7^{1/3} f^2(\sigma)} \left[\frac{2\mu^2}{\nu}\varphi_t^2 \right]^{1/2}. \quad (5-30)$$

The relation (5-30) matches the field at φ_t with its value right after inflation ends. Then, if we obtain the value of φ_t by comparing with quantities at present, with the above expressions we can also obtain the value of φ_i . On the other hand, notice that at a_t , the

⁵The reference (Suárez and Chavanis, 2017) obtained this relation by considering a Universe with only a SFDM content. However a similar analysis can be used in a Universe with several types of matter contents.

scalar field behaves as dust with an effective mass $M_{eff}^2 = \mu^2 + \lambda\varphi_t^2$. This implies that dust-like oscillations of the SF began a little before than in the non-interacting case. If we allow μ to start its dust-like behavior during the radiation-dominated Universe and using the fact that μ^2 is about the same order that $\nu\varphi_t^2$, we get that such oscillations start during the same epoch than in the non-interacting case. In fact, because the decreasing behavior of the SFDM during the dust-like period ($\varphi \sim 1/a^{3/2}$), the self-interacting term contribution quickly vanishes, and then, the dynamics of the field is described only by the mass term μ . Thus, once the dust-like behavior starts, the dynamics is described similarly to the non-interacting case, in such case, the condition (5-15) is fulfilled by the SFDM as well, but interchanging subindex i with t ⁶.

5.2.2.2. Constraints from isocurvature perturbations

As we showed in the last section, we have two different scenarios for this model: a weak self-interacting, and a strong self-interacting. In the weak limit, our SFDM behaves effectively as a free field without self-interaction, and in such case the constrictions for the free field apply to this scenario as well. On the other hand, when the self-interacting term is big enough, the SFDM will have a new period with a behavior similar to a radiation-like fluid. In this way, the constrictions we obtained before will not apply to this model anymore.

In the strong self-interacting regime, during the inflationary era, the SFDM follows the solution (5-22). The value the homogeneous field acquired after inflation depends on the amount of time the inflationary process takes place, and the condition $\varphi_{att} \lesssim \mu/\sqrt{\nu} \equiv \varphi_t$ – if the inflationary period is short, then the field φ remains frozen at value $\varphi_i \simeq \varphi_{it}$, while if it lasts long enough, the SFDM reaches the attractor behavior (5-23)–. If the SFDM reaches the solution (5-23), and for $\varphi_{att} < \varphi_t$, the field follows the attractor solution until $\varphi \simeq \varphi_t$. Then, the SFDM is frozen at that value, and starts oscillating as a free field when $\mu \sim H$. We can constrain this scenario by noticing that it is the same case than the free one, but with the initial condition $\varphi_i = \varphi_t$. Matching equation (5-15) with φ_t , and making use of the constriction (5-17), we obtain

$$\left(\frac{\lambda_{90}}{10^{-6}}\right) \leq 0.6 \left(\frac{2 \times 10^{-4}}{r}\right)^5. \quad (5-31)$$

In Fig. 5-3 we have plotted the above condition that is valid during the strong self-interacting regime, when $\varphi_{att} < \varphi_t$. The pink region corresponds to the region allowed by isocurvature perturbations in this limit. As we observe, the self-interacting term for this model can be constrained in a similar way than the mass parameter in the free case. This scenario must fulfill the relation (5-17) as well, since its cosmological evolution, after inflation, is only like a free SFDM.

⁶In fact, this is a lower limit for the strong self-interacting case.

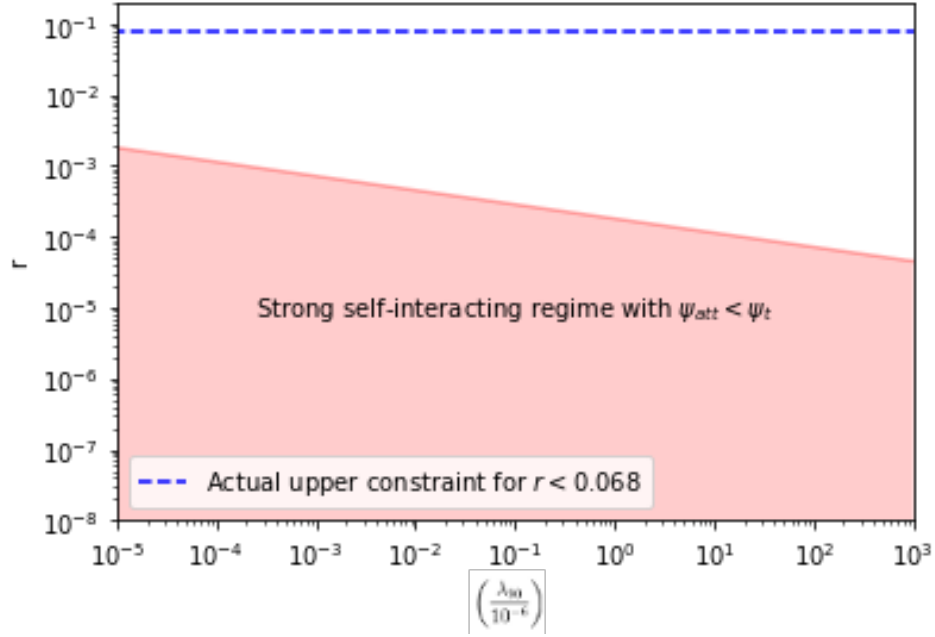


Figure 5-3.: Isocurvature constraints for the strong self-interacting regime with $\varphi_{att} < \varphi_t$ (Figure taken from (Padilla et al., 2019)).

Additionally, in this scenario, the inflationary potential fulfills the condition

$$\left(\int_{\phi}^{\phi_{it}} V_{,\phi}^{-1} d\phi \right)^{-1/2} < \sqrt{2}\mu. \quad (5-32)$$

We can see that it is very difficult to obtain this relation for an ultra-light SFDM candidate. For example, if we consider a chaotic-like inflationary potential, $V(\phi) = \frac{1}{2}M_{inf}^2\phi^2$, the above conditions imply that

$$\left(\log \frac{\phi_{it}}{\phi} \right)^{-1/2} < \sqrt{2} \frac{\mu}{M_{inf}}. \quad (5-33)$$

However, for this potential, the mass M_{inf} of the inflaton that best matches the observations⁷ is of order $M_{inf} \sim 10^{12} GeV$ (Lyth and Liddle, 2009). If now, we assume an ultra-light SFDM candidate with a mass $m_{22} \sim 1$, given that the cosmological and astrophysical constrictions for this model are the same than in the free case and in this scenario it is necessary to obtain an ultra-light SFDM, the above conditions imply that the logarithmic part of the expression should be lower than $\sim 10^{-43}$. The inflationary behavior for a chaotic-like inflaton ends when $\phi_{end} \simeq m_{pl}/\sqrt{2\pi}$ (Harigaya et al., 2013, Lyth and Liddle, 2009). Moreover, as it is explained in (Harigaya et al., 2013), the initial condition of the inflaton cannot be arbitrarily large since the stochastic behavior is significant for $\dot{\phi}H^{-1} < H/2\pi$. If the Universe started when

⁷This chaotic-like inflationary potential is ruled-out now for observations, however we use it as an example in order to obtain general constraints for our models.

the inflaton escapes from this behavior, we have that its initial condition should be

$$\phi_{it} \sim \frac{10^5}{\sqrt{8\pi}} \times m_{pl} \left(\frac{10^{13} GeV}{M_{inf}} \right)^{1/2}, \quad (5-34)$$

where we can easily see that the condition given in (5-33) cannot be fulfilled. In fact, if we insert the left part of (5-33) in equation (5-22), and by considering the above result, and the fact that in this scenario the self-interacting term must be incredible small (see equation (5-31)) in order to fulfil cosmological and astrophysical constrictions, we can observe that the attractor behavior is not reached when it is assumed a chaotic-like inflationary potential. This implies that, if a self-interacting SFDM candidate coexists with the inflaton, and that during the beginning of the inflationary period it starts in the strong-field scenario, it should remain within the strong regime since their conditions are easier to satisfy.

If the SFDM reached the solution (5-23), and when $\varphi_{att} > \varphi_t$, we have that the field follows the attractor solution during all the inflationary period. Hence, the initial condition for the SFDM is given by (5-25)

$$\varphi_{att}^i = \left(2\nu \int_{\phi_{end}}^{\phi_{it}} V_{,\phi}^{-1} d\phi \right)^{-1/2}. \quad (5-35)$$

Then, the SFDM remains frozen at value φ_{att}^i until $M_{eff} \sim H$, and starts oscillating with a quartic potential. In this scenario, the SFDM density behaves as $\rho_\varphi \propto \varphi^4$, and in such case we can write $\delta\rho_\varphi/\rho_\varphi = 4\delta\varphi/\varphi_i$. Therefore, the primordial isocurvature perturbations for a strong self-interacting SFDM is given by

$$P_{SFDM}(k) = \left(\frac{2H_{inf}}{\pi\varphi_i} \right)^2. \quad (5-36)$$

In the last section we showed the relation of the initial condition with the value of the field today. Using equations (5-30) and (5-15), with $g_{*osc} = 3.36$ and $g_{s*osc} = 3.91$, and appropriate units we obtain

$$r < \frac{1.172 \times 10^{-4}}{7^{1/3} f^2(\sigma)} \left[\frac{2m_{22}^{3/2}}{\left(\frac{\lambda_{90}}{10^{-6}} \right)} \right]^{1/2}. \quad (5-37)$$

Notice that the above relation is independent of whether the SFDM followed the attractor solution or not, and, therefore, the result is general always that the SFDM remains in the strong self-interacting regime at the end of inflation, and its dust-like behavior started in the radiation dominated Universe.

Similarly to the free case, the above relation must be compared with observations in order to get constrictions for the strong self-interacting SFDM scenario. For such porpoise, we use some of the different constrictions presented in section 4.5. The ones that we decided

not to use are constrictions that considers scenarios where our model is not applicable. For example, such observations that consider an early stiff-like behavior for the SFDM.

In Fig. 5-4 we have plotted contour levels of the numerical value of the right hand side of the relation (5-37). The grey region corresponds to values larger than 0.064, which is the actual upper constraint on tensor-to-scalar ratio. This means that, within that region, we are certain that (5-37) is fulfilled and, by the moment, just this region is completely allowed by observations. With this in mind, the plot should be understood as follows: let us suppose that in the near future we measure a value for r . Such value will coincide with a curve in Fig. 5-4. Then, the parameter space allowed by the data should be the one where the contour levels are bigger than the detected value of r , while the one with smaller values in the contour levels must be discarded. Similar to the free case, if r is not detected but it continues with an upper limit, this implies that regions with contour levels bigger than such upper value will be allowed by the data, however regions with smaller values can not be discarded until r is detected.

The λ_{90} value that satisfies observations of dSph's line-of-sight is given by the dot-dashed red line, while the region of parameters necessary for rotational curves is presented in blue. Similar to the plot for the free case (fig. 5-1), we plotted the cosmological constrictions in purple by drawing a curve that refers to the upper value of λ_{90} and an arrow that points out to the valid region from the constriction. We did the same for the observations for BBN, but in color fuchsia. The white region corresponds to the weak limit. We can see from Fig. 5-4 that it is possible to fulfill observations for whichever value for the mass, as long as the self-interacting constant is large enough. In other words, for a given mass, the measurement of r can only constrain the self-interacting constant with a lower limit. Isocurvature observations (or equivalently observations on r) can also help to impose upper values from other kind of constrictions. As an example, let us suppose that we want to be completely sure that the measurements obtained by rotational curves are fulfilled. Then, given the actual upper constraints in r , the only region of parameters that we can be sure that fulfills observations are the ones in the blue region that are also inside the gray region.

Remark: This scenario is of special interest given that it is natural to avoid isocurvature perturbations when the self-interacting parameter of the SFDM is big enough. Additionally, if the SFDM reached the attractor solution, it is possible to justify the initial conditions for the SFDM model.

Similarly to the above description, we can compute general constraints for the inflationary potential that should generate inflation on these kind of scenarios. First, we have that

$$\left(\int_{\phi}^{\phi_{it}} V_{,\phi}^{-1} d\phi \right)^{-1/2} > \sqrt{2}\mu, \quad (5-38)$$

which is very easy to fulfill as we saw in the chaotic-like example. Using isocurvature

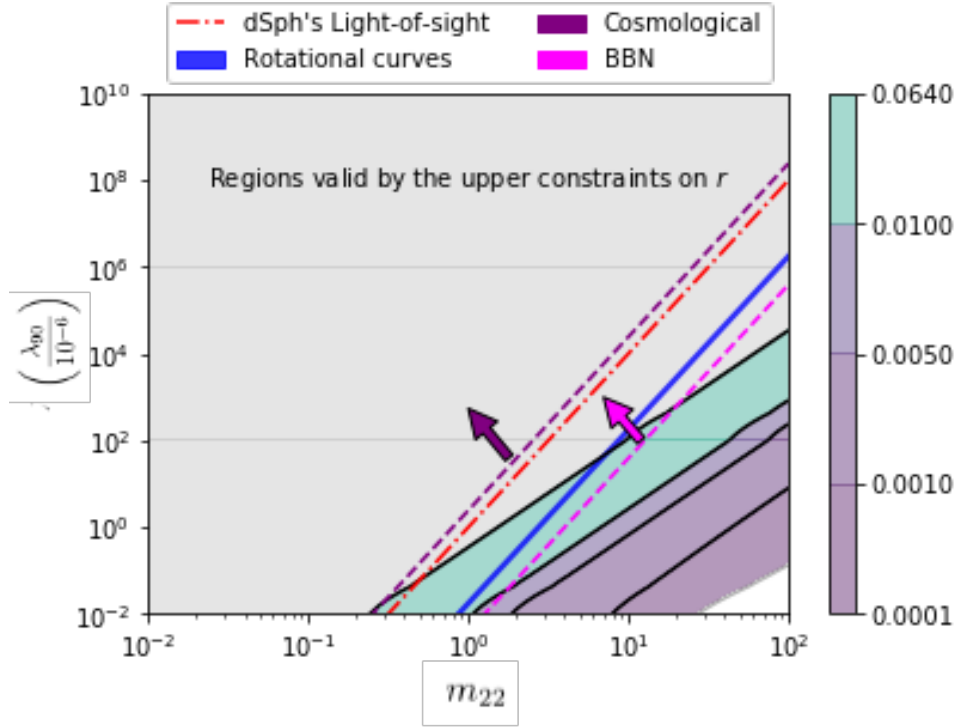


Figure 5-4.: Isocurvature constraints for the strong self-interacting scenario with $\varphi_{att} > \varphi_t$ (Figure taken from (Padilla et al., 2019)).

constriction we also have

$$r < \frac{0.6 \times 10^{40}}{\left(\frac{\lambda_{90}}{10^{-6}}\right)} \left(\frac{1}{\int_{\phi_{end}}^{\phi_{it}} V_{,\phi}^{-1} d\phi} \right), \quad (5-39)$$

that can be satisfied as far as the self-interacting term and the integral are small enough; for example in the chaotic-like scenario by using (5-33) and (5-34) and taking $M_{inf} \sim 10^{-6} m_{pl}$, we can obtain the constriction

$$\left(\frac{\lambda_{90}}{10^{-6}} \right) < \frac{0.3288 \times 10^{84}}{r}. \quad (5-40)$$

that is easily satisfied for whichever value of λ_{90} of our interest. If now we compare (5-25) and (5-30), we have

$$\left(\int_{\phi_{end}}^{\phi_{it}} V_{,\phi}^{-1} d\phi \right)^{-1} = \frac{6}{7^{1/3} f^2(\sigma)} (2\mu^2 \nu \varphi_t^2)^{1/2}. \quad (5-41)$$

This relation is interpreted as follows: consider that the self-interacting SFDM candidate coexists with the inflaton, and it reached the attractor solution (5-23), and suppose there are several measurements constraining the mass parameter m_{22} as well as the self-interacting parameter λ_{90} , therefore such constraints are translated into restrictions to the inflationary potential. In order to use the above expression to constraint inflationary potentials, we need

to be sure that the term φ_{it}^{-2} can be ignored in (5-22), i.e., the right-hand side term in equation (5-22) is big enough compared with φ_{it}^{-2} .

It is also necessary to be careful that the SFDM does not come to dominate the inflationary period. This is guaranteed by demanding that

$$\frac{\nu}{4} < \frac{H_{inf}^2 m_{pl}^2}{8\pi\varphi_i^4}, \quad (5-42)$$

or in terms of (5-35)

$$\nu > \left(\frac{2}{\pi} H_*^2 m_{pl}^2 \mathcal{G} \left(\int_{\phi_{end}}^{\phi_{it}} V_{,\phi}^{-1} d\phi \right)^2 \right)^{-1}. \quad (5-43)$$

Taking the chaotic-like example and using $H_{inf} = 10^{14} GeV$, we obtain the constriction

$$\frac{\lambda_{90}}{10^{-6}} > 1.444 \times 10^{77}. \quad (5-44)$$

Notice that the above expression requires $\lambda_{90} > 10^{71}$, and then by considering the cosmological and astrophysical constrictions we should have a mass parameter of order $m_{22} \sim 10^{17}$. We have to stress out that (5-44) is obtained for a chaotic-like potential, then, depending on the inflationary potential we will have different limits allowed for the self-interacting scenario. On the other hand if equation (5-43) is not fulfilled and we remain in the strong-self interacting model, it should be necessary to consider a two-field inflationary scenario where the SFDM could obtain a non-negligible dynamics during inflation.

6. SFDM configurations around Super-massive Black Holes

As we already commented in the very beginning in this thesis, there exist a host of observations that indicate the existence of SMBHs placed in the center of most massive galaxies and some observations of SMBHs in ultra-compact dSphs. The consequences that these SMBHs entails in the SFDM model have not been considered in the results that we studied in the above chapters and then they represent a very interesting topic for studying in the model, either by considering the coexistence of these SMBHs with the soliton profile in galactic nuclei or the possible formation of SMBHs in the SFDM scenario. In this chapter, we consider the first of these possibilities. We focus in the simplest scenario, where in the free field limit we include the extra physics obtained when considering a central SMBH in galaxies. Of course, given the large difference between the size of a total halo and the radius at which the central SMBH affects the SFDM distributions is very different, we decided to deal only with the effect of the SMBH in the central region of the SFDM profile. In the next chapter we shall contemplate a mechanism of formation of SMBHs in the SFDM model through the collapse of the SFDM soliton profile. For such purpose we shall consider to extend the results in the above chapter by including a self-interacting parameter in the model.

It is necessary to mention that the correct way for modelling a central galactic soliton in presence of a SMBH should be by solving the EKG system and contemplating an extra gravitational term provided by the central SMBH. Given that for the range of parameters needed for describing the SFDM model in the free limit it is usually enough to describe these solitons in the weak field limit and the mass expected for the soliton profile is much larger than the mass of its possible SMBH, it could be enough to solve the SchP system with the addition of a central SMBH as a perturbative term. In fact, in a very recent work (Davies and Mocz, 2019) it was studied this last scenario. However, this chapter will be strongly based on an earlier work (Avilez et al., 2018), where we studied this possibility in a simpler manner. For that purpose we considered the extension of the model proposed in (Robles and Matos, 2013) (see chapter 4.4.2 and equation (4-30)) and then we contemplate the possibility that the central SFDM halo in presence of a SMBH could be well described by a Schwarzschild-like geometry and then we only deal with the KG equation. Of course, this scenario is not very realistic (as we discussed in section 4.4.2) since we are ignoring the effects of self-gravitation of the SFDM particles. However, this analysis could help us to understand a little more the consequences that arise when introducing these SMBHs to the

model. It is worth to mention that in this approach the back-reaction either of the scalar and visible matter onto the metric is neglected. Since the space-time is assumed to have Schwarzschild geometry, the black hole is the only one that has a gravitational contribution at the level of the field equations. Nonetheless, these simplifications are worth since we derive an analytical approximation for the density profile of dark matter in the faraway neighbourhood of a black hole instead of solving the highly-non-linear fully relativistic EKG system. It must be mentioned that our analysis should be correct in the regions very close to the SMBH (where the gravitational attraction of the SMBH dominates over the one generated by the SFDM). In fact, in appendix E we show under which circumstances our approximation is valid.

The way we decided to work in this chapter is by computing theoretical predictions of the mean velocity dispersions corresponding to each solution for a fixed mass of the SMBH, for different values of the characteristic length of the soliton profile. We achieve this by solving the isotropic Jeans equation and modelling the density and mass distributions using the phenomenological Plummer profile (Plummer, 1911) which is suitable to describe density distributions of spherical stellar systems like bulges, dwarf and elliptical galaxies (Ahn et al., 2017, Walker et al., 2009). Then, we can see that additionally to consider the extra physics due to the central SMBH in galaxies, we also contemplate the baryonic component.

In order to fully construct SFDM soliton profiles in a space-time surrounding a SMBH which is compatible with observations, we determine values of the free parameters central density and characteristic length of the SF configuration, using theoretical and observational constraints. Firstly, by imposing boundary conditions on the classical solutions of the KG equation, we derive an upper bound for the characteristic length of the SF configuration, as performed in (Barranco et al., 2011). Secondly, we reduce the space of parameters of our solutions, by establishing a relation between the central density of the SFDM profile and its characteristic length by considering the universality of the maximum acceleration of DM particles reported in (Ureña-López et al., 2017). This result was recently derived from the mass-discrepancy-acceleration-relation (MDAR) coming from observations of a large set of galaxies (Lelli et al., 2017, McGaugh et al., 2016). A complementary result of the present chapter is a modification on the constraint over the central surface density found in (Ureña-López et al., 2017), but introducing the effect of a SMBH. We carry out their analysis for the special sort of galaxies hosting SMBHs, and found a maximal relation between the DM central surface density and the mass of the BH, which corresponds to an increasing function, a result consistent with previous results (Barranco et al., 2011, 2012, Lee et al., 2015).

Finally, for each value in the considered range of masses of the SMBH, we fix the value of the characteristic length of the SFDM profile such that the theoretical stellar velocity dispersion fits the corresponding value given by the $M - \sigma^*$ correlation reported in (McConnell and Ma, 2013). We carry out such procedure in two different cases: 1) Dark-Matter-Dominated systems (DMD): In this idealized case the gravitational potential of DM dominates within the Jeans equation. This scenario is potentially interesting observationally since it could

be useful for studying ultra-compact dwarf (UCD) galaxies with a central SMBH, as the ones that were observed in (Ahn et al., 2017). 2) Luminous-Galaxies (LGAL): we solved the Jeans equation for a catalogue of six luminous galaxies housing SMBHs in their centres. In contrast to DMD, in this case, the profiles for the visible matter are already known. Additionally, the gravitational contributions of dark and visible matter are considered within the Jeans equation. From the results from the fits in each case we can conclude: In the DMD case we found that it is possible to predict the observed stellar velocity dispersion for galaxies hosting SMBH with masses smaller than $10^8 M_\odot$. In the LGAL, by considering all the galactic matter contributions, it is possible to reproduce σ^* for all galaxies in our catalogue.

Now, we would like to point out that, in despite of the simplicity of this model (our Schwarzschild-like geometry assumption), it is worth to keep studying and improving it, since it has been helpful to reproduce the observed values of velocity dispersion of stars in the LGAL case (taking into account the importance of baryons) and it gives us an idea of the power of predictability of the DMD case for modelling low-brightness galaxies with BHs with masses up to $10^8 M_\odot$. Observations of the deep-inner galactic region are very likely to be improved in short time and this would bring up a new source of evidence of the properties of the SMBH and its influence on stars laying in the galactic bulge. In addition, from observations of the stellar evolution across this region, wealthy information of the DM configurations would be inferred, which would be useful to discriminate between different DM models. Either to test our hypothesis about SMBH formation and to compare different DM models in the deep-inner galactic regions using these and upcoming direct observations of SMBHs in a short future, is a compelling goal that we are after.

6.1. Black holes wigs as long-lasting dark matter solitons

The first question that arises in the model is: Once a SMBH is formed, independently of the mechanism at which it was generated, does a self-gravitating and stable scalar galactic soliton remain? Strictly speaking, no-hair theorems lead us to give a negative answer to the question. However, for realistic circumstances and practical purposes, the answer is surprisingly affirmative. No-hair theorems condemn these solutions to pass away after some time (Bekenstein, 1995, Gürlebeck, 2015); while that is true, it also has been demonstrated that some solutions survive at least a cosmic time. That is, although BHs are condemn always to be bald, nothing prevent them to wear quasi-stationary SF configurations along their whole life. This kind of SF configurations are typically referred to as wigs in the literature. The boson excitations making up the wigs are subject to gravity and also to their own dispersive nature inherit by the KG equation, i.e. the equivalent to the quantum force defined in (4-21) in the hydrodynamic representation. Although a perfect balance between these competing effects can not be achieved, at least the decay time can be controlled choosing a proper mass for the configuration. (Barranco et al., 2011, 2012), and more recently (Sanchis-Gual

et al., 2017), studied analytically and numerically configurations of a free SF embedded in a Schwarzschild space-time, once the SMBH has been formed. They realized that it is possible to find physically meaningful, long-lived SF multistate configurations. In particular, for ultra-light SFs laying around SMBHs and axions around primordial BHs. They found that for masses $m_{22} < 1$ and SMBHs of $M < 5 \times 10^{10} M_{\odot}$, the configurations can survive for times larger than 10^{10} yrs. In this sense, their results strongly support the hypothesis that the DM is a SF in the galaxies hosting SMBHs. Furthermore, the whole dynamics of the system, including its formation and evolution along the cosmic history, arises from a single physical framework without aid of baryonic physics.

Remark: The importance of survival of these solitons surrounding SMBHs is because typically in dSph galaxies is where a core structure in the inner region of the galaxy is more appreciable, and in fact, from the results presented in the last chapter about the galactic profiles in the SFDM model, such dSph should be formed nearly by only the soliton profile. Then, galaxies with a central SMBH as the ones found in (Ahn et al., 2017) should be necessarily explained by these scalar wigs configurations.

6.2. The model: Ultra-light scalar field configurations in a Schwarzschild space-time

As we already commented, we start studying the simplest model for a free SFDM central density profile hosting a SMBH by assuming that the geometry of the space-time surrounding a SMBH is described by the Schwarzschild metric which, in spherical coordinates, is given by

$$ds^2 = - \left(1 - \frac{2M}{r}\right) dt^2 + \left(1 - \frac{2M}{r}\right)^{-1} dr^2 + r^2 d\Omega^2, \quad (6-1)$$

where M is the mass of the SMBH in units of distance (for this chapter we use units where $G = 1$ since it is clearer to write the different equations that arise in this description) and $d\Omega^2 \equiv d\theta^2 + \sin^2 \theta d\varphi^2$ is the solid angle square differential. Observe also that we have used r instead of x , and then in this chapter we shall work in physical coordinates instead of comoving coordinates.

The dynamics of the SFDM described by the KG equation (2-14), or equivalently (2-16), written in a Schwarzschild background space-time is given by

$$- \partial_t^2 \varphi + \frac{g}{r^2} \partial_r [r^2 g \partial_r \varphi] - g \frac{L_{\theta, \varphi}(\varphi)}{r^2} - g \mu^2 \varphi = 0, \quad (6-2)$$

where we have assumed $r \neq 2M$ to avoid singular points and we have introduced the following definitions of the angular-momentum operator and the g function:

$$L_{\theta, \varphi}(\varphi) \equiv \frac{1}{\sin \theta} (\sin \theta \partial_{\theta} \varphi) + \frac{1}{\sin^2 \theta} \partial_{\varphi}^2 \varphi; \quad (6-3)$$

$$g(r) \equiv \left(1 - \frac{2M}{r}\right). \quad (6-4)$$

It is easy to realize that equation (6-2) is a separable equation with respect to time and space coordinates. Thus, it admits solutions of the form

$$\varphi(t, r, \theta, \varphi) = \phi(r, \theta, \varphi) e^{-i\gamma t}, \quad (6-5)$$

with an harmonic time dependence for an arbitrary frequency γ . Observe here that this harmonic dependence is equivalent to consider a stationary configuration, as we showed that it is needed for finding boson stars (see equation (2-31)). After plugging equation (6-5) into (6-2) we obtain

$$(\gamma^2 - g\mu^2) \phi + \frac{g}{r^2} \partial_r [r^2 g \partial_r \phi] - g \frac{L_{\theta, \varphi}(\phi)}{r^2} = 0. \quad (6-6)$$

The last equation is linear and admits solutions of the form

$$\phi(r, \theta, \varphi) = R_l(r) Y_l^n(\theta, \varphi), \quad (6-7)$$

where R_l is a function depending only on the radial coordinate r and the angular solution is given by the spherical harmonics Y_l^n for non-negative integers $l \geq |n|$. After using equation (6-4), the radial equation is given by

$$\mu^2 R_l - \frac{g}{r^2} \partial_r [r^2 g \partial_r R_l] + g \frac{l(l+1)}{r^2} - \frac{2M\mu^2}{r} R_l = \gamma_l^2 R_l, \quad (6-8)$$

where γ_l is the corresponding frequency for the solution with the integer l . Notice that the last term on the left-hand side in equation (6-8) becomes small far away from the SMBH's event horizon. In the case $2M\mu^2/r \rightarrow 0$, equation (6-8) turns into the free Schroedinger equation. This last point is rather important in what follows. The length-scale $2M\mu^2$ shall turn out to be a natural measure of the size of the configuration. Even though the scale of the SMBH is very different to that at which the galactic dynamics occurs, masses M for SMBHs give rise to $2M\mu^2 \sim \text{kpc}$. Moreover, since we are interested in describing the phenomenology occurring inside the central region of the SFDM halo, close to its edge at scales of few kpc, solutions of equation (6-8) in the regime where $r > 2M\mu^2$ are actually what we are looking for. In the following sections we are going to handle equation (6-8) in such a limit. Before doing so, we shall stop to analyse the spectrum of solutions arising for the range of parameters relevant for SMBHs.

6.2.1. About the eigenvalue problem for the Schwarzschild-Klein-Gordon system

For given masses of the SFDM and the SMBH, the spectrum of solutions has been determined numerically and semi-analytically in (Barranco et al., 2011, 2012). In these works, the

authors follow a standard procedure: they use convenient radial coordinates, so the KG equation can be transformed into a Schroedinger-like equation with a corresponding effective potential. They demonstrate that the frequencies of the solution cannot be larger than the depth of the well-potential (which is dubbed as ‘resonance band’). Besides, this is equivalent to the standard procedure of solving the Schroedinger equation analytically and to use boundary conditions to determine the full spectrum allowed at each physical setup. A similar analysis can be done by analysing the KG equation with parameters in a range of values corresponding to models for galactic soliton haloes. Here we follow such a procedure, including realistic values of the parameter $\alpha \equiv M\mu$, corresponding to realistic masses of SMBHs and assuming a mass of the SF $m_{22} = 1$ (see Table **6-1**).

For convenience, we can pick coordinates such that equation (6-8) takes a fully hyperbolic form; in the radial case we use the Regge-Wheeler tortoise coordinate defined as $r^* \equiv r + 2M \ln(r/2M - 1)$, such that (6-8) can be written as

$$-\partial_{r^*}^2 Q^l + V_{eff} Q^l = \gamma_l^2 Q^l, \quad (6-9)$$

where $Q^l \equiv rR^l$, and we have introduced an effective potential given by

$$V_{eff}(r; l, \mu, r_s) \equiv g(r) \left[\mu^2 + \frac{l(l+1)}{r^2} + \frac{2M}{r^3} \right]. \quad (6-10)$$

By solving exactly the eigenvalue problem established by equation (6-9), we would be able to determine the full spectrum of solutions allowed for this setup. However, in real galaxies, the SFDM halo coexists with stars and gas that might modify considerably the features of the system. For that reason, and for simplicity, we consider it is reasonable to set the characteristic length r_s of the solution as a free parameter, defined as the inverse of the wave-number k_s , i.e. $r_s \equiv 1/k_s$ (with $k_s^2 \equiv \gamma^2 - \mu^2$), and to determine an upper cut-off for k_s , denoted by k_s^{max} (see Table **6-1**). Let us now consider the spherically symmetric case with $l = 0$. For $m_{22} = 1$, the potential wells for realistic cases are quite shallow (as shown in Table **6-1** and Fig. **6-1**). As a consequence, even for the most massive BH observed so far, the resonance band is pretty narrow. This suggests that the spectrum of solutions is almost empty for the lightest BHs, and hence such solutions can be approximated as a single state with $\gamma \sim \mu^1$, as assumed (see also [Ureña-López and Liddle, 2002](#)).

¹For real scenarios, although $\gamma \sim \mu$ it should exist an infinite number of solutions that fulfill with the appropriate initial and boundary conditions. Those similar than what we found for multi-state boson stars. In that sense we could also define a multi-state SSFDM configuration. However, thanks to that the potential wells for real scenarios is very narrow we could say that the difference between each γ that fulfill the boundary conditions should be extremelly small and then, for sake of simplicity we assume that the complete system can be approximated by an unique state solution.

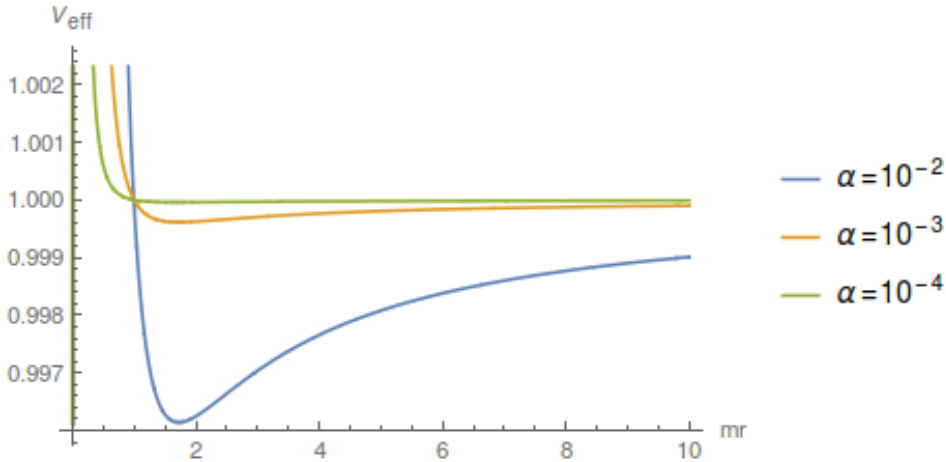


Figure 6-1.: The effective potential for the general Schwarzschild-Klein-Gordon equation for different values of the parameter α (Figure taken from (Avilez et al., 2018)). For configurations to form DM haloes hosting SMBHs, smaller values of α should be considered, and pretty shallow potentials arise. As a consequence, very large characteristic lengths r_s are expected, which is in agreement, at order of magnitude, with other values of r_s obtained from fits to rotation curves of galaxies (see e.g. Bernal et al., 2018).

M/M_\odot	α	k_s^{max}/μ	r_s^{min}/kpc
10^7	10^{-6}	8.8×10^{-4}	1.14
10^8	10^{-5}	2×10^{-3}	0.25
10^9	10^{-4}	6×10^{-3}	0.083
10^{10}	10^{-3}	2×10^{-2}	0.025
1.2×10^{10}	2.5×10^{-3}	3×10^{-2}	0.017
2.5×10^{10}	5×10^{-3}	4×10^{-2}	0.013
5×10^{10}	7.5×10^{-3}	5×10^{-2}	0.010

Table 6-1.: Maximum wave-numbers, k_s^{max} , and minimum characteristic lengths, r_s^{min} , of a single state solution of the SF of mass $m_{22} = 1$, for a range of parameters including typical observational masses of SMBHs. Quasi-bound states of the system have square frequencies laying in the resonance band ($V_{eff}(x^{min}), \mu^2$).

According to (Barranco et al., 2011, 2012), stationary modes with real frequencies $\gamma^2 > \mu^2$ do not exist. They found that the spectrum of solutions is continuous. The previous statement is in agreement with no-hair theorems. Furthermore, these modes do not decay at spatial infinity. If $0 < \gamma^2 < \mu^2$, then the modes have purely imaginary frequencies and they form a discrete set for which the amplitude inside the potential-well takes very large values when compared with the amplitude close to the horizon; for that reason they are called *stationary resonances* within the band $V_{eff} < \gamma^2 < \mu^2$. When the conditions of no-waves coming from the horizon and the requirement of spatial infinity decay are imposed, the spectrum of stationary resonances become discrete and complex. This set of solutions has been called *quasi-resonances* in the literature (Ohashi and Sakagami, 2004). Unfortunately,

both sorts of solutions are non-physical due to the conserved energy density corresponding to a Killing vector, which diverges at the horizon. Nevertheless, from numerical calculations, (Barranco et al., 2011) found healthier solutions dubbed as *dynamical resonances* with finite energy density in all regions. These solutions are damped oscillations driven by the SMBH and survive for very long times. The spectrum of such sort of solutions is the same than the stationary resonances. Actually, (Barranco et al., 2012) showed that the real part of the frequency of the quasi-resonant modes coincides with the frequency of oscillation of the stationary and dynamical resonances, and the imaginary part coincides with the decay rate of the dynamical resonances. Now, since within this scenario it is assumed that SMBHs are surrounded by quasi-resonances that are as long-lived as the Universe, we can assume they are stationary and then we can, as a first approximation, neglect the decaying part of the solution controlled by the imaginary part of the frequencies. In principle, k_s could be taken as a free parameter, however we argue that the range of its values is restricted by α . As mentioned above, k_s is allowed to take values below k_s^{max} . Because α takes such small values for typical galactic SMBH masses, the characteristic length is expected to be quite large.

Usually, within the models accounting for SFDM configurations as galactic solitons, the values for k_s run between 0.35 kpc^{-1} and 10 kpc^{-1} (Bernal et al., 2018, Robles et al., 2015). As we shall see below, the presence of a SMBH produces a considerable reduction in the size of the soliton compared to fits of SFDM models without SMBH.

6.2.2. The SFDM configuration far away from the black hole

In the following, we aim to study the behaviour of matter at regions far away from the SMBH, thus we need to solve equation (6-8) in the limit in which $2M/r \rightarrow 0$, that is

$$k_{s,l}^2 R_l + \frac{1}{r^2} \partial_r [r^2 \partial_r R_l] - \frac{l(l+1)}{r^2} + \frac{2M\mu^2}{r} R_l = 0. \quad (6-11)$$

This equation is valid for most of the central region of the SFDM halo, i.e. the region where a central soliton is expected. It must be stressed that the evolution of the SMBH and the galactic system lay in very different spatial scales. Even stars living in the deepest galactic regions, well inside the central halo, are parsecs away from the centre, while the Schwarzschild radius of the SMBH is one part in a million smaller. On one hand, $2M \sim 10^{-14} \text{ pc}$ for a solar mass and $2M \sim 10^{-6} \text{ pc}$ for a SMBH with $M \sim 10^{10} M_\odot$. On the other hand, typically the size of the central halo (the soliton) runs from 1 – 10 kpc.

By taking again the change of variable $Q_l \equiv r R_l$, equation (6-11) becomes

$$\partial_{rr} Q_l + k_{S,L}^2 Q_l - \frac{l(l+1)}{r} + \frac{2M\mu^2}{r} Q_l = 0. \quad (6-12)$$

For $l = 0$, which is sufficient for spherically symmetric soliton profiles, a solution is given by

$$\phi(r) = \phi_0 e^{-ik_s r} {}_1F_1 \left(1 - i \frac{M\mu^2}{k_s}, 2, i2k_s r \right), \quad (6-13)$$

where ϕ_0 is a constant and ${}_1F_1$ is the hyper-geometric function of order $(1, 1)$. From now on we shall refer to linear combinations of this sort of solutions as Schwarzschild SFDM (SSFDM) configurations. We shall analyse the features of the profiles arisen from this solution in detail in Section 6.4. Well inside the central halo it happens that $k_s r \ll 1$, therefore the solution approximates to

$$\phi \simeq \phi_0 (1 - M\mu^2 r) + \mathcal{O}[(k_s r)^2] + \mathcal{O}[(M\mu^2)^2]. \quad (6-14)$$

This profile is in agreement to that proposed in (Lee et al., 2015). For small radii inside the central halo, i.e. for $r \ll r_s$, still far away from the SMBH ($2M \ll r$), the profile remains constant. Still inside the soliton but closer to its edge ($r \sim r_s$), the profiles start decaying. In the next section we will show that the SMBH produces a driving effect on the SF halo solution, and the more massive it is more cuspy is the profile of the halo.

6.3. The driving effect of the black hole on the halo solution

Although equation (6-8) can be solved exactly and analytically, in this section we treat the problem perturbatively in order to have a more intuitive understanding of the effect that a SMBH exerts onto a bare SFDM solution. From equation (6-8) it can be noticed that the last term on the left-hand side is actually a perturbation to the KG equation in flat space for a region $r \gg 2M$. Thus we can split the SF into a bare solution plus a small perturbation induced by the SMBH:

$$\phi = \bar{\phi} + \delta\phi + \mathcal{O}(\mu^2), \quad (6-15)$$

being $\bar{\phi}$ the solution for the soliton in flat space-time given by equation (4-30), which is an exact solution of the KG equation for a SFDM perturbation², that corresponds to the galactic DM halo in the Newtonian limit found in the case of a temperature-corrected SF potential for $T \simeq 0$. As we already commented, the corresponding density profile coming from the linear combination of solution (4-30) for different values of k_s and $\bar{\phi}_0$ is dubbed as multistate SFDM.

By plugging equation (6-15) with solution (4-30) into (6-11), and setting $l = 0$, we obtain an ordinary differential equation for the perturbation given by

$$\delta R_{,rr} + k_s^2 \delta R = -\bar{\phi}_0 \frac{r_0}{r} \frac{\sin[(k_s + dk_s)r]}{r}, \quad (6-16)$$

²In fact the above is not the correct solution for the SFDM density profile given that it does not have a finite energy in all space. However, as it was showed in (Bernal et al., 2018, Robles et al., 2015), this solutions represent a very good approximation to the model and then, for simplicity, we decided to use this kind of solutions in our description.

that corresponds to a driven harmonic oscillator. Notice that the mass of the SMBH quantifies the amplitude of the external force which has the same functional form than the bare solution and has a wave-number $k_s + dk_s$; dk_s quantifies the closeness to the natural frequency of the oscillator: when $dk_s \rightarrow 0$, the corresponding solution is in resonance with the external force and its amplitude is enhanced. Equation (6-16) holds the following analytic solution:

$$\phi_{1s}^k = \bar{\phi}_{1s}^k \left(\frac{\mu}{k_s} \right)^2 \left(\frac{r_s}{r} \right) (Ci^{(-)} \cos k_s r - Si^{(+)} \sin k_s r), \quad (6-17)$$

where $Ci^{(-)} \equiv Ci[dk_s r] - Ci[(k_s + dk_s) r]$ and $Si^{(+)} \equiv Si[dk_s r] + Si[(k_s + dk_s) r]$ are the cosine and sine integral functions, respectively. From the behaviour of the $Ci^{(-)}$ and $Si^{(+)}$ functions, some physical information about the resonant solution can be extracted. Firstly, the bigger the mass of the SMBH is, the solution for the SF becomes more cuspy (see Fig. 6-2). As expected, when the frequency of the oscillator is equal to that of the driving force, the amplitude of the oscillator blows-up. This happens because we are considering an idealized situation in which the driving force is formed by a single state of the bare solution; however, a more realistic configuration would correspond to a driven force as a coherent package made of multiple bare solutions with different frequencies, laying within a frequency band of width dk_s . In such case, dk_s would never vanish and therefore the solution for the oscillator would never be purely resonant; in turn, while the driving force becomes narrower, the amplitude increases without blowing up. Nonetheless, for the purposes of this subsection, the idealized situation is enough to realize that the perturbative term due to the presence of a SMBH works as a driving force which produces enhancement of the amplitude of the solution of the SF. Fig. 6-2 shows solutions in this simple case with $dk_s \ll 1$ for different masses of the SMBH.

6.4. Dark Matter Mass and Density Profiles

As mentioned above, in this work we model the central region of a SFDM halo housing a SMBH. We assume that the observer is placed in a region far away from the SMBH in a radius smaller than the characteristic size of the halo; in such regime, the back-reaction of the SMBH and scalar dark matter can be neglected.. We model such a system by assuming that DM is described by a configuration of a complex SF laying in a Schwarzschild space-time. This framework is valid in the quasi-static limit in which the SMBH is already formed and it remains still without accreting any matter or gas. Within this regime, the velocity field of matter is affected by the SMBH presence only by means of the halo solution given by

$$\rho_\varphi \equiv \varphi \varphi^* = \rho_s \left| {}_1F_1 \left(1 - \frac{i\alpha\mu r_s}{2}, 2, i2x \right) \right|^2, \quad (6-18)$$

where the central density ρ_s is a free parameter and we have defined the dimensionless variable $x \equiv k_s r = r/r_s$. As expected the order of magnitude of the parameters involved

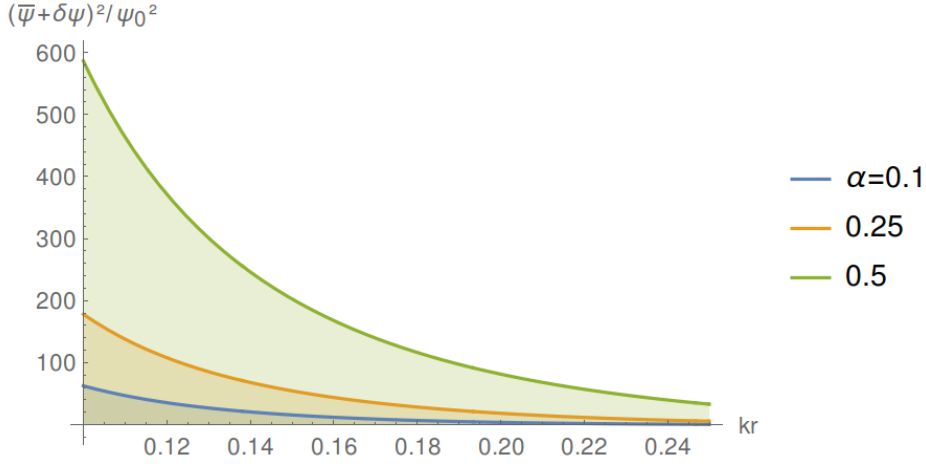


Figure 6-2.: Dimensionless solutions of the SF perturbed by a SMBH for different values of the α parameter. As the mass of the BH increases, the solution becomes more cuspy and its width decreases. This effect is produced by a driving force due to the presence of the SMBH (Figure taken from (Avilez et al., 2018)).

in the solution naturally coincides with typical sizes of cores in observed galaxies: for an ultra-light SF with mass $m_{22} \sim 1$ we have $\mu^{-1} \sim 0.5$ pc and for a SMBH with mass $M \sim 10^{10} M_{\odot}$, $(M\mu^2)^{-1} \sim$ kpc. Taking advantage of these scaling relations, we choose the following parametrization for the characteristic length r_s of the solution:

$$r_s = \frac{\eta}{\alpha\mu}, \quad (6-19)$$

where we introduced η as free parameter that scales r_s in units of $(M\mu^2)^{-1}$. Using this parametrization, the dimensionless SSFDM density of the SF configuration reads as

$$\hat{\rho}_{\varphi}(x; \eta) \equiv \frac{\rho_{\varphi}(x; \gamma)}{\rho_s} = \left| {}_1F_1 \left(1 - \frac{i\eta}{2}, 2, i2x \right) \right|^2, \quad (6-20)$$

that we show in Fig. 6-3 for different values of η . In this way, we define conveniently the dimensionless DM density profile as a function of the dimensionless variable x , parametrized with a single free parameter η .

As it can be seen in Fig. 6-3, as η increases, the point where the density profile maximizes, r_{max} , shifts apart from the centre. Therefore, below such radius DM is not as dense as in an intermediate region. This can be interpreted as follows: an initially core-like profile of DM turns into a dough-nut-like configuration when it interacts with a relativistic particle placed at the centre. This suggests that the largest amount of DM does not concentrate at the centre. At this point, we have not determined the value of the central density, thus we cannot quantify the mass of DM. Nonetheless, we can imply there is a region off the centre of the galactic disk concentrating more DM than in the centre for a fixed value of r_s .

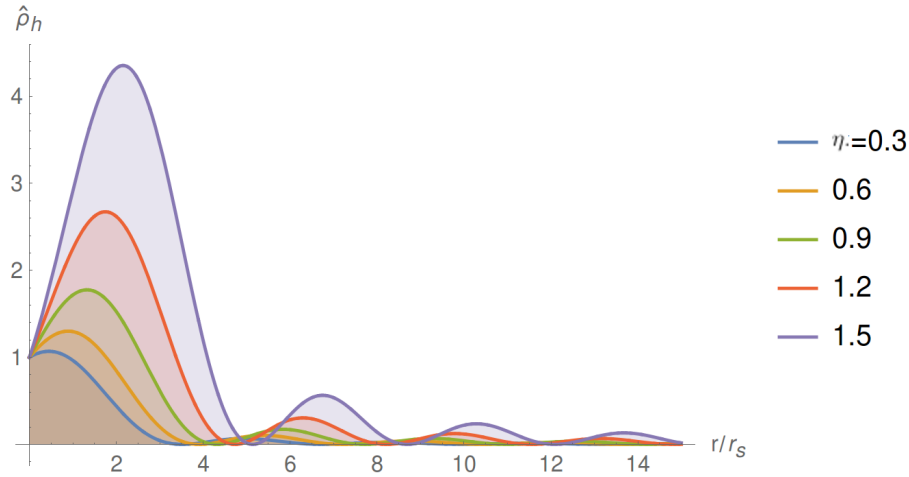


Figure **6-3**.: Dimensionless radial density profile for the SF configuration for different values of the parameter $\eta \equiv \mu^2 M r_s$. The configuration takes its peak closer to the galactic centre as its characteristic size r_s increases for a fixed value of the SMBH mass M ((Figure taken from (Avilez et al., 2018))).

From integrating out the density profile (6-20) within a given radius, we obtain the radial mass density profile for the halo as

$$M_\varphi(r) = \int_0^r \rho_\varphi(r) r^2 dr = r_s^3 \rho_s \hat{M}_\varphi(x), \quad (6-21)$$

where we have defined the dimensionless mass profile as

$$\hat{M}_\varphi(x) \equiv \int_0^{r/r_s} \hat{\rho}_\varphi(x) x^2 dx. \quad (6-22)$$

At this point, the only information we have about the values of the free parameters of these profiles, r_s and ρ_s , (or alternatively ρ_s and η) has been extracted from the condition of the existence of bound-solutions in the KG equation determined by the structure of the effective potential (6-10). As a consequence, a lower bound for r_s is established by boundary conditions, which is in agreement with results from (Lee et al., 2015):

$$\rho_s \sim \alpha. \quad (6-23)$$

However, the remaining indetermination is going to be removed by using information from some universal features of galaxies. In the next sections, we shall reduce the space of parameters of our model by imposing a relation between the value of the central SFDM density and η . We achieve this by assuming the universal maximal acceleration (UMA) of DM particles, recently reported in (Ureña-López et al., 2017). In Section 6.6, in order to have a rough estimate of r_s , we use the observed correlation between the mass of the SMBH and the velocity dispersion of baryonic matter in galaxies.

6.5. Constraint on the central DM density from the mass discrepancy-acceleration relation

Recently, it has been shown from the observed rotation curves of 153 galaxies from the SPARC (Spitzer Photometry & Accurate Rotation Curves) database (Lelli et al., 2016), including galaxies with very different features and morphologies with high-resolution gas and stars information, that the acceleration inferred from the observations strongly correlates with the acceleration due to the baryonic matter, showing a mass-discrepancy at the value $g^\dagger = 1.2 \times 10^{-10} \text{ m/s}^2$ (Lelli et al., 2017, McGaugh et al., 2016). Such mass discrepancy-acceleration relation (MDAR) can be interpreted as a correlation between the baryonic and the DM, and moreover, the maximum radial acceleration purely produced by baryonic matter and that of DM are closely related, and in the case that DM particles exist, the maximum radial acceleration they can reach in all haloes, g_φ , cannot be greater than the UMA value given by (Ureña-López et al., 2017)

$$g_\varphi^{max} = 0.65g^\dagger = 7.8 \times 10^{-11} \text{ m/s}^2. \quad (6-24)$$

On the other hand, the acceleration profile comes as a theoretical prediction for every model and its maximum value should be restricted by the last value. In our case, specific values of the parameter ρ_s for the SFDM density profile (6-18) (given a mass M of the SMBH) are required in order to predict the UMA value (6-24). The modulus of the radial acceleration profile for the bosons forming the halo can be computed in terms of the mass profile as follows:

$$g_\varphi(r; \eta, \alpha) = \frac{GM_\varphi(r; \eta, \alpha)}{r^2}, \quad (6-25)$$

which in terms of the dimensionless mass profile (6-22) and the dimensionless independent variable x can be easily rewritten as

$$\begin{aligned} g_\varphi(r; \eta, \alpha) &= G r_s \rho_s \frac{\hat{M}_\varphi(x)}{x^2}, \\ &= G \mu_\varphi \hat{g}_\varphi(x; \eta), \end{aligned} \quad (6-26)$$

where we have defined the dimensionless acceleration profile as

$$\hat{g}_\varphi(x; \eta) \equiv \frac{\hat{M}_\varphi(x; \eta)}{x^2}, \quad (6-27)$$

and we used the surface density definition given in (Ureña-López et al., 2017):

$$\mu_\varphi \equiv r_s \rho_s. \quad (6-28)$$

By imposing the constraint (6-24) over the theoretical maximum of the acceleration profile, we obtain a value for the halo's central surface density given by

$$\mu_\varphi = \frac{0.65 g^\dagger}{G \hat{g}_\varphi^{\max}(\eta)}, \quad (6-29)$$

and consequently the central value for the density profile is

$$\rho_s = \alpha \frac{\rho^\dagger}{\eta \hat{g}_\varphi^{\max}(\eta)}, \quad (6-30)$$

where

$$\rho^\dagger = \frac{0.65 \mu g^\dagger}{G} = 0.807 \times 10^3 \frac{M_\odot}{\text{pc}^3}. \quad (6-31)$$

for $m_{22} = 1$. Notice that relation (6-30) is consistent with the boundary condition (6-23).

In (Ureña-López et al., 2017), using the UMA value for DM profiles, solutions of the Schroedinger-Poisson system (valid at the Newtonian limit only), they conclude that the central surface density μ_φ is a universal constant. In the context of the ultra-light SFDM model, for the so-called fuzzy or wave DM soliton profile (Schive et al., 014a), $\mu_\varphi = 648 M_\odot \text{pc}^{-2}$. This result brings as a consequence that the Wave DM soliton profile should be a universal feature of the SFDM haloes. However, in the context of this work, where central SMBHs in galaxies manifestly affect the DM profile in the core and also the central density, while it is true that g_φ^{\max} is a constant, from equation (6-29) it is clear that the central density μ_φ is not necessarily constant. Rather, it obeys the following implicit relation between ρ_s and r_s :

$$r_s \rho_s - \mu_\varphi(\eta \equiv M \mu^2 r_s) = 0. \quad (6-32)$$

Therefore, the universality of the Wave DM soliton profile for galaxies hosting a SMBH not necessarily holds unless $M \mu^2 r_s = \text{constant}$. Two interesting points arise from this last conclusion: Firstly, haloes of galaxies with not-too-massive BHs in their centres nearly satisfy $M \mu^2 r_s = 1$. This can be realized using the analysis made in Subsection 6.2.1, where we saw that for small masses $k_s \rightarrow 0$, the SF profile can be described by the Ureña-Liddle solution (Ureña-López and Liddle, 2002), for which r_s can be read off as $(M \mu^2)^{-1}$. Secondly, assuming the UMA value (6-24) actually holds, in the case of observing galaxies that violate the universal Wave DM soliton profile, variations to the constraint (6-32) can be owed either: i) to the influence of baryons on the solitonic halo through gravity, or ii) to the influence of a SMBH at the centre of such galaxies. Consider we were studying the features of a SFDM halo for an specific galaxy and from fits of its rotation curve, or another observation, it turns out that μ_φ differs from the universal value proposed in (Ureña-López et al., 2017); therefore, we could set as a possibility the existence of a SMBH at its centre and, from the inferred value of μ_φ , the mass of the SMBH can be estimated.

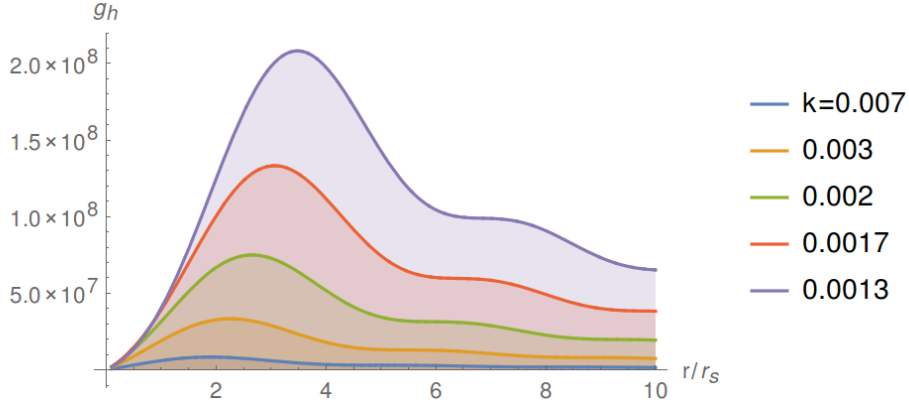


Figure 6-4.: For a fixed mass of the SMBH $M \sim 10^{10} M_{\odot}$, the radial acceleration profile $g_{\varphi}(\eta(k_s))$ is plotted for different wave-numbers k_s of the solution ((Figure taken from (Avilez et al., 2018))).

In order to completely fix the central density of our SFDM profiles we still need to fix r_s (or η). In Section 6.6 we shall determine r_s by fitting the observed correlation between the mass of the SMBH and the velocity dispersion of baryonic matter inside the stellar bulge (see e.g. Ferrarese and Merritt, 2000). However, at this point, we are able to set some restrictions over ρ_s from theoretical grounds. The following subsection is devoted to that purpose.

6.5.1. Theoretical upper bound for the central density of the SFDM configuration

In Subsection 6.2.1 we derived an upper bound for the wave-number k_s of the solutions of the Schwarzschild-Klein-Gordon system, for a range of values of the SMBH mass (see Table 6-1). Here, we derive the values of the central SSFDM density profile from the UMA constraint (6-24), by using the procedure explained at the beginning of Section 6.5.

For a fixed value of the mass of the BH, M , the theoretical radial acceleration strongly depends on r_s (or k_s), as Fig. 6-4 shows. As the value of k_s increases, g_{φ}^{max} decreases, and together with equation (6-30), we can see that $\rho_s(\alpha, \eta(k_s^{max}))$ increases. Therefore, for a fixed M , the value $\rho_s(\alpha, \gamma(k_s^{max}))$ is an upper bound for all its possible values.

Let us denote such maximum value for the central density as $\rho_{max}^{\alpha} \equiv \rho_{\varphi}(x = 0; \eta = M\mu^2 r_s^{min})$, in order to distinguish these values purely associated to theoretical quantities from those corresponding to a generic r_s , which are going to be inferred from observations later. The top panel of Fig. 6-5 shows the correlation between the parameter α (that quantifies the mass of the SMBH for a fixed mass of the SFDM) and its corresponding central density for the minimal value of r_s allowed. According to this relation, the intuitive and ideal picture drawn in Section 6.3 is correct: the larger the mass of the central SMBH is, the denser is the surrounding SFDM configuration (see the bottom panel of Fig. 6-5). This would be actually true if nature would choose $r_s^{min} = 1/k_s^{max}$; however, the complexity of baryons in real galaxies is mostly likely to mess up such assumption. Nonetheless, it gives us an idea of

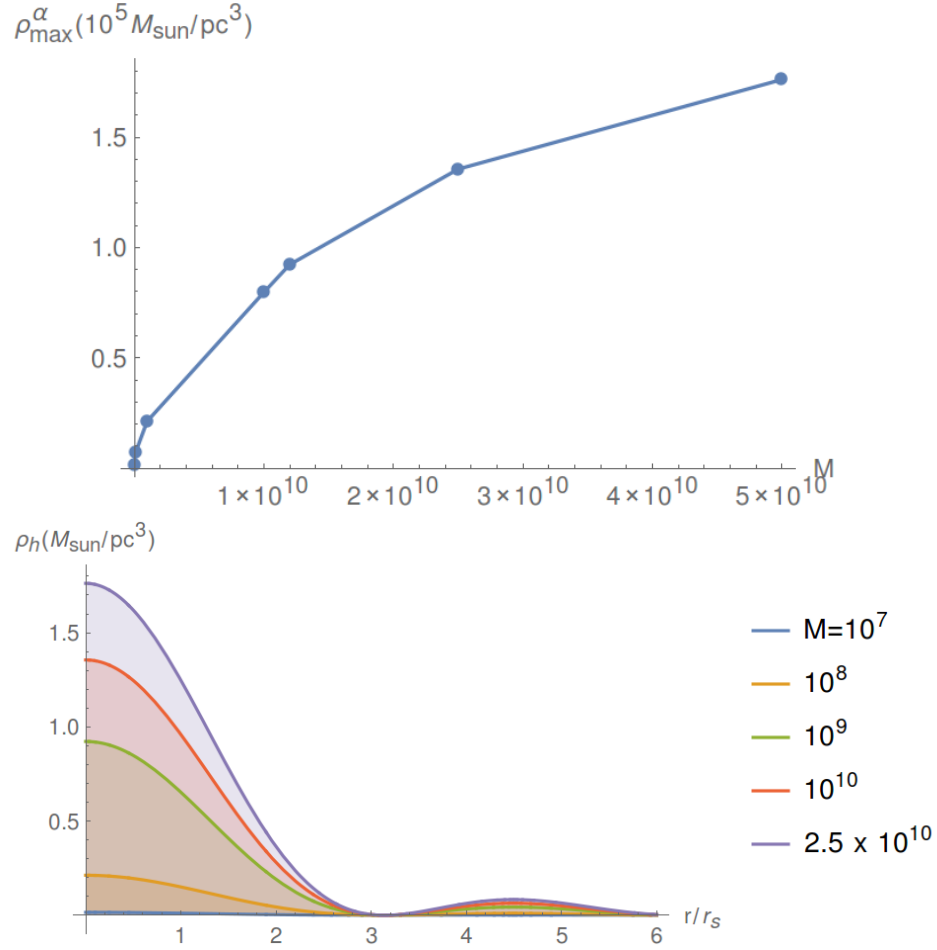


Figure 6-5.: Top panel: Upper bounds for the central density values ρ_{\max}^{α} as function of the mass M of the SMBH. These values are obtained for SF profiles fixing the characteristic length as $r_s^{\min} = 1/k_s^{\max}$. Bottom panel: Density profiles for different values of M and $r_s^{\min}(M)$. As expected, the halo is denser at the centre for more massive SMBHs; effectively, the SMBH increases the height and shrinks the length of the SF profile. This is in agreement with results from our toy model discussed in Section 6.3 (Figure taken from (Avilez et al., 2018)).

how the haloes would ideally be without baryons, also it sets up some restrictions over the central density.

6.6. Kinematics of visible matter inside the gravitational potential of the SFDM halo

In practice, the mass of a SMBH is derived from measurements of different features of the velocity field of stars and gas moving along the gravitational well-potential produced by the whole system formed by the dark matter halo, stars, gas and the SMBH. From theoretical grounds, the procedure goes the other way round: we assume a SMBH fully specified by its

mass and we derive some kinematic features of the velocity field of the system. In this Section our goal is to give an estimate for the free parameters of our SFDM model in concordance with some observational features of galaxies. This shall serve us to test at which extent our formalism is capable to describe the central regions of haloes laying in a space-time considerably influenced by the presence of a SMBH. As a first step, we shall use the UMA constraint (6-24) (Ureña-López et al., 2017) to reduce the space of parameters. Similarly as we did at theoretical level in Section 6.5.1 by bounding the values of the central density, the UMA constraint provides a relation between ρ_s and r_s . As a second step, in order to obtain an estimate of the remaining free parameter r_s , we compute the baryonic stellar velocity dispersion by solving the Jeans equation for different values of the mass of the SMBH. For each value of M , we derive an estimate of r_s that gives rise to the target value of the velocity dispersion σ^* reported in (McConnell and Ma, 2013). We carry out such procedure in two cases:

- 1) In Subsection 6.6.2 we assume the gravitational pull of DM is dominant. We dub such case DMD. Here, the velocity dispersion of baryons only depends on the DM parameters and the ratio of r_s and the effective radius associated to the stellar density profile. In this idealized case, as a first result, we obtain a correlation between r_s and the mass of the SMBH. This allows us to derive, as a complementary result, the central surface density profile μ_φ of SFDM as function of η , which is a generalization of the main result from (Ureña-López et al., 2017) for DMD galaxies hosting SMBHs. This idealized case may be applicable to ultra-compact dwarf (UCD) galaxies, which are claimed to possibly host SMBHs and it is assumed that they host a small amount of baryons, as inferred from their poor luminosities (Ahn et al., 2017, Drinkwater et al., 2000). Additionally, we consider that this description should be equivalent to what should be obtained if we had used the model provided in (4-26), instead of the generalization of (4-30).
- 2) In Subsection 6.6.3 we study the second case LGAL, in order to consider large galaxies. We consider that the gravitational influence of both baryons and DM described by the SSFDM model is important³. We must point out here that, since we are using a Schwarzschild geometry of space-time a priori, we are ignoring the feedback of baryons and the SF itself on the solution of the SFDM profile, and therefore the formalism used in these cases only provides a rough description of the system. However, the results are still useful to compare with other estimates arisen from similar models of DM within the regime of applicability, in order to figure out possible effects due to the presence of a SMBH.

In both cases we consider an elliptical shape for the baryons distribution. In the second case, our formalism is valid to describe massive, dispersive and early-type galaxies and bulges

³We assume the gravitational influence of the SMBH only happens through the DM solution.

of late-type galaxies. We take as cases of study specific real elliptical galaxies and bulges.

6.6.1. Visible matter in the galaxies and the Jeans equation

Because we are assuming spherical symmetry, our model predicts that stars only move along the radial direction. The stellar spatial distribution is fully described by the distribution function $f(r, v)$, which is the probability of finding a star at radius r with velocity v . This distribution satisfies the Boltzmann equation and once it is known, all the macroscopic statistical quantities associated to the visible part of the galaxy can be determined. However, to determine such distribution is not straightforward, and sometimes it is not even necessary to compute some observables, as it happens with the stellar velocity dispersions⁴, σ_* , which obey the Jeans equation. This relation can be derived from the Boltzmann equation in the case that stars in the system are non-collisional and when spherical symmetry is imposed, and is given by (Binney and Tremaine, 2008)

$$\frac{1}{\rho_*(r)} \frac{d(\rho_* \sigma_*^2)}{dr} + \frac{2\beta \sigma_*^2}{r} = -\frac{GM_{tot}(r)}{r^2}, \quad (6-33)$$

where ρ_* is the stellar density profile and β the anisotropy parameter that we shall ignore since, even in the more complex cases, it modifies the results no more than 5% (Binney and Tremaine, 2008, McConnell and Ma, 2013). The total mass of the galactic system, M_{tot} , is defined by

$$M_{tot}(r) = M_{bar}(r) + M_\varphi(r), \quad (6-34)$$

where M_{bar} and M_φ are the mass of the baryons (gas and stars) and the SFDM, respectively, enclosed inside a given radius r . The left-hand side of equation (6-33) corresponds to kinematic terms of the visible matter, while the right side involves the dynamical sources that produce the galactic well-potential that triggers the kinematics.

In this work we assume M_{bar} can be described by the Plummer density profile, which is typically used to describe stars in galactic bulges, but also for elliptical and dwarf galaxies (see e.g. Walker et al., 2009). For this profile, the radial density distribution of stars is given by

$$\rho_*(r) = \frac{\rho_*^0}{[1 + (r/R_{eff})^2]^{5/2}}, \quad (6-35)$$

where $\rho_*^0 \equiv 3M_*^{tot}/(4\pi R_{eff}^3)$ is the stellar central density and M_*^{tot} is the mass of stars enclosed within the effective radius R_{eff} , which is defined as the radius at which the luminosity of the galaxy decreases to a half of its central value. The corresponding Plummer mass profile M_*

⁴The stellar velocity dispersion is defined as the square root of the standard deviation of the velocity probability distribution: $\sigma_*^2 \equiv \int_V f(x, v)(v - \bar{v})^2 d^3x d^3v$, where \bar{v} is the mean radial velocity.

is obtained by integrating the density profile (6-35) within a radius r . The dimensionless Plummer mass profile of stars, \hat{M}_* , is defined as

$$\hat{M}_*(r) \equiv \frac{M_*(r)}{M_*^{tot}} = \frac{(r/R_{eff})^3}{[1 + (r/R_{eff})^2]^{3/2}}. \quad (6-36)$$

6.6.2. Determining the SSFDM characteristic length from the ‘M sigma’ relation for the DMD case

The mass of visible matter in galaxies is an important parameter to consider in order to understand the co-evolution of the SMBH, the SFDM halo and the messy system of stars and gas. Real galaxies hosting SMBHs usually contain an important fraction of visible matter in-falling into the gravitational well-potential and, thanks to such component, these objects can be detected. In the next subsection we shall take into consideration the gravitational contribution of baryons into the Jeans equation for very specific luminous galaxies. However, in this subsection we start considering a simpler idealized case, that is, an hypothetical system where the gravitational well-potential is mainly produced by the SF configuration forming the DM halo.

Here we model the baryonic distribution using the Plummer profile (6-35) assuming a spherical system. The parameters of this profile have been well tested and it can be used to model systems of different sizes and luminosities (Walker et al., 2009). As mentioned before, this case may be applied and tested in the future in UCD galaxies (Ahn et al., 2017). In this respect, we must to mention that, at the date, there is not enough information to realize whether UCDs are actually galaxies or compact clusters (Drinkwater et al., 2000). For that reason, not even information about the stellar kinematics is still available. Although this sort of systems need to be further investigated, at the moment we cannot exclude the possibility of the existence of these old galaxies. From the theoretical point of view (Barranco et al., 2011, 2012, Escorihuela-Tomas et al., 2017), it is reasonable to expect the existence of these systems at some point when all baryons have been accreted, let us recall that in these models DM decays much slower than baryons.

The Jeans equation (6-33) in this case reads

$$\frac{1}{\hat{\rho}_*(r)} \frac{d(\hat{\rho}_* \sigma_*^2)}{dr} = - \frac{GM_\varphi(r)}{r^2}. \quad (6-37)$$

Notice that M_*^{tot} is not a free parameter any more. The last equation is equivalent to

$$\sigma_*^2(r) = \frac{1}{\hat{\rho}_*(r)} \int_0^r \frac{GM_\varphi(r') \hat{\rho}_*(r')}{r'^2} dr', \quad (6-38)$$

where $\hat{\rho}_* \equiv \rho_*/\rho_*^0$. The last equation, written in terms of dimensionless quantities, turns into

$$\sigma_*^2(x) = \frac{G\rho^\dagger}{\mu^2\alpha} \frac{\eta}{\hat{g}_\varphi^{max}(\eta)} \frac{1}{\hat{\rho}_*(x, a)} \int_0^x \frac{\hat{M}_\varphi(x', \eta) \hat{\rho}_*(x', a)}{x'^2} dx', \quad (6-39)$$

where we have redefined the Plummer profile in terms of the dark-to-visible-size ratio, $a \equiv r_s/R_{\text{eff}}$, as

$$\hat{\rho}_*(x, a) \equiv \frac{1}{(1 + a^2 x^2)^{5/2}}. \quad (6-40)$$

It is worth to notice that equation (6-39) results to be a product of a term depending only on η and other only depending on α . The square of the stellar velocity dispersion evaluated in the effective radius is given by

$$\sigma_*^2(R_{\text{eff}}) = \frac{(v^\dagger)^2}{\alpha} \sigma_{(a)}^2(\eta), \quad (6-41)$$

where we have introduced the SFDM characteristic velocity v^\dagger and the dimensionless quantity $\sigma_{(a)}^2(\eta)$ depending on the value of a as

$$(v^\dagger)^2 \equiv \frac{0.65 g^\dagger}{\mu} = 1.209 \times 10^6 \text{ m}^2 \text{ s}^{-2}, \quad (6-42)$$

$$\sigma_{(a)}^2(\eta) \equiv \frac{\eta}{\hat{g}_\varphi^{\text{max}}(\eta)} \frac{1}{\hat{\rho}_*(1/a)} \int_0^{1/a} \frac{GM_\varphi(x', \eta) \hat{\rho}_*(x', a)}{x'^2} dx'. \quad (6-43)$$

Notice that the square of the actual velocity dispersion is just a rescaling of equation (6-43) which exclusively depends on α and the mass of the SF, μ . The last point is interesting because, unlike other observables, the dependences on α and μ in $\sigma_{(a)}^2$ are separated and hence they are not degenerated. In Fig. 6-6, $\sigma_{(a)}^2$ is plotted for some values of the dark-to-visible-size ratio a , for a fixed mass M of the SMBH. Notice that as the size of the halo increases in relation to the size of the bulge, the whole velocity dispersion profile is suppressed. Now, as it can be noticed from the integral in equation (6-43), the stellar density profile serves as a weight of the radial acceleration profile, therefore, the larger a is, such weight becomes steeper and the integrand falls down at smaller radius. This suggest a connection between baryons and their hosting SSFDM haloes, this is, for fixed M and R_{eff} , visible matter in galaxies is less dispersive if it is embedded in larger haloes. Besides, for a given M , visible matter has larger maximum velocity dispersions if the dark-to-visible matter ratio is smaller, as shown in Fig. 6-6. This means that, in this model, the presence of baryons in the central galactic region enhances the velocity dispersion of stars.

Let us turn to find the values of the characteristic size of the halo, r_s , such that, for a given value of M , we can reproduce the value of σ_* given by the relation

$$\log_{10} \left(\frac{M}{M_\odot} \right) = \alpha + \beta \log_{10} \left(\frac{\sigma_*}{200 \text{ km s}^{-1}} \right). \quad (6-44)$$

The previous equation corresponds to the best fit of measurements of M and σ_* of a host of galaxies within three main samples: early and late-type galaxies, and the full sample considering both types (McConnell and Ma, 2013). The resulting parameters and errors of the $M - \sigma_*$ relation for different samples are summarized in Table 6-2.

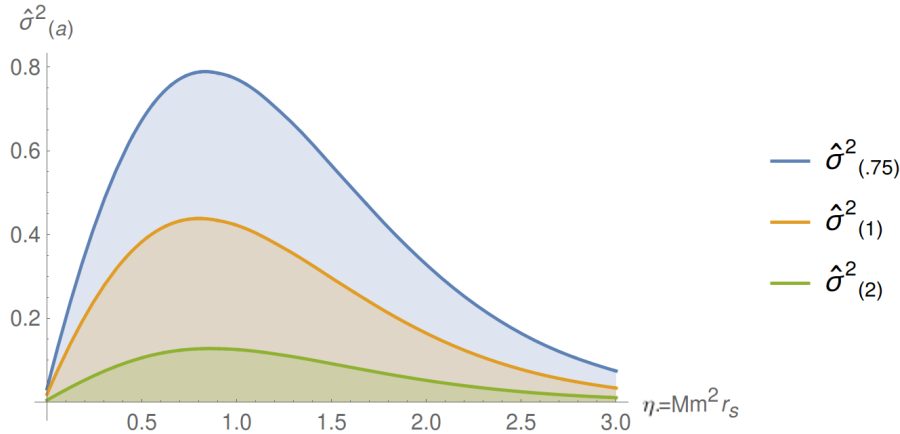


Figure 6-6.: Dimensionless velocity dispersion $\hat{\sigma}_{(a)}^2$ as function of η for different values of a . If the size of the halo increases in relation to the size of the bulge, the velocity dispersion profile is suppressed (Figure taken from (Avilez et al., 2018)).

type	α	β
early	8.07 ± 0.21	5.20 ± 0.36
late	8.39 ± 0.06	5.06 ± 1.16
full sample	8.32 ± 0.05	5.64 ± 0.32

Table 6-2.: Parameters for the $M - \sigma_*$ relation for samples of different classes of galaxies.

We constructed a set of bins of values of M running from $10^6 M_\odot$ to $10^8 M_\odot$, and for each bin we use the prescription explained above to compute σ_* by solving equation (6-39). In our procedure we set $a = 1$, that is, $r_s = R_{eff} \sim \text{kpc}$. We tried different values of η and picked the one that best reproduced the value of σ_* associated to M by relation (6-44). Fig. 6-7 shows theoretical curves of σ_* as function of η corresponding to different masses M of the SMBH; the points correspond to the picked values reproducing the observational value of σ_* along with the error bars corresponding to each sample. The resulting values of the characteristic length from this procedure are summarized in Fig. 6-8.

An important result of this subsection is that models with values of $a \geq 1$ fail to reproduce σ_* from equation (6-44) for masses $M > 10^8 M_\odot$; however, the results change for $a < 1$. This is important since it tells us that within the DMD model, only systems with $R_{eff} > r_s$ are able to reproduce the observed stellar velocity dispersion for a limited range of values of M . However, this scenario falls out of the regime of validity of DMD. Therefore, we can conclude that for DMD systems (with $a \geq 1$) the phenomenological σ_* can only be reached for BHs with masses up to $M \sim 10^8 M_\odot$ at most ($a = 1$) within the model, assuming that the gravitational field of DM is dominant (see Figs. 6-7 and 6-9). Equivalently, this is consistent with the following: i) large SMBHs live in visible-matter-dominated galaxies and ii) in hypothetical DMD systems –like UCD galaxies might be– SMBHs could be found with masses of $M \sim 10^8 M_\odot$ at most or without a SMBH.

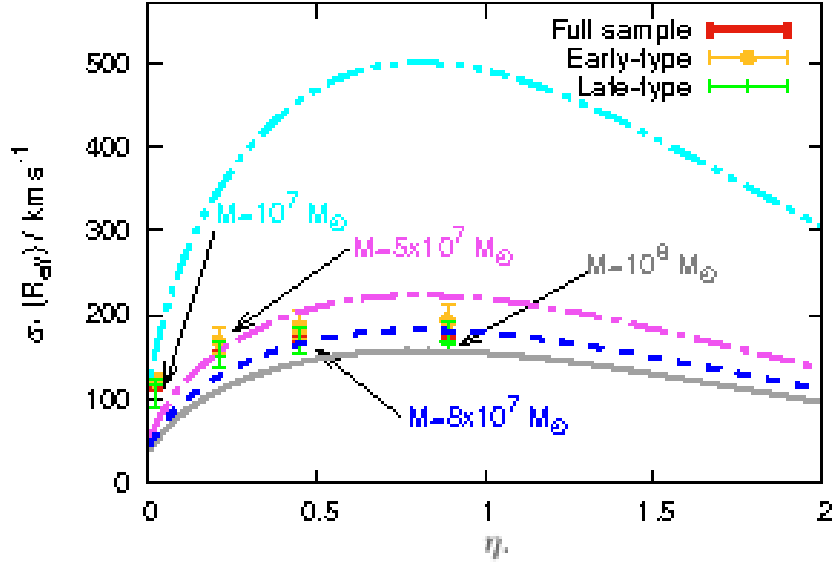


Figure 6-7.: Lines correspond to theoretical $\eta - \sigma_*$ curves for different values of the SMBH mass: $M = 10^7 M_\odot$ (double-dot-dashed), $M = 5 \times 10^7 M_\odot$ (dot-dashed), $M = 8 \times 10^7 M_\odot$ (dashed) and $M = 10^8 M_\odot$ (solid). The points with error bars correspond to picked values of η that satisfy the phenomenological $M - \sigma_*$ relation (6-44) for different samples of galaxies. Notice that the solid line corresponding to $10^8 M_\odot$ barely reaches the observed σ_* for the late-type sample (Figure taken from (Avilez et al., 2018)).

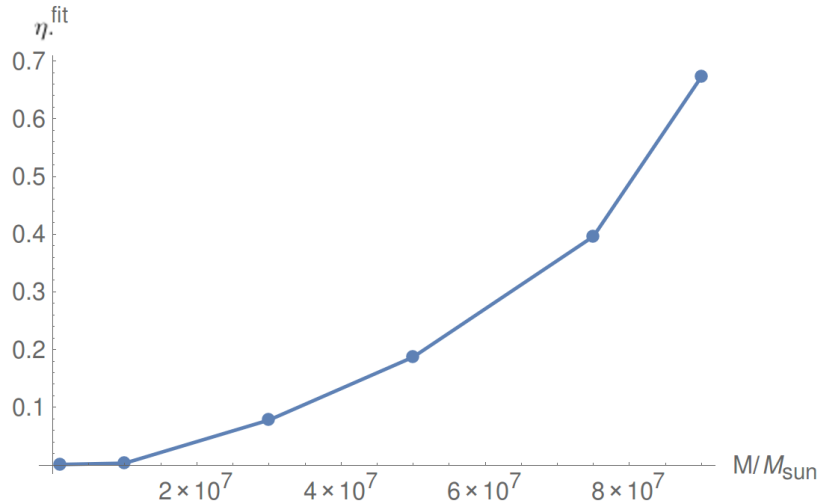


Figure 6-8.: Scaling relation between the fit for η characterizing the size of the SSFDM halo and the mass of the hosted SMBH for DMD systems. This relation is derived from fitting the observed $M - \sigma_*$ relation (Figure taken from (Avilez et al., 2018)).

A complementary result of this work is the corresponding constraint (6-32) for values of r_s shown in Fig. 6-8. As mentioned before, unlike the standard SFDM profiles, in the

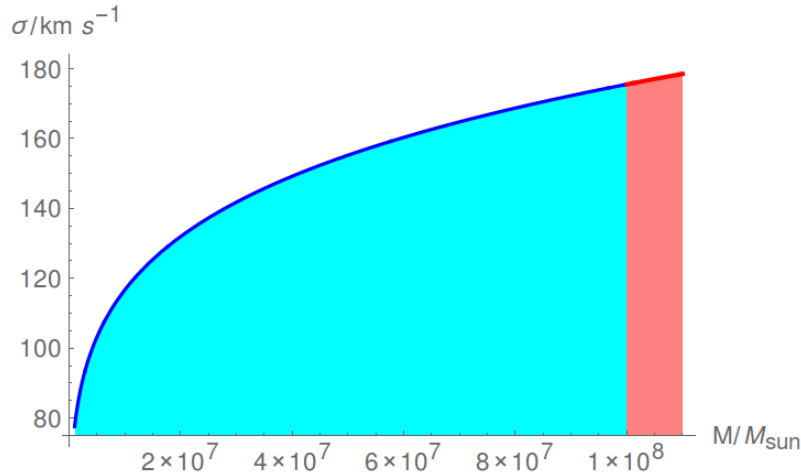


Figure 6-9.: Empirical $M - \sigma_*$ correlation (McConnell and Ma, 2013) for a full sample of early and late-type galaxies. The DMD regime within SSFDM can be only applied for SMBH with masses within the blue region (Figure taken from (Avilez et al., 2018)).

case of SSFDM profiles μ_φ is not a constant, rather, as Fig. 6-10 shows, it depends on the parameter $\eta = M\mu^2 r_s$. In SFDM models within the Newtonian regime, the constancy of μ_φ , along with some scaling relations of the parameters, bring up an important prediction for these models: the existence of a universal soliton-like profile in the central halo (Ureña-López et al., 2017). In satellite dwarf galaxies of the Milky Way, which are the closest to pure DM systems known at the date, this property would mean having a common mass around $10^7 M_\odot$ at 300pc which seems to have a strong observational support (Strigari et al., 2008). Here, when the influence of a SMBH on the DM profile is considered, the result of $\mu_\varphi \neq \text{constant}$ implies that the soliton behaviour is altered and then the mass at $r \ll 300\text{pc}$ is expected to be different depending on the mass of the guest SMBH.

6.6.3. Determining the SSFDM characteristic length from the ‘M sigma’ relation for a Sample of Luminous Galaxies

As mentioned above, in a similar way than for the previous case, in this subsection we aim to obtain estimates of the free parameters of the SSFDM profiles according to observations in the central regions of some large galaxies hosting SMBHs. Unlike subsection 6.6.2, in which an idealized case is considered, here we model six real, luminous and baryon dominated galaxies (enlisted in Table 6-3). We refer this instance as LGAL, a case which technically differs from the DMD one studied in Subsection 6.6.2, since we take into consideration the full gravitational pull of baryons and DM into the Jeans equation. As mentioned above, although our models are far from being realistic approaches to the complex non-linear systems forming real large galaxies, the results in this subsection are obtained from observations from central galactic regions and it would be helpful to compare them with other estimates arisen in other

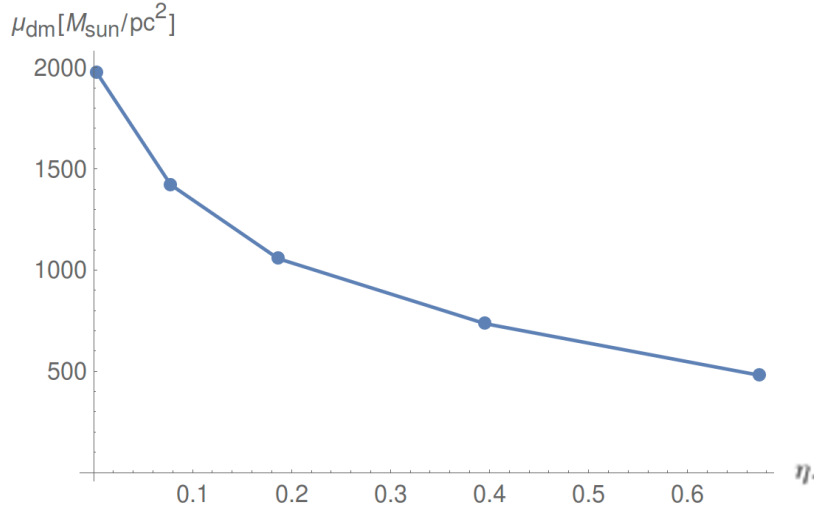


Figure 6-10.: Surface density for several values of η . As expected in this model, this quantity is not a constant, in contrast to that from SFDM models (Figure taken from (Avilez et al., 2018)).

SFDM models used to describe external galactic regions, like the multistate SFDM model (see equation (4-30)).

We solved numerically the equation (6-37) using the Plummer mass profile to model the visible matter contained in spherical systems and the mass profile corresponding to SSFDM described before for different elliptical galaxies hosting SMBHs in their centres. The corresponding parameters for each galaxy are enlisted in Table 6-3; they were extracted from catalogues in (McConnell and Ma, 2013) and (Larkin and McLaughlin, 2016). On the other hand, in (Larkin and McLaughlin, 2016), a correlation between the stellar total mass and the effective radius is reported and they infer the mean-stream trend in different galaxies by means of the following phenomenological relation:

$$R_{eff}/\text{kpc} = 1.5 \times \bar{M}^{0.1} (1 + \bar{M}^5)^{0.1}, \quad (6-45)$$

where $\bar{M} \equiv M_*^{tot}/2 \times 10^{10} M_\odot$. We used this result in order to estimate the effective radius of some galaxies in our catalogue (Table 6-3) labelled with †. Such table also summarizes the parameters used to solve the Jeans equation for each case.

After reducing the space of parameters using the UMA constraint derived in subsection 6.5.1, we determined the characteristic length of the haloes corresponding to each galaxy in our catalogue such that, along with the other parameters of baryons in Table 6-3, the velocity dispersion σ_* from (6-44) is obtained. Once the set of points in the $r_s - \sigma_*$ space were determined, a clear correlation between both parameters is observed which can be described by the following law:

$$\frac{\sigma_*(R_{eff})}{\text{km s}^{-1}} = 109.0 + 38.4 \times \left(\frac{r_s}{\text{kpc}} \right). \quad (6-46)$$

Galaxy	M_{BH}/M_{\odot}	M_*^{tot}/M_{\odot}	R_{eff}/kpc	r_s/kpc	$\sigma(R_{eff})/\text{km s}^{-1}$
Milky Way Bulge	4.1×10^6	9×10^9	1.4	0.615	$103 \pm 20^*$
N3384	1.1×10^7	1.9×10^{10}	1.58^\dagger	2.85	$143.4 \pm 7^*$
N3585	3.2×10^8	1.6×10^{11}	5.2^\dagger	2.1	$213 \pm 10^*$
N3379	4.2×10^8	6.86×10^{10}	3.143^\dagger	1.08	$206 \pm 10^*$
M87	3.2×10^9	3.3×10^{11}	8.0	3.04	$264 \pm 13^{**}$
M49	2.5×10^9	4.2×10^{11}	9.3	3.44	$250 \pm 13^{**}$

Table **6-3**.: This table summarizes some physical parameters of some representative galaxies and their SMBH and the derived values of the parameter r_s within SSFDM obtained from fitting the $M - \sigma_*$ reported in (*) (McConnell and Ma, 2013) and (**) (Larkin and McLaughlin, 2016) (SMBH mass, total stellar mass, effective radius, characteristic size of the halo and velocity dispersion). Values of R_{eff} labelled with \dagger were estimated using (6-45).

Fig. **6-11** illustrates the main result of this subsection: the observed velocity dispersion of baryons in centres of large and luminous galaxies like the Milky Way –which typically contain a dominant amount of baryons in those regions– can not be produced only by gravitational potential wells of SSFDM haloes (as it has been shown in Subsection 6.6.2 as well), rather an important contribution of this wells should come from the baryons.

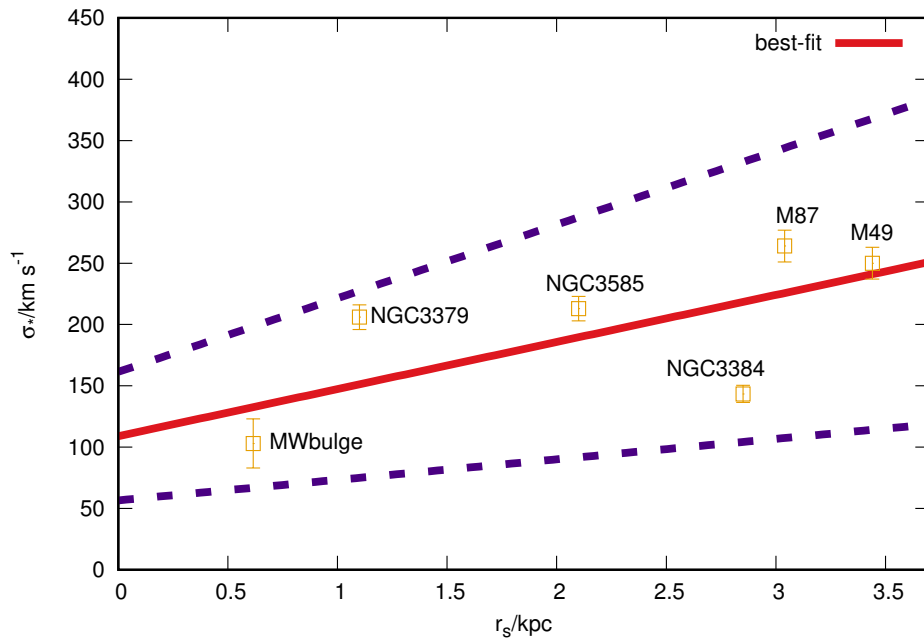


Figure **6-11**.: The solid line corresponds to the best-fit of $r_s - \sigma_*$ for the six galaxies in our catalogue given by the yellow points with their corresponding error-bars (Table **6-3**). The dashed lines correspond to the $\pm 1\sigma$ theoretical errors from our best-fit given by relation (6-46) (Figure taken from (Avilez et al., 2018)).

7. Consequences of the core-halo mass relation in the self-interacting scalar field dark matter model

In the last section, we have studied the SFDM model in presence of SMBHs. Most importantly, in this section we would like to explain the formation of SMBHs in this SFDM scenario. For such purpose, we consider again the possibility that the SFDM model could be self-interacting and then, extend the core-halo mass relation that have been obtained in the SFDM model (see equation (4-26)). Observe that we can relate halo quantities in terms of soliton quantities via equations (4-27) or (4-28). For such porpoise, in this chapter, we shall extend the review we did in section 2.4.2 in order to understand a little more soliton properties, and then, explore possible extension of the core-halo mass relation in the self-interacting scenario.

It is important to stress that the core-envelope structure of SFDM halos with self-interaction has not yet been established by numerical simulations, because the latter were confined to the free case. Yet, we adopt the premise that there ought to be a core-envelope structure also in models with self-interaction and we shall study the consequences. In fact, the (quantum) cores of SFDM alone cannot explain the big range of galactic halo masses found in the Universe, and it is this simple observation which "mandates" that cores (with or without self-interaction) have to be enshrouded by some envelopes. For instance, early indications of the problem of the core-halo mass relationship and a toy model for strongly self-interacting SFDM models can be found in (Rindler-Daller and Shapiro, 2014). Halo envelopes were later confirmed in the free case by simulations by (Schive et al., 2014b) and follow-up studies (see above).

The chapter is organized as follows: in section 7.1 we extend the basic description of the SFDM soliton profile by adoptiong a Gaussian ansatz to describe the soliton in order to maintain some freedom in working with the self-interaction parameter of the SFDM model. We show that, in general, this ansatz maintains practically all the relations that are found in the numerical description (the parameter dependence for the maximum mass for collapse of the soliton, parameter dependence in the TF regime, etc), even if relativistic corrections are considered. This implies that the Gaussian ansatz represents a good approximation for the soliton. Also in this section, we show that the results provided by this ansatz can be easily obtained in the hydrodynamic representation of the GPP system and by considering

a simple dimensional argument, without the need of considering any functional form for the core profile. In section 7.2, we extend the core-halo mass relation to self-interacting SFDM by considering the conditions (4-27), or (4-28), which are fulfilled by core and halo quantities in the simplest SFDM model. As a sequel to section 7.2, in section 7.3 we consider some heuristic arguments on the nature of the halo envelopes extensions to try to understand what extension should imply a more physical consequence for core-halo relations. In section 7.5, we compare our results with previous works, with the emphasis on the implied constraints of the SFDM model parameters. For this comparison, we focus on the core properties found in the central region of SFDM halos. We find that for a repulsive SFDM candidate, the central soliton should be represented in the TF regime, while for attractive SFDM, we have scenarios where the soliton collapses and forms a SMBH for the most massive galaxies, while remaining stable for the least massive galaxies. Finally, in section VII we present our conclusions.

7.1. Extending soliton properties

7.1.1. The weak-field limit

In this section, we decided to re-introduce explicitly the values for \hbar and c to be consistent with the typical works reported in the SFDM for galaxy formation with self-interactions. Additionally, we decided to work in physical coordinates, instead of comoving.

As we explained before, the Structure formation of halos in a matter-dominated Universe can be well described by the Gross-Pitaevskii-Poisson (GPP) system (4-16):

$$i\hbar\frac{\partial\psi}{\partial t} = -\frac{\hbar^2}{2m}\nabla^2\psi + m\Phi\psi + g|\psi|^2\psi, \quad (7-1a)$$

$$\nabla^2\Phi = 4\pi G\rho, \quad (7-1b)$$

We will ignore the baryonic contribution in what follows, in order to be consistent with most of the numerical simulations for structure formation in the SFDM model (Levkov et al., 2018, Mocz et al., 2017a, Schive et al., 2014a,b, Schwabe et al., 2016, Veltmaat and Niemeyer, 2016)). Then, we will consider that $\rho = m|\psi|^2$.

For simplicity, we shall re-express in physical units the different energy quantities that we reviewed in (2-44) and (2-46):

$$M_t = m \int_V |\psi|^2 d^3\mathbf{r}, \quad E_t = \int_V \left[\frac{\hbar^2}{2m} |\nabla\psi|^2 + \frac{m}{2} \Phi |\psi|^2 + \frac{g}{2} |\psi|^4 \right] d^3\mathbf{r}, \quad (7-2)$$

and

$$K_t = \int_V \frac{\hbar^2}{2m} |\nabla\psi|^2 d^3\mathbf{r}, \quad W_t = \int_V \frac{m}{2} \Phi |\psi|^2 d^3\mathbf{r}, \quad U_{SI,t} = \int_V \frac{g}{2} |\psi|^4 d^3\mathbf{r}. \quad (7-3)$$

We shall also work with the dimensionless GPP system (2-49), in such case the dimensionless variables defined in (2-48) are rewritten in physical units as

$$\begin{aligned}\hat{\psi} &= \sqrt{\frac{4\pi G\hbar^2}{mc^4}}\psi, & \hat{\mathbf{r}} &= \frac{mc}{\hbar}\mathbf{r}, & \hat{t} &= \frac{mc^2}{\hbar}t, \\ \hat{\Phi} &= \frac{\Phi}{c^2}, & \hat{\Lambda} &= \frac{c^2}{4\pi G\hbar^2}g = \frac{m_{pl}^2}{m^2}\frac{\lambda}{8\pi},\end{aligned}\quad (7-4)$$

As we explained in section 4.4.2, all the soliton solutions are virialized structures that fulfill equation (2-47). They can be modeled by the boson stars reviewed in section 2.4.2. Additionally, by multiplying (7-1) by ψ^* , considering a similar ansatz solution than (2-52) but in physical units, i.e.

$$\psi(r, t) = \phi(r)e^{-\mu_c t/\hbar}, \quad (7-5)$$

and integrating over all space, we obtain that such solutions also fulfill

$$K_c + 2W_c + 2U_{c,SI} = \mu_c \frac{M_c}{m}, \quad (7-6)$$

where μ_c is the chemical potential in physical units and, as we commented before, subindex c means total soliton quantities (M_c is the total mass of the soliton, K_c is the total kinetic energy of the soliton, etc.). Observe that in the free case, we arrive at the well-known relation $2K_c = -W_c$ and $K_c = -E_c$, where

$$E_c = \frac{\mu_c}{3} \frac{M_c}{m}. \quad (7-7)$$

As we already explained, by using the re-scaling property in (2-50), it is possible to construct all the soliton solution in the free field model, once one of the solutions is known, whereas in the self-interacting case, it is possible to construct all the soliton solution for a given Λ if one of such solutions is known.

We shall show that a Gaussian ansatz can describe correctly the soliton properties. For such consideration, let us address the case of the soliton profile a little more in the non interacting case. The first solution that is usually convenient to solve in the free case is that one for which the central value $\hat{\psi}(\hat{r} = 0) = 1$. In this case, the numerical value of the dimensionless chemical potential is given by $\hat{\mu} \simeq -0.69$, which corresponds to a soliton with the total mass

$$M_c^{(1)} \simeq \frac{2.79 \times 10^{12}}{m_{22}} M_\odot. \quad (7-8)$$

Then, from the above equation and the re-scaling parameter γ in (2-51), it is possible to construct solitons with different masses by considering

$$\gamma = 3.6 \times 10^{-6} m_{22} M_{c,7}^{(\gamma)}, \quad (7-9)$$

where again $M_{c,7}^{(\gamma)} \equiv M_c^{(\gamma)} / (10^7 M_\odot)$. Notice that we have left explicitly the γ dependence for the numerical solution of the soliton.

Another important quantity is the radius that contains 99% of the soliton mass and is given by¹

$$R_{99}^{(\gamma)} \simeq \frac{8.445 \times 10^4}{(m_{22})^2 M_{c,7}^{(\gamma)}} pc. \quad (7-10)$$

Finally, the soliton additionally fulfills the relation (see also equ.(7-20))

$$M_c^{(\gamma)} \simeq 4.3 \left(\frac{K_c^{(\gamma)}}{M_c^{(\gamma)}} \right)^{1/2} \frac{m_{pl}^2}{mc}. \quad (7-11)$$

7.1.1.1. The Gaussian ansatz in the weak-field limit

Previous literature has made extensive use of two different analytic approximations for the numerical, exact soliton profile of SFDM halos without self-interaction. On the one hand, we have the polynomial approximation (4-22), which was proposed in (Schive et al., 2014a), and which is based upon an empirical fit to the central region of simulated halos. On the other hand, a Gaussian profile has been used to approximate SFDM solitons in (Chavanis, 2011, Guzmán and Áviles, 2018). The use of a Gaussian is motivated by the fact that Gaussian “wave packets” not only appear in many contexts of a linear Schrödinger equation, it may also constitute a solution for laboratory Bose-Einstein condensates without particle self-interaction, see e.g. (Baym and Pethick, 1996). In this chapter, we decided to use the Gaussian approach, given its better physical foundation and the fact that it is easier to find physical relations of interest from it. The difference between the two analytic profiles can be seen in appendix F: the polynomial description appears to match better to the numerical result for the soliton for small \hat{r} , while the Gaussian approach matches better to the numerical solution at large \hat{r} . However, what is more important in our context is the fact that the Gaussian ansatz arrives at the same physical relationships as the numerical solution, and the difference in the prefactors is $O(1)$, as we shall see.

Now, the question arises to what extent the Gaussian can be used, if self-interaction is included. In fact, (Baym and Pethick, 1996) already used a Gaussian ansatz as a trial function in a variational analysis, in order to find modified physical relationships, valid when self-interaction is included. The same approach was proposed in (Chavanis, 2011) in order to extend the modeling of the SFDM soliton profile with self-interaction by considering the Gaussian density distribution

$$\rho_c^{(g)}(r) = \frac{M_c}{(\pi R_c^2)^{3/2}} e^{-r^2/R_c^2}, \quad (7-12)$$

where R_c is a characteristic core radius associated with the radius that contains 99% of the total mass of the distribution² as $R_{99} = 2.38167 R_c$.

¹This result is obtained from the mass-radius relationship (4-25).

²This number follows simply by calculating the radius which includes 99%, i.e. 2σ of the mass of the Gaussian distribution.

A mass-radius relation was found by way of minimizing the energy³ functional (7-2), and considering the ansatz (7-12) as a trial function. That procedure yields

$$M_c = 3\sqrt{2\pi} \frac{\frac{\hbar^2}{Gm^2 R_c}}{1 - \frac{6g}{4\pi Gm^2 R_c^2}}, \quad (7-13)$$

or equivalently

$$M_{c,7} \simeq \frac{10.076 \times 10^5}{m_{22}} \frac{\hat{R}_c}{\hat{R}_c^2 - 6\hat{\Lambda}}. \quad (7-14)$$

We note that when $g, \hat{\Lambda} > 0$ and $R_c \Rightarrow \sqrt{6g/(4\pi Gm^2)}$, or equivalently $\hat{R}_c \Rightarrow \sqrt{6\hat{\Lambda}}$, we obtain $M_c \Rightarrow \infty$, equivalent to the statement that R_c does not depend on the mass M_c . (Chavanis, 2011) showed that this limit corresponds to the well-known Thomas-Fermi (TF). The simplest way to see that consequence is by noticing from the above equation that

$$\hat{R}_c = \frac{5.038 \times 10^5}{M_{c,7} m_{22}} \left[1 + \sqrt{1 + 6\hat{\Lambda} \left(\frac{M_{c,7} m_{22}}{5.038 \times 10^5} \right)^2} \right], \quad (7-15)$$

and then, when the second term in the square root dominates, we obtain $\hat{R}_c \simeq \sqrt{6\hat{\Lambda}}$, independent of $M_{c,7}$ ⁴.

More precisely, the radius for the soliton profile follows in each case, as expected:

1. In the weak self-interacting limit

$$\frac{\sqrt{6\hat{\Lambda}} M_{c,7} m_{22}}{5.038 \times 10^5} \ll 1 \quad \text{and} \quad \hat{\Lambda} \geq 0, \quad (7-16a)$$

we obtain the relation $M_c R_c \simeq \text{const}$ ⁵.

2. In the strong self-interacting limit

$$\frac{\sqrt{6\hat{\Lambda}} M_{c,7} m_{22}}{5.038 \times 10^5} \gg 1, \quad (7-16b)$$

we obtain $\hat{R}_c \simeq \text{const}$, i.e. independent of core mass.

³Notice that (Chavanis, 2011) uses an uncommon definition of W which differs from the second equation in (7-3) by a factor of 1/2.

⁴We can compare the radius that contains 99% of the total mass in this limit and the radius obtained in the TF approach (4-32). Considering that for the Gaussian ansatz (Chavanis, 2011) $R_{99} \simeq 2.38167 R_c \simeq 5.834 \sqrt{g/(4\pi Gm^2)}$, while for the TF approach $R^{(TF)} = \pi \sqrt{g/(4\pi Gm^2)}$, we can see that both quantities are practically of the same order of magnitude.

⁵The equality is obtained when $\hat{\Lambda} = 0$. See also equation (4-25).

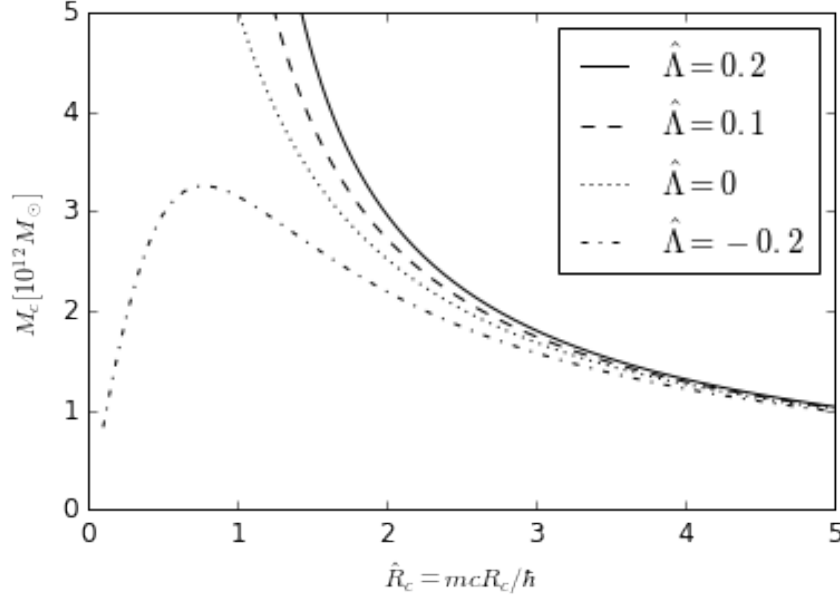


Figure 7-1.: Mass-radius relation in the self-interacting SFDM model. We consider a Gaussian ansatz which describes very well the results obtained in the numerical simulations.

By comparing Figure 7-1 and the numerical solution (Figure 2-3), we can observe that the relation (7-13), or (7-14), maintains the same basic parameter dependences than the numerical solution. For the attractive case ($\hat{\Lambda} < 0$), this means that there exists a maximum mass allowed by the SF configuration given by

$$M_{c,max} \simeq 7.6952 \frac{m_{pl}}{\sqrt{|\lambda|}}, \quad (7-17)$$

wich is comparable with the numerical result (2-54), while in the repulsive and free case ($\hat{\Lambda} \geq 0$), it appears there is no maximum mass for the soliton profile. Another important property that is also maintained is the fact that, the larger the coefficient $\hat{\Lambda}$, the more massive the equilibrium configuration. Interestingly, the radius at which the attractive case reaches its maximum mass is given by $\hat{R}_c = \sqrt{6|\hat{\Lambda}|}$, which is just the same radius at which the repulsive case goes over to the TF regime.

Now, we can easily show that the total kinetic energy (7-3) for the SFDM Gaussian ansatz with self-interaction is as follows (compare also to (7-38))

$$K_c = \frac{3}{4} \frac{\hbar^2 M_c}{m^2 R_c^2}, \quad (7-18)$$

which can be re-arranged to

$$\frac{1}{R_c} = \frac{2m}{\sqrt{3}\hbar} \left(\frac{K_c}{M_c} \right)^{1/2}. \quad (7-19)$$

Using the $M_c - R_c$ relation (see equation (7-13)), we arrive at

$$M_c \simeq 8.68 \frac{m_{pl}^2}{m} \frac{\left(\frac{K_c}{M_c}\right)^{1/2} / c}{1 - 8\hat{\Lambda} \left(\frac{K_c}{M_c}\right) / c^2}. \quad (7-20)$$

This last expression will be very important in the next section. However, observe that in the free case ($\hat{\Lambda} = 0$) the above result differs only from (7-11) by a factor of 2.

Considering the free-field limit, we obtain

$$R_c \simeq \frac{6.44 \times 10^4}{(m_{22})^2 M_{c,7}} pc. \quad (7-21)$$

Its radius R_{99} which contains 99% of the total mass of the soliton is $R_{99} \simeq 2.38167R_c$, which from the above equation yields

$$R_{99} \simeq \frac{15.34 \times 10^4}{(m_{22})^2 M_{c,7}^{(\gamma)}} pc. \quad (7-22)$$

Comparing to the numerical result in (7-10), we see that the difference in radius is small, of order $O(1)$.

7.1.1.2. Understanding the $M_c - R_c$ relation from the hydrodynamic representation of the GPP system

Although the Gaussian ansatz has been extensively used in the literature and is well motivated to represent the numerical ground state solution of the GPP system, we need to entertain the possibility that we could have introduced inaccuracies in the different relations that we obtained in the previous subsection by limiting ourselves to a functional form of the profile that is not the exact solution. In this subsection, we thus consider an alternative procedure, independent of the functional form of the "trial function", to re-obtain the most important results discussed in the above subsection. For that purpose, we use the hydrodynamic representation of the GPP system (4-20), which in physical units is given by

$$\rho \frac{\partial \bar{v}}{\partial t} + \rho(\bar{v} \cdot \nabla) \bar{v} = -\rho \nabla Q - \rho \nabla \Phi - \nabla P_{SI}, \quad (7-23a)$$

$$\frac{\partial \rho}{\partial t} + \nabla \cdot (\rho \bar{v}) = 0, \quad (7-23b)$$

where

$$\psi(\mathbf{r}, t) = \sqrt{\frac{\rho(\mathbf{r}, t)}{m}} e^{iS(\mathbf{r}, t)}, \quad \bar{v} = \frac{\hbar}{m} \nabla S, \quad (7-24)$$

and

$$Q \equiv -\frac{\hbar^2}{2m^2} \frac{\nabla^2 \sqrt{\rho}}{\sqrt{\rho}} \quad P_{SI} \equiv \frac{g}{2m^2} \rho^2. \quad (7-25)$$

In order to understand the parameter dependence of the soliton profile in the self-interacting SFDM model, we may consider the following simplification: We saw that soliton structures fulfill the relation $\partial\bar{v}/\partial t = 0 = \bar{v}$. Then, if we take for simplicity that $\nabla \sim 1/\mathcal{R}_c$, where \mathcal{R}_c is the characteristic radius of the system, then

$$\nabla Q \sim \frac{\hbar^2}{2m^2\mathcal{R}_c^3}, \quad \nabla P_{SI} \sim \frac{g\rho^2}{2m^2\mathcal{R}_c}, \quad \nabla\Phi \sim -\frac{GM_c}{\mathcal{R}_c^2}. \quad (7-26)$$

By considering for simplicity that $\rho \sim 3M_c/(4\pi\mathcal{R}_c^3)$, which is equivalent to say that the soliton profile possesses a nearly constant density, we obtain from (7-23)

$$-\frac{\hbar^2}{2m^2\mathcal{R}_c^2} + a\frac{GM_c}{\mathcal{R}_c} - b\frac{3gM_c}{8\pi m^2\mathcal{R}_c^3} = 0, \quad (7-27a)$$

$$\frac{\partial\rho}{\partial t} = 0, \quad (7-27b)$$

where a and b are some constants that we introduced to apply the summation in the above expression (i.e. we are considering, for example, that $\nabla Q \simeq \text{const} * \hbar^2/(2m^2\mathcal{R}_c^3)$).

First, equation (7-27b) reflects our assumption for an stationary solution, which is in agreement with (2-52) and (7-5). On the other hand, from (7-27a) and by considering that $g > 0$ we obtain

$$a\frac{GM_c}{\mathcal{R}_c} = \frac{\hbar^2}{2m^2\mathcal{R}_c^2} + b\frac{3gM_c}{8\pi m^2\mathcal{R}_c^3}, \quad (7-28)$$

and then from this description it is easy to see that solitons are produced by the equilibrium between the attraction of the gravitational potential force (left-hand side in the above expression) and the repulsion due to the quantum uncertainty pressure and the pressure due to the self-interaction.

Two well studied limit cases are

- **The fuzzy limit:** This regime is obtained when the second term in the right-hand side of equation (7-28) can be ignored, and then the soliton solution results in an equilibrium between quantum pressure and gravity. In this limit, the $M_c - \mathcal{R}_c$ relation reads

$$M_c\mathcal{R}_c = \frac{1}{2a} \frac{\hbar^2}{Gm^2}, \quad (7-29)$$

which maintains the same parameter dependence found in the numerical treatment (see equation (4-25)).

- **The Thomas-Fermi approximation:** This regime is obtained when the first term in the right-hand side of equation (7-28) can be ignored, and then the soliton profile results as an equilibrium between gravity and the pressure due to self-interaction. In this limit, the soliton fulfills the $M_c - \mathcal{R}_c$ relation

$$\mathcal{R}_c = \sqrt{\frac{b}{2a} \frac{3g}{4\pi Gm^2}}, \quad (7-30)$$

which also maintains the same parameter dependence found by the exact solution (see equation (4-32)).

On the other hand, if $g < 0$ we have

$$a \frac{GM_c}{\mathcal{R}_c} + b \frac{3|g|M_c}{8\pi m^2 \mathcal{R}_c^3} = \frac{\hbar^2}{2m^2 \mathcal{R}_c^2}, \quad (7-31)$$

and then the soliton profile can be understood as an equilibrium between the attraction due to gravity plus the self-interacting pressure and the repulsion due to the quantum pressure term. Observe that in this scenario, we can also define a new limiting case

- **The Thomas-Fermi approximation in the attractive scenario:** This regime is obtained when the first term in the left-hand side of equation (7-31) can be ignored, and then the soliton profile can be understood as the equilibrium between quantum pressure and attractive self-interaction. In this limit, the $M_c - \mathcal{R}_c$ relation is

$$\mathcal{R}_c = b \frac{3|g|}{4\pi \hbar^2} M_c. \quad (7-32)$$

These configurations correspond to soliton profiles with radius smaller than the one with the maximum possible mass shown in Figure 7-1.

Generically, re-arranging equation (7-27a), we have

$$M_c = \frac{1}{2a} \frac{\frac{\hbar^2}{Gm^2 \mathcal{R}_c}}{1 - \frac{b}{2a} \frac{3g}{4\pi Gm^2 \mathcal{R}_c^2}}, \quad (7-33)$$

and it is easy to see that this relation is equivalent to the one shown in (7-13).

At this point, we have not yet specified the numerical values of a and b . In order to do so, we could proceed in two different ways: first, by taking the Gaussian result and considering that $\mathcal{R}_c = R_c$. In this case,

$$\frac{1}{2a} = 3\sqrt{2\pi}, \quad \frac{b}{2a} = 2, \quad (7-34)$$

should be fulfilled and the $M_c - R_c$ relation is given exactly by (7-13). On the other hand, we could also obtain the numerical values of a and b by matching our result with the exact, numerical result. For example, let us suppose that R is the radius that contains 99% of the total mass of the configuration, and that such a radius can always be written as $R = \text{const} * \mathcal{R}_c$. Then, from (7-33) we obtain

$$M_c = \frac{1}{2\hat{a}} \frac{\frac{\hbar^2}{Gm^2 R}}{1 - \frac{\hat{b}}{2\hat{a}} \frac{3g}{4\pi Gm^2 R^2}}, \quad (7-35)$$

where \hat{a} and \hat{b} are new constants. By matching the last expression with the well-known numerical result in the fuzzy limit and the exact result in the Thomas-Fermi approximation (see equation (4-25) and (4-32)), respectively, we have

$$\frac{1}{2\hat{a}} = 9.9, \quad \sqrt{\frac{\hat{b}}{2\hat{a}}} = \pi, \quad (7-36)$$

and then the final $M_c - R$ relation should be

$$M_c \simeq 9.9 \frac{\frac{\hbar^2}{Gm^2R}}{1 - \pi^2 \frac{3g}{4\pi Gm^2R^2}}. \quad (7-37)$$

Finally, in order to obtain the core-halo mass extension in the self-interacting scenario, it will be necessary to use (7-20) in the next section. To be sure that (7-20) is correct, it should be enough to demonstrate that the $M_c - R_c$ relation is correct, as well as (7-18). If we continue with the same approximation ($\nabla \sim 1/\mathcal{R}_c$) and we calculate the integral for K_t defined in (7-3), we finally obtain

$$K_c = \frac{A_c}{2} \frac{\hbar^2 M_c}{m^2 \mathcal{R}_c^2}, \quad (7-38)$$

where we have introduced yet another constant A_c . Again, from the Gaussian ansatz, if we set $\mathcal{R}_c = R_c$ we obtain

$$A_c = \frac{3}{2}. \quad (7-39)$$

We stress that this way of obtaining the relations for the soliton profile is particularly interesting, given that in this analysis the only thing we needed to do was to take into account the characteristic scales of the system. We note that in all cases we can see that the ansatz reproduced correctly the results already known from the numerical and analytical descriptions of the soliton profile, as well as our result in this section. The only differences which occur involve the numerical values of the constants that accompany the parameter dependence of the different relations, and they are all of order $O(1)$. Thus, our analysis should still provide the correct orders of magnitude for the different constraints of the SFDM parameters. Nevertheless, for the sake of concreteness, we decided to continue to use the results obtained from the Gaussian ansatz for the rest of this chapter.

7.1.2. Fully relativistic treatment

The analysis of the previous subsections was carried out in the weak-field regime. This regime is a good approximation, given that it is very well justified at galactic scales. Yet, it leaves out an important physical phenomenon that we reviewed in section 2.4.1, namely the fact that a limiting maximum mass is also predicted to exist for the soliton for the free and the repulsive self-interacting cases, once general-relativistic effects are considered.

It is then natural to anticipate that for certain masses of the soliton, a relativistic treatment should be important – as it turns out, it is possible that some of the cores of SFDM halos are not covered by the weak-field limit, for example the cores of the most massive galaxies that possess the most massive solitons (see equation (4-26) or the next section for the generalization to the self-interacting case). In this circumstance, the correct way to model such solitons should be in the general relativistic scenario, i.e. by considering the complete boson stars described in section 2.4.1. For this reason, in this subsection, we confront our Gaussian ansatz with the results that are obtained in the general relativistic scenario. Specifically, we confront the Gaussian ansatz with the critical mass of Collapse for the soliton profile.

We assume that the Gaussian ansatz will collapse into a BH, once $R_{99} = 2.38167R_c \simeq R_{sch}$, where $R_{sch} \equiv 2M_c G/c^2$ is the Schwarzschild radius associated with the soliton profile. By considering (7-15), expressing hat quantities in terms of physical ones with (7-4) and equating $R_{99} = R_{sch}$, we obtain in the free case $M_{c,max}^{(g)} \simeq 2.11m_{pl}^2/m$, whereas in the strong, repulsive self-interaction regime $M_{c,max}^{(g)} \simeq 3.57\sqrt{\Lambda}m_{pl}^2/m$. We note that once comparing the above results with the exact numerical results, (2-39) and (2-40), we obtain the same parameter dependence for $M_{c,max}$ in both cases, with the only difference again in the numerical prefactors that accompany each relation. Of course, the difference between those prefactors is rooted in the fact that we are trying to match a Newtonian ansatz with a general-relativistic result, and, as expected, the critical masses from general relativity are smaller than the Newtonian analysis suggests.

7.2. SFDM density profiles and the core-halo mass relation in the self-interacting scenario

As we already explained in section 4.4.2, the numerical simulations performed by (Schive et al., 2014a,b) have shown that, at cosmological redshifts $z = 0$, halos made of SFDM without self-interaction can be well approximated by a core-envelope structure, where a central core transitions at a certain radius to a “NFW-like” halo envelope. In their work, they obtained the core-halo mass relation given by (4-26)

$$M_{c,7} \simeq 1.4 \times 10^2 M_{h,12}^{1/3} m_{22}^{-1} M_{\odot}. \quad (7-40)$$

Let us elaborate on the above relation and how it can be understood by simple heuristics: suppose the soliton core radius is of order the de Broglie wavelength, $R_c \sim \lambda_{dB}$, which we expect in the free field case from analytic considerations and what is found in numerical simulations, as well. For a virialized halo with mass M_h and nearly constant density, approximating $R_h \sim M_h^{1/3}$, the characteristic velocity increases as $v \propto M_h^{1/3}$. In fact, this simple relation can be understood more broadly: for example, in (Chavanis, 2019), the same parameter dependence for halo quantities was obtained by assuming that the SFDM galactic

halo is composed of a central solitonic core plus an isothermal atmosphere⁶. Combining the expressions yields $R_c \propto m^{-1} M_h^{-1/3}$. Using the mass-radius relation of the soliton, $R_c \sim M_c^{-1}$ (see also equation (4-25)), we arrive at the above relations.

More formally than the above simple description, in this section we shall explore the core-halo mass extension for self-interacting SFDM models by considering equations (4-27) and (4-28).

We can use equation (4-27) to derive the core-halo mass relation yet another way, again restricting to the free case. Suppose that the core is in virial equilibrium, fulfilling

$$2K_c + W_c = 0. \tag{7-41}$$

Next, we assume that the halo itself also fulfills his own virial equilibrium, i.e.

$$2K_h + W_h = 0. \tag{7-42}$$

Of course, we might question in which sense it is meaningful to assume separate virial equilibrium, for the core and for the halo. In practice, the above relationships will only hold approximately, especially for the halo which takes a longer time to virialize during which time the core might have already virialized. From (7-41), we have

$$\frac{K_c}{M_c} = -\frac{1}{2} \frac{W_c}{M_c}, \tag{7-43}$$

and (7-42) implies

$$\frac{K_h}{M_h} = -\frac{1}{2} \frac{W_h}{M_h}. \tag{7-44}$$

Combining the above relationships, equation (4-27) and using expressions for the potential energy,

$$W_c = -C_c \frac{GM_c^2}{R_c}, \quad W_h = -C_h \frac{GM_h^2}{R_h}, \tag{7-45}$$

with positive constants C_c, C_h of order $O(1)$, which depend upon the core and halo profiles, respectively, this yields

$$C_c \frac{R_c}{M_c} = C_h \frac{R_h}{M_h}. \tag{7-46}$$

Now, by using the $M_c - R_c$ relation provided in equation (4-25) and assuming that

$$M_h \propto R_h^3, \tag{7-47}$$

we get eventually

$$M_c^2 \propto M_h^{2/3} m^{-2}, \text{ i.e. } M_c \propto M_h^{1/3} m^{-1}. \tag{7-48}$$

⁶We stress that an isothermal exterior is not expected for SFDM halos, given that there are observational constraints that rule out this scenario, see (Slepian and Goodman, 2012).

Thus, we can see that the core-halo mass relation has something to do with overall and local virial equilibrium.

Observe that equation (7-46) is almost the same than (4-28), which implies that equations (4-28) and (4-27) are equivalent in the fuzzy limit. However, we can see that when a self-interaction is added to the model, both equations are not equivalent anymore. In this chapter, we shall derive that $M_c - M_h$ relation for both approximations. However, we are interested in studying the consequences obtained from equation (4-27), in such case we shall consider for that such relation is the correct one to describes core-halo quantities. We shall also try to justify our assumption in the next section. On the other hand, as we have already pointed out in the beginning of this chapter, the core-envelope structure has not been established in the self-interacting model by numerical simulations. Nevertheless, we may assume that a similar core-envelope structure could result, in the wake of halo formation and merging, and hence we adopt this premise in what we study in this section.

It is not difficult to derive that the $M_c - R_c$ relation for the Gaussian ansatz can be rewritten as

$$M_c = \left(\frac{3\sqrt{2\pi}\hbar^2}{m^2G^2} + \frac{6g}{4\pi m^2G^3} \frac{GM_c}{R_c} \right)^{1/2} \left(\frac{GM_c}{R_c} \right)^{1/2}. \quad (7-49)$$

Using equation (4-28), and considering again that $M_h \sim R_h^3$, we finally obtain

$$M_c = AM_h^{1/3} \left[\frac{3\sqrt{2\pi}\hbar^2}{m^2G} + A^2 \frac{6g}{4\pi^2 m^2G} M_h^{2/3} \right]^{1/2}, \quad (7-50)$$

where A^2 is a constant with units of density that depends on halo properties. We can take for simplicity the result obtained by (Chavanis, 2019), in such case $A^2 = 1.7\rho_c$. We won't continue extending the above relation. However, notice that the central value of the soliton profile can be obtained by considering the re-scaling property discussed in equations (2-50) and (2-51).

We now extend the core-halo mass relation to self-interacting SFDM models by considering (4-27), again. Observe that once we consider the contribution of the self-interaction parameter and we adopt again the separate virial equilibrium description, the core and halo in virial equilibrium should fulfill

$$2K_c + W_c + 3U_{SI,c} = 0, \quad (7-51a)$$

$$2K_h + W_h + 3U_{SI,h} = 0. \quad (7-51b)$$

We note that, once self-interaction is added to the model, we cannot contemplate the simple description from above, taking advantage of the individual (core and halo) gravitational potential energy. However, we can use the different relations that we have derived so far.

Notice that from (7-20) and (4-27), we obtain

$$M_c \simeq 8.68 \frac{m_{pl}^2}{m} \frac{\left(\frac{K_h}{M_h}\right)^{1/2} / c}{1 - 8\hat{\Lambda} \left(\frac{K_h}{M_h}\right) / c^2}, \quad (7-52)$$

which relates the mass of the core and halo quantities. Then, we assume a simplification at this point, as follows. We expect that the energy due to self-interaction is important only if the self-interaction parameter is large enough. For example, we know from the free case that the soliton makes up all or almost all of the halo for small galaxies. The same would apply in the self-interacting models, once galaxies are small enough to be basically described by the soliton only. However, that soliton is not just in the fuzzy limit, but includes a self-interaction, albeit small. Thus, we can contemplate the following scenario: by analogy to the free case, we expect the most massive solitons in the central regions of the most massive galaxies, where the energy due to self-interaction could be small, compared to the other energy contributions of the total halo. This assumption is justified on the grounds that on the scales of large halos, SFDM should behave similar than CDM. On the other hand, the least massive galaxies should harbor the lightest solitons, and then the self-interaction energy could be also negligible (observe from Figure 7-1 that the lightest solitons are basically indistinguishable from the ones obtained in the free case). These small galaxies should always be in a regime where the self-interaction parameter is not too large, i.e. their solitons would neither be in the TF limit, nor would they collapse to a BH⁷. In that circumstance, we may expect that the entire galactic halo fulfills the virial theorem of the free case, $K_h \simeq -W_h/2$, even if that relation is not fulfilled by the central solitons in the largest halos. On the other hand, in (Schive et al., 2014b) the following⁸ relation was obtained

$$\frac{1}{c} \left(\frac{|W_h|}{2M_h}\right)^{1/2} \simeq 2.47 \times 10^{-4} M_{h,12}^{1/3}, \quad (7-53)$$

by considering the definition of virial mass provided in (Bryan and Norman, 1998). Then, we finally arrive at our novel core-halo mass relation for self-interacting SFDM models, given by

$$M_{c,7} \simeq \frac{2.8 \times 10^2 M_{h,12}^{1/3} m_{22}^{-1}}{1 - 4.88 \times 10^{-7} \hat{\Lambda} M_{h,12}^{2/3}}. \quad (7-54)$$

We must emphasize that, in general, the above result is not valid in the case when the energy due to self-interaction in the total halo is not small, compared to the kinetic and gravitational energy, different to the result we obtained in (7-50), which is valid for whichever value of

⁷In the case of a repulsive self-interaction, there is actually no problem if the smallest galaxies reach the TF limit. However, as we shall see later, in that case our core-halo mass extension cannot be applied anymore.

⁸In fact, this relation follows easily by using $|W_h| \simeq M_h^2/R_h$ and $M_h \simeq R_h^3$ (assuming a nearly constant density of the halo), resulting in $|W_h|/2 \simeq M_h^{5/3}$.

Λ . However, we stress that this result is very interesting, given that it could represent a very important property which can help to distinguish between SFDM models, i.e. we can anticipate notable differences at galactic scales, depending upon the sign of the self-interaction parameter. For example, notice that in the above relation there is a critical mass

$$M_{h,12}^{(crit)} = \left(\frac{10^7}{4.88|\hat{\Lambda}|} \right)^{3/2}, \quad (7-55)$$

at which the mass of the soliton tends to infinity for $\hat{\Lambda} > 0$, or the soliton arrives at its maximum possible mass for $\hat{\Lambda} < 0$. Then, in analogy to the description of 7.1.1.1, we adopt the criterion that for $M_{h,12} \geq M_{h,12}^{(crit)}$, the central soliton of an SFDM halo should follow this description, i.e. arrive at the TF regime, or collapse to a BH. Additionally, if the above critical mass is very small, which would happen if $\hat{\Lambda}$ is large, we can also see that the energy contribution due to self-interaction cannot be ignored anymore.

Observe that once considering equation (4-27) for the extension for the core-halo mass relation, we arrive naturally to the critical masses for solitons to reach the Thomas-Fermi approximation or collapse to form a SMBH. This is a property that is not shared for the extension done when considering (4-28). In fact, when there is an attractive self-interaction, it appears that is possible to have zero-mass solitons from equation (7-50).

Remark: Notice that our formula (7-54) has a problem in the repulsive case once the critical mass of the halo reaches the mass $M_{h,12}^{(crit)}$. By analogy to the explanation we did before, this should suggest that such mass is the maximum mass allowed by a galaxy (remember the discussion about $R^{(TF)}$). However, such interpretation is not correct given that, once a soliton profile reaches the TF limit, we have that $K_c = 0$, which, from (4-27), should imply $K_h = 0$. Then, the interpretation for such divergence is that, after the central soliton reaches the TF limit, our formula can not continue be used to describe the core-halo mass relation. On the other hand, observe that in the attractive case, we do not have this problem given that the kinetic energy is the only one that accounts to oppose to the attraction due to gravity and the self-interaction.

In order to elaborate more on the consequences of equation (7-54), we plot in Figure (7-2) M_c (top panel) and R_c (bottom panel) as a function of M_h with $m_{22} = 1$. This is the mass and radius that a core in a galactic halo with mass M_h should have if SFDM is ultra-light and self-interacting. We can see that the effect of the self-interaction parameter is such as to increase (decrease) the soliton mass with respect to the soliton in the free field limit, when SFDM is repulsive (attractive). This result is expected, because when the self-interaction parameter is positive (negative), the soliton profile admits more (less) massive configurations and, consequently, more (less) of the total halo mass is accumulated in the central soliton profile.

On the other hand, the radius changes very little between the three cases. Of course, this result is a consequence of the term $\hat{\Lambda} M_c^2 m^2 / m_{pl}^4$ in (7-15), which for an ultra-light SFDM

particle is of order $\sim \hat{\Lambda}(M_c/10^{12}M_\odot)^2$. This number is always small, as long as $\hat{\Lambda}$ is not too large. We can see that a final consequence of the above relation is the somewhat counter-intuitive statement that for a repulsive (attractive) SFDM candidate, the central soliton profile is denser (less dense) than in the free case.

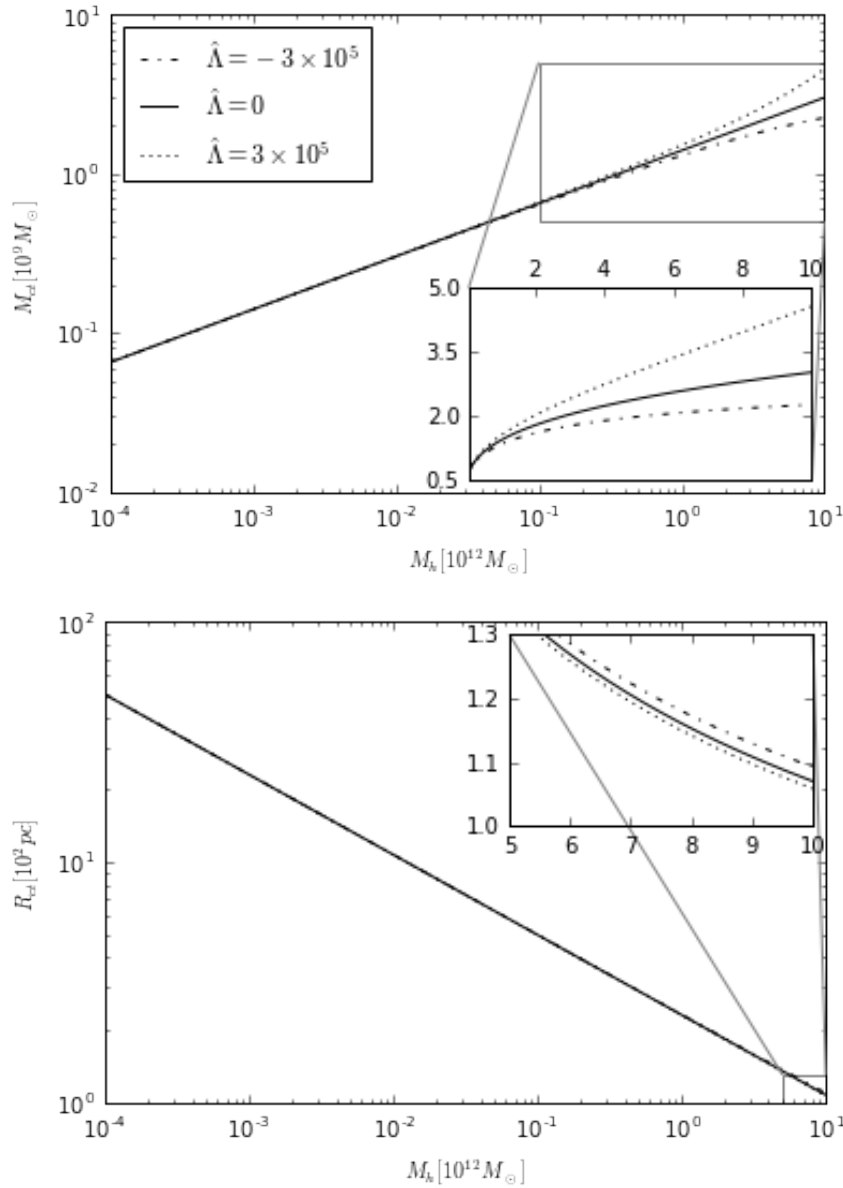


Figure 7-2.: Mass and radius for a soliton in self-interacting SFDM halos, in terms of total halo mass.

7.3. Contrasting two approximations

If we continue working with the hydrodynamical variables, we have that the kinetic energy term K_t (see equation (2-46a)) can be rewritten upon the hydrodynamic variables (7-24) as

$$K_t = \int_V \frac{\rho}{2} \vec{v}_Q^2 d^3\mathbf{r} + \int_V \frac{\rho}{2} \vec{v}^2 d^3\mathbf{r} = \int_V \frac{\rho}{2} \vec{v}_{tot}^2 d^3\mathbf{r}, \quad \vec{v}_Q^2 = \frac{\hbar^2}{m^2} \frac{(\nabla\sqrt{\rho})^2}{\rho}, \quad (7-56)$$

where \vec{v}_Q is a quantum velocity term associated with the quantum uncertainty principle of quantum mechanics, and $\vec{v}_{tot}^2 \equiv \vec{v}^2 + \vec{v}_Q^2$. This quantum velocity term is motivated in the spirit of the virial theorem in the fuzzy limit. By considering that \vec{v}_{tot} equals the virial velocity in a halo, we obtain

$$K_t = \frac{M_t v_{vir}^2}{2}. \quad (7-57)$$

Observe that, in the free case, we arrive at the relation $M_c = R_c M_h / R_h$, which is the consequence that has been proposed in (4-28). In that limit, the virial velocity should match the circular velocity in the SFDM model. From our point of view, a more physical consequence for the extension in the core-halo mass relation should be given by considering that the virial velocity at the core and halo radius match each other. That consequence is obtained if the relation (4-27) is fulfilled.

We can focus a little on understanding what kind of consequences are derived from the condition $M_c = R_c M_h / R_h$. Observe that, from (7-45), we should have that for such approximation, SFDM haloes must fulfill the condition

$$\frac{W_c}{M_c} \sim \frac{W_h}{M_h}, \quad (7-58)$$

i.e., the gravitational energy density should be near the same at the core radius than at the halo radius, independently on the fact that the SFDM is self-interacting or not.

7.4. Understanding the NFW envelope structure from the hydrodynamic representation

Continuing with the Hydrodynamic representation, we have

$$\begin{aligned} K_t &= \int_V \frac{\hbar^2}{2m^2} (\nabla\sqrt{\rho})^2 d^3\mathbf{r} + \int_V \frac{\rho}{2} \vec{v}^2 d^3\mathbf{r} \\ &\equiv K_{t,Q} + T_t, \end{aligned} \quad (7-59)$$

where we define the total kinetic energy due to the quantum part $K_{t,Q}$ and the "rest" T_t , which is basically related to any bulk motion of the fluid (e.g. rotation, large-scale flows, etc.). Now, as supposed from (4-27), we consider that the core and halo will have their own

respective terms, i.e. $K_c = K_{c,Q} + T_c$, $K_h = K_{h,Q} + T_h$. Suppose that the core has no bulk motion, i.e. $T_c = 0$, which is equivalent to assume a static soliton. The halo, however, may have a non-vanishing bulk motion, $T_h \neq 0$. That is, we can write

$$\frac{K_c}{M_c} = \frac{K_{c,Q}}{M_c}, \tag{7-60a}$$

$$\frac{K_h}{M_h} = \frac{K_{h,Q}}{M_h} + \frac{T_h}{M_h}. \tag{7-60b}$$

Now, we can consider a similar heuristics than in section 7.1.1.2. For instance, we already estimated the quantum-part of the core in equation (7-38). We can do a very similar heuristics for the respective halo term $K_{h,Q}$, however, we do not know at this point what the characteristic length scale looks like for the halo. We cannot simply use R_h , i.e. the characteristic size of the halo, as the characteristic scale, because this would be equivalent to say that the quantum-kinetic energy has the same importance for the halo, than it has for the core. And this would imply that $R_h \simeq R_c$. Therefore, we set the characteristic scale to $\nabla_h \sim 1/(B_h R_h)$, i.e. a fraction of R_h , where the constant B_h fulfills $0 < B_h \leq 1$. The value of $B_h R_h$ may describe a characteristic size for structures that accounts for the total halo, for example the size of “granules” in the halo envelope structure. Thus, we can write

$$\frac{K_h}{M_h} = A_h \left(\frac{\hbar}{m} \right)^2 \frac{1}{B_h^2 R_h^2} + \frac{T_h}{M_h}, \tag{7-61}$$

where A_h is a constant depending on halo details.

If we now demand that the relation (4-27) should be fulfilled by our system, we end up with a condition on T_h/M_h , as follows:

$$\frac{T_h}{M_h} \simeq \left(\frac{\hbar}{m} \right)^2 \left(\frac{A_c}{R_c^2} - \frac{A_h}{B_h^2 R_h^2} \right). \tag{7-62}$$

Observe that in the case when $R_c = R_h$, i.e. the total halo is constructed by the soliton only, we should have that $T_h \simeq 0$, and then

$$A_c = \frac{A_h}{B_h}. \tag{7-63}$$

In this way (7-62) can be rewritten as

$$\begin{aligned} \frac{T_h}{M_h} &\simeq A_c \left(\frac{\hbar}{m} \right)^2 \left(\frac{1}{R_c^2} - \frac{1}{R_h^2} \right), \\ &= \left[1 - \left(\frac{R_c}{R_h} \right)^2 \right] \frac{M_h}{M_c} K_{c,Q}. \end{aligned} \tag{7-64}$$

The above quantity represents a very interesting consequence. Although the soliton solution has been very well understood under what circumstances it can be formed (for example as

a balance between the quantum pressure and the gravitational force in the fuzzy limit), the halo quantities are not well understood. Thus, our simple heuristic analysis seems to suggest that the NFW envelope should be supported through a non-vanishing T_h term. Additionally, our description appears to suggest that the envelope structure should be related with the quantum nature of the SFDM particle, since in the final relation that we found, it still appearing \hbar in the result.

7.5. Astrophysical consequences for the self-interacting SFDM model

A fundamental question that arises in the SFDM scenario concerns the values of its free parameters. As we showed in chapter 4, many constraints have been derived already, using cosmological and astrophysical data. In this section, we first review and elaborate a little more some of the most representative results introduced in that section, and then apply them to our model. We consider the different constrictions we reviewed in chapter 4. However, we do not contemplate all the constrictions, given that some of them already consider scenarios that should not be applicable to our scenario. For example, in the repulsive scenario, most of the constrictions are for galactic dynamics in the TF regime, and then, they already considered that a galaxy should be represented with a TF soliton. We only consider constraints for the self-interacting scenario, given that our main purpose in this chapter is to study the consequences of equations (7-54) and (7-55).

We should stress that some previous literature have shown that even small values of the self-interaction parameter can lead to qualitatively different behavior, compared to the free case. While this phenomenon has been appreciated in the boson star community, it is only recently that DM cosmologists appreciate this variety, as well.

7.5.1. Repulsive case ($\hat{\Lambda} > 0$)

As we already commented, this scenario has been extensively studied in the literature and its free parameters have been fitted by using different observations. Usually, the strong self-interaction regime is considered, because of simplicity, and in this case, it is the ratio $g/(m^2c^4)$ or $m_{22}/\lambda_{90}^{1/4}$, which is subject to constraints. Observe that the only constrictions that do not consider galactic dynamics in section 4.5 are the ones for BBN and the value necessary for the SFDM to behave as a dust-like fluid at the time of radiation-matter equality. For such constrictions, we have values for the two kind of ratios constrained in the model. Given that they are equivalent, in this section we decided to consider only one of them, which we pick to be the ones that constraint the ratio $g/(m^2c^4)$, given that they are newer. Observe that, from (7-4), we have

$$\hat{\Lambda} = 1.5441m_{22}^2 \times 10^{37} \left(\frac{g}{m^2c^4} \right) \frac{ev}{cm^3}, \quad (7-65)$$

i.e. we can likewise constrain $\hat{\Lambda}$. Whereas our results in (7-54) and (7-55) have been derived assuming that self-interaction is not important at the scales of large galactic halos, and which therefore may not be valid in the strong self-interaction limit, we still want to summarize some of the constraints of the previous literature, which were limited to the strong self-interaction regime. For one thing, the bounds are stronger and may hold for weak self-interaction, as well. On the other hand, these bounds are put into context to our results.

As we commented, the first constraint, applicable to all candidates for dark matter, refers to the fact that by the redshift of radiation-matter equality z_{eq} , they must all be non-relativistic, i.e. behaving like a pressureless fluid. It is well known that a scalar field with an arbitrary potential $V(\varphi)$ will have a varied dynamics during its cosmological evolution. In particular, the dynamics of a self-interacting SFDM candidate with a repulsive self-interaction has been studied previously and can be briefly summarized as follows (Arbey et al., 2002a, Li et al., 2014, Suárez and Chavanis, 2017): after inflation, the SFDM energy density behaves either like a cosmological constant ($\rho_\varphi \propto a^0$), or like a stiff fluid ($\rho_\varphi \propto a^{-6}$), depending upon whether SFDM is effectively a real or complex field, respectively. This behavior of SFDM is rooted in the *slowly oscillating* phase and is characterized by $\Omega^2 \equiv 2c^2 dV/d|\varphi|^2 \ll H^2$. In its *fast oscillating* regime ($\Omega^2 \gg H^2$), there are two possible branches for SFDM (Li et al., 2014, Padilla et al., 2019): for *weak self-interaction*, SFDM transitions from the stiff phase to the pressureless phase without having a radiation-like behavior in between. This happens, because the first term in the scalar field potential dominates over the second term at the moment of transition from slow to fast oscillation. On the other hand, for *strong self-interaction*, SFDM transitions from the stiff phase to a radiation-like phase, before behaving like a pressureless fluid. Demanding that at z_{eq} , SFDM should be in its pressureless phase implies a constraint as follows (Li et al., 2014):

$$\hat{\Lambda} \leq 6.176 m_{22}^2 \times 10^{20}. \tag{7-66}$$

This result represents an upper bound for the self-interaction parameter, including the weak self-interacting regime. This last result is also independent of whether SFDM is real or complex, given that the strong and the weak regimes are applicable to both cases. Hence, the above result is applicable to all self-interacting SFDM models with a repulsive self-interaction.

On the other hand, the repulsive SFDM model has been also probed by considering the effective number of relativistic degrees of freedom during Big Bang nucleosynthesis (BBN), $N_{eff,BBN}$ (Li et al., 2014). The analysis was performed in the strong self-interacting regime for a complex SFDM candidate, and it was shown that this scenario can be made in accordance with BBN bounds. Using the allowed 1σ -band on $N_{eff,BBN}$ at that time, it was shown that the ratio $g/(m^2 c^4)$ must fulfill an upper *and* a lower bound. However, if the lower bound of the 1σ -band on $N_{eff,BBN}$ is relaxed, i.e. if BBN is considered in accordance with the standard value of $N_{eff} = 3.046$, then the ratio $g/(m^2 c^4)$ can be smaller than the above upper bound, as long as the boson mass m fulfills a corresponding lower bound con-

straint, which ensures that the stiff-like era ends at an early enough time. We extended this analysis in (Li et al., 2017), to include a scenario where the stochastic gravitational wave background (SGWB) from inflation could be amplified, as a result of the stiff-like behavior of SFDM in the very early Universe, after reheating, when SFDM dominates the mean energy density in the Universe. In this case both, SFDM and the inflationary SGWB, contribute to $N_{eff,BBN}$. The modified bounds which result effectively shrink the available parameter space of complex SFDM further, but in doing so the SGWB is boosted to a level where it can be potentially observed by LIGO (see (Li et al., 2017)). However, if the stiff phase ends early enough, such that the SGWB remains negligible, the lower and upper bounds on $g/(m^2c^4)$ are determined basically again by demanding that SFDM fulfills BBN bounds. An updated value for $N_{eff,BBN}$ has been used in (Li et al., 2017) to derive newer bounds for this case, as well. Using (7-65), the corresponding bounds read as

$$3.55 \times 10^{19} \leq \frac{\hat{\Lambda}}{m_{22}^2} \leq 6.33 \times 10^{20}. \quad (7-67)$$

Observe that if we were to insert the above result into equation (7-55), we would obtain that practically all soliton structures should be in the TF regime of strong self-interaction, never mind the total mass of the galactic halo. As shown in (Li et al., 2014, 2017), by considering the above numerical value for $g/(m^2c^4)$ and considering the ratio $R^{(TF)}$ in the TF regime (see equation (4-32)), the size for a soliton in the repulsive case is of order $\sim kpc$. Thus, at this point (7-55) would have only confirmed previous works. Observe also that our result predicts that all galactic halos should possess a central soliton with the same radius $R^{(TF)}$. Unfortunately, the dependence of the mass of the central soliton with respect to halo quantities cannot be obtained from (7-54), given that we would need to take into account the self-interaction energy contribution of all halo sizes. Finally, if we combine the critical mass for collapse (2-40) in the repulsive case and the above constraints, we obtain

$$M_{c,max} \simeq (1.75 \times 10^{21} - 7.39 \times 10^{21})M_{\odot}, \quad (7-68)$$

implying that the mass of the soliton formed in this scenario is below the critical mass of collapse by many orders of magnitudes.

Remark: The constraint in (7-67) can be applied only to certain SFDM models, namely complex SFDM in the strong self-interaction regime, which behaves radiation-like during BBN. If we relax this constraint by considering SFDM without self-interaction or with a weak self-interaction, we could allow smaller values for $\hat{\Lambda}/m_{22}^2$, and then we can use (7-54). For example, if the central soliton is never described by the TF regime, we should have from (7-55) that

$$0 < \hat{\Lambda} < \frac{10^7}{2.44 \left(M_{h,12}^{(max)} \right)^{2/3}}, \quad (7-69)$$

where $M_{h,12}^{(max)} \equiv M_h^{(max)}/(10^{12}M_{\odot})$ and $M_h^{(max)}$ is the maximum mass for a galactic halo. In that case, small-scale structures would be suppressed basically in the same way than in the

free field case, which implies a mass for the SFDM particle of around $m_{22} \sim 1$. However, as seen from Figure 7-2, the implication of this scenario is such that the central soliton for the most massive galactic halos should be denser than in the free case.

7.5.2. Attractive case ($\hat{\Lambda} < 0$)

In contrast to the repulsive case, the attractive scenario does not possess the same mechanism to suppress small-scale structures and the self-interaction parameter λ (or g) is usually neglected, for it is extremely small in many models. The constraints which thereby result are indistinguishable from the free case. However, as soon as self-interaction is included, the picture changes. In this section, we shall review some representative constraints obtained a for negative self-interaction parameter. Again, we can re-express these constraints in terms of our parameter $\hat{\Lambda}$ by using (7-4) as

$$\hat{\Lambda} = 5.93 \times 10^8 \frac{\lambda_{90}}{m_{22}^2}. \quad (7-70)$$

For instance, it was demonstrated in (Suárez and Chavanis, 2015) that there is also a distinctive behaviour between strong and weak self-interaction. In the weak regime, the dynamics of SFDM is similar than in the repulsive case: SFDM experiences a stiff-like era before it ends up behaving like a pressureless fluid. On the other hand, in the strong self-interacting regime, SFDM follows a completely different cosmological history: it first behaves effectively as a cosmological constant, then it transitions to a cosmic string-like era, before ending up behaving as a pressureless fluid. However, this analysis was limited to cosmologies where SFDM is the only component in the Universe, i.e. its free parameters could not be constrained by cosmological data. Additionally, in (Suárez and Chavanis, 2015) linear perturbations were studied, and it was shown that perturbations in this SFDM model grew faster than in the Λ CDM model, even for small values of the self-interaction parameter, implying that galaxies could form earlier than in the Λ CDM model.

On the other hand, if the SFDM candidate is an ultra-light axion-like particle ($m_{22} \sim 1$) – a pseudo Nambu-Goldstone boson generated by a spontaneously broken global $U(1)$ symmetry –, it was suggested in (Visinelli, 2017) that these particles should be generated during inflation in order to avoid observational constraints from Planck data, due to topological defects. In the same work, it was argued that by demanding that the total dark matter observed today is composed of these ultra-light axions, they should have a self-interaction parameter⁹ $\hat{\Lambda} \sim -5.93 \times 10^4$ ($\lambda_{90} \sim -10^{-4}$), though some larger values $\hat{\Lambda} \sim -5.93 \times 10^{12}$ ($\lambda_{90} \sim -10^4$) could be also possible (Cicoli et al., 2012). Observe that these values for λ_{90} are extremely small, which corroborate the fact that self-interaction is usually ignored. However, the fact that $\hat{\Lambda}$ is grater than 1, should suggested us that for certain circumstances,

⁹The self-interaction parameter is obtained as $\lambda = m^2/f^2$, where f is the axion-decay constant. For an ultra-light axion, the decay constant is of order $f \sim 10^{16} GeV$.

the self-interacting parameter could not be ignored. Astrophysical considerations can lead to further novel constraints, e.g. the soliton with the maximum mass and smallest radius was matched to the smallest galaxy then known – Willman I – in (Chavanis, 2016). By demanding that the halo of Willman I is dominated by the self-interacting soliton, the SFDM parameters were constrained to

$$m_{22} = 0.0193, \quad \hat{\Lambda} = -3.2476 \times 10^{16}. \quad (7-71)$$

In that case, the maximum mass of collapse of a soliton should be close to the Willman I mass, i.e. $M_{c,max} \sim 10^6 M_\odot$, which is close to the smallest masses of SMBHs that are typically found in the centers of massive galaxies. It is for that reason that the author considers this mechanism for generating SMBHs. However, using our $M_c - M_h$ relation (7-54), we would need to conclude that, if even the soliton of Willman I is close to the maximum mass of collapse, then this would imply that the solitons of more massive galaxies would also have collapsed, and we would in general expect SMBHs in the centers of dSphs. Observations do not favor such a conclusion. In addition, we would end up with a model which is not able to explain the cores of dSphs, unless a substantial scalar-field remnant survives the collapse. Surely, both problems can be avoided if we relax the fit given in (7-71), considering that Willman I is not made up solely by a soliton close to or at the critical maximum mass.

Still, in this section we build upon the idea of (Chavanis, 2016) and constrain the free parameters for the attractive case by considering a more realistic scenario, instead. We wish to adopt a conservative criterion for the SFDM model, which is to explain only those SMBHs that formed in the most massive galaxies. It is now well-accepted that SMBHs exist in almost all large galaxies, while this is not the case for the smallest ones (like small dSphs¹⁰). We need to emphasize that, different to (Chavanis, 2016), we have found a dependence of the soliton mass in terms of halo quantities (7-54) which allow us to constrain the free parameters of the model, by demanding that SMBHs should only be generated in massive galaxies. Low-mass galaxies should have a stable soliton, giving rise to a core-like structure. This is a particularly interesting scenario given that, in this case, we could explain the core structure in typical dSphs, as well as SMBHs in the most massive galaxies. For this purpose, we use equations (7-54) and (7-55) to find a minimum SMBH mass generated by the collapse of the soliton, for a given minimum halo mass $M_{h,12}^{(crit)}$ whose central soliton should be collapsed. These minimum-mass SMBHs could serve as seeds for the growth of even more massive SMBHs that have been reported to exist in galactic nuclei. Their further growth could then proceed by accretion. In Figure 7-3, we plot with a straight-line in purple, blue, green and red the minimum mass of a SMBH that could be generated by this scenario for $M_{h,12}^{(crit)} = 0.001, 0.01, 0.1, \text{ and } 1$, which correspond to masses $M_h = 10^9, 10^{10}, 10^{11}$ and $10^{12} M_\odot$, and a self-interaction parameter $\hat{\Lambda} \simeq -2.049 \times 10^8, -4.415 \times 10^7, -0.957 \times 10^7$, and -2.049×10^6 , respectively. Additionally, in the same figure we also show filled regions with

¹⁰In fact, there are few observations where astronomers have detected SMBHs in dSphs; see for example (Ahn et al., 2017, ?). The formation of such SMBHs is not covered by our scenario.

the same colors, which indicate that such masses for the central soliton cannot exist, given that such masses are higher than the maximum possible mass allowed by an SFDM soliton configuration. We show these four values as examples, however, we adopt as a conservative criterion that the central soliton could collapse and form a SMBH in the centers of those galaxies, whose halo masses are larger than $M_h^{crit} \sim (10^9 - 10^{12})M_\odot$. Observe that different to standard descriptions, in this model the SMBHs start out already as supermassive objects which could explain why there are no medium-sized BHs. Also, thanks to the rapid growth of SFDM perturbations in the repulsive case (Suárez and Chavanis, 2015), SMBHs could have formed even at high redshifts. This possibility is particularly favored by many observations (Bañados et al., 2014, Fan et al., 2003, Jiang et al., 2008, 2007, Matsuoka et al., 2018a, 2017, 2016, 2019, 2018b, Mortlock et al., 2011, Venemans et al., 2013, Willott et al., 2007, 2010, Wu et al., 2015). that indicate that SMBHs do exist at large redshifts ($z > 5.6$), which standard scenarios have difficulties to explain.

Remark: Notice that in all cases the values of $\hat{\Lambda}$ are comparable to the values obtained if SFDM is an axion-like particle which was generated during inflation. In principle, by adopting this scenario we could also constrain the halo mass $M_{h,12}^{(crit)}$ in terms of axion quantities, as is the case for the axion-decay constant (see footnote 15) and the parameter dependence of the model shown in (Visinelli, 2017). However, since we wish to be as general as possible, we adopted a more general criterion.

In Figure 7-3, we also plot in a yellow band the mass region for 43 SMBHs reported in (Bandara et al., 2009). In all cases, the mass of the host galaxy for each SMBH is $M_h > 10^{12}M_\odot$, hence larger than all of our fiducial critical halo masses $M_{h,12}^{(crit)}$. Additionally, we plot in a dot-dashed black line the mass for Sagittarius A*, which is the SMBH located at the center of our Milky Way ($M_h \sim 10^{12}M_\odot$). Observe that, if we would like to explain all these SMBH masses, then the critical mass of collapse for the central soliton should be smaller than all the SMBHs reported in big galaxies. For example, in the data that we are considering, the smallest SMBH corresponds to Sagittarius A*. If we consider a scenario in which a SMBH at such a mass was generated (not having grown by another mechanism), once the mass of the galactic halo was around $10^{12}M_\odot$, we arrive at the following constraints for the mass of the SFDM boson (red square in the figure) and its self-interaction parameter,

$$m_{22} \simeq 3.25 \times 10^2, \quad \hat{\Lambda} \simeq -2.254 \times 10^6. \quad (7-72)$$

However, a more realistic picture may actually be as follows: the central SMBH formed with a mass of $M_{SMBH} \simeq 10^6 M_\odot$ (black dashed line), which implies a range for the boson mass parameter (intersection between the grey filled region, the black dashed line, and the purple - red line that we draw for our example models for $M_{h,12}^{(crit)} = 0.001 - 1$) in our fiducial model of

$$m_{22} \simeq 1.4 \times 10^2 - 1.4 \times 10^3, \quad (7-73a)$$

and a range for the self-interaction parameter of

$$\hat{\Lambda} \simeq -(2.049 \times 10^8 - 2.049 \times 10^6). \quad (7-73b)$$

Observe that we could also generate smaller SMBHs, if m_{22} is larger than the upper limit in (7-73a) (region pointed out by the grey arrow).

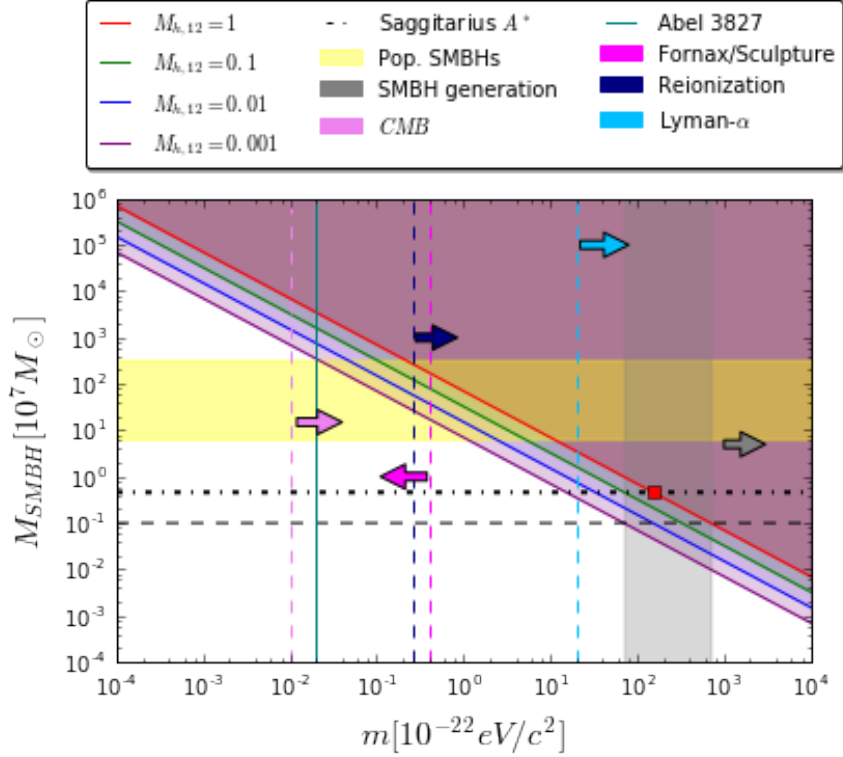


Figure 7-3.: Attractive SFDM model: critical mass of soliton collapse vs. boson mass. Filled regions correspond to masses for the soliton that are not stable against collapse. We also plot different constraints for the boson mass from other cosmological and astrophysical data.

We could also consider an even more conservative scenario. For example, SMBHs with masses similar to Sagittarius A^* seem not be common in big galaxies, since most of such SMBHs possess a much higher mass. Therefore, we could relax our attempt to try to explain the formation of all SMBHs in galactic nuclei and focus only on the most massive ones, instead. This should imply that a SMBH like Sagittarius A^* should be formed by some other mechanism, different to the one we are describing here. In this way, we use only the data provided in (Bandara et al., 2009) in which all SMBHs possess a mass of $M_{SMBH} \gtrsim 10^8 M_\odot$, in order to constrain our model. The lowest-mass galaxy reported in (Bandara et al., 2009) has a halo mass of $M_{h,12} = 9.46$. If we use the above mass in $M_{h,12}^{(crit)}$ and we require that a seed SMBH with a mass of $M_{SMBH} \simeq 10^8 M_\odot$ should be forming, we have from (7-54) and (7-55) that the free parameters for the model are

$$m_{22} \simeq 29.6, \quad \hat{\Lambda} \simeq -4.581 \times 10^5. \quad (7-74)$$

We need to emphasize that, although we are providing numerical values for each parameter, they should be taken with caution, because we have obtained our different results by con-

sidering heuristics and ansatz profiles. Nevertheless, as mentioned previously, we expect to achieve correct orders of magnitudes in all of our derived constraints.

In any case, an important point of this section is the realization that the addition of a self-interaction parameter can be advantageous, because under a certain range of parameters, it could be possible to explain the formation of SMBHs in galactic nuclei. Of course, much more remains to be done in order to really understand if this mechanism works out to describe all the details. For example, numerical simulations of the collapse should be performed, also to see what happens to the central SFDM profiles, after the formation of these SMBHs.

Although the effects of self-interaction are important for the central solitons in big galaxies, the numbers for the self-interaction parameter λ are still very small (compare our different constrictions with equation (7-70)). If we consider that the impact of self-interaction on small halos is negligible¹¹, which can be easily justify from Figure 7-2 or our $M_c - M_h$ relation (7-54), we would rediscover the constraints for the free case derived in previous papers. Therefore, we include these bounds in our comparison, as well. The constraints we consider include, for example, those obtained for the mass of the SFDM particle, using stellar velocity dispersion to fit the Milky Way’s dSphs galaxies with a soliton core, assuming the halo is dominated by that soliton. By studying the dynamics in Fornax and Sculpture, a constraint on the mass parameter $m_{22} < 0.4$ was obtained in (González-Morales et al., 2017). Placing constraints from the CMB in (Hložek et al., 2018) revealed a lower bound of $m_{22} > 0.01$. The model has been also probed by reionization: using N-body simulations and demanding an ionized fraction of HI of 50% by $z = 8$, (Sarkar et al., 2016b) obtained the result $m_{22} > 0.26$. Considering the hydrodynamic representation of the SFDM model, it was suggested in (Paredes and Michinel, 2016) that SFDM’s quantum pressure be the origin of the offset between dark matter and ordinary matter in Abel 3827, which required a mass of $m_{22} \simeq 2 \times 10^{-2}$. Finally, using the Lyman- α forest flux power spectrum demands that the mass parameter fulfills $m_{22} > 20 - 30$. In Figure 7-3, we also display the aforementioned constraints. In order to simplify the figure, we have only plotted the upper/lower bound of the constraints that fit the boson mass with a vertical dashed line, and we added arrows that point to those regions that remain valid in each case. Then, our plot should be read as follows: for example, the lower bound constraint for m_{22} obtained from the CMB ($m_{22} = 0.01$) is plotted with a pink vertical dashed line, while the pink arrow points to those masses that are also valid from this constraint, i.e. $m_{22} > 0.01$. Observe that our scenario previously described to obtain (7-72) or (7-73) is in agreement with most of these constraints, being in tension only with the results obtained in (González-Morales et al., 2017) and (Paredes and Michinel, 2016). On the other hand, our model (7-74) fulfills all constraints, except the ones obtained for Lyman- α and Abel 3827.

Finally, we comment on the consequence if the central soliton never collapses. Typically, most massive galaxies possess a mass $M_{h,12} < 1 \times 10^2 M_\odot$. From equation (7-55) this implies

¹¹The difference for large haloes should be that the final galaxy should have its central soliton collapsed.

that the self-interaction parameter must fulfill

$$\hat{\Lambda} < -9.511 \times 10^{-3}. \quad (7-75)$$

In this case, the formation of SMBHs must be explained by another mechanism. However, similarly than in the repulsive case, the attractive scenario does imply that the density of the central soliton is modified for the most massive galaxies, compared to the free case.

8. Conclusions

In this thesis, we have extended the story line for SFs as a DM component in the Universe. For such purpose, we reviewed in chapter 1 the standard cosmological model to understand what is the preferable model used to describe our Universe. Posteriorly, and given that our main purpose was to consider SFs as a DM candidate, in chapter 2, we discuss the most important concepts about SFs in general relativity. After that, in chapter 3, we report the main observational evidences for DM. In the same chapter, we continued commenting about the standard cosmological model, putting special attention in the structure formation process and the problems that the CDM sector – the DM sector – possesses at small scales. Motivated for such problems, in section 4, we reviewed the SFDM model as an alternative candidate for DM. We allowed in such chapter the possibility for the DM to be self-interacting or not, and then, we focused in distinguished which works have been done for self-interacting scenarios, and the ones that were carried out for the free case only. After this last 4 chapters, we extended the story line for the SFDM model in the next 3 chapters.

In chapter 5, we studied the possibility that a real free or self-interacting SFDM particle could coexist with the inflaton during inflation. In our assumptions, we have considered the SFDM as a spectator in the inflationary process. Then, the SFDM contributes to the primordial spectrum by generating isocurvature perturbations. By using the actual upper constraints in the measurements of the tensor-to-scalar ratio r was possible to test the free parameters for each model. As we discussed, at the moment it is difficult to rule-out some regions of parameters; however, it could be possible if r is measured soon.

Our main results in that chapter are shown in figures 5-1 and 5-4. In Fig. 5-1 we have identified the masses allowed in the free model by isocurvature as well as cosmological and astrophysical observations. We obtained that in order to fulfill the constrictions imposed by CMB, we should not detect gravitational waves until $r \simeq 1.3 \times 10^{-3}$, while if we were interested in fulfilling all the observations, we should not detect gravitational waves until $r \lesssim 2.33 \times 10^{-5}$. This last result is important given that the detectability of gravitational waves could represent a strong constriction for the free model. Analogously, in figure 5-4, we have plotted in a $m_{22} - \lambda_{90}$ plane the region of parameters for the strong-self-interacting model that are allowed by observations. We noticed that, for a given mass of the SFDM, it is always possible to avoid isocurvature constrictions and fit astrophysical and cosmological observations if a large enough self-interaction is added. Then, we notice with this result that the addition of a self-interacting component to the SFDM seems to be a natural solution for the model given that is possible to fulfill naturally all the constrictions that the model has.

On the other hand, we explain how the SFDM spectator scenario could help to choose the inflationary potential responsible to produce the inflationary period.

In this chapter, we only explored the SFDM model as a real field spectator. However, there are some motivations suggesting that a complex field should represent a better candidate for DM, given that there are observations where its complex nature could help to agree with observations (for example, observations coming from BBN). In this way, it continues being interesting to explore the possibility for the spectator field to be a complex field and analyze the kind of restrictions that such scenarios should obtain.

In chapter 6, we assume the possibility that galactic systems hosting a SMBH in their centres were formed earlier in the Universe from the collapse of a Bose-Einstein condensate made of modes of a SF, most of them laying in the ground state. Based on previous studies, we consider the hypothesis that the centres of DM haloes are made of quasi-resonant solutions of a real ultra-light SF that are being swallowed by the SMBH at such slow rate that their lifetime scales as the age of the Universe. Within the most general and realistic context, the SF would be self-interacting and self-gravitating and, along with the metric of space-time, form a complicated system of coupled non-linear differential equations which has been studied numerically by many groups since long time ago within some range of applicability. However, the available computing and numerical tools at the moment have allowed to explore these systems in a range of parameters corresponding to models of boson stars at most, and assuming some symmetries that wipe out some effects that should be present in more realistic models. Solutions for configurations of SF with the size of a galactic halo and BHs as massive as SMBH has not been obtained at the date in a general three dimensional space-time including all the possible effects.

In order to turn around such technical problem, in that chapter we intent to construct a simple approach based in a semi-analytical procedure in order to model galactic systems in the quasi-static limit. As a first step towards addressing the problem, we propose the simplest prescription to describe DM in the centres of galactic systems hosting a central SMBH. We model the haloes of galaxies as configurations made of solutions of the KG equation with a Schwarzschild background. We find analytic solutions for a range of masses of the BH, M , in the limit $r > 2M$, that is, when the observer is placed far away from the SMBH and well within a radius smaller than the characteristic length of the SFDM halo ($r < r_s$). In such regime, the back-reaction of the SMBH and SFDM can be neglected. By using such solutions we derive the corresponding density and mass profiles with ρ_s and r_s as free parameters, which were constrained using some observational features of galaxies. In specific, the space of parameters of the DM model was reduced by using the UMA constraint (Ureña-López et al., 2017). Later, the remaining free parameter r_s was fixed by fitting measurements of the velocity dispersion. In this procedure we considered two cases: Firstly, DMD, an idealized case where it is assumed that the gravitational contribution of DM dominates the galactic potential well. The main result in this part is that it is possible to reproduce the observed stellar velocity dispersion at the effective radius of systems hosting SMBHs of at

most $10^8 M_\odot$. This hypothetical case could be used in the future to study UCD galaxies. However, our analysis in this case stands as theoretical so far, due to the lack of evidence and observational data regarding to these systems at the date.

Secondly, in the LGAL case we considered a sample of six real, large and luminous galaxies hosting SMBHs and managed to reproduce their observed stellar velocity dispersions evaluated at the effective radius in every case. We realized in this case, that in the context of the SSFDM model, the role of gravity produced by baryons is crucial to reproduce the observed velocity dispersions. A complementary result of this work is a generalization of the constraint of μ_φ derived in (Ureña-López et al., 2017) for the case in which the galactic haloes host central SMBHs and it dominates the gravitational potential of the system. By reproducing the observational points of the $M - \sigma_*$ relation, we derive a $r_s - \sigma_*$ correlation in both cases. These results bring up new information about the SFDM model.

In chapter 7 we studied the consequences of the core-halo mass relation in the self-interacting SFDM scenario. For such porpoise we considered a Gaussian ansatz to describe a core profile in the SFDM to simplify our description and maintain the liberty of working with the self-interacting parameter associated to the SFDM particle. We also showed, with the help of the hydrodynamic representation of the GPP system, that the solutions obtained for the soliton profile are general, and that they can be obtained simply from scale arguments. Later, we showed the way the core-halo mass relation, typically found in numerical simulations of structure formation in the free SFDM model, can be generalized to the case of having a self-interacting parameter. For such porpoise, we considered that such relation should remain in the self-interacting case, although no cosmological simulations have been done for the model, in contrast to the free case. After obtaining this new result (7-54), which we consider to be one of the main results in that chapter, we considered previous works in order to constrain our finding. An interesting consequence that we observed in our model is that, in the case of having a repulsive self-interacting parameter, the central soliton profile that appears in the SFDM simulations should be in the TF approach, while in the case of having a attractive self-interaction, we can obtain a scenario where the central soliton could collapse and form SMBHs in the most massive galaxies, and then, give us a possibility to explain the SMBHs typically found in galactic nuclei.

This last result represents a first step of trying to understand the effects of self-interaction in the SFDM model for big galaxies and, in general, the consequence obtained for the collapse of the soliton profile should be also considered carefully since we have not taken into account more contributions that should be important in a big galaxy, as it is the case of the baryonic matter. On the other hand, in the numerical simulations done by (Schive et al., 2014a,b), it was obtained that a SFDM halo is constructed by a granular distribution, where the granules have a size similar than the central soliton, being the NFW profile obtained only after having done a radial average for the SFDM distribution. Then, if such granules posses a similar mass than the mass of the central soliton profile, we could obtain that they should also collapse in the case of having an attractive self-interaction, and then, our scenario could

represent a problem to the model. However, such problem could be easily avoided always that the self-interacting parameter were small enough (see equation (7-75)). Interestingly, this parameter should be even smaller than the one found for ultra-light axions.

Observe that most of the results in this chapter are based in semianalytical descriptions, and they are also strongly at the mercy of the mechanism we take as the real consequence for core-halo quantities. Then, if the extension we decided to use (4-27) is not correct, our finding should not be correct for modeling the core-halo mass relation for self-interacting particles. However, and based on the description we analyzed, we believe (4-27) represents a correct consequence for core-halo quantities. In any way, there still too much work to do in this direction; for example, it should be necessary to support our findings with numerical simulations, and, after obtaining the collapse of the soliton profile, we should continue exploring the process of growing for such SMBH seeds, and understanding what happens with the central region of galaxies after the central soliton collapsed.

9. Future works

We found interesting the fact that it appears that the core-halo mass relation results only when 3D simulations are carried out, whereas in the spherical symmetric case, what is obtained is that the configurations, no matter how arbitrary they are, are relaxed via a gravitational cooling effects, and migrate to the ground state – the soliton –. We believe that such problem could be avoided once we consider correct cosmological initial conditions for structure formation in spherical symmetry. For such porpoise, we have adopted the possibility to describe the structure formation process in the SFDM model with spherical symmetry, with a secondary infall model.

9.1. Scale-free gravitational collapse

Analytical approximations have been developed to model the formation of haloes by the $1D$ growth of spherical cosmological density perturbations. In this section, we review some of the different studies that have been done in this direction to apply them for the SFDM model.

The concept of the so-called “secondary infall model (SIM)” was first presented by (Gunn and Gott III, 1972). This SIM refers to the effect of adding a point mass to a uniform, expanding Friedmann-Robertson-Walker Universe, as a perturbation, causing in this way the deceleration with respect to the background of a spherical region until it reaches a maximum radius of expansion, and then, recollapse. Subsequent works generalized this approach to include spherically symmetric initial perturbations for which the overdensity profile depends upon radius of mass as a scale-free power law. Along this lines, (Fillmore and Goldreich, 1984) studied the dynamics of collisionless CDM haloes using a self-similar model, adopting a scale-free initial overdensity parametrized by its shape: ϵ in equation (9-1). In (Hoffman and Shaham, 1985) it was shown that a power-law power spectrum would indeed generate a scale-free initial condition, such as was adopted by (Fillmore and Goldreich, 1984). They then argued that the resulting non-linear structure would be described by a power-law profile determined by the shape of the power spectrum.

9.1.1. Halo formation from scale-free linear perturbations

In an Einstein-de Sitter background Universe, an initial linear perturbation, whose mass profile is spherically symmetric and has a scale-free power-law form

$$\frac{\delta M}{M_{un}} \propto M_{un}^{-\epsilon}, \quad (9-1)$$

results in structure formation, where M_{un} is the unperturbed mass enclosed at radius r and δM is defined such as $M_{per} \equiv M_{un} + \delta M$, M_{per} is the total mass enclosed within the same radius. From now-on we shall neglect subindex un in order to simplify the writing of this chapter. Each spherical mass shell around the centre expands until it reaches a maximum radius (turn-around radius r_{ta}), and recollapses. For a given ϵ , we have

$$r_{ta} \propto t^\epsilon, \quad (9-2)$$

where

$$\epsilon = \frac{2}{3} \left(\frac{2\epsilon + 1}{3\epsilon} \right). \quad (9-3)$$

9.1.2. Halo formation from peaks of the Gaussian random noise primordial density fluctuations

The theory of halo formation from peaks in the density field which result from Gaussian-random-noise initial density fluctuations draws an interesting connection between the average density profile around these peaks and the shape of the fluctuation power spectrum. According to (Hoffman and Shaham, 1985), local maxima of Gaussian random fluctuations in the density can serve as the progenitors of cosmological structures. They show that rare density peaks ($\nu \gtrsim 3$, where ν corresponds to $\nu\sigma_M$ peak) have a simple power law profile

$$\Delta_0(r) \propto r^{-(n+3)}, \quad (9-4)$$

where $\Delta_0(r)$ is the accumulated overdensity inside radius r and n is the effective index of the power spectrum $P(k)$ approximated as a power law $P(k) \propto k^n$ at wavenumber k , which corresponds to the halo mass as described in appendix G. The overdensity $\Delta_0(r)$ is equivalent to the fractional perturbation $\delta M/M$ inside radius r ,

$$\Delta_0(r) = \delta M/M \propto M^{-[(n+3)/3]}. \quad (9-5)$$

Comparing the above expression with equation (9-1) we obtain

$$\epsilon = (n + 3)/3. \quad (9-6)$$

According to this model, haloes of a given mass M originate from density perturbations given by equation (9-5) with n determined by the primordial power spectrum after it is transferred according to the parameters of the background Universe and the nature of the dark matter.

Remark: The final virialized halo distribution is completely specified by the nature of the dark matter component.

In this future work we shall analyze a SFDM distribution with the initial conditions given by expression (9-1). We also decided to work in the field approach, then the way the initial condition in (9-1) is translated to initial conditions for the SFDM is given in appendix G.

9.2. Initial condition for the SFDM model

Our main porpoise in this section is to consider correct initial conditions for the SFDM model. Typically, a solver for the SchP system considers a discretization of the space-time coordinates, in such case we should have a complete profile for the initial conditions of the SFDM in all space. Notice that, if we would like to use equation (9-1) for our initial conditions, we should deal with the problem that for such configurations, there exist a region where the perturbations are strongly non-linear ($\delta M/M > 1$). For such reason, we can consider the following simplification: As we already saw, in the hydrodynamical description, the only difference between the SFDM model (in the free field limit) and the Λ CDM model is the quantum potential term. If we concentrate in a small perturbation $\Delta M/M \ll 1$, we could consider that for such mass shell we could neglect its quantum potential term, and then, describes its dynamics in the same way that is described the Λ CDM model. In that limit, the SFDM model should be described by the cycloid solution

$$r_i = \frac{3r_i(r_{init}^i)}{10\Delta_i(t_{init})}(1 - \cos \theta_i), \quad t = \frac{3t_{init}}{4(5\Delta_i(t_{init})/3)^{3/2}}(\theta_i - \sin \theta_i), \quad (9-7)$$

where t_{init} and $r_i(t_{init})$ is given by the time where $\Delta(t_{init}^i) \equiv \delta M_i/M_i \ll 1$, and subindex i refers to different shells enclosing a mass M_i . At that time, the velocity of each shell is given by

$$v_i \equiv \frac{dr_i}{dt} = H_i r_i [1 - \Delta_i(t_{init})/3] \quad (9-8)$$

Observe that at time t_{init} , we could take an initial condition of the form (9-1), and concentrate in a shell with a particular mass M_c . We could follow its dynamics from the time it continues expanding and after collapsing. In general, the cycloidy solution allowed us to follow that dynamics until $r = 0$, however, we know *a priori* that before to reach such radius, the non-linear terms will take place and the shell should stop at a certain radius where a virialized structure should formed. With this idea, we can consider that the cycloid solution remains valid until $r_c(T_c) = R_c$, i.e. the radius of the cycloid solutions equals the radius of a core profile with a mass M_c . Then, we assume that the structures that exist for radius smaller than R_c is the soliton profile, whereas we can concentrate in the dynamics for shells with a mass greater than M_c . Such configurations should represent the infalling matter that will be aggregating to the final galaxy in order to increase its mass and size. In order to find what

is the mass enclosed at a certain radius at time T_c – the time when the shell with mass M_c reaches the radius R_c – we can notice that the value of the angle $\hat{\theta}_c$ when $r_c = R_c$, is given by

$$r_c(T_c) = \frac{3r_c(t_{init})}{10\Delta_c(t_{init})}(1 - \cos \hat{\theta}_c) = 9.9 \frac{\hbar^2}{Gm^2 M_c}, \quad (9-9)$$

which implies

$$\hat{\theta}_c = \arctan \left[1 - \frac{10}{3} \frac{R_c}{r_c(t_{init})} \delta_c(t_{init}) \right]. \quad (9-10)$$

And that happens at time T_c , given by

$$T_c = \frac{3t_{init}}{4(5\Delta_c(t_{init})/3)^{3/2}} \left[\hat{\theta}_c - \sin \hat{\theta}_c \right], \quad (9-11)$$

where we have introduced hat quantities to specify that such quantity is measured at time T_c . Observe that, after finding $\hat{\theta}_c$, we can calculate T_c from the above expression. On the other hand, for shells with a mass greater than M_c we have

$$T_c = \frac{3t_{init}}{4(5\Delta_i(t_{init})/3)^{3/2}} (\hat{\theta}_i - \sin \theta_i). \quad (9-12)$$

The above two relations imply

$$\frac{\hat{\theta}_i - \sin \hat{\theta}_i}{\Delta_i t_{init}^{3/2}} = \frac{\hat{\theta}_c - \sin \hat{\theta}_c}{\Delta_c t_{init}^{3/2}}, \quad (9-13)$$

whereas the radius and velocity for each shell is rewritten as

$$r_i(T_c) = \frac{3r_i(t_{init})}{10\Delta_i(t_{init})}(1 - \cos \hat{\theta}_i), \quad v_i(T_c) = \frac{2}{3} \frac{r_i(t_{init}) \sqrt{5\Delta_i(t_{init})/3}}{t_{init}} \left(\frac{\sin \hat{\theta}_i}{1 - \cos \hat{\theta}_i} \right). \quad (9-14)$$

Simplifying our calculations

Observe that if we concentrate in the perturbation with mass M_c , we can reexpress such mass as

$$M_c = M_b(1 + C), \quad (9-15)$$

where $C \equiv \delta M_c/M_c \ll 1$. In terms of this mass, our profile at time t_{init} can be re-expressed as

$$\Delta_i(t_{init}) = \left(\frac{M_i}{M_c} \right)^{-\epsilon} \left(\frac{C}{1 + C} \right). \quad (9-16)$$

The radius at which the shell with mass M_i is contained at time t_{init} is

$$r_i(t_{init}) = \left[\frac{3M_i(1 - \Delta_i(t_{init}))}{4\pi\bar{\rho}} \right]^{1/3} = \left[\frac{3M_i \left(1 - \left(\frac{C}{1+C} \right) \left(\frac{M_i}{M_c} \right)^{-\epsilon} \right)}{4\pi\bar{\rho}} \right]^{1/3}, \quad (9-17)$$

where $\bar{\rho}$ is the background density. Particularly at $r_c(t_{init})$

$$r_c(t_{init}) = \left[\frac{3M_c}{4\pi\bar{\rho}(1+C)} \right]^{1/3}. \quad (9-18)$$

Obtaining the SFDM initial conditions

The SchP solver we have access discretizes the space coordinate as $r(j) = jdr$. In that case, what we need is to know the value of the SFDM amplitude and phase at each radius $r(j)$. First at all, observe that, from (9-13) and (9-16), we can express the ratio M_i/M_c as

$$\frac{M_i}{M_c} = \left(\frac{\hat{\theta}_c - \sin \hat{\theta}_c}{\hat{\theta}_i - \sin \hat{\theta}_i} \right)^{2/3\epsilon}. \quad (9-19)$$

Then, from equation (9-14) we can find the value of $\hat{\theta}_c$ after imposing a value for $r_i(T_c) = r(j)$. In such case we have only one free parameter $\hat{\theta}_i$, which can be found by a shooting method. After that, we can obtain the value of the mass enclosed at such radius by considering the above relation, and the velocity for such shell once we consider equation (9-14). After knowing the mass enclosed at each radius $r(j)$, we obtained a density profile via the general formula

$$\rho(j+1) = \frac{1}{r(j+1)^2} \left[\frac{M(j+1) - M(j)}{2\pi dr} - \rho(j)r(j)^2 \right] \quad (9-20)$$

Our initial conditions for the hydrodynamical variables can be seen in figure 9-1. For such figures we used $\epsilon = 1/3$ to exemplify our procedure.

On the other hand, the field variables can be obtained simply by remembering that

$$|\psi| = \sqrt{\bar{\rho}}, \quad \int_{s_c}^{s_i} ds = m \int_{\hat{\theta}_c}^{\hat{\theta}_i} v \frac{dr}{d\hat{\theta}} d\hat{\theta}. \quad (9-21)$$

We showed in 9-2 the initial conditions for the field variables. We believe that such initial conditions represents a more physical cosmological initial condition for structure formation in the SFDM model.

What follows?

Now, I am modifying a SchP solver that I have at my disposal, in order to consider cosmological boundary conditions. After that, we can run our initial conditions and observe what kind of configurations are formed after they relax.

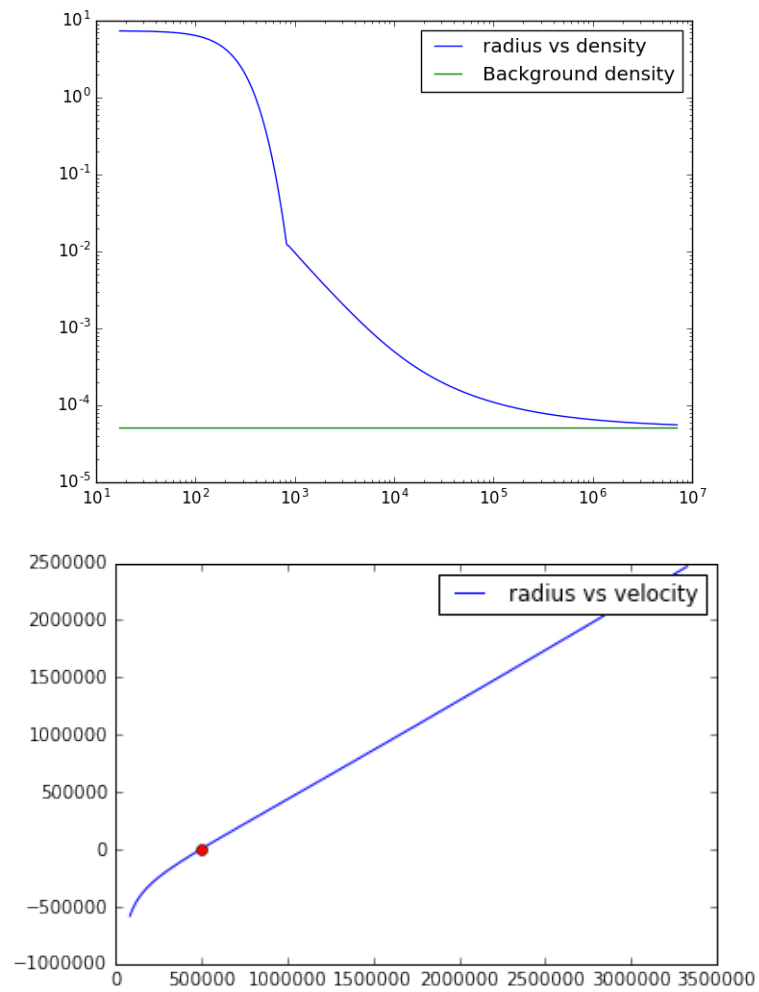


Figure 9-1.: (top) Radius vs density profile for the SFDM model at time T_c . (bottom) radius vs velocity for the SFDM at time T_c .

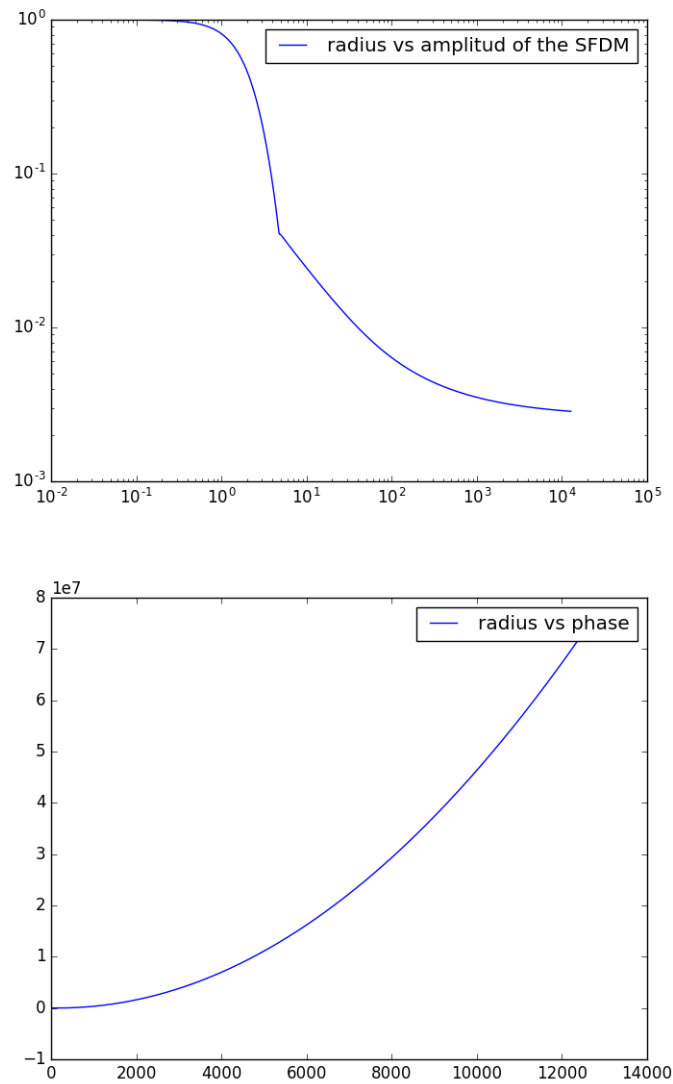


Figure 9-2.: (top) Amplitude for the SFDM in terms of radius at T_c . (bottom) Phase for the SFDM model as a function of radius at T_c .

A. Compendium of General Relativity

While gravity is negligibly weak on scales of individual particles, unlike the other forces of nature, it is also universal – acting on anything with mass or energy. For such property at cosmological and astrophysical scales the dominant force that governs the dynamics of all systems is gravity. In this appendix we shall review the main ideas of Einstein’s General theory of relativity.

For hundreds of years the concept of gravity could be well described by the Newton’s universal law of gravity

$$\partial_i \partial^i \Phi(x^i) = 4\pi G \rho(x^i) \tag{A-1}$$

in which the force of attraction is proportional to the masses of objects and inversely related to the square of distances. This description was very successful in modeling the orbital motion of Earth and the planets, validating the theory as the leading theory of gravity for several centuries, but it possesses several inconsistencies when it was tested with more accurate experiments. For example more precise experiments were carry out for the orbit of Mercury, finding that it precess in a way that could not be explained in Newton’s gravity. On the other hand, the concept of instantaneous force acting, which is follow immediately from Newton’s gravity, corresponds to a unreal description. In fact this problem was problem was known more-or-less since the inception of the Theory. For this discrepancies it was understood that it should be necessary to find a more general theory of gravity.

Einstein’s theory of General relativity solves all the problems that Newton’s law could not and then it is now accepted as the mainstream theory for gravity. It set aside the idea of instantaneous force acting and introduced the concept of curvature of the spacetime. In this context gravity can be understand as a geometric theory in which the fundamental objects of interest are mathematically modelled as tensor fields. The quantity encoding the gravitational potential in the theory is not longer the scalar gravitational potential Φ , but instead a four-dimensional symmetric metric tensor, $g_{\mu\nu}$. The “proper distance” between two neighboring points in spacetime is defined as

$$ds^2 = g_{\mu\nu} dx^\mu dx^\nu, \tag{A-2}$$

where dx^μ are tensors specifying the displacement in space and time between the two points. In the simplest case that the metric tensor can be written as $(-1, 1, 1, 1)$ – the Minkowsky metric $\eta_{\mu\nu}$ – we recover the special theory of Relativity. In the general way $g_{\mu\nu}$ encodes the geometry of the spacetime (as its curvature), and it manifests the “force” that objects feel

as a gravitational attraction. In reality, there is not a force in the Newtonian sense; objects simply move along geodesics of spacetime described by the metric, just as a free particle in classical physics moves along geodesics of the geometry of its surrounding, which happens to be typically flat. The difference in GR is that, in general, space is not a flat geometry and then geodesics are not in general the typical straight lines of the Newtonian world. The spacetime location of a test particle can be shown to obey the *geodesic equation*

$$\frac{d^2 x^\mu}{d\lambda^2} + \Gamma_{\alpha\beta}^\mu \frac{dx^\alpha}{d\lambda} \frac{dx^\beta}{d\lambda} = 0, \quad (\text{A-3})$$

where λ is an affine parameter. The Γ in the above equation are called the *Christoffel symbols* (Carroll, 2013) and are expressed in terms of the spacetime metric $g_{\mu\nu}$ as:

$$\Gamma_{\alpha\beta}^\mu = \frac{1}{2} g^{\mu\delta} (\partial_\alpha g_{\beta\delta} + \partial_\beta g_{\alpha\delta} - \partial_\delta g_{\alpha\beta}). \quad (\text{A-4})$$

They enter in the definition of the covariant derivative operator ∇_μ , whose action over a vector field v^ν and dual vector field ω_ν is respectively given by

$$\nabla_\mu v^\nu = \partial_\mu v^\nu + \Gamma_{\mu\rho}^\nu v^\rho, \quad (\text{A-5a})$$

$$\nabla_\mu \omega_\nu = \partial_\mu \omega_\nu - \Gamma_{\mu\nu}^\rho \omega_\rho. \quad (\text{A-5b})$$

In the general form for a tensor with contravariant indices $(\mu_1 \dots \mu_m)$ and covariant indices $(\nu_1 \dots \nu_n)$ we have

$$\begin{aligned} \nabla_\sigma T_{\nu_1, \dots, \nu_n}^{\mu_1, \dots, \mu_m} = & \frac{\partial T_{\nu_1, \dots, \nu_n}^{\mu_1, \dots, \mu_m}}{\partial x^\sigma} + \Gamma_{\rho\sigma}^{\mu_1} T_{\nu_1, \dots, \nu_n}^{\sigma, \dots, \mu_m} + \dots + \Gamma_{\rho\sigma}^{\mu_m} T_{\nu_1, \dots, \nu_n}^{\mu_1, \dots, \sigma} + \\ & - \Gamma_{\nu_1\sigma}^\rho T_{\rho, \dots, \nu_n}^{\mu_1, \dots, \mu_m} - \dots - \Gamma_{\nu_n\sigma}^\rho T_{\rho, \dots, \nu_n}^{\mu_1, \dots, \mu_m}. \end{aligned} \quad (\text{A-6})$$

Equation (A-3) can be understood as the generalisation of Newton's second law. The analogue to equation (A-1) in this context can be obtained always that we define some new quantities, such as the *Riemann Tensor*, which is defined by the action of the commutator of two covariant derivatives over a dual vector:

$$(\nabla_\mu \nabla_\nu - \nabla_\nu \nabla_\mu) \omega_\eta = R_{\mu\nu\eta}^\sigma \omega_\sigma. \quad (\text{A-7})$$

The Riemann tensor can be expressed in terms of Christoffel symbols as

$$R_{\mu\rho\nu}^\sigma = \partial_\rho \Gamma_{\mu\nu}^\sigma - \partial_\nu \Gamma_{\rho\nu}^\sigma + \Gamma_{\alpha\rho}^\sigma \Gamma_{\mu\nu}^\alpha - \Gamma_{\alpha\nu}^\sigma \Gamma_{\rho\mu}^\alpha. \quad (\text{A-8})$$

From this quantity it can be defined the Ricci tensor

$$R_{\mu\nu} = R_{\mu\sigma\nu}^\sigma = \partial_\sigma \Gamma_{\mu\nu}^\sigma - \partial_\nu \Gamma_{\sigma\nu}^\sigma + \Gamma_{\alpha\sigma}^\sigma \Gamma_{\mu\nu}^\alpha - \Gamma_{\alpha\nu}^\sigma \Gamma_{\sigma\mu}^\alpha, \quad (\text{A-9})$$

and then the Ricci scalar

$$R \equiv g^{\mu\nu} R_{\mu\nu}. \quad (\text{A-10})$$

The construction of this scalar measure of curvature is important since it allows us to introduce the Einstein-Hilbert action

$$S_G = \kappa \int d^4x \sqrt{-g} R, \quad (\text{A-11})$$

where g is the determinant of the metric and κ is a constant (for now). This action describes curvature from the geometry of the spacetime, and its variation with respect to the metric leads to Einstein's field equation in vacuum:

$$G_{\mu\nu} \equiv R_{\mu\nu} - \frac{1}{2} R g_{\mu\nu} = 0, \quad (\text{A-12})$$

where $G_{\mu\nu}$ is called the *Einstein tensor*, and is a symmetric, divergence-free, matrix of functions of the metric and its first and second derivatives. The extension needed to introduce the matter contribution in the Einstein equation is given when considering the total action

$$S = S_G + S_m, \quad (\text{A-13})$$

where

$$S_m = \int d^4x \sqrt{-g} \mathcal{L}_m, \quad (\text{A-14})$$

is the action due to the matter content in the system. The variation of (A-13) with respect to the metric tensor leads to

$$G_{\mu\nu} = \frac{1}{2\kappa} T_{\mu\nu}, \quad (\text{A-15})$$

where $T_{\mu\nu}$ is defined as the *energy-momentum tensor* for the matter content of the theory. It can be derived in terms of the lagrangial \mathcal{L}_m as

$$T_{\mu\nu} = -\frac{2\delta\sqrt{-g}\mathcal{L}_m}{\sqrt{-g}\delta g^{\mu\nu}} = g_{\mu\nu}\mathcal{L}_m - 2\frac{\delta\mathcal{L}_m}{\delta g^{\mu\nu}}, \quad (\text{A-16})$$

and is a covariant conserved quantity, i.e. it fulfills with

$$\nabla_\mu T^{\mu\nu} = 0, \quad (\text{A-17})$$

generalizing the Newton's idea of conservation of energy. On the constant term κ is fixed by requiring that in the weak gravitational limit we recover equation (A-1). From this it is found that $\kappa^{-1} = 16\pi G$.

Finally, one can also add a constant term Λ in the action (A-13) as

$$S = S_G + S_m + S_\Lambda, \quad (\text{A-18})$$

where

$$S_\Lambda = -16\pi G \int d^4x \sqrt{-g} \Lambda, \quad (\text{A-19})$$

which leads to the field equations

$$G_{\mu\nu} + \Lambda g_{\mu\nu} = 8\pi G T_{\mu\nu}. \quad (\text{A-20})$$

This extra term represents the vacuum energy of spacetime itself, which in general we can not assume that it is equal to zero and then it should gravitate according to GR.

B. Gauge invariant quantities

In this section we show the Gauge invariant quantities. From (Durrer, 2001) the gauge invariant energy-momentum perturbations are defined by

$$V \equiv \delta u - \frac{1}{k} \dot{H}_T = \delta u^{(longit)}, \quad (\text{B-1a})$$

$$\begin{aligned} D_g &\equiv \delta + 3(1 + \omega) \left(H_L + \frac{1}{3} H_T \right), \\ &= \delta^{(longit)} + 3(1 + \omega) \Phi, \end{aligned} \quad (\text{B-1b})$$

$$D \equiv \delta^{(longit)} + 3(1 + \omega), \quad (\text{B-1c})$$

$$\Gamma \equiv \pi_L - \frac{c_s^2}{\omega} \delta, \quad (\text{B-1d})$$

where (longit) labels perturbations in the longitudinal gauge.

The Einstein's equations rewritten in the above quantities are given by:

$$4\pi G a^2 \bar{\rho} D = k^2 \Phi, \quad (\text{B-2a})$$

$$4\pi G a^2 (\bar{\rho} + \bar{p}) V = k \left(\frac{a'}{a} \Psi - \Phi' \right), \quad (\text{B-2b})$$

$$8\pi G a^2 \bar{p} \Pi = -k^2 (\Phi + \Psi), \quad (\text{B-2c})$$

while from the energy-momentum conservation follows

$$D'_g + 3(c_s^2 - \omega) \frac{a'}{a} D_g + kV(1 + \omega) + 3 \frac{a'}{a} \omega \Gamma = 0, \quad (\text{B-3a})$$

$$V' = \frac{a'}{a} (3c_s^2 - 1)V + k [\Psi - 3c_s^2 \Phi] + \frac{c_s^2 k}{1 + \omega} D_g + \frac{\omega k}{1 + \omega} \left[\Gamma - \frac{2}{3} \Pi \right]. \quad (\text{B-3b})$$

The gauge invariant expression for the *comoving curvature perturbation* is given by

$$\mathcal{R} = H_L + \frac{1}{3} H_T + \frac{a'}{ak} (V - B). \quad (\text{B-4})$$

This is the perturbation to the intrinsic curvature scalar of comoving hypersurfaces: hypersurfaces orthogonal to the worldlines that comove with the total matter ($\delta u_i = 0$). In the case that the Universe is dominated by a SF, \mathcal{R} in gauge invariant form can be written as

$$\mathcal{R} = H_L + \frac{1}{3} H_T - \frac{a'}{a} \frac{\delta \phi}{\bar{\phi}'}. \quad (\text{B-5})$$

C. Bayesian statistics and parameter inference

As we explained in the thesis, Bayesian statistics is necessary to constraint different parameters for cosmological models. Then, in this appendix we briefly explain several basic concepts necessary to understand the parameter inference procedure with Bayesian statistics.

C.1. Bayesian vs Frequentist statistics

Fundamentally, the main difference between Bayesian and Frequentist statistics is on the definition of probability. From a Frequentist point of view, probability has meaning in limiting cases of repeated measurements

$$P = \frac{n}{N}, \tag{C-1}$$

where n denotes the number of successes and N the total number of trials. Frequentist statistics defines probability as the limit for the number of independent trials going to infinity. Then, **for Frequentist statistics, probabilities are fundamentally related to frequencies of events**. On the other hand, in Bayesian statistics the concept of probability is extended to cover degrees of certainty about a statement. **For Bayesian statistics, probabilities are fundamentally related to our knowledge about an event**.

Here we introduce some key concepts to understand the consequences this difference entails; for an extended review see (Heavens, 2009, Trotta, 2008, 2017, Verde, 2010). Let x be a random variable related to a particular event and $P(x)$ its corresponding probability distribution, for both cases the same rules of probabilities apply¹:

$$P(x) \geq 0, \tag{C-2a}$$

$$\int_{-\infty}^{\infty} dx P(x) = 1. \tag{C-2b}$$

For *mutually exclusive* events we have

$$P(x_1 \cup x_2) = P(x_1) + P(x_2), \tag{C-2c}$$

¹These rules are defined for a continuous variable; however, the corresponding discrete definition can be given immediately by replacing $\int dx \rightarrow \sum$.

but in general

$$P(x_1 \cup x_2) = P(x_1) + P(x_2) - P(x_1 \cap x_2).$$

These rules are summed up as follow. The first condition (C-2a) is necessary due to the probability of having an event is always positive. The second rule (C-2b) is a normalized relation, which tells us that we are certain to obtain one of the possible outcomes. Now, in the third point (C-2c) we have that the probability of obtaining an observation, from a set of mutually exclusive events, is given by the individual probabilities of each event. Finally, and in general, if one event occurs *given* the occurrence of another then the probability that both x_1 and x_2 happen is equal to the probability of x_1 times the probability of x_2 given that x_1 has already happened

$$P(x_1 \cap x_2) = P(x_1)P(x_2|x_1). \quad (\text{C-2d})$$

If two events x_1 and x_2 are mutually exclusive then

$$P(x_1 \cap x_2) = 0 = P(x_2 \cap x_1). \quad (\text{C-3})$$

The rules of probability distributions must be fulfilled by both Frequentist and Bayesian statistics. However, there are some consequences derived by the fact these two scenarios have a different definition of probability, as we shall see.

C.1.1. Frequentist statistics

Any frequentist inferential procedure relies on three basic ingredients: the data, the model and an estimation procedure. The main assumption in Frequentist statistics is that the data has a definite, albeit unknown, underlying distribution to which all inference pertains.

The **data** is a measurement or observation, denoted by X , that can take any value from a corresponding sample space. A **sample space** of an observation X can be defined as a measurable space (x, \hat{B}) that contains all values that X can take upon measurement. In Frequentist statistics it is considered that there is a probability function $P_0 : \hat{B} \rightarrow [0, 1]$ in the sample space (x, \hat{B}) representing the “true distribution of the data”

$$X \sim P_0.$$

Now there is the model. For Frequentist statistics the **model** Q is a collection of probability measurements $P_\theta : \hat{B} \rightarrow [0, 1]$ in the sample space (x, \hat{B}) . The distributions P_θ are called *model distributions*, with θ as the model parameters; in this approach θ is unchanged. A model Q is said to be well-specified if it contains the true distribution of the data P_0 , i.e.

$$P_0 \in Q.$$

Finally, we need a point-estimator (or estimator) for P_0 . An *estimator* for P_0 is a map $\hat{P} : x \rightarrow Q$, representing our “best guess” $\hat{P} \in Q$ for P_0 based on the data X .

Frequentist	Bayesian
Data are a repeatable random sample. There is a frequency.	Data are observed from the realized sample.
Underlying parameters remain constant during this repeatable process.	Parameters are unknown and described probabilistically.
Parameters are fixed.	Data are fixed.

Table C-1.: Main differences between the Bayesian and Frequentist interpretations.

Hence, the Frequentist statistics is based on trying to answer the following questions: “what the data is trying to tell us about P_0 ?” or “considering the data, what can we say about the mean value of P_0 ?”.

C.1.2. Bayesian statistics

In Bayesian statistics, data and model are two elements of the same space, i.e. no formal distinction is made between measured quantities X and parameters θ . One may envisage the process of generating a measurement’s outcome $Y = y$ as two draws, one draw for Θ (where Θ is a model with associated probabilities to the parameter θ) to select a value of θ and a subsequent draw for P_θ to arrive at $X = x$. This perspective may seem rather absurd in view of the definitions for a Frequentist way of thinking, but in Bayesian statistics where probabilities are related to our own knowledge, it results natural to associate probability distributions to our parameters. In this way an element P_θ of the model is interpreted simply as the distribution of X given the parameter value θ , i.e. as the conditional distribution $X|\theta$.

Table C-1 provides a short summary of the most important differences between the two statistics.

C.2. A first look at Bayesian statistics

Before we apply Bayesian statistics in cosmology it is necessary to understand the most important mathematical tools in the Bayesian procedure. In this section, we present an informal revision but encourage the reader to look for the formal treatment in the literature, cited in each section.

C.2.1. Bayes theorem, priors, posteriors and all that stuff

When anyone is interested on the Bayesian framework, there are several concepts to understand before presenting the results. In this section we quickly review these concepts.

The Bayes theorem. The Bayes theorem is a direct consequence of the axioms of probability shown in Eqs. (C-2). From Eqn. (C-2d), without loss of generality, it must be fulfilled that $P(x_1 \cap x_2) = P(x_2 \cap x_1)$. In such case the following relation applies

$$P(x_2|x_1) = \frac{P(x_1|x_2)P(x_2)}{P(x_1)}. \quad (\text{C-4})$$

As already mentioned, in the Bayesian framework data and model are part of the same space. Given a model (or hypothesis) H , considering $x_1 \rightarrow D$ as a set of data, and $x_2 \rightarrow \theta$ as the parameter vector of said hypothesis, we can rewrite the above equation as

$$P(\theta|D, H) = \frac{P(D|\theta, H)P(\theta|H)}{P(D|H)}. \quad (\text{C-5})$$

This last relation is the so-called **Bayes theorem** and the most important tool in a Bayesian inference procedure. In this result, $P(\theta|D, H)$ is called the **posterior** probability of the model. $P(D|\theta, H) \equiv L(D|\theta, H)$ is called the **likelihood** and it will be our main focus in future sections. $P(\theta|H) \equiv \pi(\theta)$ is called the **prior** and expresses the knowledge about the model before acquiring the data. This prior can be fixed depending on either previous experiment results or the theory behind. $P(D|H) \equiv \mathcal{Z}$ is the evidence of the model, usually referred as the **Bayesian Evidence**. We notice that this evidence acts only as a normalizing factor, and is nothing more than the average of the likelihood over the prior

$$P(D|H) = \int d^N \theta P(D|\theta, H)P(\theta|H), \quad (\text{C-6})$$

where N is the dimensionality of the parameter space. This quantity is usually ignored, for practical reasons, when testing the parameter space of a unique model. Nevertheless, the Bayesian evidence plays an important role for selecting the model that best “describes” the data, known as *model selection*. For convenience, the ratio of two evidences

$$K \equiv \frac{P(D|H_0)}{P(D|H_1)} = \frac{\int d^{N_0} \theta_0 P(D|\theta_0, H_0)P(\theta_0|H_0)}{\int d^{N_1} \theta_1 P(D|\theta_1, H_1)P(\theta_1|H_1)} = \frac{\mathcal{Z}_0}{\mathcal{Z}_1}, \quad (\text{C-7})$$

or equivalently the difference in log evidence $\ln \mathcal{Z}_0 - \ln \mathcal{Z}_1$ is often termed as the **Bayes factor** $\mathcal{B}_{0,1}$:

$$\mathcal{B}_{0,1} = \ln \frac{\mathcal{Z}_0}{\mathcal{Z}_1}, \quad (\text{C-8})$$

where θ_i is a parameter vector (with dimensionality N_i) for the hypothesis H_i and $i = 0, 1$. In Eqn. (C-8), the quantity $\mathcal{B}_{0,1} = \ln K$ provides an idea on how well model 0 may fit the

$ \mathcal{B}_{0,1} $	Odds	Probability	Strength
< 1.0	$< 3 : 1$	< 0.750	Inconclusive
1.0-2.5	$\sim 12 : 1$	0.923	Significant
2.5-5.0	$\sim 150 : 1$	0.993	Strong
> 5.0	$> 150 : 1$	> 0.993	Decisive

Table C-2.: Jeffreys guideline scale for evaluating the strength of evidence when two models are compared.

data when is compared to model 1. Jeffreys provided a suitable guideline scale on which we are able to make qualitative conclusions (see Table C-2).

We can see that Bayes theorem has an enormous implication with respect to a statistical inferential point of view. In a typical scenario we collect some data and hope to interpret it with a given model, however, we usually do the opposite. That is, first we have a set of data and then we can confront a model considering the probability that our model fits the data. Bayes theorem provides a tool to relate both scenarios. Then, thanks to the Bayes theorem, in principle, we are able to select the model that best fits the data.

C.2.2. Updating the probability distribution

In general we won't be able to get the real value of a given parameter p because the lack of enough data. Given this, it is clear that in order to confront a parameter model and be more accurate about the most probable (or "real") value, it is necessary to increase the amount of data (and the precision) in any experiment. Then, we have some model parameters that have to be confronted with different sets of data. This can be done in two alternative ways: (a) by considering the sum of all datasets we have; or (b) by taking each data set as the new data, but our prior information updated by the previous information. The important point in Bayesian statistics is that it is indeed equivalent to choose any of these two possibilities.

In fact, if we rewrite Bayes theorem so that all probabilities are explicitly dependent on some prior information I (Heavens, 2009)

$$P(\theta|DI, H) = \frac{P(\theta|I, H)P(DI|\theta, H)}{P(D|I, H)}, \quad (\text{C-9})$$

and then we consider a new set of data D' , letting the old data become part of the prior information $I' = DI$, we arrive at

$$P(\theta|D'I', H) = \frac{P(\theta|I, H)P(DD'I|\theta, H)}{P(DD'|I, H)} = P(\theta|[DD']I, H), \quad (\text{C-10})$$

where we can explicitly see the equivalence of the two different options.

C.2.3. About the Likelihood

We mentioned that the Bayesian evidence is usually set apart when doing any inference procedure in the parameter space of a single model. Then, without loss of generality, we can fix it to $P(D|H) = 1$. If we ignore the prior² we can identify the posterior with the likelihood $P(\theta|D, H) \propto L(D|\theta, H)$ and thus, by maximizing it, we can find the most probable set of parameters for a model given the data. However, having ignored $P(D|H)$ and the prior, we are not able to provide an absolute probability for a given model, but only relative probabilities. On the other hand, it is possible to report results independently of the prior by using the *Likelihood ratio*. The likelihood at a particular point in the parameter space can be compared with the best-fit value, or the maximum likelihood L_{max} . Then, we can say that some parameters are acceptable if the likelihood ratio

$$\Lambda = -2 \ln \left[\frac{L(D|\theta, H)}{L_{max}} \right], \quad (\text{C-11})$$

is bigger than a given value.

Let us assume we have a Gaussian posterior distribution, which is single-peaked. We consider that $\hat{\theta}$ is the **mean** of the distribution

$$\hat{\theta} = \int d\theta \theta P(\theta|D, H). \quad (\text{C-12})$$

If our model is well-specified and the expectation value of $\hat{\theta}$ corresponds to the real or most probable value θ_0 , we have

$$\langle \hat{\theta} \rangle = \theta_0, \quad (\text{C-13})$$

then we say that $\hat{\theta}$ is *unbiased*. Considering a Taylor expansion of the *log likelihood* around its maximum

$$\ln L(D|\theta) = \ln L(D|\theta_0) + \frac{1}{2}(\theta_i - \theta_{0i}) \frac{\partial^2 \ln L}{\partial \theta_i \partial \theta_j} (\theta_j - \theta_{0j}) + \dots, \quad (\text{C-14})$$

where θ_0 corresponds to the parameter vector of the real model. In this manner, we have that the likelihood can be expressed as a multi-variable likelihood given by

$$L(D|\theta) = L(D|\theta_0) \exp \left[-\frac{1}{2}(\theta_i - \theta_{0i}) H_{ij} (\theta_j - \theta_{0j}) \right], \quad (\text{C-15})$$

where

$$H_{ij} = -\frac{\partial^2 \ln L}{\partial \theta_i \partial \theta_j}, \quad (\text{C-16})$$

is called the **Hessian matrix** and it controls whether the estimates of θ_i and θ_j are correlated. If it is diagonal, these estimates are uncorrelated.

²It is expected that the real value of any given parameter for a large enough dataset is independent of the prior.

The above expression for the likelihood is a good approximation as long as our posterior distribution possesses a single-peak. It is worth mentioning that, if the data errors are normally distributed, then the likelihood for the data will be a Gaussian function as well. In fact, this is always true if the model is linearly dependent on the parameters. On the other hand, if the data is not normally distributed we can resort to the central limit theorem. In this way, the central limit theorem tell us that the resulting distribution will be best approximated by a multi-variate Gaussian distribution (Verde, 2010).

C.2.4. Letting aside the priors

In this section we present an argument for letting aside the prior in the parameter estimation. For this, we follow the example given in (Trotta, 2008). In this example there are two people, A and B, that are interested in the measurement of a given physical quantity θ . A and B have different prior beliefs regarding the possible value of θ . This discrepancy could be given by the experience, such as the possibility that A and B have made the same measurement at different times. Let us denote their priors by $P(\theta|I_i)$, ($i = A, B$), and assume they are described by two Gaussian distributions with mean μ_i and variance Σ_i^2 . Now, A and B make a measurement of θ together using an apparatus subject to a Gaussian noise with known variance σ . They obtain the value $\theta_0 = m_1$. Therefore they can write their likelihoods for θ as

$$L(D|\theta, HI) = L_0 \exp \left[-\frac{1}{2} \frac{(\theta - m_1)^2}{\sigma^2} \right]. \quad (\text{C-17})$$

By using the Bayes formula, the posterior of the model A (and B) becomes

$$P(\theta|m_1) = \frac{L(m_1|\theta I_i)P(\theta|I_i)}{P(m_1|I_i)}, \quad (\text{C-18})$$

where we have skipped writing explicitly the hypothesis H and used the notation given in Eqn. (C-9). Then, the posterior of A and B are (again) Gaussian with mean

$$\hat{\mu}_i = \frac{m_1 + (\sigma/\Sigma_i)^2 \mu_i}{1 + (\sigma/\Sigma_i)^2}, \quad (\text{C-19})$$

and variance

$$\tau_i^2 = \frac{\sigma^2}{1 + (\sigma/\Sigma_i)^2}, \quad (i = A, B). \quad (\text{C-20})$$

Thus, if the likelihood is more informative than the prior i.e. $(\sigma/\Sigma_i) \ll 1$ the posterior mean of A (and B) will converge towards the measured value, m_1 . As more data are obtained one can simply replace the value of m_1 in the above equation by the mean $\langle m \rangle$ and σ^2 by σ^2/N . Then, we can see that the initial prior μ_i of A and B will progressively be overridden by the data. This process is illustrated in Figure C-1 where the green (red) curve corresponds to the probability distribution of θ for person A (B) and the blue curve corresponds to their likelihood.

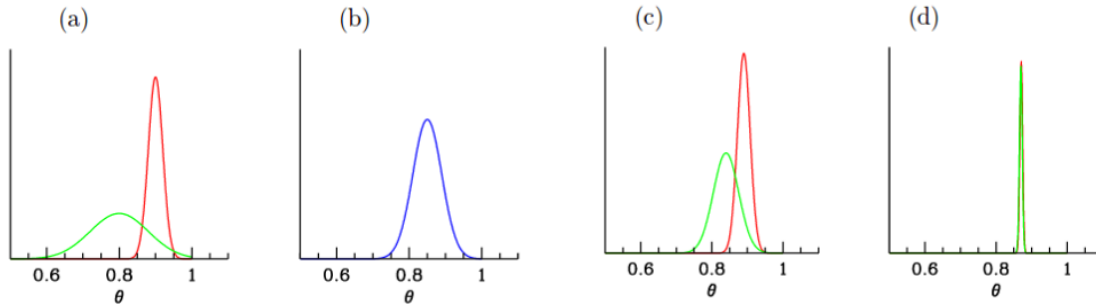


Figure C-1.: Converging views in Bayesian inference (taken from (Trotta, 2008)). A and B have different priors $P(\theta|I_i)$ for a value θ (panel (a)). Then, they observe one datum with an apparatus subject to a Gaussian noise and they obtained a likelihood $L(\theta; HI)$ (panel (b)), after which their posteriors $P(\theta|m_1)$ are obtained (panel (c)). Then, after observing 100 data, it can be seen how both posteriors are practically indistinguishable (panel (d)).

C.2.5. Chi-square and goodness of fit

We mentioned the main aim of parameter estimation is to maximize the likelihood in order to obtain the most probable set of model parameters, given the data. If we consider the Gaussian approximation given in Eqn. (C-15) we can see the likelihood will be maximum if the quantity

$$\chi^2 \equiv (\theta_i - \theta_{0i})H_{ij}(\theta_j - \theta_{0j}), \quad (\text{C-21})$$

is minimum. The quantity χ^2 is usually called **chi-square** and is related to the Gaussian likelihood via $L = L_0 e^{-\chi^2/2}$. Then, we can say that maximizing the Gaussian likelihood is equivalent to minimizing the chi-square. However, as we mentioned before, there are some circumstances where the likelihood cannot be described by a Gaussian distribution, in these cases the chi-square and the likelihood are no longer equivalent.

The probability distribution for different values of χ^2 around its minimum, is given by the χ^2 distribution for $v = n - M$ degrees of freedom, where n is the number of independent data points and M the number of parameters. Hence, we can calculate the probability that an observed χ^2 exceeds by chance a value $\hat{\chi}$ for the correct model. This probability is given by $Q(v, \hat{\chi}) = 1 - \Gamma(v/2, \hat{\chi}/2)$ (Press et al., 2007), where Γ is the incomplete Gamma function. Then, the probability that the observed χ^2 (even the correct model) is less than a given value $\hat{\chi}^2$ is $1 - Q$. This statement is strictly true if the errors are Gaussian and the model is a linear function of the likelihood, i.e., for Gaussian likelihoods.

If we evaluate the quantity Q for the best-fit values (minimum chi-square) we can have a measure of the goodness of fit. If Q is small (small probability) we can interpret it as:

- The model is wrong and can be rejected.
- The errors are underestimated.

σ	p	$\Delta\chi^2$		
		$M = 1$	$M = 2$	$M = 3$
1	68.3%	1.00	2.30	3.53
2	95.4%	4.00	6.17	8.02
3	99.73%	9.00	11.8	14.20

Table **C-3**.: $\Delta\chi^2$ for the conventional 68.3%, 95.4% and 99.73% as a function of the number of parameters (M) for the joint confidence level.

- The error measurements are not normally distributed.

On the other hand, if Q is too large there are some reasons to believe that:

- Errors have been overestimated.
- Data are correlated or non-independent.
- The distribution is non-Gaussian.

C.2.6. Contour plots and confidence regions

Once the best fit parameters are obtained we would like to know the confidence regions where values could be considered good candidates for our model. The most logical election is to take values inside a compact region around the best fit value. Then, a natural choice are regions with constant χ^2 boundaries. When the χ^2 possesses more than one minimum, it is said that we have non-connected confidence regions, and for multi-variate Gaussian distributions (as the likelihood approximation in Eqn. (C-15)) these are ellipsoidal regions. In this section we exemplify how to calculate the confidence regions, following (Verde, 2010).

We consider a little perturbation from the best fit of chi-square $\Delta\chi^2 = \chi^2 - \chi_{best}^2$. Then we use the properties of χ^2 distribution to define confidence regions for variations on χ^2 to its minimum. In Table **C-3** we see the typical 68.3%, 95.4% and 99.73% confidence levels as a function of number of parameters M for the joint confidence level. For Gaussian distributions (as likelihood) these correspond to the conventional 1, 2 and 3 σ confidence levels.

The general recipe to compute constant χ^2 confidence regions is as follows: after finding the best fit by minimizing χ^2 (or maximizing the likelihood) and checking that Q is acceptable for the best parameters, then:

1. Let M be the number of parameters, n the number of data and p be the confidence limit desired.

2. Solve the equation:

$$Q(n - M, \min(\chi^2) + \Delta\chi^2) = p. \quad (\text{C-22})$$

3. Find the parameter region where $\chi^2 \leq \min(\chi^2) + \Delta\chi^2$. This defines the confidence region.

C.2.7. Marginalization

It is clear that a model may (in general) depend on more than one parameter. However, some of these parameters θ_i may be of less interest. For example, they may correspond to nuisance parameters like calibration factors, or it may be the case that we are interested in only one of the parameter constraints rather than the joint of two or more of them simultaneously. Then we **marginalize** over the uninteresting parameters by

$$P(\theta_1, \dots, \theta_j, H|D) = \int d\theta_{j+1} \dots d\theta_m P(\theta, H|D), \quad (\text{C-23})$$

where m is the total number of parameters in our model and $\theta_1, \dots, \theta_j$ denote the parameters we are interested in.

C.3. Numerical tools

In typical scenarios it results very difficult to compute the posterior distribution analytically. For these cases the numerical tools available play an important role during the parameter estimation task. There exist several options to carry out this work, nevertheless in this section we focus only on the Markov Chain Monte Carlo (MCMC) with the Metropolis Hastings algorithm (MHA). Additionally, in this section we present some useful details we take into account to make more efficient our computation.

C.3.1. MCMC techniques for parameter inference

The purpose of a MCMC algorithm is to build up a sequence of points (called “**chain**”) in a parameter space in order to evaluate the posterior of Eqn. (C-5). In this section we review the basic results for this procedure in a simplistic way, but for curious readers it is recommendable to check (Gelman et al., 2013, Gilks et al., 1995, Ross, 2014, Tanner, 2012) for the Markov chain theory.

A **Monte Carlo** simulation is assigned to algorithms that use random number generators to approximate a specific quantity. On the other hand, a sequence X_1, X_2, \dots of elements of some set is a **Markov Chain** if the conditional distribution of X_{n+1} given X_1, \dots, X_n depends only on X_n . In other words, a Markov Chain is a process where we can compute subsequent steps based only in the information given at the present. An important property of a Markov Chain is that it converges to a stationary state where successive elements of

the chain are samples from the target distribution, in our case it converges to the posterior $P(\theta|D, H)$. In this way we can estimate all the usual quantities of interest out of it (mean, variance, etc).

The combination of both procedures is called a **MCMC**. The number of points required to get good estimates in MCMCs is said to scale linearly with the number of parameters, so this method becomes much faster than grids as the dimensionality increases.

The target density is approximated by a set of delta functions

$$p(\theta|D, H) \simeq \frac{1}{N} \sum_{i=1}^N \delta(\theta - \theta_i), \quad (\text{C-24})$$

being N the number of points in the chain. Then, the posterior mean is computed as

$$\langle \theta \rangle = \int d\theta \theta P(\theta, H|D) \simeq \frac{1}{N} \sum_{i=1}^N \theta_i, \quad (\text{C-25})$$

where \simeq follows because the samples θ_i are generated out of the posterior by construction. Then, we can estimate any integrals (such as the mean, variance, etc.) as

$$\langle f(\theta) \rangle \simeq \frac{1}{N} \sum_{i=1}^N f(\theta_i). \quad (\text{C-26})$$

As mentioned before, in a Markov Chain it is necessary to generate a new point θ_{i+1} from the present point θ_i . However, as it is expected, we need a criteria for accepting (or refusing) this new point depending on whether it turns out to be better for our model or not. If this new step is worse than the previous one, we may accept it, since it could be the case that, if we only accept steps with better probability, we could be converging into a local maximum in our parameter space and, therefore, not completely mapping all of it. The simplest algorithm that contains all this information in its methodology is known as the Metropolis-Hastings algorithm.

C.3.2. Metropolis-Hastings algorithm

In the **Metropolis-Hastings algorithm** (Hastings, 1970, Metropolis et al., 1953) it is necessary to start from a random initial point θ_i , with an associated posterior probability $p_i = p(\theta_i|D, H)$. We need to propose a candidate θ_c by drawing from a **proposal distribution** $q(\theta_i, \theta_c)$ used as a generator of new random steps. Then, the probability of acceptance the new point is given by

$$p(\text{acceptance}) = \min \left[1, \frac{p_c q(\theta_c, \theta_i)}{p_i q(\theta_i, \theta_c)} \right]. \quad (\text{C-27})$$

If the proposal distribution is symmetric the algorithm is reduced to the *Metropolis algorithm*

$$p(\text{acceptance}) = \min \left[1, \frac{p_c}{p_i} \right]. \quad (\text{C-28})$$

In this way the complete algorithm can be expressed by the following steps:

1. Choose a random initial condition θ_i in the parameter space and compute the posterior distribution.
2. Generate a new candidate from a proposal distribution in the parameter space and compute the corresponding posterior distribution.
3. Accept (or not) the new point with the help of the Metropolis-Hastings algorithm.
4. If the point is not accepted, repeat the previous point in the chain.
5. Repeat steps 2-4 until you have a large enough chain.

C.3.3. Convergence test

It is clear that we need a test to know when our chains have converged. We need to verify that the points in the chain are not converging to a “false convergent point” or to a local maximum point. In this sense, we need that our algorithm takes into account this possible difficulty. The simplest way (the informal way) to know if our chain is converging to a global maximum is by running several chains starting with different initial proposals for the parameters we are interested in. Then, if we see by naked eye, that all the chains seem to converge into a single region of the possible value for our parameter, we may say that our chains are converging to that region.

The convergence method explained above is very informal and we would like to have a better way to ensure that our result is correct. The usual test is the *Gelman-Rubin* convergence criterion (Brooks and Gelman, 1998, Gelman et al., 1992). That is, by starting with M chains with very different initial points and N points per chain, if θ_i^j is a point in the parameter space of position i and belonging to the chain j , we need to compute the mean of each chain

$$\langle \theta^j \rangle = \frac{1}{N} \sum_{i=1}^N \theta_i^j, \quad (\text{C-29})$$

and the mean of all the chains

$$\langle \theta \rangle = \frac{1}{NM} \sum_{i=1}^N \sum_{j=1}^M \theta_i^j. \quad (\text{C-30})$$

Then, the chain-to-chain variance B is

$$B = \frac{1}{M-1} \sum_{j=1}^M (\langle \theta^j \rangle - \langle \theta \rangle)^2, \quad (\text{C-31})$$

and the average variance of each chain is

$$W = \frac{1}{M(N-1)} \sum_{i=1}^N \sum_{j=1}^M (\theta_i^j - \langle \theta^j \rangle)^2. \quad (\text{C-32})$$

If our chains converge, W and B/N must agree. In fact we say that the chains converge when the quantity

$$\hat{R} = \frac{\frac{N-1}{N}W + B(1 + \frac{1}{M})}{W}, \quad (\text{C-33})$$

which is the ratio of the two estimates, approaches unity. A typical convergence criteria is when $0.97 < \hat{R} < 1.03$.

C.3.3.1. Some useful details

The proposal distribution. The choice of a proposal distribution q is crucial for the efficient exploration of the posterior. If the scale of q is too small compared to the scale of the target (in the sense that the typical jump is small), then the chain may take very long to explore the target distribution which implies that the algorithm will be very inefficient. On the other hand, if the scale of q is too large, the chain gets stuck and it does not jump very frequently, so we will have different “peaks” in our posterior.

In order to fix this issue in a more efficient way, it is recommendable to run an exploratory MCMC, compute the covariance matrix from the samples, and then re-run with this covariance matrix as the covariance of a multivariate Gaussian proposal distribution. This process can be computed a couple of times before running the “real” MCMC.

The burn-in. It is important to notice that at the beginning of the chain we will have a region of points outside the stationary region (points inside the ellipse in the right panel of Figure ??). This early part of the chain (called “burn-in”) must be ignored, this means that the dependence on the starting point must be lost. Thus, it is important to have a reliable convergence test.

More samplers. The generation of the elements in a Markov chain is probabilistic by construction and it depends on the algorithm we are working with. The MHA is the easiest algorithm used in Bayesian inference. However, there are several algorithms that can help us to fulfill our mission. For instance, some of the most popular and effective ones, are the Hamiltonian Monte Carlo (see e.g. (Hanson, 2001, Neal et al., 2011)) or the Adaptive Metropolis-Hastings (AMH) (see e.g. (Tokdar and Kass, 2010)).

D. The attractor behaviour for the SFDM candidate

In this appendix we comment about the attractor behaviour of the strong-self-interacting SFDM during inflation. For this purpose let us remember the dynamical equations that the Universe follows when it contains only two real scalar fields ϕ and φ . In that case the Universe is described by the Friedmann and Klein-Gordon differential equations

$$H^2 = \frac{8\pi}{3m_{pl}^2} \left[\frac{1}{2}\dot{\phi}^2 + \frac{1}{2}\dot{\psi}^2 + V(\phi, \varphi) \right], \quad (\text{D-1a})$$

$$\ddot{\phi}_i + 3H\dot{\phi}_i + V_{,\phi_i} = 0 \quad (\text{D-1b})$$

where $\dot{\phi}_i \equiv d\phi_i/dt$, $V_{,\phi_i} \equiv dV/d\phi_i$, and $\phi_{1,2} = \phi, \varphi$. In what follows we consider the full potential $V(\phi, \varphi) \simeq \hat{V}(\phi) + \mu^2\varphi^2/2 + \nu\varphi^4/4$.

In the inflationary scenario, it is assumed that the Universe is dominated by the inflaton and that it is slowly-rolling during that process, i.e. that the slow-roll parameters

$$\epsilon_\phi \equiv \frac{m_{pl}^2}{16\pi} \left(\frac{V_{,\phi}}{V} \right)^2, \quad \eta_\phi \equiv \frac{m_{pl}^2}{8\pi} \left(\frac{V_{,\phi\phi}}{V} \right) \quad (\text{D-2a})$$

are small ($\epsilon_\phi \ll 1$ and $\eta_\phi \ll 1$). In that case the Friedmann equation and the KG equation associated to the inflaton are reduced to

$$H^2 \simeq \frac{\hat{V}(\phi)}{3M_{pl}^2}, \quad (\text{D-2b})$$

$$3H\dot{\phi} + V_{,\phi} = 0, \quad (\text{D-2c})$$

while the dynamics for the SFDM continue being, in general, described by equation (D-1b).

D.1. Justifying the slow-roll condition for the SFDM candidate

In order to obtain a slowly-rolling SFDM during the inflationary process, it is necessary that it fulfills a similar relation that the one by the inflaton, i.e. the slow-roll parameters associated for the SFDM ϵ_φ and η_φ – defined in a similar way than in (D-2a) – being

small ($\epsilon_\varphi, \eta_\varphi \ll 1$). Considering that in the inflationary scenario $V \simeq \hat{V}$ and from (D-2b) $\hat{V} \simeq 3m_{pl}^2 H^2 / (8\pi)$, we obtain that the slow-roll parameters for the SFDM can be written as

$$\epsilon_\varphi \simeq 4\pi \left(\frac{\nu\varphi^3}{3m_{pl}^2 H_{inf}^2} \right)^2, \quad \eta_\varphi \simeq \frac{\nu\varphi^2}{H_{inf}^2}. \quad (\text{D-3})$$

where H_{inf} is the Hubble parameter at the epoch of inflation and we have considered that we are in the strong-self-interacting regime. Typically, the self-interacting parameter ν is very small (see section 4.5). In that case we can observe that the slow-roll condition can be fulfilled for most of the values of the field φ .

D.1.1. Attractor solution for the SFDM

The dynamic of the SFDM during inflation is described by equation (D-2c), but interchanging ϕ for φ . In that case notice that both fields must follow the relation

$$\frac{d\varphi}{V_{,\varphi}} = \frac{d\phi}{V_{,\phi}}. \quad (\text{D-4})$$

In the strong-self-interacting regime (where $V_{,\varphi} \simeq \nu\varphi^3$) the above equation results in

$$\frac{1}{\varphi^2} - \frac{1}{\varphi_{it}^2} = 2\nu \int_{\phi}^{\phi_{it}} \frac{d\phi}{V_{,\phi}}. \quad (\text{D-5})$$

Then, after enough time, the field φ becomes far smaller than φ_{it} and then the field reaches the attractor solution

$$\varphi_{att} = \left(2\nu \int_{\phi}^{\phi_{it}} V_{,\phi}^{-1} d\phi \right)^{-1/2}. \quad (\text{D-6})$$

Notice that the time needed to obtain the attractor behavior for the SFDM is described by the inflationary potential and the self-interaction parameter. Then, the attractor behavior is reached more quickly for the SFDM models with large self-interaction compared to models with small self-interaction. As an example, notice that when the SFDM has an extremely small self-interaction and if the inflationary period does not last for a long time, the attractor behavior is not reached and then the dynamics is described by (D-5). In fact, if the self-interaction is extremely small, we can approximate $\varphi_{end} \sim \varphi_{it}$, where φ_{end} is the value of φ at the end of inflation.

E. Self-Gravity in the Newtonian Limit of the Klein-Gordon-Poisson System

The fully relativistic regime of the system formed by a BH and a DM halo, ends up at small radii away from the centre. To give an idea of that, let us think in the Milky-Way, where $2M \sim 10^{-4} pc$. Therefore, at few parsecs away from the centre, the Newtonian limit is valid, that is for $r \gg 2M$ and the gravitational potential produced by the DM halo being $\Phi_h \ll 1$. The metric describing the space-time at such region is approximately:

$$ds^2 = - \left(1 - \frac{2M}{r} + \Phi_h \right) dt^2 + \left(1 + \frac{2M}{r} - \Phi_h \right) dr^2 + r^2 d\Omega^2, \quad (\text{E-1})$$

and the gravitational potential of the halo obeys the Poisson equation given by

$$\nabla^2 \Phi_h = 4\pi G \varphi^2, \quad (\text{E-2})$$

which in spherical symmetry can be approximated by

$$\begin{aligned} \frac{1}{r^2} \partial_r (r^2 \partial_r \Phi_h) &= 4\pi G \varphi^2, \\ &\sim \frac{3}{r^2} \Phi_h \sim 4\pi G \varphi^2. \end{aligned} \quad (\text{E-3})$$

On the other hand, the Klein-Gordon equation for the radial part of the scalar solution in this metric in the limit $r \gg 2M$ and $\Phi_h \ll 1$ reads

$$k_s^2 R + \frac{1}{r^2} \partial_r [r^2 \partial_r R] + \mu^2 \left(\frac{2M}{r} - \Phi_h \right) R = 0. \quad (\text{E-4})$$

After plugging (E-3) in the last equation we have

$$k_s^2 R + \frac{1}{r^2} \partial_r [r^2 \partial_r R] + \mu^2 \left[\frac{2M}{r} - r^2 \left(\frac{4\pi}{3} G \rho_s R^2 \right) \right] R = 0. \quad (\text{E-5})$$

Assuming that the observer is placed in a region nearby the BH influence radius r_0 (defined as $4\pi\rho_s r_0^2 R^2 = 2M/r_0$, $r_0 \sim 100 pc$ for the Milky Way), if $2M \ll r \ll \mu^{-1}$, the last term in equation (E-5) (which roughly accounts for self-gravity effects of the scalar halo nearby the centre) can be dropped away. In a region even further from the influence region, $R \sim \sin(k_s r)/r$, if $r < r_s$ and then $R \sim k_s$ and equation (E-5) becomes

$$k_s^2 R + \frac{1}{r^2} \partial_r [r^2 \partial_r R] + \mu^2 \left[\frac{2M}{r} - (k_s r)^2 \left(\frac{4\pi}{3} G \rho_s \right) \right] R = 0. \quad (\text{E-6})$$

Under the considered conditions, we have demonstrated that if $2M \ll r \ll r_s$, the last two terms in equation (E-6) can be ignored.

F. Gaussian vs polynomial semi-analytic approximations

Previous literature has made extensive use of two different analytic approaches for the central soliton in SFDM halos without self-interaction (the free case). On the one hand, there is a polynomial density distribution $\rho_c^{(p)}$ given by (Schive et al., 2014a)

$$\rho_c^{(p)}(r) = \frac{\rho_0}{\left(1 + 0.091 \left(\frac{r}{r_c}\right)^2\right)^8}, \quad (\text{F-1})$$

where ρ_0 is the central density of the soliton

$$\rho_0 = 1.93 \times 10^7 m_{22}^{-2} \left(\frac{r_c}{1 \text{ kpc}}\right)^{-4} M_\odot \text{ kpc}^{-3}, \quad (\text{F-2})$$

and the core radius r_c is defined as the radius where the mass density drops by a factor of 2 from its value at the origin

$$r_c \simeq \frac{2.27 \times 10^4}{(m_{22})^2 M_{c,7}} \text{ pc}. \quad (\text{F-3})$$

On the other hand, it has been noted that the soliton profile can be well approximated by a Gaussian density distribution $\rho_c^{(g)}$ (Chavanis, 2011)

$$\rho_c^{(g)}(r) = \frac{M_c}{(\pi R_c^2)^{3/2}} e^{-r^2/R_c^2}, \quad (\text{F-4})$$

where we take R_c in such a way that the radius that contains 99% of the mass of the Gaussian ansatz matches with the numerical solution. Then,

$$R_c \simeq \frac{3.54 \times 10^4}{(m_{22})^2 M_{c,7}} \text{ pc}. \quad (\text{F-5})$$

Observe from (2-50) and (2-51) that both cases, (F-1) and (F-4), follow the same re-scaling dependence $\rho_c^{(p)}, \rho_c^{(g)} \propto \gamma^{-4}$, as expected.

We can compare the above analytic profiles with the numerical solution. For that purpose, it is convenient to rewrite each approximation in terms of dimensionless variables (7-4), i.e. “hat” quantities, and by considering the solution that has a central SF value equal to 1. In this manner, we can compare each approximation with the numerical solution with $\gamma = 1$.

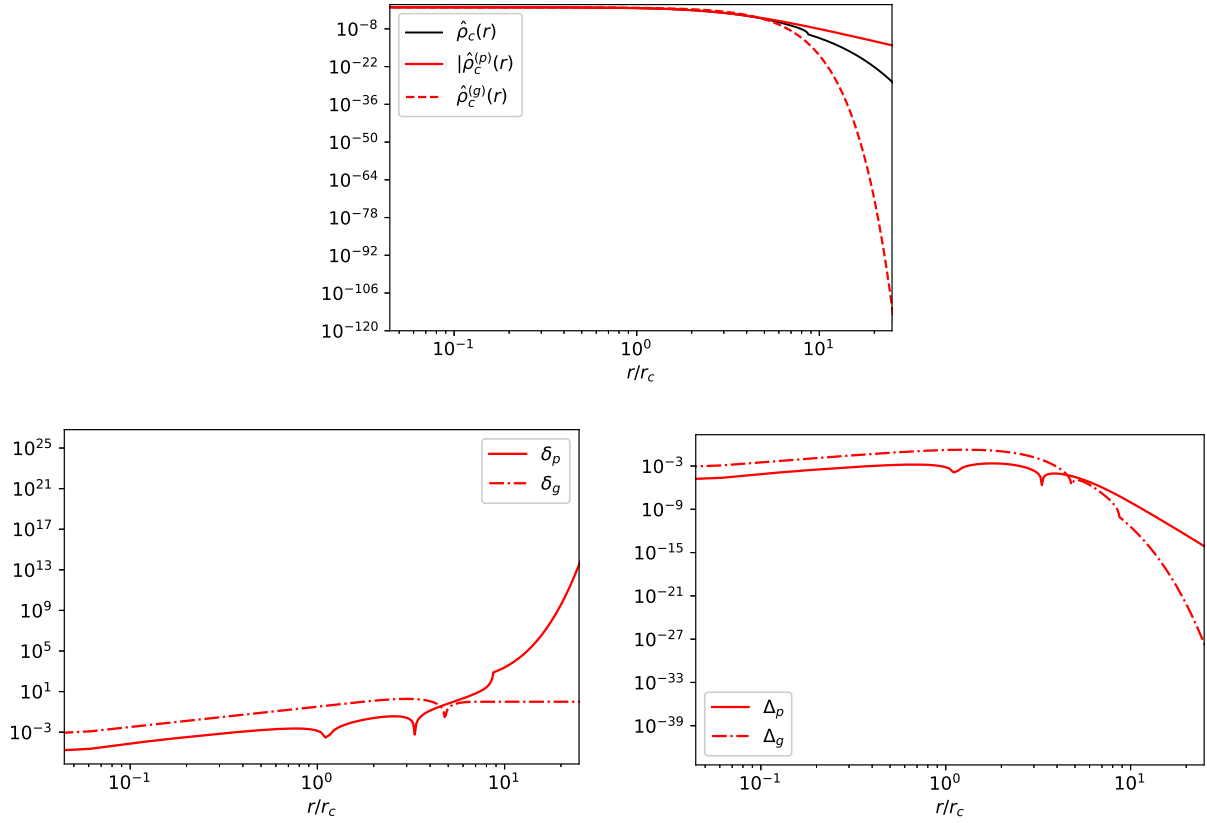


Figure **F-1.**: Polynomial (red solid) vs. Gaussian (red dashed) density distributions. In the top figure, we plot each case and the numerical solution (black solid), while in the bottom figures we plot the relative (left) and the absolute (right) errors for each approximation.

We emphasize that the analytic approach given in (F-1) results in a better approximation for the soliton at small \hat{r} than the Gaussian, as can be seen from figure **F-1**. In the top figure, we plot the dimensionless squared wave solution $|\hat{\psi}^{(1)}|^2$, where subscript 1 refers to $\gamma = 1$, together with the Gaussian and the polynomial approximations. The middle figure shows the relative error $\delta_i \equiv |\hat{\rho}_c^{(1)} - \hat{\rho}_c^{(i)}|/\hat{\rho}_c^{(i)}$, $i = p, g$, while the bottom figure shows the total error $\Delta_i \equiv |\hat{\rho}_c^{(1)} - \hat{\rho}_c^{(i)}|$, $i = p, g$ for each approximation.

G. Appendix for future works

G.1. Effective index of the power spectrum

We show how we got n_{eff} for different mass scales. It is slightly different from the usual way to obtain it, which is by differentiating the rms mass fluctuation, $\sigma_{M_{un}}$,

$$n_{eff} = -3 \left(1 + \frac{d \ln \sigma_{M_{un}}^2}{d \ln M_{un}} \right), \quad (\text{G-1})$$

where

$$\sigma_{M_{un}}^2 \equiv \frac{\langle (M_{per} - M_{un})^2 \rangle}{M_{un}^2} = \frac{1}{2} \int_0^\infty P(k) W^2(kR) k^2 dk, \quad (\text{G-2})$$

where M_{per} is the mass enclosed by a sphere of radius R , which also defines the *unperturbed* mass M_{un} through

$$M_{un} = \frac{4\pi}{3} R^3 \rho_0, \quad (\text{G-3})$$

where ρ_0 is the present matter density, and the average $\langle \rangle$ is taken over all positions of the centre of these spheres. This ‘‘Top-hat’’ filtering results in a window function

$$W(X) = \frac{3}{X} (\sin(X) - X \cos(X)). \quad (\text{G-4})$$

It is then straightforward to calculate n_{eff} as a function of M_{un} using equation (G-1).

However, we are interested in the n_{eff} that is valid when we consider the initial average overdensity around density peaks, $\Delta_0(R)$. Notice that $\Delta_0(R)$ is given by

$$\Delta_0(R) \equiv \frac{\delta M}{M_{un}} = \frac{\delta_0}{\sigma^2} \frac{1}{2\pi^2} \int_0^\infty P(K) W(kR) k^2 dk, \quad (\text{G-5})$$

where M_{un} and $W(X)$ are defined by equation (G-3) and (G-4), respectively. From equation (G-3) and the above expression, we can see that for a power spectrum $P(k) \propto k^n$,

$$\Delta_0(R) \propto R^{-(n+3)} \propto M^{-(n+3)/3}. \quad (\text{G-6})$$

Therefore, one can obtain n_{eff} as follows:

$$n_{eff} = -3 \left(1 + \frac{d \ln \Delta_0(M_{un})}{d \ln M_{un}} \right). \quad (\text{G-7})$$

Bibliography

- Ade, P., Aghanim, N., Akrami, Y., Aluri, P., Arnaud, M., Ashdown, M., Aumont, J., Baccigalupi, C., Banday, A., Barreiro, R., et al. (2016a). Planck 2015 results-xvi. isotropy and statistics of the cmb. *Astronomy & Astrophysics*, 594:A16.
- Ade, P., Aghanim, N., Arnaud, M., Arroja, F., Ashdown, M., Aumont, J., Baccigalupi, C., Ballardini, M., Banday, A., Barreiro, R., et al. (2016b). Planck 2015 results-xx. constraints on inflation. *Astronomy & Astrophysics*, 594:A20.
- Ade, P. A., Aghanim, N., Arnaud, M., Ashdown, M., Aumont, J., Baccigalupi, C., Banday, A., Barreiro, R., Bartlett, J., Bartolo, N., et al. (2016c). Planck 2015 results-xiii. cosmological parameters. *Astronomy & Astrophysics*, 594:A13.
- Aghanim, N., Akrami, Y., Ashdown, M., Aumont, J., Baccigalupi, C., Ballardini, M., Banday, A., Barreiro, R., Bartolo, N., Basak, S., et al. (2018). Planck 2018 results. vi. cosmological parameters. arXiv preprint arXiv:1807.06209.
- Aghanim, N., Arnaud, M., Ashdown, M., Aumont, J., Baccigalupi, C., Banday, A., Barreiro, R., Bartlett, J., Bartolo, N., Battaner, E., et al. (2016). Planck 2015 results-xi. cmb power spectra, likelihoods, and robustness of parameters. *Astronomy & Astrophysics*, 594:A11.
- Ahn, C. P., Seth, A. C., Den Brok, M., Strader, J., Baumgardt, H., Van Den Bosch, R., Chilingarian, I., Frank, M., Hilker, M., McDermid, R., et al. (2017). Detection of supermassive black holes in two virgo ultracompact dwarf galaxies. *The Astrophysical Journal*, 839(2):72.
- Ahn, C. P., Seth, A. C., den Brok, M., Strader, J., Baumgardt, H., van den Bosch, R., Chilingarian, I., Frank, M., Hilker, M., McDermid, R., Mieske, S., Romanowsky, A. J., Spitler, L., Brodie, J., Neumayer, N., and Walsh, J. L. (2017). Detection of Supermassive Black Holes in Two Virgo Ultracompact Dwarf Galaxies. , 839:72.
- Akiyama, K., Alberdi, A., Alef, W., Asada, K., Azulay, R., Baczko, A.-K., Ball, D., Baloković, M., Barrett, J., Bintley, D., et al. (2019). First m87 event horizon telescope results. iv. imaging the central supermassive black hole. *The Astrophysical Journal Letters*, 875(1):L4.

- Akrami, Y., Arroja, F., Ashdown, M., Aumont, J., Baccigalupi, C., Ballardini, M., Banday, A., Barreiro, R., Bartolo, N., Basak, S., et al. (2018). Planck 2018 results. x. constraints on inflation. arXiv preprint arXiv:1807.06211.
- Alcubierre, M. (2008). Introduction to 3+ 1 numerical relativity, volume 140. Oxford University Press.
- Alvarez, M. A., Busha, M., Abel, T., and Wechsler, R. H. (2009). Connecting reionization to the local universe. The Astrophysical Journal Letters, 703(2):L167.
- Ambrosio, M., Collaboration, M., et al. (2002). Final results of magnetic monopole searches with the macro experiment. The European Physical Journal C-Particles and Fields, 25(4):511–522.
- Arbey, A., Lesgourgues, J., and Salati, P. (2001). Quintessential halos around galaxies. Physical Review D, 64(12):123528.
- Arbey, A., Lesgourgues, J., and Salati, P. (2002a). Cosmological constraints on quintessential halos. Phys. Rev., D65:083514.
- Arbey, A., Lesgourgues, J., and Salati, P. (2002b). Cosmological constraints on quintessential halos. Physical Review D, 65(8):083514.
- Arbey, A., Lesgourgues, J., and Salati, P. (2003). Galactic halos of fluid dark matter. Physical Review D, 68(2):023511.
- Arkani-Hamed, N., Dimopoulos, S., and Dvali, G. (1999). Phenomenology, astrophysics, and cosmology of theories with submillimeter dimensions and tev scale quantum gravity. Physical Review D, 59(8):086004.
- Armengaud, E., Palanque-Delabrouille, N., Yèche, C., Marsh, D. J., and Baur, J. (2017). Constraining the mass of light bosonic dark matter using sdss lyman- α forest. Monthly Notices of the Royal Astronomical Society, 471(4):4606–4614.
- Arvanitaki, A., Dimopoulos, S., Dubovsky, S., Kaloper, N., and March-Russell, J. (2010). String axiverse. Physical Review D, 81(12):123530.
- Avilez, A. A., Bernal, T., Padilla, L. E., and Matos, T. (2018). On the possibility that ultra-light boson haloes host and form supermassive black holes. Monthly Notices of the Royal Astronomical Society, 477(3):3257–3272.
- Bañados, E., Venemans, B., Morganson, E., Decarli, R., Walter, F., Chambers, K., Rix, H.-W., Farina, E., Fan, X., Jiang, L., et al. (2014). Discovery of eight $z \approx 6$ quasars from pan-starrs1. The Astronomical Journal, 148(1):14.

- Bandara, K., Crampton, D., and Simard, L. (2009). A relationship between supermassive black hole mass and the total gravitational mass of the host galaxy. The Astrophysical Journal, 704(2):1135.
- Bar, N., Blas, D., Blum, K., and Sibiryakov, S. (2018). Galactic rotation curves versus ultralight dark matter: Implications of the soliton-host halo relation. Physical Review D, 98(8):083027.
- Bar, N., Blum, K., Sato, R., and Eby, J. (2019). arxiv: Ultra-light dark matter in disk galaxies. Technical report.
- Bardeen, J. M. (1980). Gauge-invariant cosmological perturbations. Physical Review D, 22(8):1882.
- Barranco, J., Bernal, A., Degollado, J. C., Diez-Tejedor, A., Megevand, M., Alcubierre, M., Núñez, D., and Sarbach, O. (2011). Are black holes a serious threat to scalar field dark matter models? Physical Review D, 84(8):083008.
- Barranco, J., Bernal, A., Degollado, J. C., Diez-Tejedor, A., Megevand, M., Alcubierre, M., Núñez, D., and Sarbach, O. (2012). Schwarzschild black holes can wear scalar wigs. Physical review letters, 109(8):081102.
- Baumann, D. (2009). Cosmological inflation: Theory and observations. Advanced Science Letters, 2(2):105–120.
- Baumgarte, T. W. and Shapiro, S. L. (2010). Numerical relativity: solving Einstein’s equations on the computer. Cambridge University Press.
- Baym, G. and Pethick, C. J. (1996). Ground-State Properties of Magnetically Trapped Bose-Condensed Rubidium Gas. , 76(1):6–9.
- Bekenstein, J. D. (1995). Novel “no-scalar-hair” theorem for black holes. Phys. Rev. D, 51:R6608–R6611.
- Belinsky, V., Khalatnikov, I., Grishchuk, L., and Zeldovich, Y. B. (1985). Inflationary stages in cosmological models with a scalar field. Technical report, International Centre for Theoretical Physics.
- Bellazzini, M., Oosterloo, T., Fraternali, F., and Beccari, G. (2013). Dwarfs walking in a row—the filamentary nature of the ngc 3109 association. Astronomy & Astrophysics, 559:L11.
- Benson, A., Frenk, C., Lacey, C., Baugh, C., and Cole, S. (2002). The effects of photoionization on galaxy formation—ii. satellite galaxies in the local group. Monthly Notices of the Royal Astronomical Society, 333(1):177–190.

- Bernal, A., Barranco, J., Alic, D., and Palenzuela, C. (2010). Multistate boson stars. Physical Review D, 81(4):044031.
- Bernal, T., Fernández-Hernández, L. M., Matos, T., and Rodríguez-Meza, M. A. (2018). Rotation curves of high-resolution lsb and sparc galaxies with fuzzy and multistate (ultra-light boson) scalar field dark matter. Monthly Notices of the Royal Astronomical Society, 475(2):1447–1468.
- Bertschinger, E. (1998). Simulations of structure formation in the universe. Annual Review of Astronomy and Astrophysics, 36(1):599–654.
- Bičák, J. and Ledvinka, T. (2014). General Relativity, Cosmology and Astrophysics: Perspectives 100 Years After Einstein’s Stay in Prague, volume 177. Springer.
- Binney, J. and Tremaine, S. (2008). Galactic Dynamics: Second Edition. Princeton University Press.
- Boehmer, C. and Harko, T. (2007). Can dark matter be a bose–einstein condensate? Journal of Cosmology and Astroparticle Physics, 2007(06):025.
- Böhmer, C. G. and Harko, T. (2007). Can dark matter be a Bose Einstein condensate? , 6:025.
- Bona, C., Palenzuela-Luque, C., and Bona-Casas, C. (2009). Elements of numerical relativity and relativistic hydrodynamics: from Einstein’s equations to astrophysical simulations, volume 783. Springer.
- Boylan-Kolchin, M., Bullock, J. S., and Kaplinghat, M. (2011). Too big to fail? the puzzling darkness of massive milky way subhaloes. Monthly Notices of the Royal Astronomical Society: Letters, 415(1):L40–L44.
- Boylan-Kolchin, M., Bullock, J. S., and Kaplinghat, M. (2011). Too big to fail? The puzzling darkness of massive Milky Way subhaloes. , 415:L40–L44.
- Boylan-Kolchin, M., Bullock, J. S., and Kaplinghat, M. (2012). The milky way’s bright satellites as an apparent failure of λ cdm. Monthly Notices of the Royal Astronomical Society, 422(2):1203–1218.
- Boylan-Kolchin, M., Springel, V., White, S. D., Jenkins, A., and Lemson, G. (2009). Resolving cosmic structure formation with the millennium-ii simulation. Monthly Notices of the Royal Astronomical Society, 398(3):1150–1164.
- Bozek, B., Marsh, D. J., Silk, J., and Wyse, R. F. (2015). Galaxy uv-luminosity function and reionization constraints on axion dark matter. Monthly Notices of the Royal Astronomical Society, 450(1):209–222.

- Brooks, S. P. and Gelman, A. (1998). General methods for monitoring convergence of iterative simulations. Journal of computational and graphical statistics, 7(4):434–455.
- Bryan, G. L. and Norman, M. L. (1998). Statistical properties of x-ray clusters: Analytic and numerical comparisons. The Astrophysical Journal, 495(1):80.
- Bullock, J. S. and Boylan-Kolchin, M. (2017). Small-scale challenges to the Λ cdm paradigm. Annual Review of Astronomy and Astrophysics, 55.
- Byrnes, C. T. and Wands, D. (2006). Curvature and isocurvature perturbations from two-field inflation in a slow-roll expansion. Physical Review D, 74(4):043529.
- Calabrese, E. and Spergel, D. N. (2016). Ultra-light dark matter in ultra-faint dwarf galaxies. , 460:4397–4402.
- Calabrese, E. and Spergel, D. N. (2016). Ultra-light dark matter in ultra-faint dwarf galaxies. Monthly Notices of the Royal Astronomical Society, 460(4):4397–4402.
- Cappellari, M. (2011). Astrophysics: Monster black holes. Nature, 480(7376):187.
- Carroll, S. (2013). Spacetime and geometry: An introduction to general relativity, always learning.
- Carroll, S. M. (2001). The cosmological constant. Living reviews in relativity, 4(1):1.
- Cedeño, F. X. L., González-Morales, A. X., and Ureña-López, L. A. (2017). Cosmological signatures of ultralight dark matter with an axionlike potential. Physical Review D, 96(6):061301.
- Challinor, A. and Peiris, H. (2009). Lecture notes on the physics of cosmic microwave background anisotropies. In AIP Conference Proceedings, volume 1132, pages 86–140. AIP.
- Chavanis, P.-H. (2011). Mass-radius relation of newtonian self-gravitating bose-einstein condensates with short-range interactions. i. analytical results. Physical Review D, 84(4):043531.
- Chavanis, P.-H. (2012). Growth of perturbations in an expanding universe with bose-einstein condensate dark matter. Astronomy & Astrophysics, 537:A127.
- Chavanis, P.-H. (2016). Collapse of a self-gravitating bose-einstein condensate with attractive self-interaction. Physical Review D, 94(8):083007.
- Chavanis, P.-H. (2019). Predictive model of bec dark matter halos with a solitonic core and an isothermal atmosphere. Physical Review D, 100(8):083022.

- Chavanis, P.-H., Lemou, M., and Méhats, F. (2014). The fermionic king model. arXiv preprint arXiv:1411.6154.
- Chen, S.-R., Schive, H.-Y., and Chiueh, T. (2017). Jeans analysis for dwarf spheroidal galaxies in wave dark matter. Monthly Notices of the Royal Astronomical Society, 468(2):1338–1348.
- Cicoli, M., Goodsell, M. D., and Ringwald, A. (2012). The type iib string axiverse and its low-energy phenomenology. Journal of High Energy Physics, 2012(10):146.
- Clowe, D., Bradač, M., Gonzalez, A. H., Markevitch, M., Randall, S. W., Jones, C., and Zaritsky, D. (2006). A direct empirical proof of the existence of dark matter. The Astrophysical Journal Letters, 648(2):L109.
- Coles, P. and Lucchin, F. (2003). Cosmology: The origin and evolution of cosmic structure. John Wiley & Sons.
- Collaboration, P. et al. (2006). The scientific programme of planck. arXiv preprint astro-ph/0604069.
- Colpi, M., Shapiro, S. L., and Wasserman, I. (1986). Boson stars - Gravitational equilibria of self-interacting scalar fields. Physical Review Letters, 57:2485–2488.
- Conn, A. R., Lewis, G. F., Ibata, R. A., Parker, Q. A., Zucker, D. B., McConnachie, A. W., Martin, N. F., Valls-Gabaud, D., Tanvir, N., Irwin, M. J., et al. (2013). The three-dimensional structure of the m31 satellite system; strong evidence for an inhomogeneous distribution of satellites. The Astrophysical Journal, 766(2):120.
- Dalfovo, F., Giorgini, S., Pitaevskii, L. P., and Stringari, S. (1999). Theory of bose-einstein condensation in trapped gases. Reviews of Modern Physics, 71(3):463.
- Davies, E. Y. and Mocz, P. (2019). Fuzzy dark matter soliton cores around supermassive black holes. arXiv preprint arXiv:1908.04790.
- Del Popolo, A. (2007). Dark matter, density perturbations, and structure formation. Astronomy Reports, 51(3):169–196.
- Derrick, G. (1964). Comments on nonlinear wave equations as models for elementary particles. Journal of Mathematical Physics, 5(9):1252–1254.
- Diemand, J., Kuhlen, M., and Madau, P. (2007). Dark matter substructure and gamma-ray annihilation in the milky way halo. The Astrophysical Journal, 657(1):262.
- Diemand, J., Kuhlen, M., Madau, P., Zemp, M., Moore, B., Potter, D., and Stadel, J. (2008). Clumps and streams in the local dark matter distribution. Nature, 454(7205):735.

- Diez-Tejedor, A., Gonzalez-Morales, A. X., and Profumo, S. (2014). Dwarf spheroidal galaxies and bose-einstein condensate dark matter. Physical Review D, 90(4):043517.
- Dodelson, S. (2003). Modern cosmology. Elsevier.
- Drinkwater, M. J., Jones, J. B., Gregg, M. D., and Phillipps, S. (2000). Compact stellar systems in the fornax cluster: super-massive star clusters or extremely compact dwarf galaxies? Publ. Astron. Soc. Austral., 17:227.
- Duc, P.-A., Paudel, S., McDermid, R. M., Cuillandre, J.-C., Serra, P., Bournaud, F., Cappellari, M., and Emsellem, E. (2014). Identification of old tidal dwarfs near early-type galaxies from deep imaging and h i observations. Monthly Notices of the Royal Astronomical Society, 440(2):1458–1469.
- Durrer, R. (2001). The theory of cmb anisotropies. arXiv preprint astro-ph/0109522.
- Eby, J., Kouvaris, C., Nielsen, N. G., and Wijewardhana, L. (2016). Boson stars from self-interacting dark matter. Journal of High Energy Physics, 2016(2):28.
- Escorihuela-Tomás, A., Sanchis-Gual, N., Degollado, J. C., and Font, J. A. (2017). Quasistationary solutions of scalar fields around collapsing self-interacting boson stars. Physical Review D, 96(2):024015.
- Escorihuela-Tomas, A., Sanchis-Gual, N., Degollado, J. C., and Font, J. A. (2017). Quasistationary solutions of scalar fields around collapsing self-interacting boson stars. Phys. Rev., D96(2):024015.
- Fan, X., Strauss, M. A., Schneider, D. P., Becker, R. H., White, R. L., Haiman, Z., Gregg, M., Pentericci, L., Grebel, E. K., Narayanan, V. K., et al. (2003). A survey of z_i 5.7 quasars in the sloan digital sky survey. ii. discovery of three additional quasars at z_i 6. The Astronomical Journal, 125(4):1649.
- Fernández-Hernández, L. M., Rodríguez-Meza, M. A., and Matos, T. (2018). Comparison between two scalar field models using rotation curves of spiral galaxies. In Journal of Physics: Conference Series, volume 1010, page 012005. IOP Publishing.
- Ferrarese, L. (2002). Beyond the bulge: a fundamental relation between supermassive black holes and dark matter halos. The Astrophysical Journal, 578(1):90.
- Ferrarese, L. and Merritt, D. (2000). A Fundamental Relation between Supermassive Black Holes and Their Host Galaxies. , 539:L9–L12.
- Fillmore, J. A. and Goldreich, P. (1984). Self-similar gravitational collapse in an expanding universe. The Astrophysical Journal, 281:1–8.

- Flores, R. A. and Primack, J. R. (1994). Observational and theoretical constraints on singular dark matter halos. [arXiv preprint astro-ph/9402004](#).
- Freese, K., Ilie, C., Spolyar, D., Valluri, M., and Bodenheimer, P. (2010). Supermassive Dark Stars: Detectable in JWST. , 716(2):1397–1407.
- Fukushige, T. and Makino, J. (2001). Structure of dark matter halos from hierarchical clustering. [The Astrophysical Journal](#), 557(2):533.
- Galianni, P., Patat, F., Higdon, J. L., Mieske, S., and Kroupa, P. (2010). Vlt observations of ngc 1097’s “dog-leg” tidal stream-dwarf spheroidals and tidal streams. [Astronomy & Astrophysics](#), 521:A20.
- Gaskins, J. M. (2016). A review of indirect searches for particle dark matter. [Contemporary Physics](#), 57(4):496–525.
- Gebhardt, K., Bender, R., Bower, G., Dressler, A., Faber, S., Filippenko, A. V., Green, R., Grillmair, C., Ho, L. C., Kormendy, J., et al. (2000). A relationship between nuclear black hole mass and galaxy velocity dispersion. [The Astrophysical Journal Letters](#), 539(1):L13.
- Gelman, A., Carlin, J. B., Stern, H. S., Dunson, D. B., Vehtari, A., and Rubin, D. B. (2013). [Bayesian data analysis](#). Chapman and Hall/CRC.
- Gelman, A., Rubin, D. B., et al. (1992). Inference from iterative simulation using multiple sequences. [Statistical science](#), 7(4):457–472.
- Georgi, H. and Glashow, S. L. (1974). Unity of all elementary-particle forces. [Phys. Rev. Lett.](#), 32:438–441.
- Gilks, W. R., Richardson, S., and Spiegelhalter, D. (1995). [Markov chain Monte Carlo in practice](#). Chapman and Hall/CRC.
- Gnedin, N. Y. (2000). Effect of reionization on structure formation in the universe. [The Astrophysical Journal](#), 542(2):535.
- Gold, B., Odegard, N., Weiland, J., Hill, R., Kogut, A., Bennett, C., Hinshaw, G., Chen, X., Dunkley, J., Halpern, M., et al. (2011). Seven-year wilkinson microwave anisotropy probe (wmap*) observations: galactic foreground emission. [The Astrophysical Journal Supplement Series](#), 192(2):15.
- Gong, J.-O. (2017). Multi-field inflation and cosmological perturbations. [International Journal of Modern Physics D](#), 26(01):1740003.
- González-Morales, A. X., Marsh, D. J., Peñarrubia, J., and Ureña-López, L. A. (2017). Unbiased constraints on ultralight axion mass from dwarf spheroidal galaxies. [Monthly Notices of the Royal Astronomical Society](#), 472(2):1346–1360.

- Gordon, W. (1926). The compton effect according to schrödinger's theory. Z. Phys, 40:117Ä–133.
- Governato, F., Willman, B., Mayer, L., Brooks, A., Stinson, G., Valenzuela, O., Wadsley, J., and Quinn, T. (2007). Forming disc galaxies in λ cdm simulations. Monthly Notices of the Royal Astronomical Society, 374(4):1479–1494.
- Groom, D. and Scott, D. (2017). Astrophysical constants and parameters.
- Gu, J.-A. and Hwang, W.-Y. (2001). Can the quintessence be a complex scalar field? Physics Letters B, 517(1-2):1–6.
- Gunn, J. E. and Gott III, J. R. (1972). On the infall of matter into clusters of galaxies and some effects on their evolution. The Astrophysical Journal, 176:1.
- Gürlebeck, N. (2015). No-hair theorem for black holes in astrophysical environments. Phys. Rev. Lett., 114:151102.
- Guth, A. H. (1981). Inflationary universe: A possible solution to the horizon and flatness problems. Physical Review D, 23(2):347.
- Guth, A. H. (1997). The Inflationary Universe: The Quest for a New Theory of Cosmic Origins. Basic Books.
- Guzmán, F. and Ávilez, A. A. (2018). Head-on collision of multistate ultralight bec dark matter configurations. Physical Review D, 97(11):116003.
- Guzmán, F. S. and Matos, T. (2000). LETTER TO THE EDITOR: Scalar fields as dark matter in spiral galaxies. Classical and Quantum Gravity, 17:L9–L16.
- Guzmán, F. S. and Matos, T. (2000). Scalar fields as dark matter in spiral galaxies. Classical and Quantum Gravity, 17(1):L9.
- Guzman, F. S. and Urena-López, L. A. (2004). Evolution of the schrödinger-newton system for a self-gravitating scalar field. Physical Review D, 69(12):124033.
- Guzman, F. S. and Urena-Lopez, L. A. (2006). Gravitational cooling of self-gravitating bose condensates. The Astrophysical Journal, 645(2):814.
- Hanson, K. M. (2001). Markov chain monte carlo posterior sampling with the hamiltonian method. In Medical Imaging 2001: Image Processing, volume 4322, pages 456–467. International Society for Optics and Photonics.
- Harigaya, K., Ibe, M., Kawasaki, M., and Yanagida, T. T. (2013). Non-gaussianity from attractor curvaton. Physical Review D, 87(6):063514.

- Harko, T. (2011). Bose-einstein condensation of dark matter solves the core/cusp problem. Journal of Cosmology and Astroparticle Physics, 2011(05):022.
- Hastings, W. K. (1970). Monte carlo sampling methods using markov chains and their applications.
- Hawley, S. H. and Choptuik, M. W. (2003). Numerical evidence for “multiscalar stars”. , 67(2):024010.
- Heavens, A. (2009). Statistical techniques in cosmology. arXiv preprint arXiv:0906.0664.
- Hetherington, N. S. (1970). The shapley-curtis debate. Leaflet of the Astronomical Society of the Pacific, 10:313–320.
- Hinshaw, G., Weiland, J., Hill, R., Odegard, N., Larson, D., Bennett, C., Dunkley, J., Gold, B., Greason, M., Jarosik, N., et al. (2009). Five-year wilkinson microwave anisotropy probe* observations: data processing, sky maps, and basic results. The Astrophysical Journal Supplement Series, 180(2):225.
- Hlozek, R., Grin, D., Marsh, D. J., and Ferreira, P. G. (2015). A search for ultralight axions using precision cosmological data. Physical Review D, 91(10):103512.
- Hložek, R., Marsh, D. J., and Grin, D. (2018). Using the full power of the cosmic microwave background to probe axion dark matter. Monthly Notices of the Royal Astronomical Society, 476(3):3063–3085.
- Hoffman, Y. and Shaham, J. (1985). Local density maxima-progenitors of structure. The Astrophysical Journal, 297:16–22.
- Hu, W., Barkana, R., and Gruzinov, A. (2000). Fuzzy Cold Dark Matter: The Wave Properties of Ultralight Particles. Physical Review Letters, 85:1158–1161.
- Hu, W. and Dodelson, S. (2002). Cosmic microwave background anisotropies. Annual Review of Astronomy and Astrophysics, 40(1):171–216.
- Hui, L., Ostriker, J. P., Tremaine, S., and Witten, E. (2017). Ultralight scalars as cosmological dark matter. Physical Review D, 95(4):043541.
- Husdal, L. (2016). On effective degrees of freedom in the early universe. Galaxies, 4(4):78.
- Ibata, R. A., Lewis, G. F., Conn, A. R., Irwin, M. J., McConnachie, A. W., Chapman, S. C., Collins, M. L., Fardal, M., Ferguson, A. M., Ibata, N. G., et al. (2013). A vast, thin plane of corotating dwarf galaxies orbiting the andromeda galaxy. Nature, 493(7430):62.
- Int., L. (2019). Introduction to gravitational lensing. <http://www.icc.dur.ac.uk/~tt/Lectures/Galaxies/GravitationalLensing/GalaxyClusters/index.html>.

- Iršič, V., Viel, M., Haehnelt, M. G., Bolton, J. S., and Becker, G. D. (2017). First constraints on fuzzy dark matter from lyman- α forest data and hydrodynamical simulations. Physical review letters, 119(3):031302.
- Iršič, V., Viel, M., Haehnelt, M. G., Bolton, J. S., and Becker, G. D. (2017). First Constraints on Fuzzy Dark Matter from Lyman- α Forest Data and Hydrodynamical Simulations. Physical Review Letters, 119(3):031302.
- Jetzer, P. (1992). Boson stars. Physics Reports, 220(4):163–227.
- Ji, S. and Sin, S.-J. (1994). Late-time phase transition and the galactic halo as a bose liquid. ii. the effect of visible matter. Physical Review D, 50(6):3655.
- Jiang, L., Fan, X., Annis, J., Becker, R. H., White, R. L., Chiu, K., Lin, H., Lupton, R. H., Richards, G. T., Strauss, M. A., et al. (2008). A survey of $z \approx 6$ quasars in the sloan digital sky survey deep stripe. i. a flux-limited sample at $z \approx 6$. The Astronomical Journal, 135(3):1057.
- Jiang, L., Fan, X., Vestergaard, M., Kurk, J. D., Walter, F., Kelly, B. C., and Strauss, M. A. (2007). Gemini near-infrared spectroscopy of luminous $z \approx 6$ quasars: chemical abundances, black hole masses, and mg ii absorption. The Astronomical Journal, 134(3):1150.
- Kallosh, R., Linde, A., Prokushkin, S., and Shmakova, M. (2002). Supergravity, dark energy, and the fate of the universe. Physical Review D, 66(12):123503.
- Karachentsev, I. D., Bautzmann, D., Neyer, F., Polzl, R., Riepe, P., Zilch, T., and Mattern, B. (2014). Three low surface brightness dwarfs discovered around ngc 4631. arXiv preprint arXiv:1401.2719.
- Kaup, D. J. (1968). Klein-gordon geon. Physical Review, 172(5):1331.
- Klein, O. (1926). Quantentheorie und fünfdimensionale relativitätstheorie. Zeitschrift für Physik, 37(12):895–906.
- Klein, O. (1927). Electrodynamics and wave mechanics from the standpoint of the correspondence principle. Z Phys, 41:407–442.
- Klypin, A., Kravtsov, A. V., Valenzuela, O., and Prada, F. (1999). Where are the missing galactic satellites? The Astrophysical Journal, 522(1):82.
- Klypin, A., Yepes, G., Gottlöber, S., Prada, F., and Hess, S. (2016). Multidark simulations: the story of dark matter halo concentrations and density profiles. Monthly Notices of the Royal Astronomical Society, 457(4):4340–4359.

- Klypin, A. A., Trujillo-Gomez, S., and Primack, J. (2011). Dark matter halos in the standard cosmological model: Results from the bolshoi simulation. The Astrophysical Journal, 740(2):102.
- Kobayashi, T., Murgia, R., De Simone, A., Iršič, V., and Viel, M. (2017). Lyman- α constraints on ultralight scalar dark matter: Implications for the early and late universe. Physical Review D, 96(12):123514.
- Koch, A. and Grebel, E. K. (2006). The anisotropic distribution of m31 satellite galaxies: a polar great plane of early-type companions. The Astronomical Journal, 131(3):1405.
- Kodama, H. and Sasaki, M. (1984). Cosmological perturbation theory. Progress of Theoretical Physics Supplement, 78:1–166.
- Kolb, E. and Turner, M. (1990). The early universe (boulder, co).
- Kolb, E. and Turner, M. (1994). The early universe, paperback ed.
- Kolb, E. W. and Turner, M. S. (1983). Grand unified theories and the origin of the baryon asymmetry. Annual Review of Nuclear and Particle Science, 33(1):645–696.
- Komatsu, E., Dunkley, J., Nolta, M., Bennett, C., Gold, B., Hinshaw, G., Jarosik, N., Larson, D., Limon, M., Page, L., et al. (2009). Five-year wilkinson microwave anisotropy probe* observations: cosmological interpretation. The Astrophysical Journal Supplement Series, 180(2):330.
- Komatsu, E., Smith, K., Dunkley, J., Bennett, C., Gold, B., Hinshaw, G., Jarosik, N., Larson, D., Nolta, M., Page, L., et al. (2011). Seven-year wilkinson microwave anisotropy probe (wmap*) observations: cosmological interpretation. The Astrophysical Journal Supplement Series, 192(2):18.
- Kroupa, P., Theis, C., and Boily, C. M. (2005). The great disk of milky-way satellites and cosmological sub-structures. Astronomy & Astrophysics, 431(2):517–521.
- Kuhlen, M., Vogelsberger, M., and Angulo, R. (2012). Numerical simulations of the dark universe: State of the art and the next decade. Physics of the Dark Universe, 1(1-2):50–93.
- Kunkel, W. E. and Demers, S. (1976). The magellanic plane. In The Galaxy and the Local Group, volume 182, page 241.
- Larkin, A. C. and McLaughlin, D. E. (2016). Dark-matter haloes and the M - σ relation for supermassive black holes. , 462:1864–1881.

- Larson, D., Dunkley, J., Hinshaw, G., Komatsu, E., Nolta, M., Bennett, C., Gold, B., Halpern, M., Hill, R., Jarosik, N., et al. (2011). Seven-year wilkinson microwave anisotropy probe (wmap*) observations: power spectra and wmap-derived parameters. The Astrophysical Journal Supplement Series, 192(2):16.
- Lee, J.-W., Lee, J., and Kim, H.-C. (2015). The M-sigma Relation of Super Massive Black Holes from the Scalar Field Dark Matter. ArXiv e-prints.
- Lee, T.-D. and Pang, Y. (1992). Nontopological solitons. Physics Reports, 221(5-6):251–350.
- Lehnert, M. D., Nesvadba, N., Cuby, J.-G., Swinbank, A., Morris, S., Clément, B., Evans, C., Bremer, M., and Basa, S. (2010). Spectroscopic confirmation of a galaxy at redshift $z= 8.6$. Nature, 467(7318):940.
- Lelli, F., McGaugh, S. S., and Schombert, J. M. (2016). SPARC: Mass Models for 175 Disk Galaxies with Spitzer Photometry and Accurate Rotation Curves. , 152:157.
- Lelli, F., McGaugh, S. S., Schombert, J. M., and Pawlowski, M. S. (2017). One Law to Rule Them All: The Radial Acceleration Relation of Galaxies. , 836:152.
- Lesgourgues, J., Arbey, A., and Salati, P. (2002). A light scalar field at the origin of galaxy rotation curves. New Astronomy Reviews, 46(12):791–799.
- Levkov, D., Panin, A., and Tkachev, I. (2018). Gravitational bose-einstein condensation in the kinetic regime. Physical review letters, 121(15):151301.
- Li, B., Rindler-Daller, T., and Shapiro, P. R. (2014). Cosmological constraints on Bose-Einstein-condensed scalar field dark matter. , 89(8):083536.
- Li, B., Rindler-Daller, T., and Shapiro, P. R. (2014). Cosmological constraints on bose-einstein-condensed scalar field dark matter. Physical Review D, 89(8):083536.
- Li, B., Shapiro, P. R., and Rindler-Daller, T. (2017). Bose-einstein-condensed scalar field dark matter and the gravitational wave background from inflation: new cosmological constraints and its detectability by ligo. Physical Review D, 96(6):063505.
- Liddle, A. R. (1999). Inflation and the cosmic microwave background. AIP Conference Proceedings, 476(1):11–17.
- Liddle, A. R. and Lyth, D. H. (1992). Cobe, gravitational waves, inflation and extended inflation. Physics Letters B, 291(4):391 – 398.
- Liddle, A. R. and Lyth, D. H. (2000). Cosmological Inflation and Large-Scale Structure.
- Liddle, A. R. and Madsen, M. S. (1992). The structure and formation of boson stars. International Journal of Modern Physics D, 1(01):101–143.

- Liddle, A. R. and Turner, M. S. (1994). Second-order reconstruction of the inflationary potential. Phys. Rev. D, 50:758–768.
- Lin, S.-C., Schive, H.-Y., Wong, S.-K., and Chiueh, T. (2018). Self-consistent construction of virialized wave dark matter halos. Physical Review D, 97(10):103523.
- Linde, A. D. (1982). A new inflationary universe scenario: a possible solution of the horizon, flatness, homogeneity, isotropy and primordial monopole problems. Physics Letters B, 108(6):389–393.
- Lora, V., Magana, J., Bernal, A., Sánchez-Salcedo, F., and Grebel, E. (2012). On the mass of ultra-light bosonic dark matter from galactic dynamics. Journal of Cosmology and Astroparticle Physics, 2012(02):011.
- Lynden-Bell, D. (1969). Galactic nuclei as collapsed old quasars. Nature, 223(5207):690.
- Lynden-Bell, D. (1976). Dwarf galaxies and globular clusters in high velocity hydrogen streams. Monthly Notices of the Royal Astronomical Society, 174(3):695–710.
- Lyth, D. (1984). A bound on inflationary energy density from the isotropy of the microwave background. Physics Letters B, 147(6):403–404.
- Lyth, D. H. and Liddle, A. R. (2009). The primordial density perturbation: Cosmology, inflation and the origin of structure. Cambridge University Press.
- Lyth, D. H. and Riotto, A. (1999). Particle physics models of inflation and the cosmological density perturbation. Physics Reports, 314(1):1 – 146.
- Lyth, D. H. and Stewart, E. D. (1992). Constraining the inflationary energy scale from axion cosmology. Physics Letters B, 283(3-4):189–193.
- Lyth, D. H. and Stewart, E. D. (1995). Cosmology with a tev mass higgs field breaking the grand-unified-theory gauge symmetry. Phys. Rev. Lett., 75:201–204.
- Lyth, D. H. and Stewart, E. D. (1996). Thermal inflation and the moduli problem. Phys. Rev. D, 53:1784–1798.
- Magana, J. and Matos, T. (2012). A brief review of the scalar field dark matter model. In Journal of Physics: Conference Series, volume 378, page 012012. IOP Publishing.
- Magaña, J., Matos, T., Suárez, A., and Sánchez-Salcedo, F. (2012). Structure formation with scalar field dark matter: the field approach. Journal of Cosmology and Astroparticle Physics, 2012(10):003.
- Marsh, D. J. (2016). Axion cosmology. Physics Reports, 643:1–79.

- Marsh, D. J. and Ferreira, P. G. (2010). Ultralight scalar fields and the growth of structure in the universe. Physical Review D, 82(10):103528.
- Marsh, D. J. and Pop, A.-R. (2015). Axion dark matter, solitons and the cusp–core problem. Monthly Notices of the Royal Astronomical Society, 451(3):2479–2492.
- Marsh, D. J. and Silk, J. (2013). A model for halo formation with axion mixed dark matter. Monthly Notices of the Royal Astronomical Society, 437(3):2652–2663.
- Martinez-Medina, L. A., Robles, V. H., and Matos, T. (2015). Dwarf galaxies in multistate scalar field dark matter halos. , 91(2):023519.
- Mather, J. C., Cheng, E., Eplee Jr, R., Isaacman, R., Meyer, S., Shafer, R., Weiss, R., Wright, E., Bennett, C., Boggess, N., et al. (1990). A preliminary measurement of the cosmic microwave background spectrum by the cosmic background explorer (cobe) satellite. The Astrophysical Journal, 354:L37–L40.
- Matos, T. and Arturo Ureña-López, L. (2001). Further analysis of a cosmological model with quintessence and scalar dark matter. , 63(6):063506.
- Matos, T., Guzmán, F. S., and Urena-López, L. A. (2000). Scalar field as dark matter in the universe. Classical and Quantum Gravity, 17(7):1707.
- Matos, T., Solís-López, J., Guzmán, F. S., Robles, V. H., and Urena-López, L. A. (2019). Scalar field dark matter as an alternative explanation for the polar orbits of satellite galaxies. arXiv preprint arXiv:1912.09660.
- Matos, T. and Urena-Lopez, L. A. (2000). Quintessence and scalar dark matter in the universe. Classical and Quantum Gravity, 17(13):L75.
- Matos, T. and Ureña-López, L. A. (2007). Flat rotation curves in scalar field galaxy halos. General Relativity and Gravitation, 39(8):1279–1286.
- Matsuoka, Y., Iwasawa, K., Onoue, M., Kashikawa, N., Strauss, M. A., Lee, C.-H., Imanishi, M., Nagao, T., Akiyama, M., Asami, N., et al. (2018a). Subaru high-z exploration of low-luminosity quasars (shellqs). iv. discovery of 41 quasars and luminous galaxies at $5.7 < z < 6.9$. The Astrophysical Journal Supplement Series, 237(1):5.
- Matsuoka, Y., Onoue, M., Kashikawa, N., Iwasawa, K., Strauss, M. A., Nagao, T., Imanishi, M., Lee, C.-H., Akiyama, M., Asami, N., et al. (2017). Subaru high-z exploration of low-luminosity quasars (shellqs). ii. discovery of 32 quasars and luminous galaxies at $5.7 < z < 6.8$. Publications of the Astronomical Society of Japan, 70(SP1):S35.

- Matsuoka, Y., Onoue, M., Kashikawa, N., Iwasawa, K., Strauss, M. A., Nagao, T., Imanishi, M., Niida, M., Toba, Y., Akiyama, M., et al. (2016). Subaru high- z exploration of low-luminosity quasars (shellqs). i. discovery of 15 quasars and bright galaxies at $5.7 < z < 6.9$. The Astrophysical Journal, 828(1):26.
- Matsuoka, Y., Onoue, M., Kashikawa, N., Strauss, M. A., Iwasawa, K., Lee, C.-H., Imanishi, M., Nagao, T., Akiyama, M., Asami, N., et al. (2019). Discovery of the first low-luminosity quasar at $z \approx 7$. The Astrophysical Journal Letters, 872(1):L2.
- Matsuoka, Y., Strauss, M. A., Kashikawa, N., Onoue, M., Iwasawa, K., Tang, J.-J., Lee, C.-H., Imanishi, M., Nagao, T., Akiyama, M., et al. (2018b). Subaru high- z exploration of low-luminosity quasars (shellqs). v. quasar luminosity function and contribution to cosmic reionization at $z = 6$. The Astrophysical Journal, 869(2):150.
- McConnachie, A. and Irwin, M. (2006). The satellite distribution of m31. Monthly Notices of the Royal Astronomical Society, 365(3):902–914.
- McConnell, N. J. and Ma, C.-P. (2013). Revisiting the Scaling Relations of Black Hole Masses and Host Galaxy Properties. Astrophys. J., 764:184.
- McConnell, N. J., Ma, C.-P., Gebhardt, K., Wright, S. A., Murphy, J. D., Lauer, T. R., Graham, J. R., and Richstone, D. O. (2011). Two ten-billion-solar-mass black holes at the centres of giant elliptical galaxies. Nature, 480(7376):215.
- McCoy, C. (2015). What is the horizon problem. Preprint.
- McGaugh, S. S., Lelli, F., and Schombert, J. M. (2016). Radial Acceleration Relation in Rotationally Supported Galaxies. Physical Review Letters, 117(20):201101.
- Membrado, M., Pacheco, A., and Sañudo, J. (1989). Hartree solutions for the self-yukawian boson sphere. Physical Review A, 39(8):4207.
- Menou, K., Haiman, Z., and Narayanan, V. K. (2001). The merger history of supermassive black holes in galaxies. The Astrophysical Journal, 558(2):535.
- Mermod, P. (2013). Magnetic monopoles at the lhc and in the cosmos. arXiv preprint arXiv:1305.3718.
- Merritt, D. and Ferrarese, L. (2001). The m_{\bullet} - σ relation for supermassive black holes. The Astrophysical Journal, 547(1):140.
- Metropolis, N., Rosenbluth, A. W., Rosenbluth, M. N., Teller, A. H., and Teller, E. (1953). Equation of state calculations by fast computing machines. The journal of chemical physics, 21(6):1087–1092.

- Metz, M., Kroupa, P., and Jerjen, H. (2006). The spatial distribution of the milky way and andromeda satellite galaxies. Monthly Notices of the Royal Astronomical Society, 374(3):1125–1145.
- Metz, M., Kroupa, P., and Libeskind, N. I. (2008). The orbital poles of milky way satellite galaxies: a rotationally supported disk of satellites. The Astrophysical Journal, 680(1):287.
- Mielke, E. W. (2016). Rotating boson stars. In At the Frontier of Spacetime, pages 115–131. Springer.
- Mocz, P., Vogelsberger, M., Robles, V. H., Zavala, J., Boylan-Kolchin, M., Fialkov, A., and Hernquist, L. (2017a). Galaxy formation with becdm-i. turbulence and relaxation of idealized haloes. Monthly Notices of the Royal Astronomical Society, 471(4):4559–4570.
- Mocz, P., Vogelsberger, M., Robles, V. H., Zavala, J., Boylan-Kolchin, M., Fialkov, A., and Hernquist, L. (2017b). Galaxy formation with becdm-i. turbulence and relaxation of idealized haloes. Monthly Notices of the Royal Astronomical Society, 471(4):4559–4570.
- Moore, B. (1994). Evidence against dissipation-less dark matter from observations of galaxy haloes. Nature, 370(6491):629–631.
- Moore, B., Ghigna, S., Governato, F., Lake, G., Quinn, T., Stadel, J., and Tozzi, P. (1999a). Dark matter substructure within galactic halos. The Astrophysical Journal Letters, 524(1):L19.
- Moore, B., Governato, F., Quinn, T., Stadel, J., and Lake, G. (1998). Resolving the structure of cold dark matter halos. The Astrophysical Journal Letters, 499(1):L5.
- Moore, B., Quinn, T., Governato, F., Stadel, J., and Lake, G. (1999b). Cold collapse and the core catastrophe. Monthly Notices of the Royal Astronomical Society, 310(4):1147–1152.
- Mortlock, D. J., Warren, S. J., Venemans, B. P., Patel, M., Hewett, P. C., McMahon, R. G., Simpson, C., Theuns, T., González-Solares, E. A., Adamson, A., et al. (2011). A luminous quasar at a redshift of $z = 7.085$. Nature, 474(7353):616.
- Mukhanov, V. (2005). Physical foundations of cosmology. Cambridge university press.
- Mukhanov, V. F. and Chibisov, G. V. (1981). Quantum Fluctuations and a Nonsingular Universe. JETP Lett., 33:532–535. [Pisma Zh. Eksp. Teor. Fiz.33,549(1981)].
- Mukhanov, V. F., Feldman, H. A., and Brandenberger, R. H. (1992). Theory of cosmological perturbations. Physics Reports, 215(5-6):203–333.
- N., E. (2019). Notes for electricity. <https://hedberg.ccnysites.cuny.edu/viewers/ebook.php?course=introphysics&topic=electric-fields&l=cal>.

- Nanoqed (2019). Dark matter & modified gravity. <http://www.nanoqed.org/2019.php>.
- Neal, R. M. et al. (2011). Mcmc using hamiltonian dynamics. Handbook of markov chain monte carlo, 2(11):2.
- Ohashi, A. and Sakagami, M.-a. (2004). Massive quasi-normal mode. Classical and Quantum Gravity, 21:3973–3984.
- Olive, K. A. (1990). Inflation. Physics Reports, 190(6):307 – 403.
- Ostriker, J. (85). k peebles, pje 1973. ApJ, 186:467.
- Padilla, L. E., Vázquez, J. A., Matos, T., and Germán, G. (2019). Scalar field dark matter spectator during inflation: the effect of self-interaction. Journal of Cosmology and Astroparticle Physics, 2019(05):056.
- Paredes, A. and Michinel, H. (2016). Interference of dark matter solitons and galactic offsets. Physics of the Dark Universe, 12:50–55.
- Paudel, S., Duc, P.-A., Côté, P., Cuillandre, J.-C., Ferrarese, L., Ferriere, E., Gwyn, S. D., Mihos, J. C., Vollmer, B., Balogh, M. L., et al. (2013). The next generation virgo cluster survey. iv. ngc 4216: A bombarded spiral in the virgo cluster. The Astrophysical Journal, 767(2):133.
- Pawlowski, M. S., Famaey, B., Jerjen, H., Merritt, D., Kroupa, P., Dabringhausen, J., Lüghausen, F., Forbes, D. A., Hensler, G., Hammer, F., et al. (2014). Co-orbiting satellite galaxy structures are still in conflict with the distribution of primordial dwarf galaxies. Monthly Notices of the Royal Astronomical Society, 442(3):2362–2380.
- Pawlowski, M. S., Famaey, B., Merritt, D., and Kroupa, P. (2015). On the persistence of two small-scale problems in λ cdm. The Astrophysical Journal, 815(1):19.
- Pawlowski, M. S. and Kroupa, P. (2013). The rotationally stabilized vpos and predicted proper motions of the milky way satellite galaxies. Monthly Notices of the Royal Astronomical Society, 435(3):2116–2131.
- Pawlowski, M. S., Kroupa, P., and Jerjen, H. (2013). Dwarf galaxy planes: the discovery of symmetric structures in the local group. Monthly Notices of the Royal Astronomical Society, 435(3):1928–1957.
- Pawlowski, M. S. and McGaugh, S. S. (2014). Perseus i and the ngc 3109 association in the context of the local group dwarf galaxy structures. Monthly Notices of the Royal Astronomical Society, 440(1):908–919.

- Pécontal, E., Buchert, T., Di Stefano, P., Copin, Y., and Freese, K. (2009). Review of observational evidence for dark matter in the universe and in upcoming searches for dark stars. European Astronomical Society Publications Series, 36:113–126.
- Peebles, P. (1982). Large-scale background temperature and mass fluctuations due to scale-invariant primeval perturbations.
- Penny, S. J., Conselice, C. J., De Rijcke, S., and Held, E. V. (2009). Hubble space telescope survey of the perseus cluster–i. the structure and dark matter content of cluster dwarf spheroidals. Monthly Notices of the Royal Astronomical Society, 393(3):1054–1062.
- Piran, T. and Williams, R. M. (1985). Inflation in universes with a massive scalar field. Physics Letters B, 163(5-6):331–335.
- Plummer, H. C. (1911). On the problem of distribution in globular star clusters. , 71:460–470.
- Prada, F., Klypin, A. A., Cuesta, A. J., Betancort-Rijo, J. E., and Primack, J. (2012). Halo concentrations in the standard λ cold dark matter cosmology. Monthly Notices of the Royal Astronomical Society, 423(4):3018–3030.
- Press, W. H., Teukolsky, S. A., Vetterling, W. T., and Flannery, B. P. (2007). Numerical recipes 3rd edition: The art of scientific computing. Cambridge university press.
- Primack, J. R. (2017). Cosmological structure formation. The Philosophy of Cosmology, page 136.
- Rashkov, V., Madau, P., Kuhlen, M., and Diemand, J. (2012). On the assembly of the milky way dwarf satellites and their common mass scale. The Astrophysical Journal, 745(2):142.
- Riebe, K., Partl, A. M., Enke, H., Forero-Romero, J., Gottlöber, S., Klypin, A., Lemson, G., Prada, F., Primack, J. R., Steinmetz, M., et al. (2013). The multidark database: release of the bolshoi and multidark cosmological simulations. Astronomische Nachrichten, 334(7):691–708.
- Rindler-Daller, T., Montgomery, M. H., Freese, K., Winget, D. E., and Paxton, B. (2015). Dark Stars: Improved Models and First Pulsation Results. , 799(2):210.
- Rindler-Daller, T. and Shapiro, P. R. (2012). Angular momentum and vortex formation in bose–einstein-condensed cold dark matter haloes. Monthly Notices of the Royal Astronomical Society, 422(1):135–161.
- Rindler-Daller, T. and Shapiro, P. R. (2014). Complex scalar field dark matter on galactic scales. Modern Physics Letters A, 29(02):1430002.
- Riotto, A. (2003). Inflation and the theory of cosmological perturbations. ICTP Lect. Notes Ser., 14:317–413.

- Robles, V. H., Martinez-Medina, L. A., and Matos, T. (2015). SFDM: A new formation mechanism of tidal debris. ArXiv e-prints.
- Robles, V. H. and Matos, T. (2012). Flat central density profile and constant dark matter surface density in galaxies from scalar field dark matter. Monthly Notices of the Royal Astronomical Society, 422(1):282–289.
- Robles, V. H. and Matos, T. (2013). Exact Solution to Finite Temperature SFDM: Natural Cores without Feedback. , 763:19.
- Rodriguez-Montoya, I., Magaña, J., Matos, T., and Pérez-Lorenzana, A. (2010). Ultra light bosonic dark matter and cosmic microwave background. The Astrophysical Journal, 721(2):1509.
- Rosa, J. G. (1999). Introduction to cosmology. <http://gravitation.web.ua.pt/cosmo>.
- Ross, S. M. (2014). Introduction to probability models. Academic press.
- Rubin, V. C., Burstein, D., Ford Jr, W. K., and Thonnard, N. (1985). Rotation velocities of 16 sa galaxies and a comparison of sa, sb, and sc rotation properties. The Astrophysical Journal, 289:81–98.
- Rubin, V. C. and Ford Jr, W. K. (1970). Rotation of the andromeda nebula from a spectroscopic survey of emission regions. The Astrophysical Journal, 159:379.
- Ruffini, R. and Bonazzola, S. (1969). Systems of self-gravitating particles in general relativity and the concept of an equation of state. Physical Review, 187(5):1767.
- Sahni, V. and Wang, L. (2000). New cosmological model of quintessence and dark matter. Physical Review D, 62(10):103517.
- Sanchis-Gual, N., Degollado, J. C., Font, J. A., Herdeiro, C., and Radu, E. (2017). Dynamical formation of a hairy black hole in a cavity from the decay of unstable solitons. Classical and Quantum Gravity, 34(16):165001.
- Sarkar, A., Mondal, R., Das, S., Sethi, S. K., Bharadwaj, S., and Marsh, D. J. (2016a). The effects of the small-scale dm power on the cosmological neutral hydrogen (hi) distribution at high redshifts. Journal of Cosmology and Astroparticle Physics, 2016(04):012.
- Sarkar, A., Mondal, R., Das, S., Sethi, S. K., Bharadwaj, S., and Marsh, D. J. (2016b). The effects of the small-scale dm power on the cosmological neutral hydrogen (hi) distribution at high redshifts. Journal of Cosmology and Astroparticle Physics, 2016(04):012.
- Sauer, T. (2008). Nova geminorum 1912 and the origin of the idea of gravitational lensing. Archive for history of exact sciences, 62(1):1–22.

- Schive, H.-Y., Chiueh, T., and Broadhurst, T. (2014a). Cosmic structure as the quantum interference of a coherent dark wave. Nature Physics, 10(7):496.
- Schive, H.-Y., Chiueh, T., and Broadhurst, T. (2014a). Cosmic Structure as the Quantum Interference of a Coherent Dark Wave. Nature Phys., 10:496–499.
- Schive, H.-Y., Liao, M.-H., Woo, T.-P., Wong, S.-K., Chiueh, T., Broadhurst, T., and Hwang, W. P. (2014b). Understanding the core-halo relation of quantum wave dark matter from 3d simulations. Physical review letters, 113(26):261302.
- Schunck, F. E. and Mielke, E. W. (2003). General relativistic boson stars. Classical and Quantum Gravity, 20(20):R301.
- Schwabe, B., Niemeyer, J. C., and Engels, J. F. (2016). Simulations of solitonic core mergers in ultralight axion dark matter cosmologies. Physical Review D, 94(4):043513.
- Seidel, E. and Suen, W.-M. (1990). Dynamical evolution of boson stars: Perturbing the ground state. Physical Review D, 42(2):384.
- Seidel, E. and Suen, W.-M. (1990). Dynamical evolution of boson stars: Perturbing the ground state. , 42:384–403.
- Seidel, E. and Suen, W.-M. (1991). Oscillating soliton stars. Physical Review Letters, 66:1659–1662.
- Seidel, E. and Suen, W.-M. (1994). Formation of solitonic stars through gravitational cooling. Physical Review Letters, 72:2516–2519.
- Seljak, U. and Zaldarriaga, M. (1996). A line of sight approach to cosmic microwave background anisotropies. arXiv preprint astro-ph/9603033.
- Sikivie, P. (2012). An argument that the dark matter is axions. arXiv preprint arXiv:1210.0040.
- Silk, J. and Rees, M. J. (1998). Quasars and galaxy formation. arXiv preprint astro-ph/9801013.
- Simon, J. D., Bolatto, A. D., Leroy, A., and Blitz, L. (2003). High-resolution measurements of the dark matter halo of ngc 2976: evidence for a shallow density profile. The Astrophysical Journal, 596(2):957.
- Simon, J. D. and Geha, M. (2007). The kinematics of the ultra-faint milky way satellites: solving the missing satellite problem. The Astrophysical Journal, 670(1):313.
- Sin, S.-J. (1994). Late-time phase transition and the galactic halo as a bose liquid. Physical Review D, 50(6):3650.

- Skillman, S. W., Warren, M. S., Turk, M. J., Wechsler, R. H., Holz, D. E., and Sutter, P. (2014). Dark sky simulations: Early data release. arXiv preprint arXiv:1407.2600.
- Slepian, Z. and Goodman, J. (2012). Ruling out bosonic repulsive dark matter in thermal equilibrium. Monthly Notices of the Royal Astronomical Society, 427(1):839–849.
- Smoot, G. F., Bennett, C. L., Kogut, A., Wright, E., Aymon, J., Boguess, N., Cheng, E., De Amici, G., Gulkis, S., Hauser, M., et al. (1992). Structure in the COBE differential microwave radiometer first-year maps. The Astrophysical Journal, 396:L1–L5.
- Springel, V., Wang, J., Vogelsberger, M., Ludlow, A., Jenkins, A., Helmi, A., Navarro, J. F., Frenk, C. S., and White, S. D. (2008a). The aquarius project: the subhaloes of galactic haloes. Monthly Notices of the Royal Astronomical Society, 391(4):1685–1711.
- Springel, V., White, S. D., Frenk, C. S., Navarro, J. F., Jenkins, A., Vogelsberger, M., Wang, J., Ludlow, A., and Helmi, A. (2008b). Prospects for detecting supersymmetric dark matter in the galactic halo. Nature, 456(7218):73.
- Springel, V., White, S. D. M., Jenkins, A., Frenk, C. S., Yoshida, N., Gao, L., Navarro, J., Thacker, R., Croton, D., Helly, J., Peacock, J. A., Cole, S., Thomas, P., Couchman, H., Evrard, A., Colberg, J., and Pearce, F. (2005). Simulations of the formation, evolution and clustering of galaxies and quasars. Nature, 435(7042):629–636.
- Stadel, J., Potter, D., Moore, B., Diemand, J., Madau, P., Zemp, M., Kuhlen, M., and Quilis, V. (2009). Quantifying the heart of darkness with ghalo—a multibillion particle simulation of a galactic halo. Monthly Notices of the Royal Astronomical Society: Letters, 398(1):L21–L25.
- Straumann, N. (1992). Fermion and boson stars. In Relativistic gravity research with emphasis on experiments and observations, pages 267–293. Springer.
- Strigari, L. E., Bullock, J. S., Kaplinghat, M., Simon, J. D., Geha, M., Willman, B., and Walker, M. G. (2008). A common mass scale for satellite galaxies of the Milky Way. , 454:1096–1097.
- Suárez, A. and Chavanis, P.-H. (2015). Hydrodynamic representation of the klein-gordon-einstein equations in the weak field limit: General formalism and perturbations analysis. Physical Review D, 92(2):023510.
- Suárez, A. and Chavanis, P.-H. (2017). Cosmological evolution of a complex scalar field with repulsive or attractive self-interaction. Physical Review D, 95(6):063515.
- Suárez, A., Robles, V., Matos, T., González, C. M., Aguilar, J. M., and Barrera, L. R. (2014a). Accelerated cosmic expansion. Astrophysics and Space Science Proceedings, 38:107.

- Suárez, A., Robles, V. H., and Matos, T. (2014b). A review on the scalar field/bose-einstein condensate dark matter model. In Accelerated Cosmic Expansion, pages 107–142. Springer.
- Tanner, M. A. (2012). Tools for statistical inference. Springer.
- Tegmark, M., Zaldarriaga, M., and Hamilton, A. J. (2001). Towards a refined cosmic concordance model: Joint 11-parameter constraints from the cosmic microwave background and large-scale structure. Physical Review D, 63(4):043007.
- Tokdar, S. T. and Kass, R. E. (2010). Importance sampling: a review. Wiley Interdisciplinary Reviews: Computational Statistics, 2(1):54–60.
- Tonatiuh, M. et al. (2000). Quintessence and scalar dark matter in the universe.
- Trotta, R. (2008). Bayes in the sky: Bayesian inference and model selection in cosmology. Contemporary Physics, 49(2):71–104.
- Trotta, R. (2017). Bayesian methods in cosmology. arXiv preprint arXiv:1701.01467.
- Ureña-López, L. A. (2009). Bose-Einstein condensation of relativistic Scalar Field Dark Matter. , 1:014.
- Ureña-López, L. A. and Bernal, A. (2010). Bosonic gas as a galactic dark matter halo. , 82(12):123535.
- Ureña-López, L. A. and Liddle, A. R. (2002). Supermassive black holes in scalar field galaxy halos. Phys. Rev., D66:083005.
- Ureña-López, L. A., Robles, V. H., and Matos, T. (2017). Mass discrepancy-acceleration relation: A universal maximum dark matter acceleration and implications for the ultralight scalar dark matter model. , 96(4):043005.
- Ureña-López, L. A. and Bernal, A. (2010). Bosonic gas as a galactic dark matter halo. Physical Review D, 82(12):123535.
- Ureña-López, L. A. and Gonzalez-Morales, A. X. (2016). Towards accurate cosmological predictions for rapidly oscillating scalar fields as dark matter. Journal of Cosmology and Astroparticle Physics, 2016(07):048.
- Ureña-López, L. A., Matos, T., and Becerril, R. (2002). Inside oscillatons. Classical and Quantum Gravity, 19(23):6259.
- Vázquez, A. (2013). Constraining alternative cosmological models with current and future observations. PhD thesis, Kavli Institute for Cosmology/ Cavendish Laboratory, Cambridge University.

- Vázquez, J. A., Padilla, L. E., and Matos, T. (2018). Inflationary cosmology: From theory to observations. arXiv preprint arXiv:1810.09934.
- Veltmaat, J. and Niemeyer, J. C. (2016). Cosmological particle-in-cell simulations with ultralight axion dark matter. Physical Review D, 94(12):123523.
- Veltmaat, J., Schwabe, B., and Niemeyer, J. C. (2019). Baryon-driven growth of solitonic cores in fuzzy dark matter halos. arXiv preprint arXiv:1911.09614.
- Venemans, B., Findlay, J., Sutherland, W., De Rosa, G., McMahon, R., Simcoe, R., González-Solares, E., Kuijken, K., and Lewis, J. (2013). Discovery of three $z \approx 6.5$ quasars in the vista kilo-degree infrared galaxy (viking) survey. The Astrophysical Journal, 779(1):24.
- Verde, L. (2010). Statistical methods in cosmology. In Lectures on Cosmology, pages 147–177. Springer.
- Vilenkin, A. and Shellard, E. P. S. (2000). Cosmic strings and other topological defects. Cambridge University Press.
- Visinelli, L. (2017). Light axion-like dark matter must be present during inflation. Physical Review D, 96(2):023013.
- Vogelsberger, M., Marinacci, F., Torrey, P., and Puchwein, E. (2020). Cosmological simulations of galaxy formation. Nature Reviews Physics, 2(1):42–66.
- Walker, M. G., Mateo, M., Olszewski, E. W., Peñarrubia, J., Wyn Evans, N., and Gilmore, G. (2009). A Universal Mass Profile for Dwarf Spheroidal Galaxies? , 704:1274–1287.
- Walsh, S., Willman, B., and Jerjen, H. (2008). The invisibles: a detection algorithm to trace the faintest milky way satellites. The Astronomical Journal, 137(1):450.
- White, S. D., Frenk, C. S., Davis, M., and Efstathiou, G. (1987). Clusters, filaments, and voids in a universe dominated by cold dark matter. The Astrophysical Journal, 313:505–516.
- Willott, C. J., Delorme, P., Omont, A., Bergeron, J., Delfosse, X., Forveille, T., Albert, L., Reylé, C., Hill, G. J., Gully-Santiago, M., et al. (2007). Four quasars above redshift 6 discovered by the canada-france high-z quasar survey. The Astronomical Journal, 134(6):2435.
- Willott, C. J., Delorme, P., Reylé, C., Albert, L., Bergeron, J., Crampton, D., Delfosse, X., Forveille, T., Hutchings, J. B., McLure, R. J., et al. (2010). The canada-france high-z quasar survey: Nine new quasars and the luminosity function at redshift 6. The Astronomical Journal, 139(3):906.

- Wu, X.-B., Wang, F., Fan, X., Yi, W., Zuo, W., Bian, F., Jiang, L., McGreer, I. D., Wang, R., Yang, J., et al. (2015). An ultraluminous quasar with a twelve-billion-solar-mass black hole at redshift 6.30. Nature, 518(7540):512.
- Zee, A. (2010). Quantum field theory in a nutshell, volume 7. Princeton university press.
- Zhang, J., Kuo, J.-L., Liu, H., Tsai, Y.-L. S., Cheung, K., and Chu, M.-C. (2017). The importance of quantum pressure of fuzzy dark matter on lyman-alpha forest. arXiv preprint arXiv:1708.04389.
- Zhang, J., Tsai, Y.-L. S., Kuo, J.-L., Cheung, K., and Chu, M.-C. (2018). Ultralight axion dark matter and its impact on dark halo structure in n-body simulations. The Astrophysical Journal, 853(1):51.
- Zwicky, F. (1933). The redshift of extragalactic nebulae. Helv. Phys. Acta, 6(110):138.